

Single-Cell Analysis of Influenza A Virus Replication:
Sources of Cell-to-Cell Heterogeneity and
Discovery of a Novel Type of Defective Interfering Particle

Dissertation

zur Erlangung des akademischen Grades

Doktoringenieur

(Dr.-Ing.)

von: Dipl.-Ing. Sascha Young Kupke

geboren am: 31. Oktober 1984 in Berlin

genehmigt durch die Fakultät für Verfahrens- und Systemtechnik
der Otto-von-Guericke Universität Magdeburg

Promotionskommission: Prof. Dr.-Ing. Kai Sundmacher (Vorsitz)

Prof. Dr.-Ing. Udo Reichl (Gutachter)

Prof. John Yin (Gutachter)

Dr. Hansjörg Hauser (Gutachter)

eingereicht am: 08. März 2019

Promotionskolloquium am: 05. Februar 2020

Abstract

Influenza A viruses (IAVs) cause respiratory disease and are a major human pathogen that can give rise to a high morbidity. Besides annual epidemics, IAVs can occasionally also cause a more severe pandemic. Typically, the best protection against the flu is provided by annual vaccination. One way to produce human influenza vaccines are cell culture-based manufacturing systems. Naturally, the smallest production unit in such a process is the infected single cell. However, it is well known that cells in a seemingly homogenous population display a vast cell-to-cell heterogeneity. In the context of this PhD work, we conducted single-cell analysis of IAV-infected cells for applications in cell culture-based influenza virus production. Specifically, we studied the cell-to-cell variability in virus titers to gain a deeper understanding and an improved description of the process. Moreover, we strived for a comprehension of high-productive single cells to possibly derive strategies to improve the production yield.

Therefore, we devised a single-cell analysis workflow for IAV-infected cells. For this, we isolated single IAV-infected Madin-Darby canine kidney (MDCK) cells in 384 well plates using a limiting dilution approach, in which single cells in individual wells were identified by microscopy. After incubation, virus titers in the supernatant were investigated by plaque assay and intracellular parameters by real-time reverse transcription quantitative PCR and conventional RT-PCR. The procedure enabled (i) absolute quantification of virus titers and intracellular genomic viral RNAs (vRNAs), (ii) a good throughput of single-cell measurements, (iii) no apparent perturbation of cellular behavior despite the processing and isolation of single cells, and (iv) multiparametric correlation of the single-cell virus yield to either: the cell size, ribosomal RNAs, up to four different genomic vRNAs (simultaneously), or to intracellular defective interfering (DI) RNAs on up to three viral genome segments (simultaneously). In future studies, we may couple our experimental platform to single-cell RNA sequencing (via next-generation sequencing technologies) to study the whole-cell transcriptome of IAV-infected cells, and specifically, to compare the transcriptomic information to the single-cell virus titer.

Next, the established single-cell analysis procedure was used to study cell-to-cell variability in IAV replication. We observed a vast heterogeneity with virus titers that ranged from 1 to about 1000 plaque-forming units per cell, and intracellular vRNAs that showed quantitative differences which spanned almost three orders of magnitude. We further showed that cell-to-cell heterogeneity in IAV replication can be generated by both, the inherent randomness in biochemical reactions (i.e., sources of intrinsic noise) and deterministic factors (i.e., sources of extrinsic noise). The latter are (yet unknown) properties, different between individual cells, that

can affect virus replication in each cell differently. However, more research in single-cell virology is required to resolve the contribution of stochasticity to the cell-to-cell heterogeneity in virus replication (in comparison to the contribution caused by sources of extrinsic noise). Taken together, we show that virus infections are highly variable at the single cell level, and that cell population-based experiments are not covering crucial aspects of virus infections.

Next, we investigated potential deterministic sources of the large cell-to-cell heterogeneity in virus titers. We showed that differences in the cell size and the ribosome content did not appear to affect the virus yield of a single cell. Moreover, the between-cell variability in the properties of individual cells (present in the non-clonal MDCK cell line) did also not seem to account for the large single-cell diversity in IAV replication. Finally, we showed that the virus-to-virus genetic heterogeneity (of the infecting virus population) did also not appear to influence the cell-to-cell heterogeneity in IAV replication, except for defective interfering particles (DIPs). DIPs are defective, non-infectious virus particles that harbor a deleted form of the viral RNA genome, which interfere with the replication of their homologous standard virus. More specifically, we demonstrated that the content of such deleted DI RNAs in an infected single cell can influence the cell-specific virus titer. However, our results also indicated that additional unknown factors may further affect the cell-to-cell variability in IAV replication, which remain to be elucidated. Altogether, our results advance single-cell virology research towards an understanding of the large cell-to-cell heterogeneity in virus infections.

Finally, utilizing single-cell analysis, we discovered (and enriched) a novel type of IAV-derived DIP, termed "OP7" virus. Conventional DIPs (cDIPs) typically harbor a large internal deletion in one genomic vRNA, whereas OP7 virus contained various point mutations in segment 7 (S7) vRNA. These substitutions affected the promotor regions, encoded proteins, and genome packaging signals. We further characterized OP7 virus replication at different intracellular viral life cycle steps in cell-population-based experiments. Most importantly, similar to cDIPs, OP7 virus showed strong interference with replication of various IAV strains, including relevant epidemic and pandemic human IAV strains. Moreover, we demonstrated that OP7 virus can also interfere with IAV replication in human cell lines. Therefore, we believe that OP7 virus may be a promising candidate for antiviral therapy. Future research efforts may focus on gathering mechanistic insights into OP7 virus molecular biology, animal trials (e.g. in mice and in ferrets) to investigate its antiviral potential, and the development of cell culture-based manufacturing of OP7 virus.

Kurzfassung

Influenza A Viren (IAV) verursachen Atemwegserkrankungen und sind ein bedeutendes humanes Pathogen, welches zu einem hohen Erkrankungsrate führen kann. Neben der jährlichen Epidemie können IAV auch gelegentlich zu schweren Pandemien führen. Üblicherweise wird der beste Schutz gegen die Grippe durch eine jährliche Impfung gewährleistet. Eine Möglichkeit, humane Influenza Impfstoffe zu produzieren, sind zellkulturbasierte Herstellungssysteme. Selbstverständlich ist die kleinste Produktionseinheit in solch einem Prozess die infizierte Einzelzelle. Es ist jedoch bekannt, dass Zellen in einer scheinbar homogenen Population eine enorme Heterogenität von Zelle zu Zelle aufweisen. Im Kontext dieser Doktorarbeit haben wir die Einzelzellanalyse von IAV-infizierten Zellen für mögliche Anwendungen in der zellkulturbasierten Influenzavirus Produktion durchgeführt. Insbesondere haben wir die Variabilität in den Virustitern zwischen den Zellen untersucht, um ein besseres Verständnis und eine verbesserte Beschreibung des Prozesses zu erreichen. Weiterhin haben wir ein Verständnis von hochproduktiven Einzelzellen angestrebt, um gegebenenfalls Strategien für eine höhere Produktionsausbeute abzuleiten zu können.

Aus diesem Grund haben wir einen Workflow zur Einzelzellanalyse für IAV-infizierte Zellen entwickelt. Hierfür haben wir einzelne, IAV-infizierte Madin-Darby canine kidney (MDCK) Zellen in 384 Well Platten mit Hilfe eines „limitierenden Verdünnungsansatzes“ isoliert, in welchem wir die Einzelzellen (in einzelnen Wells) mikroskopisch identifiziert haben. Nach der Inkubation wurden die Virustiter in den Überständen mit Hilfe des Plaque Tests quantifiziert und intrazelluläre Parameter durch quantitative real-time reverse Transkription PCR und der konventionellen RT-PCR untersucht. Die Prozedur ermöglicht (i) die absolute Quantifizierung von Virustitern und intrazellulärer genomischer viraler RNA (vRNA), (ii) einen guten Durchsatz an Einzelzellmessungen, (iii) keine offensichtliche Störung des zellulären Verhaltens trotz der Verarbeitung und Isolierung von Einzelzellen und (iv) eine multiparametrische Korrelation des Virustiters mit: der Größe der Zelle, ribosomalen RNAs, bis zu vier verschiedenen genomischen vRNAs (gleichzeitig) oder mit intrazellulären defekt-interferierenden (DI) RNAs von drei verschiedenen Genomsegmenten (gleichzeitig). In zukünftigen Studien könnten wir unsere experimentelle Plattform mit der Einzelzell-RNA Sequenzierung (mit Hilfe von „next-generation“ Sequenzieretechnologien) koppeln, um das Gesamtzelltranskriptom von IAV-infizierten Einzelzellen zu untersuchen und insbesondere, um die transkriptomische Informationen mit dem Einzelzelltiter zu vergleichen.

Anschließend wurde die etablierte Prozedur für die Einzelzellanalyse verwendet, um die Variabilität in der IAV Replikation von Zelle zu Zelle zu untersuchen. Wir haben eine enorme Heterogenität beobachtet. Die Virustiter reichten von 1 bis ca. 1000 plaqueformenden Einheiten pro Zelle und intrazelluläre vRNAs zeigten quantitative Unterschiede, die fast drei Zehnerpotenzen umfasst haben. Weiterhin zeigen wir, dass die Heterogenität von Zell zu Zelle in der IAV Replikation durch die inhärente Zufälligkeit von biochemischen Reaktionen (intrinsisches Rauschen) und deterministischen Faktoren (Quellen extrinsischen Rauschens) generiert werden kann. Das Letztgenannte sind (bisher unbekannte) Eigenschaften, die sich zwischen den Zellen unterscheiden und dadurch die Virusreplikation jeder einzelnen Zelle auch unterschiedlich beeinträchtigen können. Es ist jedoch weitere Forschung in der Einzelzellvirologie notwendig, um den Beitrag der Stochastizität zur Heterogenität von Zelle zu Zelle in der Virusreplikation aufzuklären (im Vergleich zum Beitrag von extrinsischen Faktoren). Zusammengefasst zeigen wir, dass Virusinfektionen äußerst variabel auf dem Einzelzelllevel sind, und dass Zellpopulationsexperimente kritische Aspekte der Virusinfektion nicht erfassen können.

Als Nächstes haben wir potentielle deterministische Quellen der großen Heterogenität in den Virustitern zwischen den Einzelzellen untersucht. Wir haben gezeigt, dass die vorhandenen Unterschiede in der Zellgröße und im Ribosomengehalt den Virustiter einer einzelnen Zelle nicht zu beeinflussen scheinen. Weiterhin deuten unsere Ergebnisse darauf hin, dass die Unterschiede in den Eigenschaften zwischen den Zellen (der nichtklonalen MDCK Zelllinie) nicht verantwortlich sind für die große Einzelzelldiversität in der IAV Replikation. Schlussendlich haben wir gezeigt, dass die genetische Heterogenität von Virus zu Virus (der infizierenden Viruspopulation) auch nicht die Heterogenität in der IAV Replikation zwischen den Zellen zu beeinflussen scheint, mit Ausnahme von DI Partikeln (DIPs). DIPs sind defekte, nichtinfektiöse Viruspartikel, die eine deletierte Form des viralen RNA Genoms enthalten und die mit der Replikation ihres homologen standard Virus (STV) interferieren können. Insbesondere zeigen wir, dass der Gehalt solcher intrazellulären DI RNAs den zellspezifischen Virustiter in infizierten Einzelzellen beeinflussen kann. Jedoch deuten unsere Ergebnisse auch darauf hin, dass es darüber hinaus weitere unbekannte Faktoren gibt, die die Variabilität von Zelle zu Zelle beeinflussen können und welche noch erforscht werden müssten. Insgesamt leisten unsere Erkenntnisse einen Beitrag zur Forschung in der Einzelzellvirologie hinsichtlich einer Aufklärung der großen Heterogenität in Virusinfektionen zwischen den Einzelzellen.

Zu guter Letzt haben wir einen neuartigen Typ von IAV DIP (genannt „OP7“ Virus) mit Hilfe der Einzelzellanalytik entdeckt und angereichert. Konventionelle DIPs (kDIPs) enthalten

typischerweise eine große interne Deletion in einer genomischen vRNA, wobei OP7 Virus zahlreiche Punktmutationen in Segment 7 (S7) vRNA enthält. Diese Substitutionen betreffen die Promotorregionen, die codierten Proteine und das Genomverpackungssignal. Weiterhin haben wir die Replikation von OP7 Virus in verschiedenen Schritten des intrazellulären viralen Lebenszyklus in zellpopulationsbasierten Versuchen charakterisiert. Insbesondere haben wir gezeigt, dass OP7 Virus (ähnlich wie kDIPs) eine starke Interferenz mit der Replikation von verschiedenen IAV Stämmen zeigt, inklusive relevanter epidemischer und pandemischer humaner IAV Stämme. Weiterhin demonstrieren wir, dass OP7 Virus in der Lage ist, auch mit der IAV Replikation in humanen Zelllinien zu interferiert. Aus diesem Grund sind wir davon überzeugt, dass OP7 Virus ein vielversprechender Kandidat für eine antivirale Therapie sein könnte. Zukünftige Forschungsvorhaben könnten sich auf mechanistische Einblicke in die OP7 Virus Molekularbiologie, Tierversuche (z.B. in Mäusen und Frettchen), um das antivirale Potential zu untersuchen, und die Entwicklung der zellkulturbasierten Produktion von OP7 Virus fokussieren.

Contents

Abstract	III
Kurzfassung	V
Contents	VIII
List of abbreviations	XII
1. Introduction	1
2. Theoretical background.....	4
2.1. Influenza A virus.....	4
2.1.1. Morphology	4
2.1.2. Proteins encoded by the viral genome	6
2.1.3. Intracellular viral replication cycle.....	6
2.1.4. Defective interfering particles.....	9
2.1.5. Cell culture-based influenza vaccine manufacturing.....	12
2.2. Single-cell analysis	16
2.2.1. Cell-to-cell heterogeneity	16
2.2.2. Extrinsic and intrinsic noise.....	18
2.2.3. Single-cell analysis technologies.....	20
2.2.4. Virus infection at the individual cell level	22
2.2.4.1. Bacterial cells	22
2.2.4.2. Animal cells	23
2.2.4.3. DIP co-infection	25
2.2.4.4. Innate immune response	26
2.2.4.5. Whole transcriptome analysis.....	27
3. Materials and methods	29
3.1. Cell cultivation and virus infection	29
3.1.1. Media and buffers	29
3.1.2. Cell cultivation	30
3.1.2.1. Generation of clonal MDCK cells	30
3.1.3. Virus infection	31

3.1.3.1. Cell population-based infection.....	31
3.1.3.2. Isolation of infected single cells.....	32
3.1.3.3. Generation of plaque-purified virus.....	33
3.1.3.4. Enrichment of OP7 virus.....	34
3.1.3.5. Virus inactivation for ns-TEM analysis.....	34
3.2. Analytics	35
3.2.1. Virus quantification	35
3.2.1.1. HA Assay.....	35
3.2.1.2. TCID ₅₀ assay	35
3.2.1.3. Plaque Assay	36
3.2.2. Real-Time RT-qPCR.....	36
3.2.2.1. Quantification of viral RNAs.....	37
3.2.2.2. Analysis of the innate immune response	40
3.2.2.3. Quantification of ribosomes.....	41
3.2.3. Segment-specific RT-PCR	41
3.2.3.1. Procedure for cell population-based samples	42
3.2.3.2. Procedure for single-cell-based samples.....	43
3.2.4. Determination of vRNA sequences.....	44
3.2.5. Western blot analysis	46
3.2.6. Imaging Flow Cytometric Analysis	47
3.2.6.1. Sampling and staining	47
3.2.6.2. Sample acquisition and software analysis	48
4. Results and discussion	49
4.1. Single-cell analysis of IAV replication	49
4.1.1. Development of single-cell analysis approach	49
4.1.1.1. Experimental workflow	49
4.1.1.2. Comparison of single-cell- and population-derived experiments.....	51
4.1.1.3. Technical measurement errors	52
4.1.2. Cell-to-cell heterogeneity in IAV replication	53
4.1.2.1. Virus titers.....	53
4.1.2.2. vRNA content	54
4.1.2.3. Extrinsic and intrinsic noise.....	55
4.1.2.4. Differences between virus strains	57
4.1.3. Discussion of experimental procedure.....	58
4.1.4. Discussion of cell-to-cell heterogeneity in IAV replication.....	64
4.2. Sources of cell-to-cell heterogeneity in IAV replication	68

4.2.1. Effect of virus-derived characteristics.....	68
4.2.1.1. Extrinsic noise	68
4.2.1.2. Progress of infection	69
4.2.1.3. Multiplicity of infection.....	71
4.2.1.4. Virus-to-virus heterogeneity.....	73
4.2.2. Influence of cell-based characteristics.....	75
4.2.2.1. Cell size	75
4.2.2.2. Ribosome content	76
4.2.2.3. Between-cell variability.....	77
4.2.3. Effect of DIP co-infection.....	84
4.2.4. Discussion of the effect of virus-derived characteristics	86
4.2.5. Discussion of the influence of cell-based characteristics.....	89
4.2.6. Discussion of the effect of DIP co-infection	91
4.3. Discovery of a novel type of DIP (OP7 virus).....	94
4.3.1. Discovery and enrichment	94
4.3.2. In-depth characterization.....	99
4.3.2.1. Infectivity.....	99
4.3.2.2. Genomic vRNA sequence	102
4.3.2.3. Intracellular viral RNA dynamics	104
4.3.2.4. Intracellular viral protein localization dynamics	107
4.3.2.5. Interference with virus replication	109
4.3.3. Discussion of the novel type of DIP (OP7 virus)	112
5. Conclusion and outlook	118
Bibliography.....	122
List of publications	137
List of figures.....	140
List of tables	142
Appendix.....	143
Appendix A - List of chemicals and reagents	143
Appendix B - List of equipment	145
Appendix C - Operating Instructions.....	146
Appendix C.1 - Text excerpt (Generation of clonal MDCK cells).....	146
Appendix C.2 - Text excerpt (Quantification of ribosomes).....	148

Appendix C.3 - Operating instructions (Imaging flow cytometry) 152

List of abbreviations

7-AAD	-	7-aminoactinomycin
AFM	-	Atomic force microscopy
ATCC	-	American Type Culture Collection
ATF	-	Alternating Tangential Flow
BF	-	Brightfield
BHK	-	Baby hamster kidney
BSA	-	Bovine serum albumin
CDS	-	Coding sequence
CEF	-	Chicken embryo fibroblast
CFP	-	Cyan fluorescent protein
CH	-	Channel
CRM1	-	Chromosome region maintenance 1
cRNA	-	Complementary RNA
CV	-	Coefficient of variation
DAPI	-	4',6-diamidino-2-phenylindole
DI	-	Defective interfering
DIP	-	Defective interfering particles
DMEM	-	Dulbecco's Modified Eagle's Medium
ECACC	-	European Collection of Cell Cultures
EDTA	-	Ethylenediaminetetraacetic acid
ER	-	Endoplasmic reticulum
FACS	-	Fluorescence-activated cell sorting
FCS	-	Fetal calf serum
FITC	-	Fluorescein isothiocyanate
FL	-	Full-length
FMDV	-	Foot-and-mouth disease
GFP	-	Green fluorescent protein
GAPDH	-	Glyceraldehyde 3-phosphate dehydrogenase

List of abbreviations

GMEM	-	Glasgow Minimum Essential Medium
H1N1-pdm09	-	Pandemic influenza A/California/7/2009 of subtype H1N1
H3N2	-	Influenza A/Hong Kong/4801/2014 of subtype H3N2
HA	-	Hemagglutinin
HEK 293	-	Human embryonic kidney 293
HIV	-	Human immunodeficiency virus
hpi	-	Hours post infection
HRP	-	Horseradish-peroxidase
IAV	-	Influenza A virus
IBV	-	Influenza B virus
IFN	-	Interferon
LOD	-	Limit of detection
M1	-	Matrix protein 1
M2	-	Matrix protein 2
mAb	-	Monoclonal antibody
MDCK	-	Madin-Darby Canine Kidney
MODIP	-	Multiplicity of DIP
MOI	-	Multiplicity of infection
mRNA	-	Messenger RNA
mAb	-	Monoclonal antibody
MS	-	Mass spectrometry
Mx1	-	Myxovirus resistant gene 1
NA	-	Neuraminidase
NCBI	-	National Center for Biotechnology Information
nDEP	-	Negative dielectrophoresis
NEP	-	Nuclear export protein
NES	-	Nuclear export signal
NGS	-	Next-generation sequencing
NIBSC	-	National Institute for Biological Standards and Control
NLS	-	Nuclear localization signal

List of abbreviations

NP	-	Nucleoprotein
NS1	-	Non-structural protein 1
ns-TEM	-	Negative stain transmission electron microscopy
nt	-	Nucleotides
OP7	-	Over-proportional level of S7
PA	-	Polymerase acid
pAb	-	Polyclonal antibody
PB1	-	Polymerase basic 1
PB2	-	Polymerase basic 2
PBS	-	Phosphate buffered saline
PDMS	-	Polydimethylsiloxane
PFU	-	Plaque-forming units
Poly(A)	-	Polyadenylated
PP	-	Plaque-purified
PR8	-	Influenza A/Puerto Rico/8/34 of subtype H1N1
PR8-NIBSC	-	PR8 from NIBSC
PR8-RKI	-	PR8 from RKI
PVDF	-	Polyvinylidene difluoride
qPCR	-	Quantitative PCR
RdRp	-	RNA-dependent RNA polymerase
RefSeq	-	Reference sequence
RFP	-	Red fluorescent protein
RIG-I	-	Retinoic acid inducible gene I
RKI	-	Robert Koch institute
RIPA	-	Radioimmunoprecipitation assay
rRNA	-	Ribosomal RNA
RT-qPCR	-	Reverse transcription quantitative PCR
S	-	Segment
S7-OP7	-	S7 of OP7 virus
scRNA-seq	-	Single-cell RNA sequencing

List of abbreviations

SEC	-	Steric exclusion chromatography
SOP	-	Standard operation procedure
STR	-	Stirred tank reactor
STV	-	Standard virus
TCID ₅₀	-	50% tissue culture infective dose
TPA	-	Tris-Phosphate-EDTA
UTR	-	Untranslated region
Vero	-	African green monkey kidney epithelial
vRNA	-	Viral RNA
vRNP	-	Viral ribonucleoprotein
VSV	-	Vesicular stomatitis virus
WB	-	Western blot
WCB	-	Working cell bench
WEE	-	Western equine encephalomyelitis
WHO	-	World Health Organization
YFP	-	Yellow fluorescent protein

1. Introduction

Influenza viruses cause respiratory disease, and are regarded as a major human pathogen. Every year, about five to 20% of the human population is affected by influenza virus infections. The symptoms of the disease (comprising fever, cough, headache, muscle and joint pain, sore throat, and a runny nose) usually last less than one week. Nevertheless, the flu poses a large economic burden due to worker absenteeism and productivity losses. In addition, influenza virus infections can also cause severe illness, or even death, for vulnerable individuals like the young and elderly, pregnant women, individuals with certain chronic diseases, or individuals with immunocompromised medical conditions. According to the World Health Organization (WHO), three to five million cases of severe illness and 290,000 to 650,000 cases of death are documented in every annual flu season (WHO, 2019).

Influenza viruses are able to infect a broad spectrum of hosts, including poultry, pigs, horses, dogs, sea mammals, and humans (Wright et al., 2013). Yet, the main reservoir are wild aquatic birds from which they can occasionally spread to other species. Moreover, influenza viruses are known for their quick adaptability, which is the reason why the virus is capable to re-emerge and infect their hosts every year, although the host may have already acquired protection against previous strains through the adaptive immune response. On the one hand, this quick adaptation is facilitated by point mutations that gradually occur in the viral genome, which lead to alterations in the sequence and structure of the viral surface proteins. Such an "antigenic drift" is the main cause of annual influenza epidemics. On the other hand, influenza viruses are also able to recombine and reassort their genetic material once two different virus strains infect one individual organism. This is a result of the segmented RNA genome of influenza viruses that comprises eight separate RNAs. More specifically, individual genome segments of one strain can be exchanged by segments of another strain in a co-infection, which can give rise to a new virus strain with altered properties. Such a more severe "antigenic shift" can lead to a higher susceptibility of the host to that new virus strain, a faster spread of the newly emerged virus, and possibly a pandemic. In the last century, three pandemic outbreaks occurred: the "Spanish influenza" (1918) that claimed about 40 million cases of death, the "Asian influenza" (1957) and "Hong Kong influenza" (1968) pandemics, which each resulted in the loss of one to two million lives (Hampson and Mackenzie, 2006). In 2009, the first 21st century's pandemic outbreak occurred, which resulted in more than 22 million reported infections, the closing of schools, and the blocking of borders (Rumschlag-Booms and Rong, 2013). Fortunately, back then, the number of worldwide deaths was estimated to lie only between 123,000 and 203,000

human individuals (Simonsen et al., 2013). Another potential threat are avian influenza virus strains (of which some are highly pathogenic) that can also infect domestic birds and poultry. Such strains endanger not only the animals, as they can also sporadically infect humans. Depending on the avian strain, such infections can cause a very high fatality rate of up to 60% in humans. However, so far, human-to-human transmissions are very rare, limited and non-sustained (Ma et al., 2019, Lee et al., 2017, Chatziprodromidou et al., 2018). The likelihood that avian strains are ever able to adapt, to easily transmit from human to human and cause a pandemic, is currently unknown.

In general, the best protection against influenza virus infections is provided by annual vaccination. Yet, since the 1940s, the manufacturing of influenza vaccines is still mainly based on the conventional production in embryonated hens' eggs. Here, the allantoic cavities of chicken eggs are inoculated with influenza viruses, where virus propagation takes place. Afterwards, the viral surface proteins are purified to formulate the vaccine. However, this process comprises several drawbacks, such as (for instance) a limited flexibility in terms of expanding production capacities in the case of a pandemic, the dependency on a reliable egg supply chain, issues to maintain sterility, occasionally poor growth of certain influenza virus strains, and potential allergic reactions in response to vaccination due to the presence of egg proteins. Therefore, cell culture-based production processes have been developed since the mid-1990s as an alternative manufacturing system for vaccines. In such a process, animal cell lines are propagated in large-scale cultivation systems (i.e., bioreactors) towards high cell densities, followed by infection and subsequent virus propagation. Here, the key advantages are (i) a better scale-up flexibility and platform diversity, leading to shorter response times for new vaccine strains, (ii) a closed and sterile production chain, and (iii) comparable or higher virus titers in relation to egg-based production, and (iv) the independency on the supply of embryonated eggs, which is advantageous in light of the threat of chicken layer flocks by avian influenza strains. Moreover, cell culture-based processes (which also include recombinant vaccine production in baculovirus expression systems in insect cells) are increasingly approved and utilized nowadays for the production of human vaccines.

One of the major research aims of the Bioprocess Engineering (BPE) group of the Max Planck Institute for Dynamics of Complex Technical Systems (Magdeburg, Germany) is the optimization of cell culture-based manufacturing. Naturally, the smallest production unit in such a process is the infected single cell. However, it is well known from previous research in single-cell analysis that individual cells, even of an isogenic population, usually display a large cell-to-cell variability in their properties. For instance, heterogeneity can be typically observed with

respect to the quantities of specific proteins and mRNAs, or regarding differences in the cell size and cell cycle stage. In the context of this PhD work, we were interested in the extent of cell-to-cell heterogeneity in virus titers, and in particular, what may define a high- or low-productive infected single cell. Such a knowledge would facilitate a deeper understanding and an improved description of cell culture-based influenza virus production processes, and potentially, even the derivation of strategies to improve the production yield.

An additional source of cell-to-cell heterogeneity is the inherent stochasticity (i.e., the randomness) of biochemical reactions. In principle, virtually every cellular process underlies a certain degree of randomness. This stochasticity can, for instance, arise by random diffusion (i.e., Brownian motion) or by random fluctuations in the reaction rates of enzymes. We believe that such stochastic effects might also affect the influenza virus production process. More specifically, we typically observe large differences in the onset of virus production between independent bioreactor runs. The process itself starts with only very few infected cells; therefore, virus propagation takes place over several rounds of infection cycles. Thus, in the course of the relatively long production process, a gradually increasing fraction of cells are becoming infected, which may give rise to the accumulation of variation in virus replication and propagation due to stochastic effects. Therefore, a better understanding of the stochasticity in virus replication, which can presumably affect the cell culture-based production process, was of additional interest.

Conclusively, the topic of this PhD work is single-cell analysis of influenza virus-infected cells. In chapter 2., we provide a background to influenza viruses, the viral replication cycle, virus-derived defective interfering particles (DIPs), cell culture-based influenza vaccine manufacturing, and single-cell analysis. Subsequently, we present the workflow for single cell analysis that was set-up and established in the context of this PhD work (section 4.1.), along with the results of the cell-to-cell heterogeneity in influenza virus replication. Next, we investigate factors that may potentially affect, or generate, the between-cell variability in virus titers in section 4.2. Lastly (in section 4.3.), we present the discovery of a novel type of influenza A virus (IAV)-derived DIP, facilitated by single-cell analysis, which may be utilized as an antiviral agent. Finally, a conclusion and outlook of the PhD work is given in chapter 5.

2. Theoretical background

The first section of this chapter provides a background to influenza viruses, in particular to their structure and the intracellular viral replication cycle. Subsequently, the nature of DIPs and a short overview of cell culture-based influenza vaccine manufacturing are introduced. Finally, the last section outlines cell-to-cell heterogeneity, applications and technologies for single-cell analysis, as well as a background to the exceptional features of virus replication that can be observed at the single-cell level.

2.1. Influenza A virus

Influenza viruses belong to the family of Orthomyxoviridae. They comprise four genera, namely influenza virus A, B, C, and D (Shaw and Palese, 2013, Su et al., 2017a), of which only influenza A and B can cause annual epidemics in humans. However, influenza B virus (IBV) typically accounts for only about 20% of influenza-related hospitalizations in every year (Paul Glezen et al., 2013, Tan et al., 2018). Therefore, the major human pathogen is the influenza A virus (IAV), which can also occasionally cause severe pandemics.

IAVs contain a segmented, single-stranded RNA genome of negative polarity that comprises eight individual viral RNAs (Shaw and Palese, 2013). The different IAV strains are termed based on the genus, the place of isolation, the number of the isolate, the year of isolation, and the subtype of their antigens (i.e. the surface proteins hemagglutinin (HA) and neuraminidase (NA)). For example, the strain influenza A/Puerto Rico/8/34 of subtype H1N1 (PR8), which is widely used both in academia and industry, was the 8th isolate in the year of 1934 in Puerto Rico, and contains the surface proteins HA and NA of subtype 1.

2.1.1. Morphology

Depending on the strain, IAVs can be either spherical (the diameters range from 80-120 nm) or filamentous, with elongated particles that reach up to 1 μm (Harris et al., 2006, Calder et al., 2010). Figure 2.1. shows the structure of an IAV particle. The IAV virus envelope consists of a lipid bilayer (derived from the host cells' membrane) that harbors the viral surface proteins HA, NA, and the viral ion channel matrix protein 2 (M2). Underneath, a layer comprising multiple copies of the viral matrix protein 1 (M1) can be found, which separates the virus core from the

envelope. The viral core itself contains some copies of the nuclear export protein (NEP) and eight individual IAV genome segments.

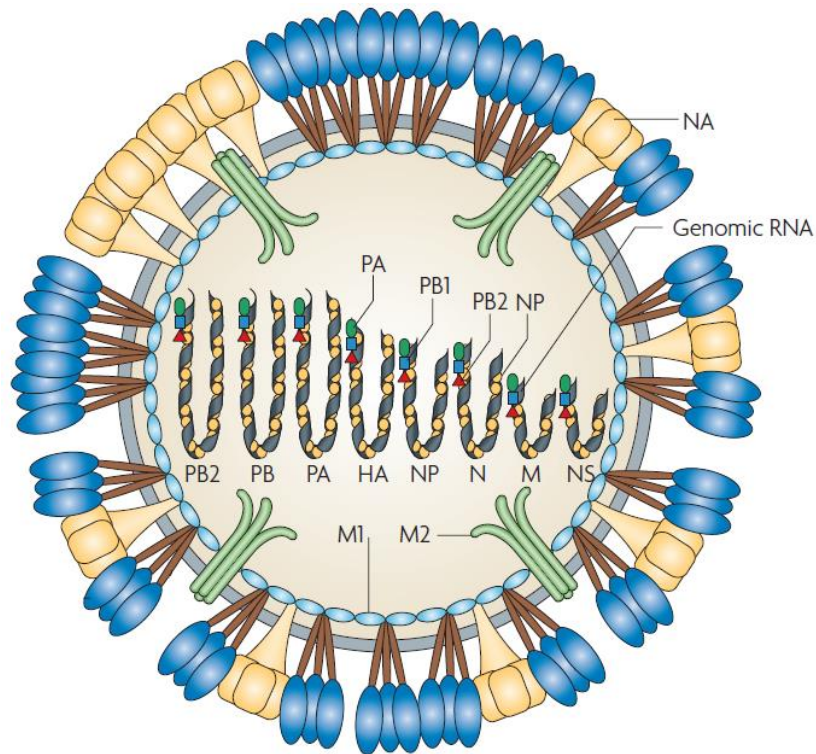


Figure 2.1. IAV particle structure. The envelope of the influenza A virus consists of a lipid bilayer membrane (of host cell origin) that contains the viral surface proteins HA, NA, and M2. Underneath, multiple copies of the viral M1 protein are located, which separate the viral core from the envelope. The viral core harbors the eight individual genomic vRNAs. The vRNAs each encode for at least one viral protein, and are associated with the viral polymerase proteins PB2, PB1, and PA, and multiple copies of the viral NP protein. Illustration modified from (Karlsson Hedestam et al., 2008).

Each of IAVs' genomic viral RNA (vRNA) occurs encapsidated with viral proteins, forming the so-called viral ribonucleoprotein (vRNP) complexes (Noda and Kawaoka, 2010, Zheng and Tao, 2013). These rod-shaped complexes (Compans et al., 1972) involve multiple copies of the nucleoprotein (NP) and the RNA-dependent RNA polymerase (RdRp) (Eisfeld et al., 2015, Compans et al., 1972, Moeller et al., 2012). The tripartite RdRp protein complex itself comprises the viral polymerase basic proteins 2 and 1 (PB2 and PB1), and the polymerase acidic protein (PA). In the virus particle, the eight vRNPs form a "7+1" configuration, where seven vRNPs form a ring-like structure around one core segment (Noda et al., 2006, Nakatsu et al., 2016, Noda and Kawaoka, 2012, Noda et al., 2018). Moreover, IAV virions can

additionally contain some host cell proteins that may have been incorporated unspecifically (Shaw et al., 2008).

2.1.2. Proteins encoded by the viral genome

Each of the eight genome segments encodes for at least one viral protein, and up to 18 IAV proteins were described so far (Vasin et al., 2014). The length of the genome segments ranges from 890-2341 bp for the PR8 strain (Lamb and Krug, 2001). Segment 1 (S1), S2, and S3 provide the polymerase subunits PB2, PB1, and PA, respectively, and the NP protein (which encapsidates the vRNAs) is encoded by S5. The surface proteins HA and NA are provided by S4 and S6, respectively. The regulatory viral protein M1 and the multifunctional non-structural protein 1 (NS1) are located on S7 and S8.

To increase the number of viral proteins encoded by each segment, IAVs employ alternative splicing mechanisms (Vasin et al., 2014), which result in the ion channel protein M2 and NEP (which facilitates nuclear export of vRNPs). These alternatively spliced proteins are encoded by S7 and S8, respectively. Moreover, IAVs utilize alternative open reading frames (e.g. in S2) and ribosomal frameshifting (in S3) that give rise to more viral proteins (Vasin et al., 2014). Yet, these proteins are not expressed by all strains (or only in cell culture), which indicates that they may be non-essential.

2.1.3. Intracellular viral replication cycle

IAVs replicate in the nucleus of their host cells (Figure 2.2.), which is, in general, uncommon to RNA viruses. The virus attaches to the host cell by binding of the viral surface protein HA to neuraminic acids (sialic acids), present on cell surface proteins on the apical surface of polarized cells (Skehel and Wiley, 2000). Once attached, the virus enters the cell by receptor-mediated endocytosis (Matlin et al., 1981). Subsequently, the virus passes through the endosomal pathway until eventually, the acidification in the late endosomes occur. The decrease in the pH value causes two effects: (i) a conformational change in the HA protein, which triggers the fusion of the viral envelope with the endosomal membrane, and (ii) entering of protons into the virus particle via the M2 ion channel protein, which leads to viral uncoating (i.e. the dissociation of vRNPs from M1 proteins) (Shaw and Palese, 2013, Skehel and Wiley, 2000). Consequently, the vRNPs are released into the cytoplasm of the host cell. The vRNPs

are then shuttled into the nucleus via the import machinery of the host cell, which is an energy-driven transport mechanism, mediated by nuclear transport receptors (Hutchinson and Fodor, 2013, Cros and Palese, 2003). For this, a nuclear localization signal (NLS) is required, which has been identified on all proteins associated to the vRNP complex (Hutchinson and Fodor, 2012), whereas, specifically, the NLS located on NP was suggested to be essential (O'Neill et al., 1995, Cros et al., 2005).

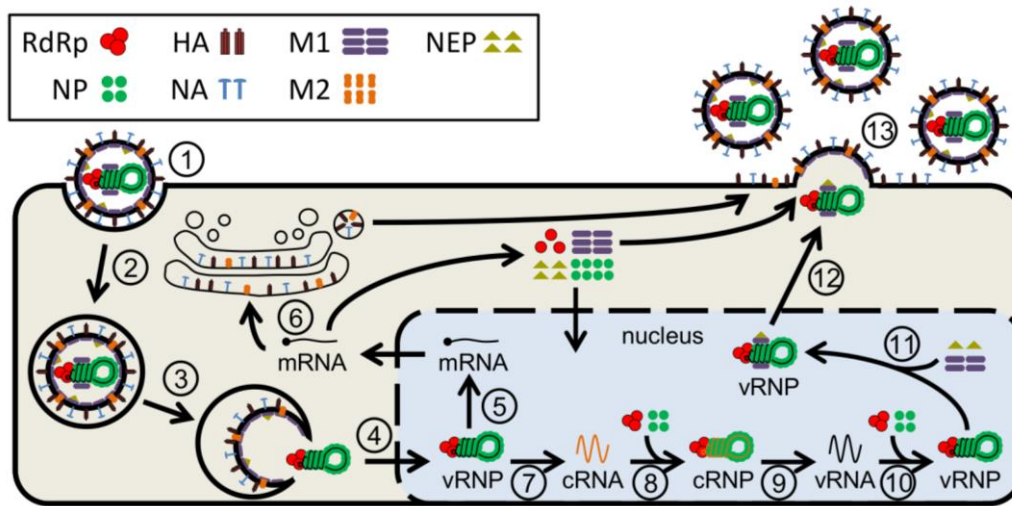


Figure 2.2. Intracellular IAV replication cycle. Schematic illustration of the intracellular viral life cycle. The different life cycle steps are assigned by numbers as follows: (1) virus attachment, (2) receptor-mediated endocytosis, (3) endosomal fusion, (4) nuclear import of vRNPs, (5) virus transcription, (6) viral protein translation, (7) cRNA replication, (8) cRNA encapsidation, (9) vRNA replication, (10) vRNA encapsidation, (11) association of M1 and NEP with the vRNP complex, (12) nuclear export of vRNPs, and (13) virus assembly and budding. Illustration from (Heldt et al., 2015), licensed under CC BY 4.0.

In the nucleus, the vRNPs are capable to perform both transcription (i.e. the synthesis of viral messenger RNAs (mRNA)) as well as replication (i.e. the polymerization of complementary RNAs (cRNA)). In general, cRNAs are intermediate copies that serve as a template for the synthesis of progeny vRNAs. Subsequent to their synthesis, they are also encapsidated with RdRps and NPs to form cRNPs (Fodor, 2013). The cRNPs then catalyze the synthesis of vRNAs, which are then encapsidated as well. Both, the synthesis of vRNAs from cRNPs and the production of cRNAs from vRNPs are primer-independent processes (Jorba et al., 2009).

In contrast, the transcription of viral mRNAs from vRNPs relies on a primer-dependent mechanism (Fodor, 2013, Elton et al., 2006). This primer is obtained in a process known as

cap-snatching, in which the viral RdRp cleaves off the 5' cap-structure (and additional 10-13 nucleotides (nt)) from host cell pre-mRNAs (Fodor, 2013). Subsequent to the 3' → 5' elongation of viral mRNAs (in which the vRNAs serve as a template), the RdRp slips and stutters over a stretch of five to seven uridine residues located at the 5' end of each vRNA, which results in the formation of a polyadenylated (poly(A)) tail for viral mRNAs (Poon et al., 1999, Zheng et al., 1999). Thus, the viral mRNAs are able to mimic the cellular mRNAs (by possessing a 5' cap and a 3' poly(A) tail), which allows them to exploit the host cells' mRNA trafficking machinery to shuttle out of the nucleus (York and Fodor, 2013). In the cytoplasm, viral mRNAs can well compete with the transcripts of cellular origin. Specifically, IAVs have evolved several mechanisms to allow for a preferential access of viral mRNAs to the translation machinery (as reviewed in (Yanguez and Nieto, 2011)). The newly synthesized proteins can then either (i) enter the nucleus (via their NLS signals) to engage in virus transcription and replication (for PB2, PB1, PA, NP and NEP) (Boulo et al., 2007, Hutchinson and Fodor, 2012), or (ii) are shuttled to the plasma membrane in order to form the viral envelope (Nayak et al., 2004). More specifically, the viral surface proteins HA, NA, and M2 are processed and directed via the endoplasmic reticulum (ER) and Golgi apparatus to lipid rafts of the host cell membrane (Zhang et al., 2000, Leser and Lamb, 2005).

vRNPs are able to synthesize both mRNA and cRNAs, thus, it was suggested that they need to be transferred to an inactive state before they can be exported from the nucleus to the cytoplasm. More specifically, it was proposed that this inactivation is mediated by the M1 protein, which was shown to inhibit and impair viral RNA transcription and replication (Baudin et al., 2001, Zvonarjev and Ghendon, 1980, Watanabe et al., 1996, Perez and Donis, 1998). Afterwards, the nuclear export of vRNPs takes place via a pathway that involves the cellular chromosome region maintenance protein 1 (CRM1). Here, it was suggested that the binding of M1 and NEP to the vRNPs (and to CRM1) mediate the nuclear export (Shaw and Palese, 2013, Cros and Palese, 2003, Paterson and Fodor, 2012, Brunotte et al., 2014). Later, the transport of vRNPs to the plasma membrane takes place via a microtubule-dependent mechanism, in which the vRNPs are associated to Rab11 and recycling endosomes (Eisfeld et al., 2011, Amorim et al., 2011).

Finally, viral assembly and budding occurs at the plasma membrane (Nayak et al., 2004, Rossman and Lamb, 2011). At the budding site, M1 is likely the key player in recruiting, concentrating, and assembling the viral components (Nayak et al., 2004, Ali et al., 2000). The formation of the bud, i.e. the outward curvature in the host cell membrane, is likely concerted by several viral proteins, such as HA, NA, and M2 (Shaw and Palese, 2013, Rossman and

Lamb, 2011, Chen et al., 2007). Thereafter, the bud extends and the vRNPs are incorporated. The final step comprises the scission at the neck of the budding virus particle, mediated by M2 (Rossman et al., 2010). Afterwards, the enzymatic activity of NA (which cleaves off sialic acid residues at the cell surface) is important for the release of the newly formed virions. Otherwise, the mature virions would either stay attached to the cell, or would aggregate with each other. In general, virus assembly and budding is a well-organized process. Moreover, it is well established that eight different vRNAs are selectively incorporated into each virus particle (Noda and Kawaoka, 2012, Chou et al., 2012, Nakatsu et al., 2016, Noda et al., 2018), and that the segment-specific genome packaging signals (which include bipartite sequences at both ends of vRNA, housing the promotor, a segment-specific non-coding region, and an adjacent part of the coding region) are involved in that process (Hutchinson et al., 2010, Fujii et al., 2003).

2.1.4. Defective interfering particles

IAV particles are highly heterogeneous in their properties, which includes variation in morphology and sequence (Brooke, 2014, Marcus et al., 2009). Moreover, a between-virus variability in the biological activities (in the context of an infection) can be observed for IAV particles (Marcus et al., 2009, Carter and Mahy, 1982, Brooke et al., 2013). Typically, the majority of the virions are non-infectious; i.e., they cannot be detected in classical infectivity assays such as the 50% tissue culture infective dose (TCID₅₀) and plaque assays. One important class of these non-infectious virions are DIPs (Huang and Baltimore, 1970, Dimmock and Easton, 2014, Nayak et al., 1985). DIPs share the same structural characteristics as their homologous standard viruses (STV). Yet, these virus particles lack an essential part of the viral genome (Figure 2.3A), which renders them defective in virus replication. Furthermore, DIPs suppress and interfere with the replication of their homologous STV in a co-infection scenario. In general, DIPs were described for most DNA and RNA viruses, including viruses that contain single- and double-stranded genomes (Huang, 1973, Nayak et al., 1985, Marriott and Dimmock, 2010, Dimmock and Easton, 2014). Traditionally, DIPs were characterized in cell culture experiments; yet, they were also described to occur *in vivo* (Saira et al., 2013, Tapia et al., 2013, Holland and Villarreal, 1975).

The first indications of DIPs were reported in 1943 for IAVs (Henle and Henle, 1943). More specifically, the authors observed that some inactive influenza virus particles have the capability to interfere with the replication of infectious virions. Later, von Magnus hypothesized

that a form of incomplete virus particle may be responsible for this interference (von Magnus, 1951). Further, he showed that such particles can be generated and accumulated by serial passaging of undiluted influenza virus preparations in embryonated chicken eggs (von Magnus, 1951, von Magnus, 1954). Specifically, he observed a decreasing ratio of infectious to total virus particles in such experiments, which was later referred to as the “von Magnus” effect. Yet, the terminology “defective interfering particle” was proposed by Huang and Baltimore, including the definition of their properties (Huang and Baltimore, 1970).

It was suggested that the large internal deletions of IAV defective interfering (DI) genomes arise by an erroneous translocation of the viral polymerase during the replication of the viral genome (Figure 2.3B); a mechanism that is referred to as the “copy-choice” mechanism (Perrault, 1981, Lazzarini et al., 1981). Other types of DI genomes comprise (i) multiply deleted forms, (ii) “hairpin”/“copyback” genomes, in which some genomic regions were copied in reverse complement, and (iii) “mosaic” DI genomes, where multiple sections (that were originally non-adjacent) were joined together. For IAVs, the deletions typically encompass several hundred, and up to approx. two thousand base pairs. However, the resulting DI genomes typically retain both terminal 3’ and 5’ ends of vRNA, which contain the promoters and packaging signals (Nayak et al., 1985). Moreover, deletions in S1-S3 vRNA (which encode for the viral polymerase protein subunits) are most commonly observed (Baum and Garcia-Sastre, 2011, Davis and Nayak, 1979, Jennings et al., 1983, Nayak et al., 1985, Dimmock and Easton, 2015). Yet, the underlying mechanisms for this observation are still not fully understood (Laske et al., 2016).

As a result of the lack in genomic information, DIPs are defective in virus replication and can, thus, not propagate on their own, once infecting a cell. However, the co-infection with a fully infectious STV can complement this defect. Yet, in such a scenario, the STV life cycle is suppressed, and mainly non-infectious DIPs are released. It is believed that this interference can be caused by the replication advantage of the DI genome in relation to the full-length (FL) counterpart (Huang and Baltimore, 1970, Dimmock and Easton, 2014, Nayak et al., 1985). More specifically, it was suggested that the DI genome may out-compete the FL genome for limiting cellular or viral resources (Marriott and Dimmock, 2010). The release of mainly non-infectious DIPs in a co-infection can be explained by the preferential packaging of the DI RNAs over the FL counterpart into progeny virions (Duhaut and McCauley, 1996, Odagiri and Tashiro, 1997). From an evolutionary point of view, it is discussed that the detrimental effect of DIPs on virus replication may be exploited by the virus biology, in order to reduce (lethal) damage, inflicted to the host organism (to promote its own spread), or to establish and maintain a

persistent infection (Barrett and Dimmock, 1986, De and Nayak, 1980, Huang and Baltimore, 1970).

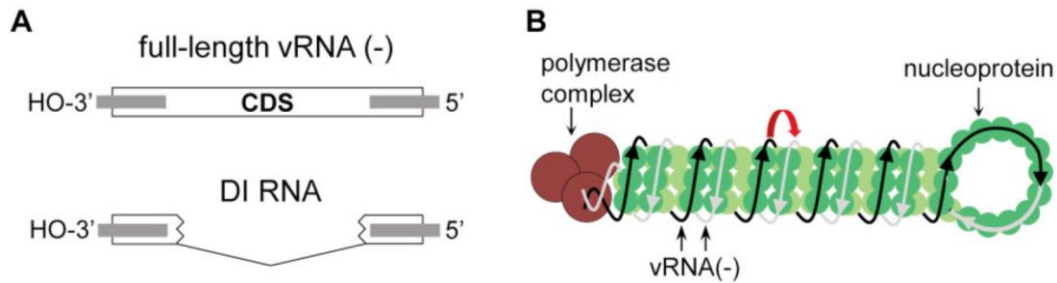


Figure 2.3. Structure and generation of conventional IAV-derived DI genomes. (A) Schematic illustration of a FL vRNA and a DI RNA genome segment. Untranslated regions, containing the promoter regions and packaging signals, at the 3' and 5' end are indicated in gray. CDS, coding sequence. (B) Proposed mechanism of DI RNA generation. The red arrow indicates an erroneous translocation of the viral polymerase, which results in skipping of replication of the internal part of vRNA. Illustration depicts the vRNP complex that consists of multiple copies of the viral NP protein (green), the tripartite polymerase complex (brown), and the single-stranded genomic vRNA. Illustration from (Frensing, 2015).

However, the precise mechanisms of the interfering ability of DIPs are still elusive. Although, it was proposed that DI genomes can out-compete the FL counterparts for viral proteins (Lazzarini et al., 1981, Perrault, 1981), and especially for viral polymerases (Giachetti and Holland, 1989, Widjaja et al., 2012). Moreover, the preferential synthesis of the DI over the FL genome (Akkina et al., 1984, Duhaut and McCauley, 1996) was suggested to originate from a faster accumulation of the DI genome as a result of their reduced length (Marriott and Dimmock, 2010, Nayak et al., 1985, Laske et al., 2016). Moreover, it was observed that DI genomes can competitively inhibit the packaging of their predecessor FL vRNAs, while the DI genomes are preferentially incorporated into progeny virions (Duhaut and McCauley, 1996, Odagiri and Tashiro, 1997). Yet, a potential mechanism for this was proposed so far. However, in this context, it was suggested that vRNAs may contain yet unidentified regulatory elements, which are either impaired or completely absent in DI genomes (Nayak et al., 1985). Moreover, please also note that not all deleted RNAs have the potency to interfere with STV replication in a coinfection scenario for unknown reasons (Nayak et al., 1985, Frensing, 2015).

Given that DIPs can inhibit the spread of infectious virus, a growing interest in their potential application as an antiviral agent can be observed (Dimmock and Easton, 2014, Dimmock and Easton, 2015, Notton et al., 2014, Rouzine and Weinberger, 2013, Zhao et al., 2018). More

specifically, it was shown that IAV-derived DIPs can protect mice and ferrets from infections with lethal doses of STVs (Dimmock and Easton, 2014, Dimmock et al., 1986, Noble et al., 2004, Dimmock et al., 2012b). Moreover, an interference with the replication of different influenza strains was shown; i.e., strains of the H3N2 subtype, pandemic influenza strain A/California/7/2009 of subtype H1N1 (H1N1-pdm09), and Influenza B virus (Dimmock et al., 2012a, Dimmock et al., 2008, Scott et al., 2011).

Finally, it was observed that DIP co-infections lead to an enhanced induction of the antiviral innate immune response (Lopez, 2014, Strahle et al., 2006, Killip et al., 2013). Here, it was shown that the retinoic acid inducible gene I (RIG-I) protein can preferentially bind to the shorter (and more abundant) DI vRNAs (Baum and Garcia-Sastre, 2011), which subsequently leads to an enhanced activation the interferon (IFN)-response (Rehwinkel et al., 2010). This elevated induction of the innate immune response (caused by DIPs) was suggested to be further beneficial for antiviral therapy, in particular for potential pan-specific treatment against other non-homologous respiratory virus diseases (Dimmock and Easton, 2015, Easton et al., 2011). Therefore, DIPs may serve as therapeutic and prophylactic antiviral agent.

2.1.5. Cell culture-based influenza vaccine manufacturing

Besides vaccination, influenza virus infections can also be treated with antiviral drugs. For instance, the M2 ion channel inhibitors amantadine and rimantadine (Vanderlinden and Naesens, 2014) or the neuraminidase inhibitors oseltamivir and zanamivir can be utilized. However, most circulating strains have acquired resistance against these antivirals, which limits their clinical efficacy (Moss et al., 2010, McKimm-Breschkin, 2013, Samson et al., 2013).

Therefore, annual vaccination is still the most effective way to prevent and control seasonal and pandemic influenza virus infections (Noh and Kim, 2013, Shaw, 2012, Hannoun, 2013, Gallo-Ramirez et al., 2015, Milian and Kamen, 2015, Grohskopf et al., 2018). Influenza vaccines can be trivalent formulations, comprising one H1N1, one H3N2, and one IBV strain. Recently, to broaden coverage, also quadrivalent mixtures are used, which include one additionally IBV strain (of another lineage) to reduce the chance of decreased vaccine effectiveness as a result of IBV lineage mismatch (Milian and Kamen, 2015, Grohskopf et al., 2018, Tan et al., 2018, Reed et al., 2012). The vaccine strains are recommended by the WHO for every flu season (for the northern and southern hemisphere), based on global surveillance of influenza viruses and a prediction of the most likely emerging strains (Grohskopf et al., 2018, Shaw, 2012).

The majority of influenza vaccines are based on chemically inactivated virus (Grohskopf et al., 2018, Couch, 2008, Stohr et al., 2006). For this, either the whole inactivated virus is utilized or the virions are disintegrated (e.g., using detergents) for “split” vaccines. The third option for chemically inactivated influenza vaccines is the purification of the viral surface proteins HA and NA for “subunit” vaccines. Moreover, non-inactivated “live-attenuated” influenza vaccines are also utilized, for which the viruses are adapted to replicate at lower temperatures (ranging from 25-33 °C). Such viruses show a weak replication at body temperature, which facilitates an adaptive immune response without major disease symptoms (Ambrose et al., 2011, Grohskopf et al., 2018, Wareing and Tannock, 2001).

Traditionally, influenza vaccines are produced in embryonated hens’ eggs. Alternatively, they can also be produced in cell culture-based production processes or recombinantly, using baculovirus expression systems in Sf9 insect cells (Noh and Kim, 2013, Shaw, 2012, Price et al., 1989, Milian and Kamen, 2015). For the production in eggs or in cell culture, each new seasons’ influenza virus strain needs to be reassorted. For this, a high-growth virus strain (i.e., the backbone), and the respective circulating strains (that provide the surface antigens HA and NA) are used (Kilbourne, 1969, Palese et al., 1997). Due to its superior growth, strain PR8 is utilized as the backbone for recombination (Fulvini et al., 2011). For this, the strains can be either co-cultured, followed by selection (Fulvini et al., 2011, Bardiya and Bae, 2005), or generated using reverse genetics (Nicolson et al., 2005, Subbarao and Katz, 2004).

The major production of influenza vaccines still relies on chicken eggs (Perdue et al., 2011, Grohskopf et al., 2018). Here, the viruses are inoculated and propagated in the allantoic fluid of nine to eleven day-old embryonated hens’ eggs (Bardiya and Bae, 2005). This technology was established more than 70 years ago (Osterhaus et al., 2011), and the first human influenza vaccine was approved and commercially available in 1945 (Stanley, 1945). In general, this procedure is robust and cheap, and provides high yields (Lee and Hu, 2012, Perdue et al., 2011). However, the main disadvantages are (i) the limited flexibility in terms of expanding production capacities in the case of a pandemic (Perdue et al., 2011, Partridge et al., 2010, Barrett et al., 2010), (ii) potential allergenic reactions in response to vaccination due to the presence of egg proteins, (iii) occasionally poor growth of certain influenza virus strains, (iv) an altered protein glycosylation as compared to the original clinical isolates, which can affect immunogenicity (Audsley and Tannock, 2008), and (v) the vulnerability of the egg supply chain in light of the threat of chicken layer flocks by highly pathogenic avian influenza strains (Ma et al., 2019, Lee et al., 2017).

Cell culture-based influenza vaccine production processes were thoroughly investigated in the last decades and are a promising alternative to traditional egg-based manufacturing. Key advantages are: (i) a better scale-up flexibility, leading to shorter response times for new vaccine strains, (ii) a large platform diversity, (iii) a closed sterile production chain (Perdue et al., 2011), and (iv) comparable or higher virus titers in relation to egg-based production (Audsley and Tannock, 2008). This two-stage process comprises cell growth towards high cell densities in large-scale cultivation systems (i.e., bioreactors like stirred tank reactors, STRs), followed by infection and subsequent virus propagation (Genzel and Reichl, 2009, Barrett et al., 2009, Milian and Kamen, 2015). In this process, the cultivation parameters are tightly monitored and controlled, which include the temperature, pH value, dissolved oxygen, and concentration of substrates for cell growth (Genzel et al., 2014a). After two or three days, the viruses can be harvested and purified from the cell culture broth. The production yield is typically assayed using the HA assay, TCID₅₀ assay, or plaque assay. Here, adherent cell lines can be cultivated on microcarriers, such as dextran beads (Genzel et al., 2004, Genzel et al., 2006). Recent developments in cell culture-based influenza vaccine production are (i) virus propagation using chemically defined media, (ii) the use of suspension cells, which facilitate higher cell concentrations and an easier scale-up, and (iii) process intensification strategies, which are directed towards maximizing cell density in fed-batch, continuous, or perfusion cultivation (Feng et al., 2011, Lohr et al., 2012, Genzel et al., 2014b, Gallo-Ramirez et al., 2015, Frensing et al., 2013).

Several different cell lines were proposed for the industrial-scale cell culture-based production of influenza vaccines (Genzel and Reichl, 2009). Among these cell lines are african green monkey kidney epithelial (Vero) cells, Madin-Darby Canine Kidney (MDCK) cells, human embryonic kidney 293 (HEK 293) cells, the immortalized chick embryo cell line PBS-1, and avian embryonic stem cell line EB66 (Schuind et al., 2015, White et al., 2018). Moreover, designer cell lines are suggested, such as the immortalized human fetal retinoblast PER.C6 (Pau et al., 2001) and the avian duck retina cells AGE1.CR (Lohr et al., 2009). However, only two cell lines are recommended as a substrate for influenza vaccine production by the WHO: MDCK and Vero (Lee and Hu, 2012, Kistner et al., 1998, Doroshenko and Halperin, 2009, Brands et al., 1999).

The MDCK cell line is widely used in influenza virus research and one of the major substrates for cell culture-based influenza vaccine production (Perdue et al., 2011, Genzel and Reichl, 2009). Originally, the cells were derived from the epithelium of a cockerspaniels' kidney in 1958 (Gaush et al., 1966). The cells were shown to be highly permissive for most influenza virus

strains (Gaush and Smith, 1968). Moreover, most virus strains typically propagate very well, even without prior adaptation (Lee and Hu, 2012). Thus, virus titers that can be achieved with this cell line are very high (Liu et al., 2009, Li et al., 2009, Moresco et al., 2010) and higher as compared to virus titers from the production in Vero cells (Audsley and Tannock, 2005, Genzel et al., 2010, Youil et al., 2004). Finally, the influenza vaccines produced in suspension MDCK cells are regarded to be safe, well tolerated, and sufficiently immunogenic (Halperin et al., 1998, Palache et al., 1997, Onions et al., 2010).

2.2. Single-cell analysis

2.2.1. Cell-to-cell heterogeneity

Individual cells in a cell population typically display a large cell-to-cell heterogeneity in their properties. This is true not only in a tissue or organ, but also when the cells are derived from the same mother cell (i.e. genetically identical cells). The differences in these characteristics comprise e.g. the abundance of mRNAs, metabolites, lipids, specific proteins (such like signaling molecules and regulatory proteins), ribosomes, and a heterogeneous morphology. This cell-to-cell variability may arise by differences in cell size, cell cycle stage, the induction status (e.g. apoptosis induction, stress response, or antiviral state), and the epigenetic status (which can greatly affect gene expression).

Yet, another additional source of cell-to-cell heterogeneity is the stochasticity inherent to all biochemical reactions (Elowitz et al., 2002). In general, gene expression (and all other cellular processes) underlie a certain degree of randomness. This stochasticity can have a pronounced effect on single cell behavior, in particular in processes that involve a low copy number (or low concentrations) of molecules that react and interact with each other. In other cases, when copy numbers (or concentrations) are high, the variation of individual biochemical reactions are expected to average out, despite noise in these reactions, which may lead to decreased between-cell heterogeneity of such processes (Elowitz et al., 2002, Raj and van Oudenaarden, 2008). Nevertheless, the molecular noise can also be amplified, for instance in autocatalytic reactions, such like virus replication (Delbruck, 1945b), or through propagation in signaling cascades (Rand et al., 2012). "Fate decisions" that arise by stochasticity in cellular processes are, for instance, also important for human immunodeficiency virus (HIV) replication, where the virus can either go into lytic or lysogenic state (Raj and van Oudenaarden, 2008). Interestingly, it was reported that cells are even able to utilize the noise generated in gene expression (Levy and Slavov, 2018). More specifically, cell-to-cell variability in specific protein levels can result in different cellular states that may lead to diverse functional outcomes (Raj and van Oudenaarden, 2008). For example, this is true for the proliferation/quiescence decisions (Spencer et al., 2013) or a graded apoptosis induction, which was suggested to improve the chances of the survival of a small subpopulation of cells at a particular stress (Raser and O'Shea, 2004). Finally, it is believed that noise in gene expression may be genomically encoded and evolved to suit the gene and its particular function (Levy and Slavov, 2018, Raser and O'Shea, 2004, Stewart-Ornstein et al., 2012).

Besides the investigation of the origins and functionalities of cell-to-cell heterogeneity, single-cell analysis can also be useful for diagnostics and medicine (Proserpio and Lonnberg, 2016, Yuan et al., 2017). For instance, single-cell analysis allows investigating the diversity of cell types and cellular states in a complex tissue with the aim to study cellular lineages, involved signaling pathways, cellular function, and the role of (rare) cell subpopulations (Levy and Slavov, 2018, Su et al., 2017b). This cellular complexity is also present during the physiological pathology of diseases, such as cancer. The elucidation of this complexity may facilitate the discovery of new biomarkers for early diagnosis (Chattopadhyay et al., 2014, Kelsey et al., 2017, Abraham and Maliekal, 2017). Additional applications of single-cell analysis in cancer research comprise the identification and study of circulating tumor cells, which appear early in the bloodstream (Miyamoto et al., 2012, Stott et al., 2010, Rhim et al., 2012). It is believed that such research efforts may ultimately guide individualized treatment strategies for personalized medicine approaches (Tellez-Gabriel et al., 2016, Navin and Hicks, 2011, Vermeulen et al., 2008, Lawson et al., 2015).

In general, the large cell-to-cell heterogeneity and in particular, the presence of cell subpopulations cannot be investigated using conventional cell population-based methodologies, as such measurements typically obscure individual cell behavior (Figure 2.4.). More specifically, measurements of cell populations yield only averaged parameters, which are not representative for single-cell behavior, and they provide no indication on single-cell diversity. In contrast, single-cell analysis reveals the extent of cell-to-cell heterogeneity of a given characteristic. The distributions of these characteristics can be either narrow, broad, or even lognormal. Occasionally, also bimodal or multimodal distributions are observed. These subpopulations are very important as they can have a profound impact on the overall, or long-term behavior of the complete population (Rand et al., 2012). Moreover, the persistence of a subset of cells can facilitate the survival of the entire population in times of environmental stress (Raser and O'Shea, 2004).

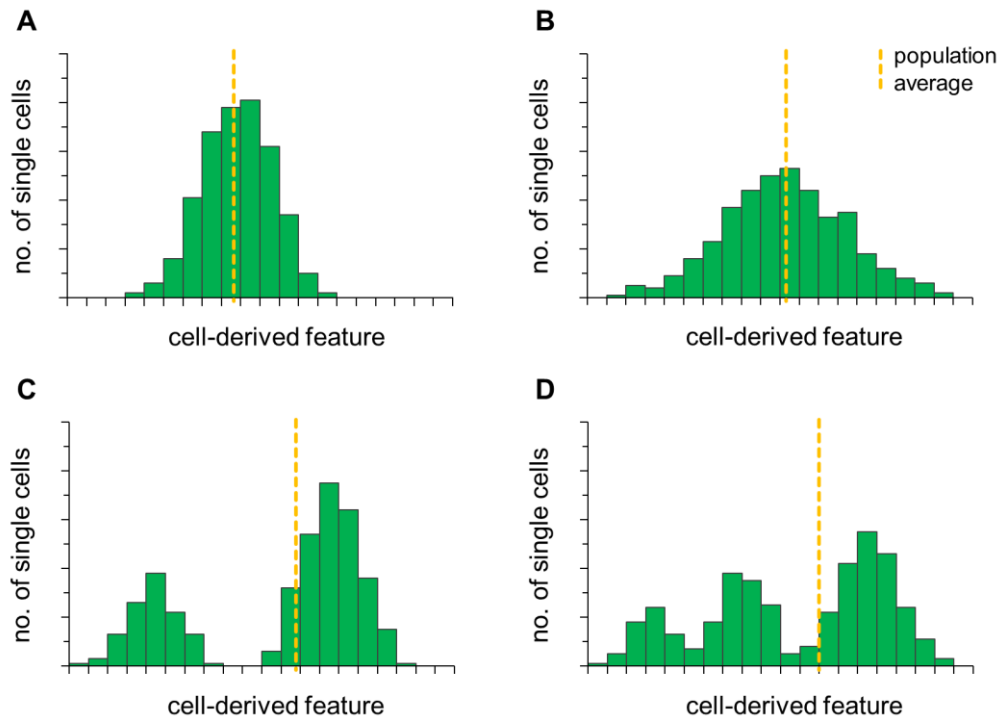


Figure 2.4. Single-cell analysis. Exemplary distributions of single-cell derived measurement data. These distributions can be (A) narrow, (B) broad, (C) bimodal and even (D) multimodal. In general, conventional cell population-based measurements (dashed yellow line) cannot provide an indication on the diversity in single-cell characteristics.

2.2.2. Extrinsic and intrinsic noise

Besides stochastic effects in biochemical reactions, also deterministic factors can well contribute to the between-cell variability. Yet, Elowitz *et al.* were the first that presented a workflow that allowed for the experimental differentiation between intrinsic (stochastic) and extrinsic (deterministic) sources of noise in gene expression (Figure 2.5.) and their specific contribution to cell-to-cell variability (Elowitz et al., 2002). It was defined that intrinsic noise in the expression of a certain gene is caused by the stochasticity inherent to biochemical processes. Extrinsic noise is generated by global, predefined differences between individual cells that affect overall gene expression in each cell differently. Sources of extrinsic noise can be, for instance, differences in the composition and number of regulatory proteins, ribosome content, the cell size and cell cycle stage, or the induction and epigenetic status (Elowitz et al., 2002, Raj and van Oudenaarden, 2008).

2.2. Single-cell analysis

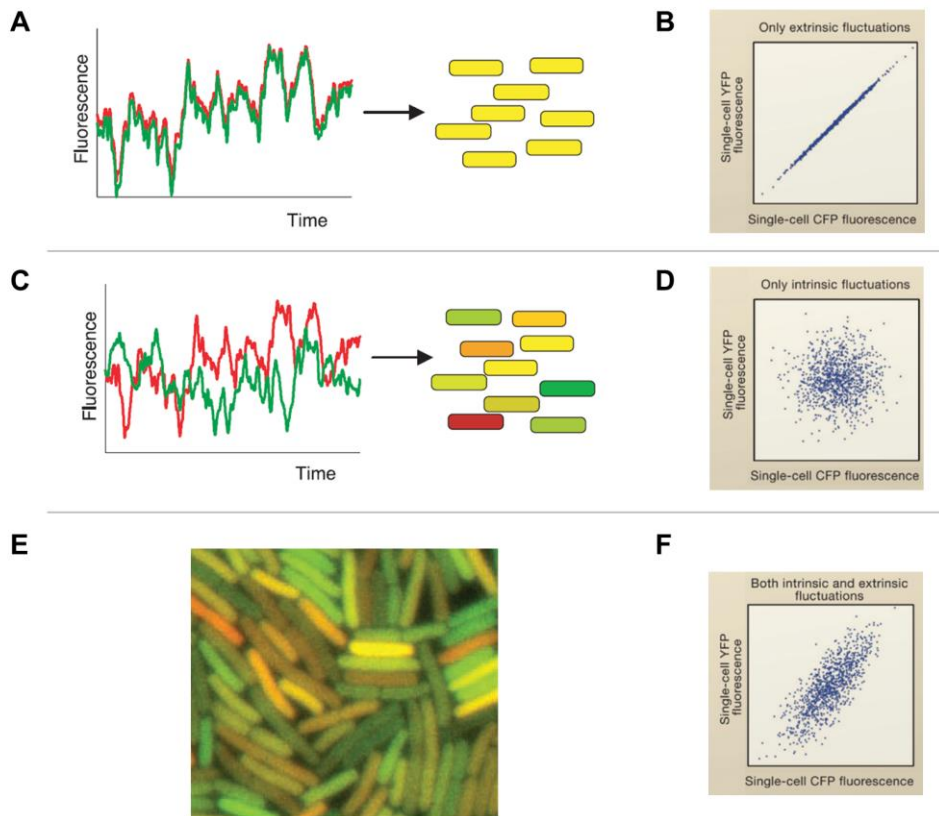


Figure 2.5. Extrinsic and intrinsic noise in gene expression. Elowitz *et al.* engineered bacteria that expressed two different fluorescence proteins (i.e. CFP and YFP) under the control of the same promoter element (Elowitz *et al.*, 2002). (A and C) Theoretical prediction of CFP and YFP protein fluctuations in a single cell in the presence of only (A) extrinsic noise or (C) intrinsic noise. (B and D) Theoretical prediction of the correlation of CFP and YFP protein levels between single cells in the presence of only (B) extrinsic noise and (D) intrinsic noise. (E) Fluorescent microscopic image of the real experiment. (F) Expected correlation between CFP and YFP when fluctuations are both, extrinsic and intrinsic. Figure modified from (Elowitz *et al.*, 2002, Raj and van Oudenaarden, 2008).

Elowitz *et al.* engineered bacteria that expressed two different fluorescent proteins (i.e. cyan fluorescent protein (CFP) and yellow fluorescent protein (YFP)) under the control of the same promoter element (Figure 2.5.) (Elowitz *et al.*, 2002). Theoretically, in the presence of only extrinsic (i.e. deterministic) sources of noise (Figure 2.5A and B), the levels of the two different proteins were expected to fluctuate identically in single cells over time (Figure 2.5A), leading to a perfect within-cell correlation in the abundance of the two proteins (Figure 2.5B). This is a result of the effect of deterministic factors, which affect the expression of the two different proteins identically in a cell. However, as deterministic factors can vary substantially between individual cells, also the expression of both genes would show large between-cell differences, as indicated by a large spread of both protein quantities along the parity line (Figure 2.5B). In

contrast, in the theoretical assumption of the presence of only intrinsic (i.e. stochastic) sources of noise (Figure 2.5C and D), the levels of the two proteins were expected to fluctuate completely randomly (and independently) within a cell (Figure 2.5C). Conclusively, this would lead to no correlation in the abundance of the two proteins between single cells (Figure 2.5D). In the experiment, a mixture of both effects could be determined (Figure 2.5E). On the one hand, a positive correlation in the expression of both proteins was observed, which could be explained by the influence of extrinsic noise. On the other hand, a deviation from the ideal correlation in the abundance of the two proteins became apparent, which can only be caused by intrinsic noise (Figure 2.5F). It was, thus, concluded that the stochasticity (inherent to biochemical processes) and deterministic factors can both substantially contribute to single-cell variability (Elowitz et al., 2002).

2.2.3. Single-cell analysis technologies

Single-cell analysis has many applications in different research areas like cancer biology, stem cell biology and regenerative medicine, microbiology and pathogenesis, neuroscience, immunology, bioprocess engineering, and many more (Weaver et al., 2014, Levy and Slavov, 2018, Wang and Bodovitz, 2010, Raj and van Oudenaarden, 2008). Moreover, as a result of highly sophisticated technological advances, single cells can meanwhile be profiled robustly and in a high-throughput fashion at a variety of omic layers, for instance at the genomic, epigenomic, transcriptomic, proteomic and metabolomics level (Linnarsson and Teichmann, 2016, Heath et al., 2016, Armbrrecht and Dittrich, 2017, Yuan et al., 2017, Kalisky et al., 2011, Kelsey et al., 2017).

Interestingly, fluorescence microscopy is still widely used for single-cell analysis (Yin et al., 2018). However, the quantification of single cell-derived parameters mostly relies on fluorescence-based read-outs, which has some drawbacks. For example, the quantification range is typically relatively narrow, the spectral overlap of different fluorescent dyes can be problematic and a potential perturbation of cellular function when using green fluorescent protein (GFP)-tagged proteins can occur (Steuerman et al., 2018, Yin et al., 2018, Breen et al., 2016). Yet, this technique allows for live-cell imaging and, thus, dynamic single-cell analysis, which offers certain advantages as compared to static single cell analysis (Warrick et al., 2016, Rand et al., 2012, Fritzsche et al., 2012).

Single cells can be isolated using well-established and standardized techniques like micromanipulation, limiting dilution, fluorescence-activated cell sorting (FACS), and laser capture microdissection (Valihrach et al., 2018, Hu et al., 2016, Gross et al., 2015). In addition, isolation and analysis of single cells can be conducted with the more recent microfluidics technology, which facilitates a variety of applications in different research fields (Armbrecht and Dittrich, 2017, Prakadan et al., 2017, Murphy et al., 2017). Using microfabrication, thumbnail-sized chips can be manufactured that contain microchannels and microchambers in the pico- and nanoliter range (Murphy et al., 2017). Such chips are made of polydimethylsiloxane (PDMS), which allow for oxygen transfer needed for the cultivation of cells on the microfluidic chip. Isolation of single cells can be conducted using mechanical entrapment (e.g. by using U-formed traps), nano-wells, integrated valve traps, negative dielectrophoresis (nDEP), or droplets (Murphy et al., 2017, Zhu et al., 2018, Prakadan et al., 2017). In particular, droplet microfluidics is one of the most advanced applications for microfluidic-based single cell analyses (Shang et al., 2017, Kaminski et al., 2016). This technology enables extremely high throughputs with thousands or tens of thousands of single cells that can be isolated and analyzed (Guo et al., 2012). Moreover, the droplets can be transported, fused (to add reagents), and sorted using on-chip processes (Teh et al., 2008). The most sophisticated on-chip analytics comprise raman spectroscopy, electrophoresis, and fluorescence microscopy, often in combination with immunofluorochemistry for quantification of proteins (or other analytes); advanced downstream off-chip analytics comprise mass spectroscopy (MS) (Murphy et al., 2017, Prakadan et al., 2017, Zhu et al., 2018). Moreover, PCR-based methods are utilized to study the genome, transcriptome, and epigenome. For example, parts of the library preparation for transcriptomic analysis of single cells (using next-generation sequencing (NGS)) can be performed on-chip (Zheng et al., 2017).

Single-cell RNA sequencing (scRNA-seq) is one of the latest and highly promising technological advances in single-cell analysis. In particular, NGS technologies allow for a massive miniaturization and parallelization of sequencing reaction on microfluidic chips (Stegle et al., 2015, Yuan et al., 2017, Kanter and Kalisky, 2015). Combined with a sophisticated sequencing chemistry, NGS allows for extremely high throughputs, and at the same time, significantly reduced costs per sample. Most importantly, the high sensitivity allows for the coverage of a significant proportion of the transcriptome of a single cell (Saliba et al., 2014). This technology is often coupled with droplet microfluidics (Macosko et al., 2015, Klein et al., 2015, Zheng et al., 2017). Currently, the most challenging task is the bioinformatic processing of the “big data” generated (Stegle et al., 2015, Liu et al., 2017). Applications of scRNA-seq comprise, for

instance: (i) the profiling of individual cells in an organ or tissue, which can prove insights into cell identity, fate, and function (Stubbington et al., 2017, Lein et al., 2017), (ii) the classification and characterization of cell subpopulations, which is often connected with the discovery of recently unknown, but biologically relevant rare cell types (Shaffer et al., 2017, Stubbington et al., 2017).

Single-cell proteomics is another widely used and relevant approach in the field (reviewed in (Su et al., 2017b, Levy and Slavov, 2018)). Here, the identification and quantification of proteins in single cells relies on genetically engineered GFP-tagged proteins, antibody-based detection methods, and MS (Levy and Slavov, 2018, Olsen et al., 2018, Yin et al., 2018). However, MS typically suffers from a high detection limit (Armbrecht and Dittrich, 2017). Recently, mass cytometry has become a promising methodology for single-cell protein analysis (Spitzer and Nolan, 2016). In this technology, a flow cytometer is combined with an MS, and the detection and quantification of proteins is accomplished using antibodies labelled with rare earth isotopes. In contrast to fluorescence-based methods, the isotope-based antibody detection results in no spectral overlap and interference of the read-outs. Mass cytometry has a very low limit of detection (LOD) (350 molecules/cell) (Olsen et al., 2018), and roughly 50 proteins in single cells at a throughput of up to 2000 cells per second can be quantified (Bendall et al., 2012, Levy and Slavov, 2018).

2.2.4. Virus infection at the individual cell level

This section provides a background to single-cell analysis of virus infections. First, single-cell virus replication in bacterial and animal cells is introduced. Later, the influence of DIPs on virus infections and the diversity of the innate immune response at the single cell level are presented. Finally, a brief background to the whole-transcriptome analysis of virus-infected single cells is provided.

2.2.4.1. Bacterial cells

Already very early in 1929, a method to study virus release from single infected bacteria (i.e. the burst size) was developed (Burnet, 1929). Single-cell analysis was accomplished by utilizing the Poisson statistic: solutions of infected bacteria were diluted and the authors then applied, on average, less than one bacterium per reaction tube. Under these conditions, only a few of the tubes contained a single bacterium (while most of them did not), and the number of tubes

that contain more than one bacterium was minimized this way. The content of every tube was then plated to obtain a plaque count. Using this method, a large variation in bacterial burst size was observed (Ellis and Delbruck, 1939, Delbruck, 1942). Yet, the throughput of this method was very limited. Later, in 1945, the first statistically sound burst size distribution of phage-infected bacteria was published with only minor modifications of this initial methodology (Delbruck, 1945b). The authors observed a very high cell-to-cell heterogeneity in the bacterial burst size distribution, ranging from below 25 to more than 1,000 phages per bacterium. Moreover, it was noted that differences in the size of bacteria, which cover a range more than two, cannot account for large variability in virus titers. A similarly large cell-to-cell heterogeneity in bacterial burst sizes was also observed later in bacteriophage-infected streptococci (Fischetti et al., 1968) and cyanophage-infected cyanobacteria (Kirzner et al., 2016).

It was speculated that the large between-cell difference in bacterial burst size may originate from stochastic fluctuations in intracellular virus growth processes (Delbruck, 1945b). More specifically, it was shown that autocatalytic reaction cascades are prone to the amplification of noise for chemical reactions (Delbruck, 1940). It was speculated that the same may be true for the autocatalytic growth of phages in bacteria, and that this might result in a large cell-to-cell variability in viral burst size (Delbruck, 1945b). This notion was later also used to explain the high cell-to-cell heterogeneity in viral burst sizes of the non-lytic filamentous virus m13 from *E. coli* cells (De Paepe et al., 2010). More specifically, the authors devised a mathematical model, which was able to capture these large differences, assuming initial growth rate differences in the autocatalytic intracellular amplification of virus. However, it appears that the inherent randomness in biochemical reactions may not be sufficient to explain the large single-cell variability in virus replication of animal cells, as outlined below.

2.2.4.2. Animal cells

The first study about single-cell infection in animal cells was published in 1953, using western equine encephalomyelitis (WEE) virus and chicken embryo fibroblast (CEF) cells (Dulbecco and Vogt, 1954). The authors used the methodology of Delbruck *et al.* (Delbruck, 1945b) and observed a similarly large between-cell heterogeneity in virus titers. Moreover, the authors presumed that the differences in cell size may at least partially explain some of the large variability in the virus titers.

A large single-cell heterogeneity in virus replication was also observed for vesicular stomatitis virus (VSV)-infected baby hamster kidney (BHK) cells (Zhu et al., 2009), with virus titers that spanned at least two orders of magnitude (50 to 8,000 plaque-forming units (PFU) per cell). Note that this study was the first in which FACS was utilized to isolate single infected cells into the cavities of individual wells of a multi-well plate. This isolation procedure was later also used in many other studies (Schulte and Andino, 2014, Kirzner et al., 2016, Cohen and Kobiler, 2016, Zanini et al., 2018, Xin et al., 2018, Steuerman et al., 2018). Zhu *et al.* showed that large cells can produce slightly more viral progeny than smaller cells. This was similarly observed in foot-and-mouth disease (FMDV)-infected cells (Xin et al., 2018), but not in poliovirus-infected single cells (Guo et al., 2017). Nevertheless, Zhu *et al.* speculated that the differences in cell size may not explain the whole variability in virus titers produced by single infected cells (Zhu et al., 2009). Similarly, the authors showed that the cell cycle phase can have a small effect on single-cell virus titers as well. This was later also confirmed for FMDV-infected cells (Xin et al., 2018). Finally, Zhu *et al.* studied the effect of the between-virus genetic variability on cell-to-cell heterogeneity in virus replication. The authors observed that the genetic differences in the infecting virus population can, to some extent, contribute to the large fluctuations in virus titers (Zhu et al., 2009). Besides static single-cell analysis, also dynamic aspects of single-cell virus production from VSV-infected cells were studied (Timm and Yin, 2012).

The effect of stochastic noise on single poliovirus-infected HeLaS3 cells was investigated by Schulte *et al.* (Schulte and Andino, 2014). In this study, intracellular viral RNA replication of infected single cells was studied for the first time using real-time reverse transcription quantitative PCR (RT-qPCR). The authors observed a high cell-to-cell variability in viral RNA levels, with differences that spanned one to two orders of magnitude. Interestingly, a significantly higher between-cell variance in viral RNA levels was observed for a low multiplicity of infection (MOI) (i.e. an MOI of 0.1) as compared to infections performed at an MOI of 10. It was speculated that RNA replication might be more susceptible to stochastic effects at such low MOIs, where only one viral RNA genome enters the cell, which may enhance the cell-to-cell variability. In contrast, at high MOIs, the differences on individual RNA replication reactions were suggested to average out, leading to a more stable and robust RNA replication, and thus, a reduced variance in viral RNA levels between single infected cells. However, the between-cell variability in virus titers did not seem to be affected by the MOI. This was also observed for phage-infected bacteria (Delbruck, 1945b) and VSV infections (Zhu et al., 2009, Timm and Yin, 2012). Moreover, Schulte *et al.* observed that the average single-cell virus yield was not

affected by the MOI, although the average of viral RNA levels were reduced (Schulte and Andino, 2014). Furthermore, the authors show that the viral RNA content and the virus titer showed a weak correlation at low MOI, but not at high MOI. Thus, it was speculated that stochastic effects may have a stronger effect on virus production at low MOIs compared to high MOIs. Altogether, it was concluded that the virus titer of an individual cell may be rather dictated by an apparent cellular resource limit at high MOIs, and not by stochastic noise in viral RNA synthesis.

2.2.4.3. DIP co-infection

The effect of DIP co-infection on single-cell virus replication was, so far, only investigated using VSV-infected cells. VSV-derived DIPs can be physically separated from infectious virus particles by velocity sedimentation in sucrose gradients (Frensing, 2015), based on the finding that they are significantly smaller in relation their parental STVs (Holland, 1987). Such a purification of DIPs facilitated the co-infection VSV-infected cells with various amounts of DIPs for single-cell studies (Sekellick and Marcus, 1980). In this work, the authors isolated single cells (from an infected cell population) by picking them with thin glass capillaries under the microscope (i.e. micromanipulation). The individual infected cells were then transferred to reaction tubes to allow for virus growth. Subsequently, the supernatants were subjected to plaque assays to quantify the virus yields. Note that this isolation procedure was also used later in another single-cell virology study (Combe et al., 2015).

First, Sekellick *et al.* co-infected VSV-infected cells with a multiplicity of DIP (MODIP) of 1 (Sekellick and Marcus, 1980). Assuming the poisson statistics, approx. ~63% of the cells would be co-infected with one or more DIPs, while the remaining cells would not receive a DIP. Consistent with this theoretical assumption, the authors observed that roughly ~61% of the infected single cells either became “non-yielders” (i.e. no infectious virus progeny was released) or “low-yielders” (a comparatively low virus yield was observed). However, the co-infection with an MODIP=16 (where all infected cells should be co-infected by at least one DIP) did not result in all cells being either “non-yielders” or “low-yielders”. Instead, the authors observed a new class of infected single cells: “intermediate-yielders”. Based on these results, it was concluded that this may be explained by the self-interference of DIPs (i.e. the interference with their own interference, which leads to a reduction in interference). Such a self-interference was later similarly described in another single-cell virology study with VSV-derived DIPs (Akpınar et al., 2016b).

In 2016, a microfluidic workflow for single-cell virology was presented that facilitated the analysis of hundreds (and up to one thousand) of infected single cells per experiment (Warrick et al., 2016). This procedure was later used to investigate single-cell VSV infection under the influence of DIPs (Akpinar et al., 2016b), or to study the effect of the innate immune response on cell-to-cell variability in VSV replication (Timm et al., 2017). For this, Warrick *et al.* combined a microwell-based device, fluorescence-based imaging, and a streamlined bioinformatic data analysis workflow. Moreover, the technology allowed for time-lapse analysis of single-cell virus infections. A very similar experimental approach was later also developed for the study of poliovirus-infected single cells (Guo et al., 2017).

Akpinar *et al.* used the workflow developed by Warrick *et al.* (Warrick et al., 2016) to study the influence of varying amounts of DIPs on VSV-infected single cells (Akpinar et al., 2016b), similar to earlier studies (Sekellick and Marcus, 1980). However, the authors utilized a recombinant VSV that expressed red fluorescent protein (RFP) as a reporter of viral protein production and time-resolved single-cell analysis (Akpinar et al., 2016b). It was observed that DIP co-infections lead to a reduction and delay of intracellular viral gene expression. Moreover, the authors developed a mathematical model that was able to recapitulate the kinetic parameters of virus replication in single cell (under the influence of varying amounts of DIP-coinfections). Later, this model was extended, and was able to describe virus growth and spread, from the single-cell to the multicellular level (Akpinar et al., 2016a). More specifically, new experimental data of the spatio-temporal spread pattern of virus infection in a plaque, under the influence of varying amounts of DIP-coinfections (Akpinar et al., 2016a), could be recapitulated.

2.2.4.4. Innate immune response

The innate immune response is the first line of defense that inhibits virus replication and spread until the adaptive immune response can deliver a more effective suppression (Trinchieri, 2010). In general, it was observed that the IFN response can be only observed in a small subpopulation of single cells upon virus infection (Zawatzky et al., 1985, Hu et al., 2007), including IAV-infected cells (Rand et al., 2012, von Recum-Knepper et al., 2015, Killip et al., 2017). In this context, it was shown that the IFN- β expression is a stochastic process, in which the type-I IFN response (which involves various components of a signaling cascade) must be self-amplified within a single cell, which ultimately leads to an all-or-nothing “fate decision” whether to secrete IFN or not (Patil et al., 2015, Rand et al., 2012). Such a bimodal behavior

is believed to exist as only a few IFN-secreting cells (the “first responder” cells) are sufficient to protect the whole cell population, which is accomplished by the paracrine stimulation of surrounding cells by the “first responder” cells (Rand et al., 2012, Talemi and Hofer, 2018, Patil et al., 2015).

Timm *et al.* studied the influence of the single-cell innate immune response upon infection with VSV (Timm et al., 2017). For this, the high-throughput microfluidic platform from Warrick *et al.* (described above) was used (Warrick et al., 2016). Moreover, the authors used a reporter cell line, which was engineered to express a GFP upon activation of the innate immune response, together with a recombinant VSV expressing RFP as a reporter of viral gene expression (Timm et al., 2017). It was observed that the relative timing (rather than the magnitude) of either host immune or viral gene expression determined the outcome of an infection. More specifically, earlier viral or anti-viral gene expression either favored or hindered virus replication, respectively.

2.2.4.5. Whole transcriptome analysis

In 2018, the first studies dealing with the whole transcriptomic analysis of infected single cells using NGS technologies were published (Russell et al., 2018, Zanini et al., 2018, Steuerman et al., 2018). Russell *et al.* isolated single cells using a droplet-based microfluidic system (Zheng et al., 2017), followed by scRNA-seq. An extreme wide cell-to-cell variation in viral mRNAs was observed in IAV-infected cells (Russell et al., 2018). Moreover, the authors observed that some cells failed to produce at least one viral transcript, in line with previous observations (Brooke et al., 2013, Heldt et al., 2015). In addition, the authors correlated cellular genes with the abundance of viral mRNAs, and observed that the oxidative stress response showed a co-variation with viral gene expression (Russell et al., 2018). Later, Zanini *et al.* studied the whole transcriptome of dengue and zika virus-infected single cells (Zanini et al., 2018). The single cells were isolated using FACS, followed by NGS analysis. Afterwards, the authors correlated the viral load (i.e. viral mRNA abundance) with host cell transcripts and identified novel antiviral and proviral factors (including proteins involved in the ER translocation, signal peptide processing, and membrane trafficking), which were validated in subsequent experiments. Steuermann *et al.* conducted scRNA-seq of *in vivo* IAV-infected cells from mouse lungs (Steuerman et al., 2018). More specifically, the lung tissues were dissociated, and the single cells were isolated using FACS, followed by subsequent scRNA-seq analysis. Moreover, a diversity of cell types was investigated (macrophages, endothelial, natural killer, and dendritic

cells). The authors identified generic infection responses, equal to all cell types (e.g. the interferon response), and those which are cell-type specific. Moreover, the authors observed that the suppression of mitochondrially encoded genes was largely independent from the IFN induction. Therefore, it was suggested that both mechanisms may represent independent lines of defense of the host cells against virus infection.

3. Materials and methods

In the following chapter, we describe all methods and procedures that were utilized in this work. A list of all chemicals and reagents can be found in the Appendix A, and a list the equipment is located in the Appendix B. Please note that we used some parts of the methods sections of previous publications (Heldt et al., 2015, Kupke et al., 2018, Frensing et al., 2016), that were achieved in the context of this PhD work. Whenever possible, we refer to our standard operation procedures (SOPs), which are available upon request from the Bioprocess Engineering group of the Max Planck Institute for Dynamics of Complex Technical Systems (Magdeburg, Germany), headed by Prof. Dr.-Ing. Udo Reichl. In addition, a few non-standard experimental procedures can be found the Appendix C, as indicated in the text.

3.1. Cell cultivation and virus infection

3.1.1. Media and buffers

For cultivation of MDCK cells (section 3.1.2.), we used media based on Glasgow Minimum Essential Medium (GMEM). The preparation of this media is described in SOP "M/02" and SOP "M/03". We then added peptone to a final concentration of 2 g/L and 10% (v/v) fetal calf serum (FCS) to yield the cultivation media for MDCK cells.

Phosphate buffered saline (PBS) was prepared according to SOP "M/01" and "1x" trypsin (for cell passaging, section 3.1.2.) according to SOP "M/07".

For virus infections of MDCK cells (section 3.1.3.), we used GMEM (containing 2 g/L peptone) without FCS and added 1% (v/v) of a trypsin solution (500 Na-benzoyl-L-arginine ethyl ester (BAEE) U/mL) to yield the infection medium for MDCK cells. The trypsin solution (500 BAEE U/mL) was prepared by dissolving "Trypsin (1:250) powder" (Gibco) in PBS to yield the corresponding final concentration (described in SOP "V/02").

The cultivation media for the human HEK 293 and A549 cell lines (section 3.1.2.) was Dulbecco's Modified Eagle's Medium (DMEM), containing 10% (v/v) FCS. Virus infections of these cell lines (section 3.1.3.) were performed in DMEM without FCS that contained 1% (v/v) of a trypsin solution (500 BAEE U/mL).

3.1.2. Cell cultivation

We used adherent MDCK cells from the European Collection of Cell Cultures (ECACC, #84121903), the HEK 293 cell line from the American Type Culture Collection (ATCC, #CRL-1573), and the A549 cell line from ATCC (#CCL-185). For cultivation, the cell lines were thawed (SOP "Z/02") from cryopreserved working cell banks (WCB, preparation described in SOP "Z/06"). All cells were cultivated at 37°C in a 5% CO₂ atmosphere.

Cells were subcultured according to SOP "Z/04". Briefly, we passaged the cells on a weekly basis in T75 flask. For this, we washed the cells with PBS and added 3 mL of a "1x" trypsin solution (section 3.1.1.). After incubation for approx. 30 min, we stopped the trypsinization reaction with 3 mL of cell culture media (containing FCS) and homogenized the cell suspension. We then added 1 mL of this cell suspension per new T75 flask, or 2 mL for a new T175 flask. For infection experiments (section 3.1.3.), we trypsinized the cells three days after passaging (to a T75, or T175 flask) and seeded the cells into 6-well plates, or 9.6 cm² dishes. For this, we determined the cell concentration using a ViCell XR (Beckman Coulter) according to the operating instruction "Kurzanleitung Zellzählgerät ViCell XR" (version 1.5). Afterwards, we seeded 1 x 10⁶ cells into each well (of a 6-well plate, or 9.6 cm² dish; note that both contain the same growth surface per well) in 2 mL of cell culture media. Infection of the cells (section 3.1.3.) was then conducted 24 h post seeding.

3.1.2.1. Generation of clonal MDCK cells

Clonal MDCK cell populations were generated in the master thesis work of Annekathrin Leupelt (Leupelt, 2017), which was conducted and supervised in the context of this PhD work. A detailed protocol for the generation can be found in Appendix C.1.

In brief, single MDCK cells were isolated in 384-well plates (as described below, section 3.1.3.2.), but with non-infected cells. The isolated cells were then cultivated in cell culture media to allow for cell division and cell growth to small colonies. Eventually, the cell monolayer reached confluency. The cells were then expanded in consecutive passages in cell culture vessels of increasing growth surface (384-, 96-, 6-well plates, and finally, T75 cell culture flasks). Once we have achieved a sufficiently large population of cells per MDCK cell clone (>10⁷ cells), the cells were cryopreserved. Afterwards, all clones (31 in total) were thawed simultaneously for subsequent experiments.

3.1.3. Virus infection

The following influenza A virus strains were used for this work: strain PR8 was provided by the Robert Koch Institute (RKI, #3138) and the National Institute for Biological Standards and Control (NIBSC, #99/716). Strain influenza A/Hong Kong/4801/2014 of subtype H3N2 (H3N2) (#15/192) and strain H1N1-pdm09 (#10/122) were supplied by NIBSC. Seed virus titers were determined by standard TCID₅₀ assay (section 3.2.1.2.) and MOIs were based on this titer.

3.1.3.1. Cell population-based infection

For cell population-based virus infections, we used confluent cells in 6-well plates (please also refer to section 3.1.2). Cells were washed with 1 mL of PBS and were then infected at the indicated MOIs in 250 µL of infection medium. During 1 h of incubation, the dish was rocked to keep the monolayer moist and to distribute viruses evenly. Afterwards, the inoculum was removed and cells were washed twice with 1 mL of PBS. We then added 2 mL of infection medium. For each investigated time point post infection, one dish was sampled.

Sampling. Aliquots of supernatants were stored at -80°C until virus titration (section 3.2.1.), virus inactivation for negative stain transmission electron microscopy (ns-TEM) analysis (section 3.1.3.5.), or the purification of vRNA in the released virions. This purification of vRNAs was conducted using “NucleoSpin RNA Virus” kit (Macherey-Nagel) according to the manufacturers’ instructions. The purified vRNAs from the released virions were either (i) quantified via real-time RT-qPCR (section 3.2.2.1.), (ii) investigated for the presence of DI RNAs via segment-specific PCR (section 3.2.3.1.), or (iii) studied in their sequence (section 3.2.4.). The remaining cells in the well were then washed twice with 1 mL of PBS. Lysis of cells and intracellular RNA extraction was performed using “NucleoSpin RNA” kit (Macherey-Nagel) according to the manufacturers’ instructions. Intracellular RNAs were analyzed for (i) viral RNAs via real-time RT-qPCR (section 3.2.2.1.), whereby the quantities of viral RNA per cell were calculated based on the cell count at time point of infection, or (ii) specific host cell mRNAs, indicative for the induction of the innate immune response, via real-time RT-qPCR (section 3.2.2.2.). Sampling for intracellular viral proteins for western blot analysis is described in section 3.2.5. and the sampling for imaging flow cytometry (for investigating intracellular viral protein localization dynamics) is described in section 3.2.6.

3.1.3.2. Isolation of infected single cells

Confluent MDCK cells in 9.6 cm² dishes (see also section 3.1.2.) were used for the isolation of infected single cells. First, we determined the cell count of three dishes. The average cell number per well was used to adjust the MOI for infection. Moreover, the cell count was necessary for single cell isolation (i.e., to adjust the cell concentration after trypsinization of the infected cells, as described below).

First, the cells were infected at the indicated MOIs in 250 µL of infection medium. During the first hour of incubation, the dish was rocked to keep the monolayer moist and to distribute viruses evenly. The volume of the infection medium was then increased to 2 mL and cells were incubated for another 1.5 h. After washing with 1 mL of PBS, cells were trypsinized with 500 µL of "1x" trypsin (section 3.1.1.) for 10-15 min. During these 10-15 min, we carefully knocked the dish to accelerate the detachment of cells from the surface of the dish and put back the dish into the incubator as quickly as possible. This was repeated two to three times during the 10-15 min of trypsinization to ensure that all cells have detached. The following steps were also quickly conducted to avoid that the cells cool down to room temperature: (i) trypsinization was stopped using 500 µL of cell cultivation media (containing 10% FCS), (ii) the cell suspension was then carefully homogenized by pipetting, (iii) the cell suspension was serially diluted in pre-warmed (37°C) infection media, (iv) subsequently, 50 µL of the diluted cell suspension (concentration: one cell per 50 µL) were quickly added to each well of a pre-warmed 384-well plate (Greiner, #781901). For the latter step (iv), we used a small plastic tub to facilitate quick pipetting (<1 min) of the cell suspension (using an electronic multichannel/multistep pipet) into the pre-warmed 384-well plate. The plate was then quickly transferred into the incubator. The 384-well plates were incubated until the indicated hours post infection (hpi). Afterwards, we identified single cells in individual wells by phase-contrast microscopy using the 5x magnification. In doing so, the whole plate could be screened in approx. one hour.

Optionally, we determined the diameter of single cells (for the results shown in Figure 4.12.). To determine both the virus yield and cell size at the same time, we isolated single infected cells in non-binding 384-well plates (Greiner, #781901). The usage of this type of plate prevents unspecific adsorption of virions to the plastic surface of a well, which can result in a loss in virus titres. It also suppresses adherence of cells and causes them to remain spherical. Thus, cell diameters could be measured using microscopic images and the software Axiovision V 1.1 (Zeiss).

Sampling. The supernatants of wells containing single cells were directly subjected to plaque assays (3.2.1.3.) to quantify virus yields. The remaining single cells were washed with 100 μ L of PBS and 5 μ L of a diluted bovine serum albumin (BSA) solution (Thermo Scientific, #B14) at a concentration of 1 mg/mL was added to the wells. The 384-well plate was sealed and immediately stored at -80°C . Lysis of cells was conducted by freeze-thawing in these BSA solutions. Such a cell disruption is very efficient, leads to a high RNA stability and enhanced downstream reverse transcription efficiency (Svec et al., 2013). The cell lysate was afterwards subjected to real-time RT-qPCR for quantification of intracellular vRNAs (section 3.2.2.1.), or for quantification of ribosomes (3.2.2.3.), or to segment-specific RT-PCR for detection of DI RNAs (section 3.2.3.2.).

3.1.3.3. Generation of plaque-purified virus

For purification of viruses, we used the plaque assay as described in section 3.2.1.3. For this, we prepared a serial ten-fold dilution series of the corresponding seed virus in infection media, and the dilutions were then incubated on confluent MDCK cells in 6-well plates. We then proceeded with the plaque assay as described in section 3.2.1.3. However, note that we here did not fix and stain the cells. Instead, four days after the infection, we identified single plaques on the 6-well plates (the plaques became visible when the plate was hold against the light) and marked the plaques with a pen at the backside of the 6-well plate. Afterwards, the plaques were picked with a pipet (with 200 μ L tip). Specifically, we touched the plaque with the tip (by puncturing the agar untill the plaque/the bottom of the well), moved the tip back and forth within the plaque, and then aspirated a small volume. Note that we only picked plaques that were situated far away from each other, to prevent cross-contamination of plaques. Afterwards, the tip was transferred to a microcentrifuge tube containing 100 μ L of infection medium. The viruses were released from the tip by pipetting up and down. This sample was then serially diluted (in ten-fold dilution steps), and these dilutions were subjected to another round of plaque assay and subsequent plaque picking after four days. In total, we picked plaques in three consecutive plaque assays for each individual plaque isolate. In the third round of plaque picking, we used the picked plaques to infect confluent MDCK cells in 6-well plates as described in 3.1.3.1. Note that we here used the $1:10^4$ dilution of the picked plaques, to ensure a low MOI infection scenario. Moreover, an infection medium volume of 3 mL was used to provide sufficient nutrient for virus growth. The plaque purified viruses were harvested at 48 hpi. Before harvesting, we confirmed that a cytopathic effect was visible, i.e., when approx. 50% of the cells have detached.

3.1.3.4. Enrichment of OP7 virus

For enrichment of OP7 virus, we utilized the procedure for isolation of infected single cells (section 3.1.3.2.). For this, we used the PR8-NIBSC seed virus working bank that was prepared on 14.12.2011, with a TCID₅₀ titer (section 3.2.1.2.) of 1.29×10^9 infectious virions/mL. Note that this virus was originally derived from NIBSC (order code: #99/716). Cells were infected at an MOI of 10 and infected single cells were isolated (section 3.1.3.2.). At 12 hpi, whole supernatants of infected single cells were used to infect confluent MDCK cells in 6-well plates (as described in section 3.1.3.1.). We then used an infection media volume of 3 mL to provide sufficient nutrient for virus growth. The single-cell derived virus seeds were harvested at 48 hpi (before harvesting, we confirmed that a cytopathic effect was visible, i.e., when approx. 50% of the cells have detached).

3.1.3.5. Virus inactivation for ns-TEM analysis

ns-TEM analysis was performed by Dr. Dietmar Riedel (Max Planck Institute for Biophysical Chemistry, Facility for Transmission Electron Microscopy, Göttingen, Germany).

For this, we inactivated virus particles, released in cell population-derived infections, using β -propiolactone according to the operating instruction "Chemische Inaktivierung" (version 1.0). Afterwards, virus particles were visualized utilizing ns-TEM. In brief, the samples were bound to a glow discharged carbon foil covered grid and stained using 1% uranyl acetate. Grids were imaged at room temperature using a "CM-120 BioTwin" transmission electron microscope (Philips). Images were acquired using a "TemCam-F416 CMOS" camera (TVIPS).

3.2. Analytics

3.2.1. Virus quantification

Virus titers of cell population-based infections were determined based on the HA assay (Kalbfuss et al., 2008) and the TCID₅₀ assay (Genzel and Reichl, 2007). The plaque assay was used for samples of cell population-based and single cell-derived experiments.

3.2.1.1. HA Assay

With this assay, all virus particles (infectious and non-infectious) can be quantified. The assay is based on hemagglutination, i.e., erythrocytes are cross-linked by the viral HA surface proteins, which can bind to the sialic acid residues present on the erythrocytes. In a titration of a virus-containing sample, this agglutination will only occur up to a certain dilution. In general, the agglutination can be evaluated visually and photometrically. A detailed protocol of the assay can be found in SOP "V/5". HA titers were expressed as log₁₀ HA units per test volume (log₁₀ HAU/100 μL). Moreover, total virus particle concentrations c_{virus} (virions/mL) were calculated, assuming that agglutination occurs up to a dilution in which the number of virions equals the number of erythrocytes (Burleson et al., 1992). The calculation was based on the HA titer and the cell concentration of the erythrocyte suspension (2×10^7 cells/mL).

$$c_{virus} = 2 \times 10^7 \times 10^{(\log_{10} HAU/100 \mu L)}$$

3.2.1.2. TCID₅₀ assay

The concentration of infectious virus particles was determined with the TCID₅₀ assay. A detailed protocol of the experimental procedure is described in SOP "V/12". Briefly, this assay is based on the infection of adherent MDCK cells in 96-well plates with serially diluted (virus-containing) samples. After incubation, infected cells were stained for the expression of the viral HA protein using fluorescence-labelled antibodies. Each sample was eight-fold processed, each on one 96-well plate. Afterwards, each well was then assessed for whether it showed viral protein expression, or not. Finally, the calculation of the TCID₅₀ titer was based on a calculation from Spearman und Kärber. In general, note that non-infectious virus particles cannot be detected with this assay.

3.2.1.3. Plaque Assay

Like the TCID₅₀ assay, only infectious virus particles can be enumerated with the plaque assay. In this titration-based assay, confluent MDCK cells are infected and then overlaid with a semi-solid media to restrict the spread of newly released viruses to nearby cells. After incubation for four days, small plaques (i.e., gaps in the cell monolayer caused by cell lysis due to virus infection) are developed. These plaques are then counted and give rise to the plaque (infectious) virus titer per mL. A detailed protocol of the plaque assay can be found in the SOP “V/10”. However, we used some minor modifications to this procedure (as described below) to facilitate a higher sensitivity of the assay, which was needed for the detection of the low concentrations of virus particles released from infected single cells.

Briefly, we used whole volumes of single-cell samples for plaque assay analysis. Specifically, two dilutions were investigated, containing 90% and 10% of the total sample in 250 µl of infection media. For cell population-based experiments, we prepared serial 10-fold dilutions of the samples. 250 µL of each dilution (of samples from cell populations and single cells) were then incubated on confluent MDCK cells in 6-well plates (section 3.1.2.). During 1 h of incubation, the plates were rocked gently every 20 min to keep the monolayer moist and to distribute viruses evenly. The inoculum was removed and cells were overlaid with 2 mL of infection media containing 1% agar (pre-warmed to 45°C). Incubation took place for 4 days. Subsequent to methanol fixation (using 2 mL of methanol) and removal of the overlay, cells were stained with a 0.2% crystal violet solution (a volume sufficient to cover the cell monolayer (approx. 500 µL) was used). The virus load of the sample, expressed as PFU, was determined using light microscopy.

3.2.2. Real-Time RT-qPCR

Real-time RT-qPCR was utilized for absolute quantification of viral RNAs of single-cell- and population-based samples (section 3.2.2.1.), for the analysis of the innate immune response of cell population-based samples (3.2.2.2.), and for quantification of ribosomes of single-cell-samples (3.2.2.3.).

3.2.2.1. Quantification of viral RNAs

For quantification of viral RNAs, a previously published method for polarity- and gene-specific amplification of individual IAV RNAs (Kawakami et al., 2011) was derived and established in the group (Frensing et al., 2014).

Please note that we here describe a modified procedure from *Frensing et al.*, which was optimized (towards higher sensitivities) in the context of this PhD work, to facilitate the investigation of single cells (section 3.2.2.1.). More specifically, this method was used for quantification of (i) intracellular vRNA of single-cell samples, (ii) intracellular vRNA, mRNA and cRNA of cell population-derived samples, and (iii) purified vRNA from virus particles of cell population-derived samples.

Generation of RNA reference standards. To facilitate absolute quantification, we generated RNA reference standards and numbers of viral RNAs were calculated based on calibration curves. For in vitro synthesis of the reference standards, we used plasmids carrying the complete sequence of vRNA, mRNA, and cRNA (of the corresponding segments) in a conventional PCR using “Phusion High-Fidelity DNA Polymerase” (Thermo Scientific) according to the manufacturers’ instructions. Thereby, the primers (Table 3.1.) introduced a T7 promoter sequence (in the desired orientation) into the PCR products. After purification (“InnuPrep PCRpure Kit” (Analytik Jena)), we used the PCR products for in vitro transcription (“TranscriptAid T7 High Yield Transcription Kit” (Thermo Scientific)). Final purification of the RNA reference standards was conducted using “NucleoSpin RNA Clean-up” (Macherey-Nagel) and standards were stored at -80°C until use.

RT. For reverse transcription (RT), we utilized a tagged primer (Table 3.2.). First, we mixed 1 µL of the RNA sample with 0.5 µL of dNTPs (10 mM) and 0.5 µL of the RT primer (10 µM for mRNA primer, or 1 µM for vRNA and cRNA primer) and filled up to 6.5 µL with nuclease-free water. Incubation was performed at 65°C for 5 min and then 5 min at different temperatures: 42°C for mRNA, or 55°C for vRNA and cRNA measurements. During the latter step, we added a pre-warmed mixture (42°C for mRNA, or 55°C for vRNA and cRNA measurements) consisting of 2 µL “5× RT buffer”, 0.25 µL (50 U) “Maxima H Minus Reverse Transcriptase” and 1.25 µL nuclease-free water (all reagents from Thermo Scientific). RT was conducted for 30 min at 60°C, followed by termination at 85°C for 5 min. In addition, we reverse transcribed RNA

reference standards in 10-fold diluted steps: 1 to 1×10^{-7} ng. Each of this reaction contained (optionally) cellular total RNA (to conform with intracellular RNA samples): (i) 350 fg for single-cell-, (ii) 350 ng for population-based measurements, and (iii) no total RNA for measurements of vRNA from purified virions. The cDNA reaction products were then diluted to 20 μ L in nuclease-free water and stored at -20°C , or immediately subjected to qPCR analysis.

Table 3.1. Primers for RNA reference standard generation

Target	RNA type	Primer name	Sequence (5' -> 3')
Segment 5	cRNA	S5 Uni T7 for	TAATACGACTCACTATAGGGAGCAAAAGCAGGGTAGATAATC
		S5 Uni rev	AGTAGAAACAAGGGTATTTTTC
	vRNA	S5 Uni for	AGCAAAAGCAGGGTAGATAATC
		S5 Uni T7 rev	TAATACGACTCACTATAGGGAGTAGAAACAAGGGTATTTTTC
	mRNA	S5 Uni T7 for	TAATACGACTCACTATAGGGAGCAAAAGCAGGGTAGATAATC
		S5 dT rev	TTTTTTTTTTTTTTTTCTTTAATTGTC
Segment 7	cRNA	S7 Uni T7 for	TAATACGACTCACTATAGGGAAGCGAAAGCAGGTAG
		S7 Uni rev	AGTAGAAACAAGGTAGTTTTT
	vRNA	S7 Uni for	AGCGAAAGCAGGTAG
		S7 Uni T7 rev	TAATACGACTCACTATAGGGAAGTAGAAACAAGGTAGTTTTT
	mRNA	S7 Uni T7 for	TAATACGACTCACTATAGGGAAGCGAAAGCAGGTAG
		S7 dT rev	TTTTTTTTTTTTTTTTACTCCAGCTCT
Segment 8	cRNA	S8 Uni T7 for	TAATACGACTCACTATAGGGAGAAAAAGCAGGGTGACAAA
		S8 Uni rev	AGTAGAAACAAGGGTGTTTT
	vRNA	S8 Uni for	AGAAAAAGCAGGGTGACAAA
		S8 Uni T7 rev	TAATACGACTCACTATAGGGAAGTAGAAACAAGGGTGTTTT
	mRNA	S8 Uni T7 for	TAATACGACTCACTATAGGGAGAAAAAGCAGGGTGACAAA
		S8 dT rev	TTTTTTTTTTTTTTTTAGTACTAAATAAGCTGAAACGAG

qPCR. For quantitative PCR (qPCR), we used the "Rotor-Gene Q real-time PCR cycler" (Qiagen) and qPCR primers are listed in Table 3.3. The qPCR mix (10 μ L) contained 1 \times "Rotor-Gene SYBR Green PCR Kit" (Qiagen), 500 nM of each primer and 3 μ L of diluted cDNA. Initial denaturation was conducted at 95°C for 5 min, followed by 40 PCR cycles (two-step protocol): 95°C for 10 s and 62°C for 20 s. Afterwards, melting curve analysis was performed from 65 to 90°C .

Table 3.2. Tagged primers for RT (for quantification of viral RNAs)

Target	RNA type	Primer name	Sequence (5' -> 3')
Segment 5	vRNA	S5 tagRT for	ATTTAGGTGACACTATAGAAGCGAGTGATTATGAGGGACGGTTGAT
	cRNA	S5 tagRT rev	GCTAGCTTCAGCTAGGCATC AGTAGAAACAAGGGTATTTTTCTT
Segment 7	vRNA	S7 tagRT for	ATTTAGGTGACACTATAGAAGCGAGCCGAGATCGCACAGAGACTT
	cRNA	S7 tagRT rev	GCTAGCTTCAGCTAGGCATCAGTAGAAACAAGGTAGTTTTTTAC
Segment 8	vRNA	S8 tagRT for	ATTTAGGTGACACTATAGAAGCGGATAGTGGAGCGGATTCTG
	cRNA	S8 tagRT rev	GCTAGCTTCAGCTAGGCATC AGTAGAAACAAGGGTGTTTTTTAG
Segment 5, 7 and 8	mRNA	Oligo tagdTRT	GTAAAACGACGGCCAGTTTTTTTTTTTTTTTTT

Absolute quantification of viral RNAs. To calculate absolute quantities of viral RNAs, we plotted the c_T values (from qPCR) of the serially 10-fold diluted RNA reference standards (ordinate) against the \log_{10} number of RNA molecules $n_{\text{molecules}}$ (abscissa) to generate calibration curves (linear regression). $n_{\text{molecules}}$ was calculated based on the quantity of the standard m_{STD} (ng), the fragment length N_{bases} (bp), the average mass of one base ($k=340$ (Da/bp)), and the Avogadro constant N_A (mol^{-1}).

$$n_{(\text{molecules})} = \frac{m_{\text{STD}}}{N_{\text{bases}} \times k \times N_A^{-1} \times 10^9}$$

Using the c_T value of a sample, the number of viral RNA molecules Q_{sample} was calculated by considering the slope (m) and y-intercept (b) of the calibration curve, the coefficient of dilution of the RT reaction F_{RT} , and the total volume of the RNA sample V_{sample} (μL).

$$Q_{\text{sample}} = 10^{\left(\frac{c_T - b}{m}\right)} \times F_{\text{RT}} \times V_{\text{sample}}$$

Table 3.3. Primers for qPCR (for quantification of viral RNAs)

Target	RNA type	Primer name	Sequence (5' -> 3')
Introduced tag sequence	vRNA	vRNA tagRealtime for	ATTTAGGTGACACTATAGAAGCG
	cRNA	cRNA tagRealtime rev	GCTAGCTTCAGCTAGGCATC
	mRNA	mRNA tagRealtime rev	GTAAAACGACGGCCAGT
Segment 5	vRNA	Seg 5 Realtime rev	CGCACTGGGATGTTCTTC
	cRNA and mRNA	Seg 5 Realtime for	GGAAAGTGCAAGACCAGAAGAT
Segment 7	vRNA	Seg 7 Realtime rev	TGAGCGTGAACACAAATCCTAAAA
	cRNA and mRNA	Seg 7 Realtime for	CATTGGGATCTTGCACTTGACATT
Segment 8	vRNA	Seg 8 Realtime rev	CACTTTCTGCTTGGGTATGA
	cRNA and mRNA	Seg 8 Realtime for	GGCGGGAACAATTAGGTCAGA

Absolute quantification of viral RNAs. To calculate absolute quantities of viral RNAs, we plotted the c_T values (from qPCR) of the serially 10-fold diluted RNA reference standards (ordinate) against the \log_{10} number of RNA molecules $n_{\text{molecules}}$ (abscissa) to generate calibration curves (linear regression). $n_{\text{molecules}}$ was calculated based on the quantity of the standard m_{STD} (ng), the fragment length N_{bases} (bp), the average mass of one base ($k=340$ (Da/bp)), and the Avogadro constant N_A (mol^{-1}).

$$n_{(\text{molecules})} = \frac{m_{\text{STD}}}{N_{\text{bases}} \times k \times N_A^{-1} \times 10^9}$$

Using the c_T value of a sample, the number of viral RNA molecules Q_{sample} was calculated by considering the slope (m) and y-intercept (b) of the calibration curve, the coefficient of dilution of the RT reaction F_{RT} , and the total volume of the RNA sample V_{sample} (μL).

$$Q_{\text{sample}} = 10^{\left(\frac{c_T - b}{m}\right)} \times F_{\text{RT}} \times V_{\text{sample}}$$

3.2.2.2. Analysis of the innate immune response

Expression of IFN-beta and myxovirus resistant gene 1 (Mx1) of infected cell populations was assessed using real-time RT-qPCR. For this, 500 ng of purified intracellular RNA was reverse transcribed using an oligo(dT) primer and "Maxima H Minus Reverse Transcriptase" (both from Thermo Scientific) according to the manufacturers' instructions. Subsequently, we performed a qPCR using the primers listed in Table 3.4. and "Rotor-Gene Q real-time PCR cyclor" (Qiagen). The qPCR mix (10 μL) contained 1 \times "Rotor-Gene SYBR Green PCR Kit" (Qiagen), 500 nM of each primer and 3 μL of diluted cDNA. Initial denaturation was conducted at 95°C for 5 min, followed by 40 PCR cycles (two-step protocol): 95°C for 10 s and 62°C for 20 s. Afterwards, melting curve analysis was performed from 65 to 90°C. Gene expression was then expressed as fold induction (over mock-infected cells) and calculated using the delta-delta c_T method with 18S rRNA as reference gene.

Table 3.4. qPCR primers (for analysis of innate immune response)

Primer name	Sequence (5' -> 3')
IFN-beta for	CCAGTTCCAGAAGGAGGACA
IFN-beta rev	TGTCCAGGTGAAGTTTTCC
Mx1 for	GAATCCTGTACCCAATCATGTG
Mx1 rev	TACCTTCTCCTCATATTGGCT
18S for	CGGACAGGATTGACAGATTG
18S rev	CAAATCGCTCCACCAACTAA

3.2.2.3. Quantification of ribosomes

We determined the ribosome quantity of infected single cells using real-time RT-qPCR. The workflow was developed in the context of the master thesis work of Alexander Ruff (Ruff, 2018), conducted and supervised in conjunction with this PhD work. A detailed procedure is provided in the Appendix C.2.

In general, the quantification of ribosomes was based on the detection of 18S rRNA. This RNA is associated with the small ribosomal subunit at exactly one 18S rRNA molecule per ribosome (Alberts, 2012). For the detection, we used small modification of the real-time RT-qPCR (described above) with a random hexamer primer (Thermo Scientific) in the RT and 18S rRNA primers (Table 3.4.) in the qPCR. For evaluation of the expression of 18S rRNA, we derived a modified $\Delta\Delta C_T$ -method, in which we calculated the fold change over the average single-cell 18S rRNA expression (Appendix C.2).

3.2.3. Segment-specific RT-PCR

We used the segment-specific RT-PCR for the detection of DI RNAs of cell population-based samples and of single-cell-derived samples. The method used for cell population-derived samples (section 3.2.3.1.) was previously established in the group (Frensing et al., 2014).

This method was further modified and optimized (in the context of this PhD work) towards single-cell sensitivity (protocol described in section 3.2.3.2.). This established protocol was then utilized in the master thesis work of Alexander Ruff (Ruff, 2018), conducted and supervised in conjunction with this PhD work.

3.2.3.1. Procedure for cell population-based samples

Purified vRNAs of virions, released from infected cell populations, were subjected to RT-PCR for two different purposes: (i) investigation of the presence of DI RNAs and (ii) the determination of vRNA sequence (described in section 3.2.4.). For RT, we used a universal “Uni12” primer (Hoffmann et al., 2001) (Table 3.5.), which hybridizes to the conserved 3’ end of all eight genome segments, to synthesize all cDNAs in one reaction. In subsequent PCR, we used individual reactions for each segment. The primer sequences (Table 3.5.) comprise the conserved 3’ or 5’ terminal vRNA end in conjunction with a segment-specific portion to allow for the specific amplification of the complete genome segment. Please note that for amplification and sequencing of S7 of over-proportional level of S7 (OP7) virus (S7-OP7) vRNA (section 3.2.4.), we used adapted primers (Table 3.5.).

Table 3.5. Primers for segment-specific RT-PCR (of population-based samples)

Reaction	Target	Primer name	Sequence (5' -> 3')
RT	All segments (WT)	Uni12	AGCAAAAGCAGG
	Segment 7 (OP7 Virus)	S7-OP7 RT	AAGCAGGTAGATATTGAAAG
PCR	Segment 1	S1 Uni for	AGCGAAAGCAGGTCAATTAT
		S1 Uni rev	AGTAGAAACAAGGTCGTTTTTAAAC
	Segment 2	S2 Uni for	AGCGAAAGCAGGCAAACCAT
		S2 Uni rev	AGTAGGAACAAGGCATTTTTTCATG
	Segment 3	S3 Uni for	AGCGAAAGCAGGTA CTGATCC
		S3 Uni rev	AGTAGAAACAAGGTA CTTTTTTGG
	Segment 4	S4 Uni for	AGCAAAAGCAGGGGAA
		S4 Uni rev	AGTAGAAACAAGGGTGTTTT
	Segment 5	S5 Uni for	AGCAAAAGCAGGGTAGATAATC
		S5 Uni rev	AGTAGAAACAAGGGTATTTTTTC
	Segment 6	S6 Uni for	AGCGAAAGCAGGGGTTAAAATG
		S6 Uni rev	AGTAGAAACAAGGAGTTTTTTGAAC
	Segment 7	S7 Uni for	AGCGAAAGCAGGTAGATATTG
		S7 Uni rev	AGTAGAAACAAGGTAGTTTTTTAC
	Segment 7 (OP7 Virus)	S7-OP7 PCR for	AAGCAGGTAGATATTGAAAG
		S7-OP7 PCR rev	AGTAGAAACAAGGTAGTTTT
	Segment 8	S8 Uni for	AGAAAAAGCAGGGTGACAAA
		S8 Uni rev	AGTAGAAACAAGGGTGTTTT

RT. For RT, 10 μL of RNA was mixed with 1 μL dNTPs (10 mM) and 1 μL primer (10 mM) and filled up to 14.5 μL with nuclease-free water. Incubation was conducted at 65°C for 5 min and 4°C for 5 min. We then added 4 μL of "5x Reaction Buffer", 50 U (0.5 μL) "RevertAid H Minus Reverse Transcriptase", 20 U (0.5 μL) "RiboLock RNase Inhibitor" and 0.5 μL nuclease-free water (all reagents from Thermo Scientific) and incubated at 42°C for 60 min. RT was terminated at 70°C for 10 min. cDNA was stored at -20°C, or immediately subjected to PCR.

PCR. For PCR, 2 μL cDNA was combined with 4 μL "5x Phusion HF Buffer", 2 μL MgCl_2 (10 mM), 1 μL dNTPs (10 mM), 1 μL of each primer (10 μM), 0.2 μL (0.4 U) "Phusion DNA Polymerase" and 8.8 μL nuclease-free water (all reagents from Thermo Scientific). Initial denaturation was performed at 98°C for 3 min, followed by 25 PCR cycles: 98°C for 25 s, 54°C for 45 s, and 72°C for different times: 2 min for S1-S3, 1.5 min for S4-S6, and 1 min for S7 and S8. Final elongation was conducted at 72°C for 10 min. PCR products were then visualized using agarose gel electrophoresis.

Agarose gel electrophoresis. Agarose gel electrophoresis was conducted with the following parameters: the gel was prepared with 2% (w/v) of agarose in Tris-Phosphat-EDTA (TPE) buffer and stained with Roti-GelStain (Roth); FastDigest Green Buffer (Thermo Scientific) was used as the loading dye for the samples; "GeneRuler DNA Ladder Mix" (Thermo Scientific) was used as the DNA ladder; and electrophoresis was performed at 75 V for 40 min.

3.2.3.2. Procedure for single-cell-based samples

We used the lysates of infected single cells (as described in section 3.1.3.2.) to investigate the occurrence of intracellular DI RNAs. Below, we describe the modified segment-specific RT-PCR methodology (optimized in the context of this PhD work) that facilitates single-cell measurements. Note that we here only investigated S1-S3 vRNAs, as DI RNAs typically predominantly occur on these segments. All primers shown in Table 3.5. were also used for the single-cell methodology, except for those shown in Table 3.6.

RT. For the RT, we mixed and homogenized the entire 5 μL of single-cell lysate in its corresponding well of the 384-well plate. Next, the complete 5 μL of the single-cell lysate was

transferred to PCR tubes and mixed it with 0.5 μ L dNTPs (10 mM) and 0.5 μ L primer (10 mM), and filled up to 7.25 μ L with nuclease-free water. Incubation was conducted at 65°C for 5 min and 4°C for 5 min. We then added 2 μ L of "5x Reaction Buffer", 25 U (0.25 μ L) "RevertAid H Minus Reverse Transcriptase", 10 U (0.25 μ L) "RiboLock RNase Inhibitor" and 0.25 μ L nuclease-free water (all reagents from Thermo Scientific) and incubated at 42°C for 60 min. RT was terminated at 70°C for 10 min. cDNA was stored at -20°C, or immediately subjected to PCR.

Table 3.6. Primers for segment specific RT-PCR (of single-cell-derived samples)

Primer name	Sequence (5' -> 3')
Seg 2 Uni for SC	AGCGAAAGCAGGCAAACC
Seg 3 Uni for SC	AGCGAAAGAAGGTACTGATCC
Seg 3 Uni rev SC	AGTAGAAACAAGGTACTTTTTTGGAC

PCR. For PCR, 3 μ L cDNA was combined with 6 μ L "5x Phusion GC Buffer", 3 μ L MgCl₂ (10 mM), 1.5 μ L dNTPs (10 mM), 1.5 μ L of each primer (10 μ M), 0.3 μ L (0.6 U) "Phusion Hot Start II DNA Polymerase" and 13.2 μ L nuclease-free water (all reagents from Thermo Scientific). Initial denaturation was performed at 98°C for 3 min, followed by 40 PCR cycles: 98°C for 25 s; then different temperatures: 59.5°C for S1 and S2 and 57.5°C for S3 for 45 s and 72°C for 2 min. Final elongation was conducted at 72°C for 10 min. PCR products were then visualized using agarose gel electrophoresis.

Agarose gel electrophoresis. Agarose gel electrophoresis was performed as described above (section 3.2.3.1.).

3.2.4. Determination of vRNA sequences

We determined the sequence of purified vRNA from virions released from infected cell populations. For sequencing of the coding regions, we used the segment-specific PCR for cell population-based samples (as described above, section 3.2.3.1.) to amplify the complete segments. After purification, the PCR products were sequenced using the same PCR primers.

All sequencing reactions were conducted by Eurofins Genomics (Ebersberg, Germany) utilizing Sanger sequencing.

For sequencing of the terminal vRNA ends, we derived and optimized a modified procedure from a previously published method (de Wit et al., 2007), which is based on the circularization of vRNA using a RNA ligase. The subsequent amplification of the junction region (containing the vRNA ends) was performed by RT-PCR. For the RT, a random hexamer primer was used. In subsequent PCR (primers are listed in Table 3.7.), we used a segment-specific primer in combination with a second primer, which was designed across the junction of the 3' and 5' vRNA end. After purification, sequencing was undertaken with indicated sequencing primers (Table 3.7.). Note that identities of the terminal 2 bp of each vRNA end were not determined (due to the primer design).

Table 3.7. Primers for vRNA sequence determination

Target	Primer name	Sequence (5' -> 3')	Sequencing primer
3' end of Segment 5	3' Seq S5 2bp for	GAAAAATACCCTTGTTTCTACTAG	
	3' Seq S5 rev	AGTTCTCTCATCCACTTTCCGT	x
3' end of Segment 7	3' Seq S7 2bp for	GTAaaaaactaccttgTTTCTACTAG	
	3' Seq S7 rev	TATGAGACCGATGCTGGGAG	x
3' end of Segment 7 (OP7 virus)	3' Seq S7-OP7 2bp for	GTAaaaaactaccttgTTTCTACTAG	
	3' Seq S7-OP7 rev	GTCACAGTCCCCATCCTGTT	x
3' end of Segment 8	3' Seq S8 2bp for	AAAAACACCCTTGTTTCTACTAG	
	3' Seq S8 rev	TTTATCCATGATCGCCTGGT	x
5' end of Segment 5	5' Seq S5 for	ACCAATCAACAGAGGGCATC	x
	5' Seq S5 2bp rev	TGATTATCTACCCTGCTTTCGCTAG	
5' end of Segment 7	5' Seq S7 for	TAGCTCCAGTGCTGGTCTGA	x
	5' Seq S7 2bp rev	TTTCAATATCTACCTGCTTTCGCTAG	
5' end of Segment 7 (OP7 virus)	5' Seq S7-OP7 for	TCCAGTGCTGGTCTGAAAGA	x
	5' Seq S7-OP7 2bp rev	TCAACATCTACCTGCTTTCACTAG	
5' end of Segment 8	5' Seq S8 for	TCACCATTGCCTTCTCTTCC	x
	5' Seq S8 2bp rev	TGTCACCCTGCTTTCGCTAG	

Ligation of vRNA ends. Circularization was performed by mixing 11.5 μ L of RNA sample with 4 μ L (40 U) of "T4 RNA Ligase 1", 2 μ L of "10x T4 RNA Ligase Reaction Buffer", 2 μ L of a 10 mM ATP solution (all reagents from New England BioLabs) and 0.5 μ L (20 U) of "RiboLock

RNase Inhibitor" (Thermo Scientific). The mixture was incubated for 1 h at 37°C, followed by heat inactivation at 65°C for 15 min. We immediately reverse transcribed the circularized RNA.

RT. For RT, a reaction mixture containing 4 µL ligated RNA, 1 µL (0.2 µg) of "Random Hexamer Primer", 1 µL of dNTPs (10 mM) and 8.5 µL of nuclease-free water was incubated at 65°C for 5 min (all reagents from Thermo Scientific) and immediately transferred on ice. We then added 4 µL of "5x RT buffer", 0.5 µL (100 U) "Maxima H Minus Reverse Transcriptase", 0.5 µL (20 U) of "RiboLock RNase Inhibitor" and 0.5 µL of nuclease-free water (all reagents from Thermo Scientific). Incubation was conducted at 25°C for 10 min and then 50°C for 30 min. Termination was performed at 85°C for 5 min. cDNA was stored at -20°C or immediately subjected to PCR.

PCR. The PCR reaction mix consisted of 4.5 µL of the RT product, 6 µL "5x Phusion HF Buffer", 3 µL MgCl₂ (10 mM), 1.5 µL dNTPs (10 mM), 1.5 µL of each primer (10 µM), 0.3 µL (0.6 U) "Phusion DNA Polymerase", and 11.7 µL of nuclease-free water (all reagents from Thermo Scientific). The cycling conditions comprised initial denaturation for 105 s at 98°C and then 40 PCR cycles: 10 s at 98°C, 30 s at 60°C and 40 s at 72°C. Final elongation was conducted at 72°C for 10 min.

Purification of PCR products. All PCR products were excised from gels (after agarose gel electrophoresis) and then purified using the "QIAquick Gel Extraction Kit" (Qiagen) according to the manufacturers' instructions.

3.2.5. Western blot analysis

We used western blot analysis for the investigation of intracellular viral proteins of cell population-based infection experiments. The detailed procedure for western blot analysis can be found in the operating instruction "MoBi 1". Briefly, infected MDCK cell populations were washed twice with PBS. We then added 150 µL of radioimmunoprecipitation assay (RIPA) buffer. Cells were harvested using a cell scraper and homogenized using 0.2 µm syringes. After centrifugation (10,000 x g, 10 min and 4°C), aliquots of supernatants were stored at -80°C

until western blot (WB). For WB, we used a polyvinylidene difluoride (PVDF) membrane. Mouse anti-NP monoclonal antibody (mAb) (Abcam, #ab128193) was used at a dilution of 1:2,000, rabbit anti-PA polyclonal antibody (pAb) (GeneTex, #GTX125932) was diluted to 1:10,000, mouse anti-M1 mAb (AbD serotech, #MCA401) was used at a dilution of 1:1,000 and mouse anti-glyceraldehyde 3-phosphate dehydrogenase (GAPDH) mAb from Merck (#CB1001) was diluted to 1:5,000. Secondary antibody stainings were performed using donkey anti-mouse pAb conjugated with horseradish-peroxidase (HRP) (Jackson ImmunoResearch, #715-036-151) and HRP-conjugated goat anti-rabbit pAb (Jackson ImmunoResearch, #111-035-003), both at a dilution of 1:10,000. Proteins on the blots were visualized using "SuperSignal West Dura Extended Duration Substrate" (Thermo Scientific).

3.2.6. Imaging Flow Cytometric Analysis

In the context of this PhD work, we have set-up and established a procedure for imaging flow cytometry. This methodology was then used for the analysis of experiments for publication (Kupke et al., 2018, Frensing et al., 2016), in conjunction with this PhD work. Detailed instructions for sampling and staining of the samples and the operation of the machine can be found in the corresponding operating instruction, located in the appendix C.3. In the following we will provide a brief summary of the procedure.

3.2.6.1. Sampling and staining

At indicated time points post infection, we rocked the population of infected MDCK cells (section 3.1.3.) to release detached cells into the infection medium. The supernatant was harvested and detached cells were separated from the supernatant by centrifugation (300 x g, 10 min and 4°C). Remaining adherent cells were trypsinized and afterwards combined with the detached cells from the previous step. Cells were then fixed with paraformaldehyde at a final concentration of 1% (30 min and 4°C) and then washed with PBS. Aliquots were stored in 70% ethanol at -20°C until imaging flow cytometric analysis.

Cell samples were washed twice with PBS containing 0.1% BSA and 2% glycine, thereby using centrifugation at 300 x g for 10 min at 4°C. Samples were then blocked for 30 min at 37°C in PBS containing 1% BSA. After washing, we performed antibody incubations (always at 37°C for 1 h in the dark). mAb mouse anti-NP mAb61A5 (a gift from Fumitaka Momose) was used at a dilution of 1:500. The antibody preferentially binds to NP in the conformation inherent to the

vRNP complex (Momose et al., 2007). Subsequent to washing, the secondary Alexa Fluor 647-conjugated goat anti-mouse pAb (LifeTechnologies, #A21235) was used at a dilution of 1:500 and cells were then washed two times. Nuclei were visualized by adding 4',6-diamidino-2-phenylindole (DAPI). For M1 staining, we used a fluorescein isothiocyanate (FITC)-conjugated mAb mouse anti-M1 (AbD serotec, #MCA401FX) at a dilution of 1:100. After cells were washed, they were resuspended in 1 mL of PBS. We then added 5 μ L PureLink RNase A (LifeTechnologies) for RNA degradation and 0.5 μ L of 7-aminoactinomycin (7-AAD) (Merck) for nuclear staining. Incubation was conducted for 30 min at room temperature in the dark. Finally, cells were washed.

3.2.6.2. Sample acquisition and software analysis

ImageStream X Mark II (Amnis, EMD Millipore) was used for acquisition of 10,000 cells per sample (debris and cell doublets were excluded) at 60x magnification. The 375 and 642 nm lasers were utilized for excitation of the vRNP-/DAPI-stained samples and the signal from channel 1 (CH1) and 5 (CH5) were acquired along with the brightfield (BF) imagery on CH6. For M1-/7-AAD-stained cells, we used the 488 and 561 nm excitation lasers and for detection CH2 and CH5 with BF on CH6. Single-stained positive controls were used to adjust laser powers and to acquire compensation files.

We used IDEAS software (version 6.1) for image analysis, using only in-focus single cells for analysis. Fractions of vRNPs in the cell nuclei were calculated based on the quantity of fluorescence signal that was co-localized with the nuclear signal (derived from DAPI). For this, we created masks "nucleus" and "whole_cell" using function "morphology" on CH1 and "object" on CH6, respectively. New features were generated, termed "intensity_CH5_nucleus" and "intensity_CH5_whole_cell" by using the feature "intensity" on CH5 within mask "nucleus" and "whole_cell", respectively. We then created a combined feature "FI_in_nucleus" with the following definition: "intensity_CH5_nucleus" / "intensity_CH5_whole_cell". CH1- and CH5-double positive cells (of focused, single cells) were plotted on histograms using this feature. The fraction of FI in the nucleus (%) was calculated by multiplying mean values of said feature by 100. M1 localization was assessed the same way, but under consideration of the corresponding detection channels.

4. Results and discussion

The following chapter is divided into three parts, starting from the establishment of the experimental workflow for single-cell analysis of IAV infection towards application of the developed technology. In the first section (4.1.), we describe the development of the single-cell analysis approach and the cell-to-cell heterogeneity in IAV replication. We then investigate potential sources of the between-cell variability in IAV infection in the second section of this chapter (4.2.). In the last section (4.3.), we report the discovery of a novel type of IAV-derived DIP, which was facilitated by single-cell analysis of IAV infection.

4.1. Single-cell analysis of IAV replication

In the first part of this section, we describe the single-cell analysis workflow that was established in the context of this PhD work (4.1.1.). Later, we investigate the cell-to-cell variability in IAV infection as well as extrinsic and intrinsic noise in IAV replication (4.1.2.). Please note that we used parts of the original research article in Nature Communications on single-cell analysis of IAV infection from Heldt and Kupke *et al.* in this section (Heldt et al., 2015).

4.1.1. Development of single-cell analysis approach

4.1.1.1. Experimental workflow

To investigate the cell-to-cell heterogeneity in IAV replication, we developed a procedure for the isolation and analysis of infected single cells (Figure 4.1.). First, a population of adherent MDCK cells was infected with influenza A virus at an MOI of 10. In general, such a high MOI ensures that all cells are infected simultaneously, which facilitates the study of a synchronized, single-cycle infection. Cells were then trypsinized, serially diluted and transferred to a 384-well plate. For the latter step, the cell suspension was adjusted to a calculated number one cell per well. Here, an electronic multichannel/multistep pipet facilitated the rapid pipetting of the cell suspension to each well (of the whole 384 well plate) in less than one minute. The identification of single cells in individual wells was conducted using manual phase-contrast microscopy. In agreement with the Poisson statistics, roughly 35% of the wells contained a single cell. Therefore, this procedure can yield up to ~ 134 single cells per plate. Using the 5x

4.1. Single-cell analysis of IAV replication

magnification of the microscope, cells could be clearly identified, and the whole 384-well plate could be examined in approx. one hour. The isolation of single cells was conducted using non-binding 384-well plates (Greiner, #781901). This type of plate was used to decrease the loss in virus titers, which can occur through unspecific adsorption of virus particles to the surface of a well.

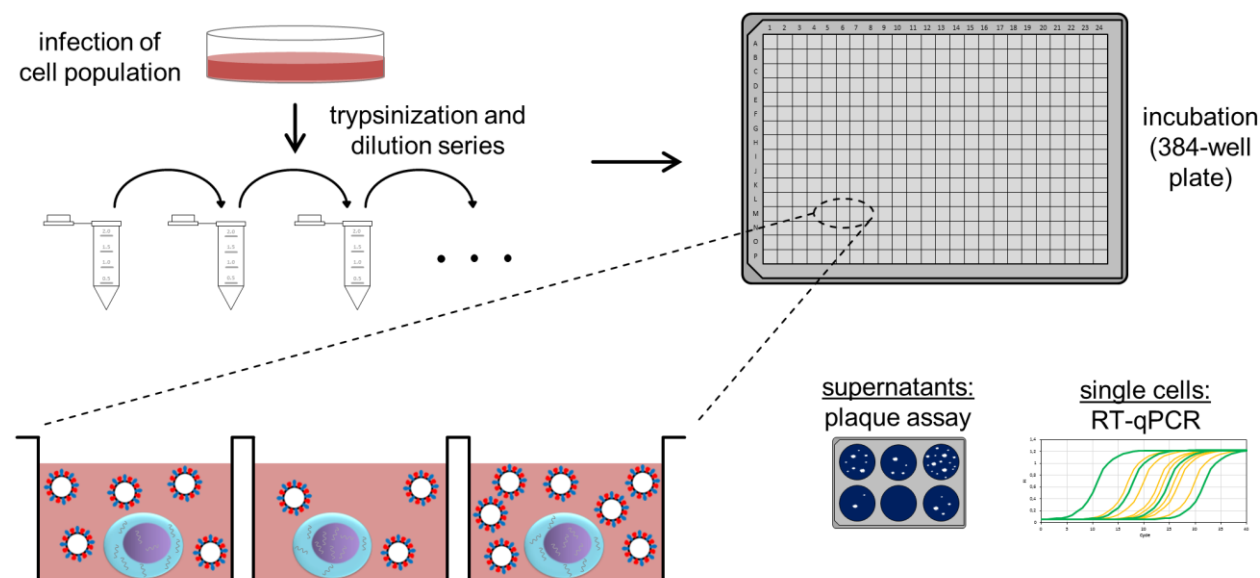


Figure 4.1. Workflow for single-cell analysis of IAV replication. Adherent MDCK cells were infected with influenza A virus at an MOI of 10. After incubation, cells were trypsinized and then serially diluted. The diluted cell suspension was transferred to a 384-well plate, and wells containing single cells were identified by phase-contrast microscopy. At time point of sample harvest, we subjected the supernatants of single cells to the plaque assay in order to quantify virus titers. Remaining single cells were lysed and then analyzed by real-time RT-qPCR, or RT-PCR. Scheme from (Kupke et al., 2018), licensed under CC BY 4.0.

After incubation, we quantified virus titers in the supernatant of individual cells using the plaque assay. Optionally, we determined the cell diameters of single cells to correlate them to the virus yield (section 4.2.2.1.). The single cell (remaining in the well) was washed and then lysed. Lysis of cells was conducted by freeze-thawing in BSA solutions. Such a cell disruption is very efficient, guarantees a high RNA stability and enhanced downstream reverse transcription efficiency (Svec et al., 2013). The cell lysate was then subjected to real-time RT-qPCR for the quantification of intracellular vRNAs (subsequent sections), or ribosomal RNAs (rRNAs) (section 4.2.2.); or to RT-PCR for the detection of DI RNAs (4.2.3.). Please note that only a small fraction of the single-cell lysate was required for analysis. This facilitated the quantification of

up to four different vRNA segments (simultaneously) and the investigation of the presence of DI RNAs on three genome segments (simultaneously). Moreover, also note that our single-cell analysis procedure was highly reproducible, as indicated by highly similar average single-cell intracellular vRNA and virus yield quantities of different independent experiments (Heldt et al., 2015). Therefore, we were able to pool data sets of independent experiments for higher sample sizes. Taken together, the experimental workflow comprises a simple, rapid and efficient procedure for absolute quantification of extracellular virus titers and intracellular vRNAs of IAV-infected single cells. Moreover, it offers a good throughput of single-cell measurements and multi-parametric correlation of virus yields to additional single-cell features.

4.1.1.2. Comparison of single-cell- and population-derived experiments

We next investigated whether our single cell isolation procedure leads to an altered cellular behavior, or perturbed virus replication. In the case of no alteration/perturbation, no differences in the outcome between single-cell- and population-based experiments should be observable. Therefore, we compared virus titers and intracellular vRNA levels of the two experimental conditions (Figure 4.2.).

Accordingly, single cells, infected with PR8 from NIBSC (PR8-NIBSC) at an MOI of 10, were isolated and analyzed for virus titers and intracellular vRNA levels at 12 hpi. Afterwards, we calculated mean values of the single-cell-derived measurements to obtain cell-specific virus titers and vRNA levels. In total, we performed up to five independent experiments for quantification of vRNAs of S3-S8 and eight independent experiments for virus titers. For population-based experiments, we used our standard infection protocol, which does not involve the trypsinization of cells. Like the single-cell experiments, cells were infected with PR8-NIBSC at an MOI of 10 until 12 hpi. Cell-specific virus titers and intracellular vRNAs were calculated based on the cell count at time point of infection. In total, three independent cell population-based experiments were performed. We observed that the single-cell- and population-based experiments yielded comparable cell-specific virus titers and vRNA levels, with measurement values that were in the same order of magnitude (Figure 4.2.). These results indicate that that our single-cell infection procedure does not lead to a perturbation, or alteration, of cell behavior and virus replication.

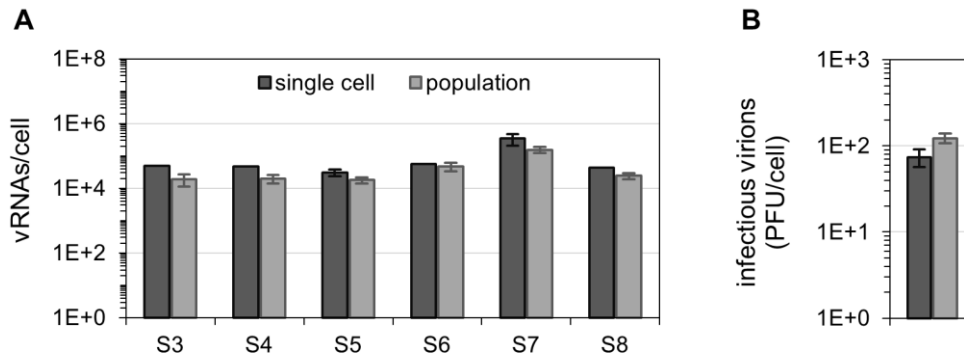


Figure 4.2. Comparison of single cell- and population-derived measurements. Mean values of single cell- and population-based measurements of intracellular vRNA (A) and of virus titers (B). Cells infected with PR8-NIBSC at an MOI of 10 were analyzed for their virus titer using plaque assay and intracellular vRNA content by real-time RT-qPCR at 12 hpi. Panels comprise pooled data of multiple independent single cell-derived experiments (n=2 for S3, S4 and S8; n=5 for S5; n=1 for S6; n=3 for S7; n=8 for virus yield). Population-based measurements comprise the data from three independent experiments. Error bars indicate standard deviations. Figure adapted from (Heldt et al., 2015), licensed under CC BY 4.0.

4.1.1.3. Technical measurement errors

Single cells typically show a large heterogeneity in a diversity of parameters, such as the protein content or specific mRNA levels (Raj et al., 2006). We next investigated the measurement error of our single-cell quantification methods to clarify the contribution of technical noise to our measurements and thus, the observed cell-to-cell heterogeneity (which may not necessarily represent the true biological between-cell variability). Therefore, we investigated the technical measurement error of the plaque assay and the real-time RT-qPCR (Figure 4.3.).

For this, we conducted multiple measurements of the same samples in technical replicates (n=4). For the plaque assay, we used samples that contained three to 1500 PFU (in 50 μ L); a sample concentration range, which typically represents the observed cell-to-cell heterogeneity in virus titers (section 4.1.2.). For real-time RT-qPCR, we used the lysates of seven infected single cells, each one used for the four measurements in technical replicates. We observed a relatively small technical measurement error of the plaque assay and the real-time RT-qPCR (Figure 4.3.), with a mean relative standard deviation of 18% and 27%, respectively. As we will show in the following sections, the observed between-cell variability exceeds these technical errors by far (section 4.1.2.). We therefore conclude that our quantification methods

4.1. Single-cell analysis of IAV replication

are accurate enough to investigate cell-to-cell variability in IAV replication, and that technical errors affect the observed cell-to-cell heterogeneity only insignificantly.

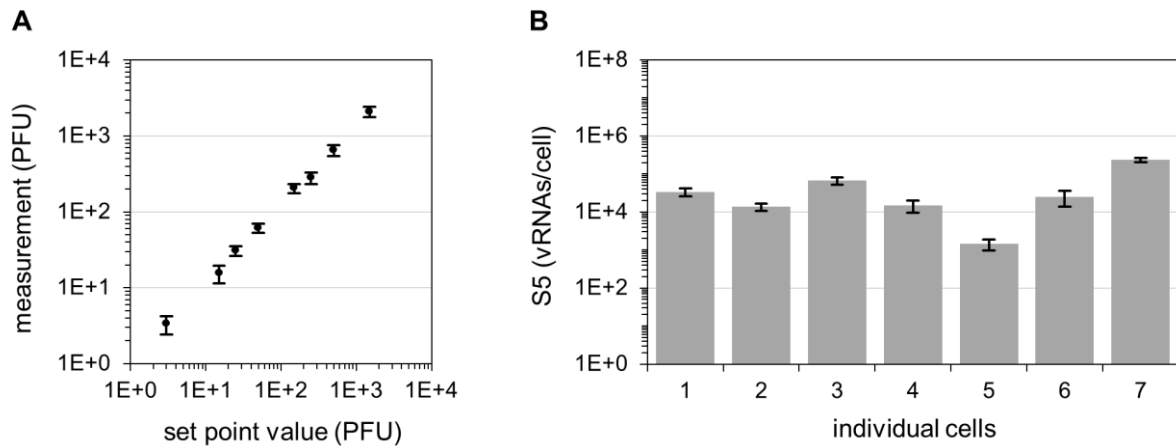


Figure 4.3. Technical measurement error. Measurement error of plaque assay (A) and real-time RT-qPCR (B). Error bars indicate standard deviation. Errors are derived from multiple measurements of the same samples in technical replicates ($n=4$). For the plaque assay (A), we used diluted seed virus, adjusted to different PFU quantifies (set point value) per 50 μ L (which corresponds to the volume of the supernatant of a single cell). For real-time RT-qPCR (B), infected single cells (MOI=10) were analyzed for S5 vRNA at 12 hpi. Figure adapted from (Heldt et al., 2015), licensed under CC BY 4.0.

4.1.2. Cell-to-cell heterogeneity in IAV replication

In this section, we use the single-cell analysis procedure presented in the previous section (4.1.1.) to investigate the cell-to-cell variability in IAV replication. Specifically, we studied the heterogeneity in virus titers and vRNA levels, extrinsic and intrinsic sources of noise, and infections with different virus strains.

4.1.2.1. Virus titers

First of all, we studied the between-cell variability in virus titers of IAV-infected single cells. For this, single MDCK cells, infected with PR8-NIBSC at an MOI of 10 (as described in Figure 4.1.), were incubated until 12 hpi. Afterwards, virus titers in the supernatant of individual cells were quantified by the plaque assay. We observed a surprisingly large cell-to-cell heterogeneity in virus yield, with virus titers that spanned almost three orders of magnitude (Figure 4.4.). Specifically, we observed single cells that released only one PFU; yet, other cells were capable

4.1. Single-cell analysis of IAV replication

to produce several hundred PFU. The highest virus titer observed was 970 PFU per cell. Overall, the distribution of virus yield of single cells was skewed to the left. Most of the cells were of a low productivity, releasing only 1 to ~ 67 PFU. Note that the coefficient of variation (CV), a statistical measure for the dispersion of a distribution, was 2.04. Interestingly, roughly 40% of the cells did not show a plaque titer. Please note that a detailed analysis of these cells is provided in section 4.3. In summary, we observed a vast cell-to-cell variability in virus titers of IAV-infected cells.

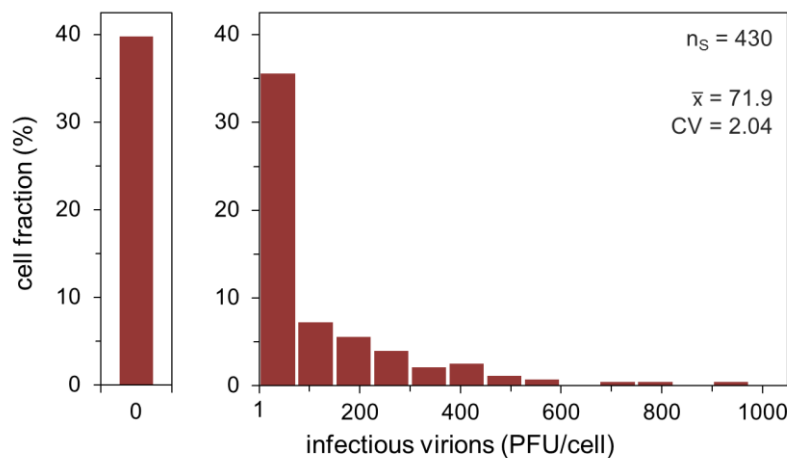


Figure 4.4. Distribution of virus titer of single IAV-infected cells. Single cells infected with PR8-NIBSC at an MOI of 10 were analyzed for their virus titers using plaque assay at 12 hpi. The bar on the left shows the fraction of cells that show no virus release (0 PFU). \bar{x} depicts mean and relative standard deviation CV is indicated. n_s indicates the number of single-cell measurements. Pooled data of multiple independent experiments ($n=8$) are shown. Figure adapted from (Heldt et al., 2015), licensed under CC BY 4.0.

4.1.2.2. vRNA content

Next, we investigated the cell-to-cell heterogeneity in intracellular vRNA content of IAV-infected cells. For this, we analyzed the cell lysates of PR8-NIBSC virus-infected (MOI=10) single cells using real-time RT-qPCR at 12 hpi. We observed a vast between-cell variability in intracellular vRNA quantities (Figure 4.5.). More specifically, the vRNAs of S3-S8 showed quantitative differences that spanned up to three orders of magnitude. The CVs ranged from 1.13 to 1.77, with a mean CV of 1.33. Moreover, the vRNA levels of most genome segments were lognormally distributed, as indicated by Shapiro-Wilk normality test ($p>0.05$). Note that the mean vRNA quantities were all in the order of 10^4 molecules per cell, except for S7 vRNA,

4.1. Single-cell analysis of IAV replication

which showed a mean vRNA level in the order of 10^5 molecules per cell, in agreement with previous population-based experiments (Figure 4.2.). Taken together, we observed a large cell-to-cell heterogeneity in intracellular vRNA levels of IAV-infected cells.

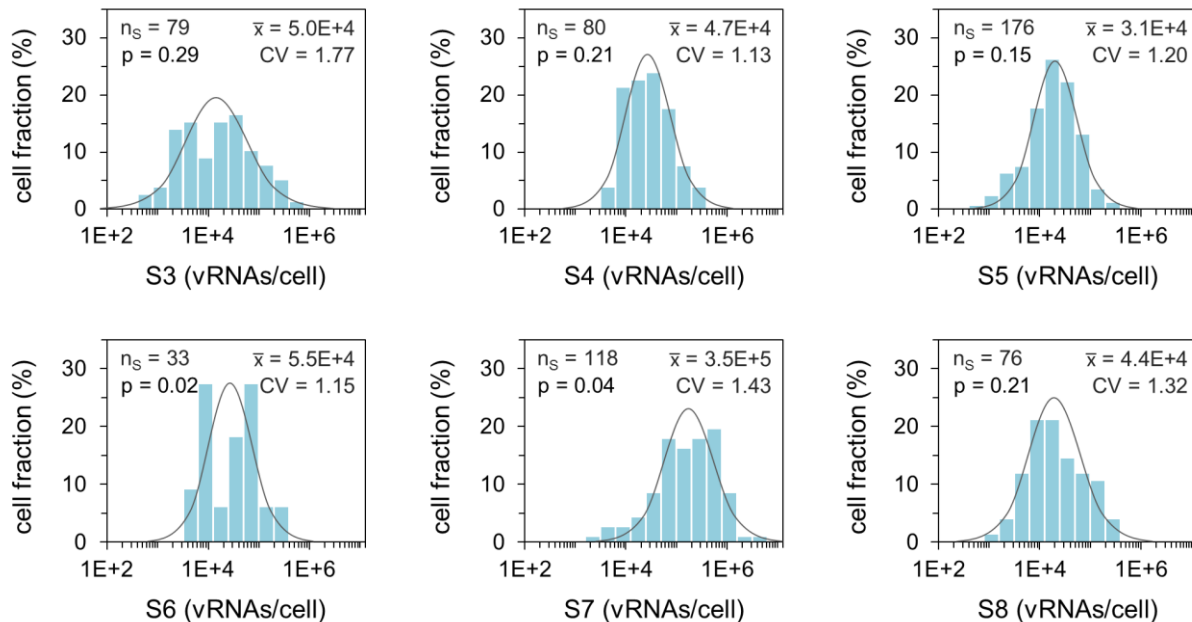


Figure 4.5. Histograms of vRNA level of IAV-infected single cells. Cells infected with PR8-NIBSC at an MOI of 10 were analyzed for intracellular vRNA content at 12 hpi using real-time RT-qPCR. The solid lines describe log-normal distributions fitted to the data. The p value from Shapiro-Wilk normality test is indicated. \bar{x} depicts mean and relative standard deviation CV is indicated. n_s indicates the number of single cells analyzed. Pooled data of multiple independent experiments are depicted ($n=2$ for S3, S4 and S8; $n=5$ for S5; $n=1$ for S6; $n=3$ for S7). Figure adapted from (Heldt et al., 2015), licensed under CC BY 4.0.

4.1.2.3. Extrinsic and intrinsic noise

As mentioned before (section 4.1.1.), only a small fraction of a single-cell lysate was sufficient for the quantification of intracellular vRNAs. Thus, up to four different genomic vRNA segments could be quantified per infected single cell. Therefore, we next studied the quantitative dependency of the different vRNAs in infected single cells (Figure 4.6.). We observed a positive correlation in the abundancies of most genome segments (Figure 4.6A); surprisingly, however, we did not observe a correlation of S7 vRNA to other genome segments (Figure 4.6C).

4.1. Single-cell analysis of IAV replication

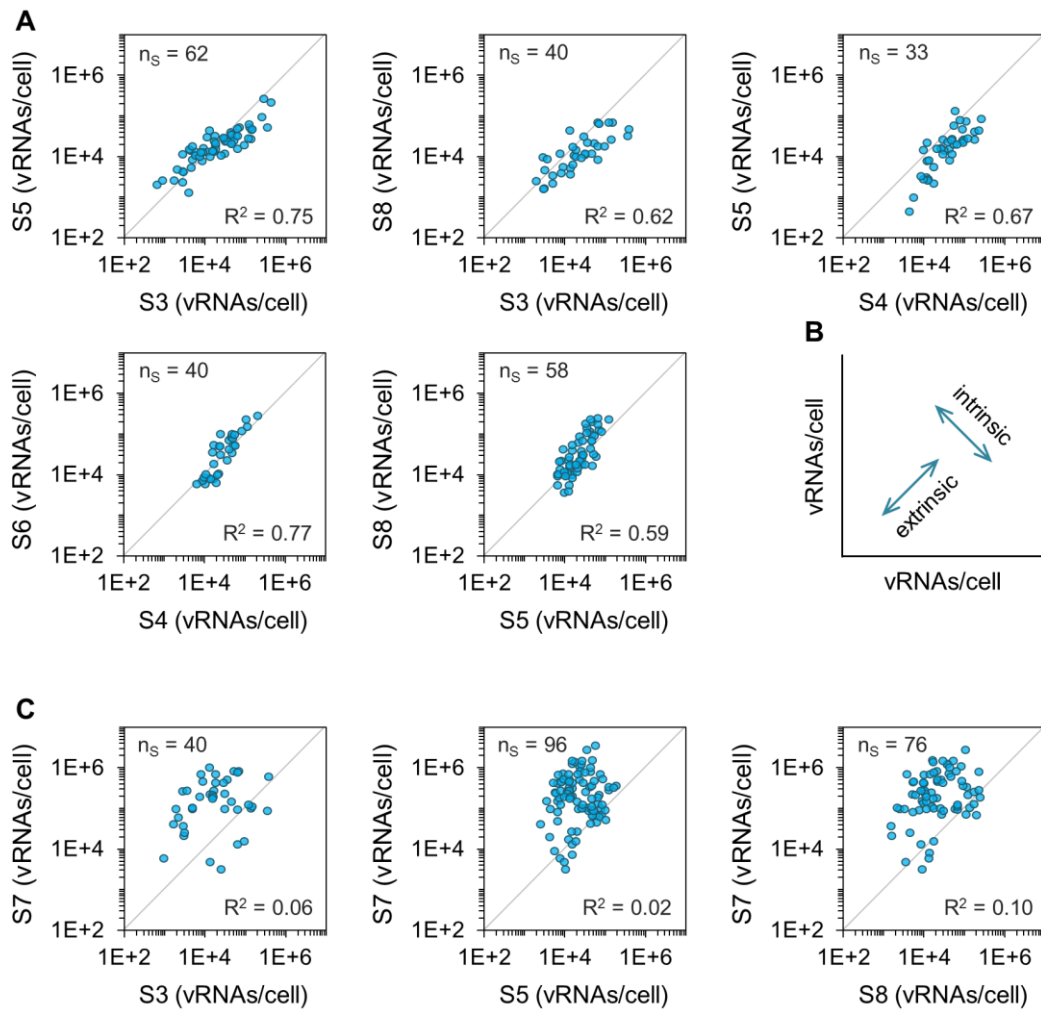


Figure 4.6. Quantitative correlation between different vRNA segments. Single cells infected with PR8-NIBSC at an MOI of 10 were analyzed for their intracellular vRNA content using real-time RT-qPCR at 12 hpi. (A) Correlation between most genomic vRNA segments. (B) Extrinsic and intrinsic noise in the vRNA levels of two different genome segments. Spread of data points perpendicular to the parity line (on which vRNA levels are equal) corresponds to intrinsic noise and spread parallel to this line is enhanced by extrinsic noise. (C) Correlation of S7 vRNA to other genome segments. The coefficient of determination (R^2) is provided; the parity line ($R^2=1$) is shown for reference. n_s indicates the number of single-cell measurements. Pooled data of multiple independent experiments are depicted ($n=2$ for S3 and S5, S5 and S8, S7 and S8; $n=1$ for S3 and S8, S4 and S5, S4 and S6, S3 and S7; $n=3$ for S5 and S7). Figure adapted from (Heldt et al., 2015), licensed under CC BY 4.0.

A positive correlation in the quantities of the different vRNA segments can be caused by extrinsic sources of noise in virus replication. Typically, such factors should affect the synthesis of every different vRNA segment in a cell evenly. Conclusively, this would increase the quantitative correlation between different vRNAs (Figure 4.6B). However, the stochasticity inherent to biochemical reactions can inevitably also generate intrinsic noise in vRNA synthesis. This randomness should affect the level of each vRNA in an individual cell differently, which

would, hence, result in a decrease in their correlation. We can observe such an intrinsic noise in IAV replication, as manifested by the deviation of vRNA quantities from the ideal correlation (i.e. the parity line) between two different genomic vRNA segments (Figure 4.6B). In summary, our experiments demonstrate the presence of extrinsic and intrinsic noise in IAV replication.

4.1.2.4. Differences between virus strains

Interestingly, single-cell infections with the same PR8 virus strain obtained from another source (i.e. PR8 from RKI (PR8-RKI)) resulted in a slightly different experimental outcome. More specifically, we observed a positive correlation in the abundance of S7 vRNA in relation to other genome segments (Figure 4.7B), which contrasts the results obtained from infections performed with PR8-NIBSC (Figure 4.6B). Furthermore, we observed that PR8-RKI virus infections did not result in a large fraction of non-productive cells (Figure 4.7D), such like in PR8-NIBSC virus infection (Figure 4.4.). Please note that a detailed analysis of these observations is provided in section 4.3.

Nevertheless, the infection with PR8-RKI appears to show a similarly large cell-to-cell heterogeneity in IAV replication compared to PR8-NIBSC virus infection. More precisely, virus titers and intracellular vRNA levels of PR8-RKI virus infection showed quantitative differences that spanned almost three orders of magnitude, similar to PR8-NIBSC virus replication. Moreover, the CV of vRNA levels ranged from 1.14 to 1.44, with an average CV of 1.33 for PR8-RKI virus infection (Figure 4.7C), which is in line with a mean CV of 1.33 for PR8-NIBSC virus replication (Figure 4.5). Yet, virus yields of PR8-RKI virus-infected single cells showed a significantly smaller CV of 1.14 compared to PR8-NIBSC virus replication (CV=2.04). Moreover, the means of cell-specific virus titers showed a large variation (146.0 and 71.9 PFU for PR8-RKI and PR8-NIBSC virus infection, respectively). Both differences can be explained by the low percentage (~1%) of non-productive cells for PR8-RKI virus replication compared to PR8-NIBSC infection (~40%). Nevertheless, cell-to-cell variability in virus titers appeared to be similarly large for infections with both seed viruses. More specifically, the range of single-cell virus titers of PR8-NIBSC infection was 1-970 PFU and 1-800 PFU for PR8-RKI virus infection. Taken together, we observed large qualitative differences in single-cell virus replication between PR8-NIBSC and PR8-RKI virus infections, which will be further elucidated in section 4.3. Nevertheless, the cell-to-cell heterogeneity in virus replication appeared to be similar for infections with both strains.

4.1. Single-cell analysis of IAV replication

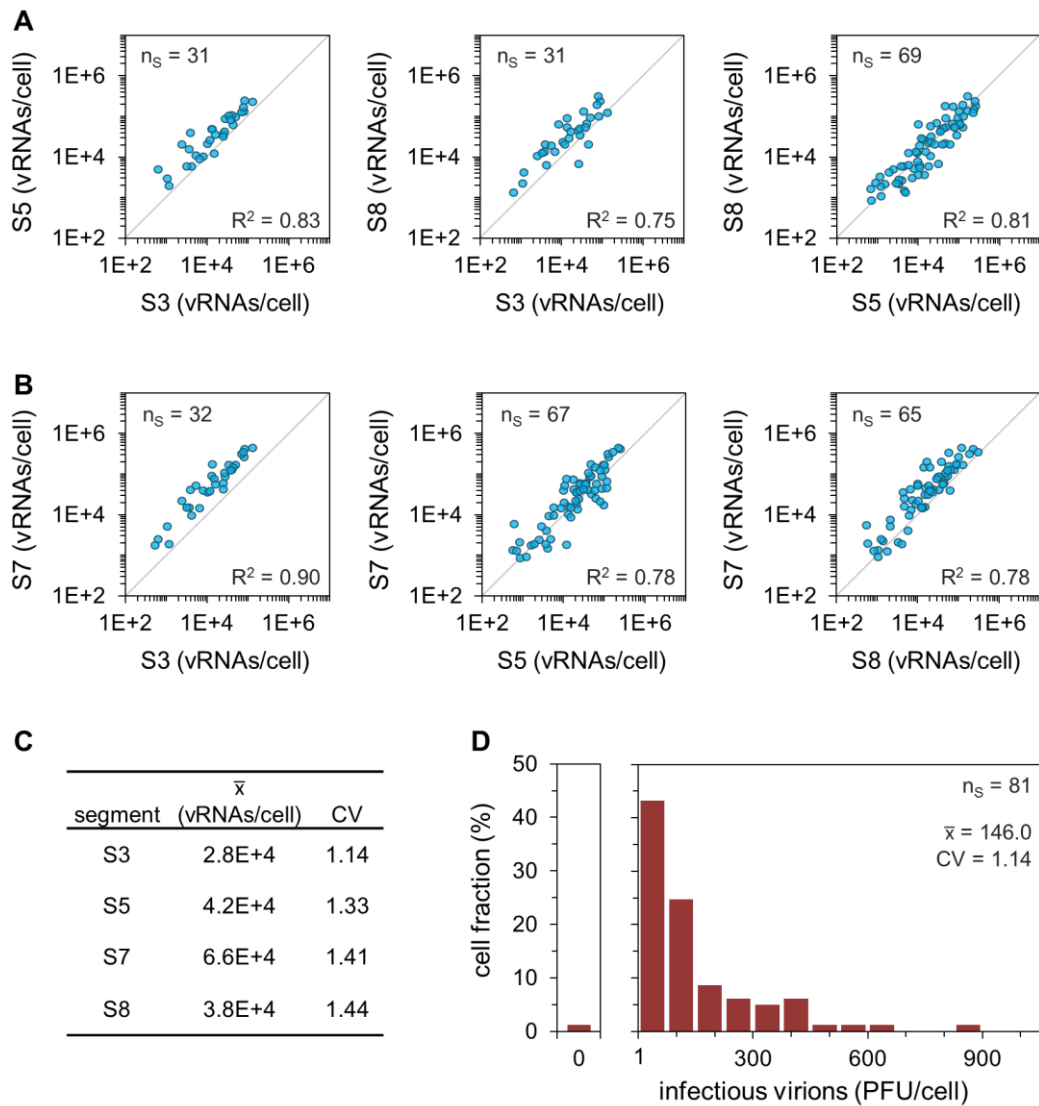


Figure 4.7. Single-cell analysis of PR8-RKI virus replication. Single cells infected with PR8-RKI at an MOI of 10 were analyzed for their intracellular vRNA content using real-time RT-qPCR and virus titers by plaque assay at 12 hpi. n_s indicates the number of single cells analyzed. (A and B) Correlation between vRNA segments. The coefficient of determination (R^2) is provided; the parity line ($R^2=1$) is shown for reference. Pooled data of multiple independent experiments are depicted ($n=1$ for S3 and S5, S3 and S8, S3 and S7; $n=2$ for S5 and S8, S5 and S7, S7 and S8). (C) Means and CVs of the data shown in (A and B). (D) Distribution of virus titers. The bar on the left shows the fraction of cells that show no virus release (0 PFU). \bar{x} depicts mean and relative standard deviation CV is indicated. Pooled data of multiple independent experiments ($n=2$) are shown.

4.1.3. Discussion of experimental procedure

In the previous two sections, we first established an experimental workflow for single-cell analysis of IAV infection (4.1.1.) and then used this procedure to study the cell-to-cell heterogeneity in IAV replication (4.1.2.). In this section, we discuss and compare our single-cell

analysis workflow for virus infections to other reported procedures from the literature. Finally, we present alternative strategies that were not chosen for single-cell analysis of IAV infection in the context of this PhD work.

In the framework of this thesis, an experimental procedure for the analysis of IAV-infected single cells was to be established. In the following, we will present the requirements for a (theoretically) optimal solution for such a procedure, formulated at the beginning of the PhD work. An absolute quantification of virus titers (and other parameters) from single cells was important to be able to provide data for mathematical modeling (performed elsewhere in the group). Moreover, a high throughput of single-cell measurements was necessary to obtain sufficient data for statistically valid frequency distributions. Next, a multiplex analysis of single cells ought to enable the correlation of virus yields to additional parameters of single cells, which would facilitate a deeper investigation of high- and low-productive single cells. Additionally, all single-cell derived read-outs needed to be unaffected by any kind of special treatment that are typical for single-cell isolation procedures. Our aim was the study of single cells that behave like non-perturbed cells and alike in a cell population. In addition, we also aimed for the option to infect an individual cell with a single virus particle. Such an infection would facilitate the investigation of the influence of the infecting virus particle (which are highly heterogeneous themselves) to the cell-to-cell heterogeneity in virus replication. Furthermore, the whole approach ought to be innovative as well, and combined with existing commercially available approaches to decrease the time needed for the establishment. Finally, it should be feasible to establish a technology, perform experiments and to generate data for publication in time and in the framework of this PhD thesis.

Most of the experimental approaches that we considered for single-cell analysis of IAV-infected cells were only able to fulfil a few of the above mentioned requirements (discussed below), while the experimental procedure (that we have finally decided for) was able to meet almost every criteria for an optimal solution. The methodology offered (i) a simple, rapid and efficient procedure that was straightaway commercially available, (ii) a good throughput of single-cell measurements per experiment (a number in the order of tens and up to ~150 measurements are possible), (iii) absolute quantification of the extracellular virus titer, together with absolute quantification of intracellular vRNAs, (iv) multi-parametric correlation of virus titers to either: up to four vRNAs (simultaneously), the presence of intracellular DI RNAs on up to three genome segments simultaneously (section 4.2.3.), rRNAs (section 4.2.2.), or to the whole-cell transcriptome using NGS (subject of ongoing studies), (v) infected, isolated single cells that show no apparent perturbation due to their processing and isolation procedure, (vi) some

minor innovative improvements and (vii) the timely generation and publication of research data.

The isolation of infected single cells using a limiting dilution approach was also performed elsewhere (Delbruck, 1945b, Dulbecco and Vogt, 1954, Fischetti et al., 1968, De Paepe et al., 2010, Timm and Yin, 2012). However, most studies did not explicitly control that their samples contained a single cell using a microscope (Delbruck, 1945b, Dulbecco and Vogt, 1954, Fischetti et al., 1968, De Paepe et al., 2010). Instead, the authors utilized the Poisson statistics to ensure that only a small fraction of their samples contained more than one cell. For example, Delbruck *et al.* applied a diluted suspension of infected bacteria to microcentrifuge tubes to yield a calculated number of 0.25 bacteria per tube (Delbruck, 1945b). Under these conditions, only ~19% will theoretically contain a single cell, and roughly 3% more than two cells, while ~78% of the samples will not contain cells. This clearly suboptimal procedure was improved by Timm *et al.* The authors used microscopy to confirm that individual wells of a 96-well plate contained a single cell (Timm and Yin, 2012). One drawback of this procedure may be the relatively large area of each cavity of a 96-well plate (~0.34 cm²), which might have resulted in a relatively long time to scan a well, resulting in a relatively low throughput. In contrast, we used 384-well plates with a surface area of only ~0.07 cm², which allowed for a very short time to investigate each well microscopically. Further, only about one hour was required to examine the whole 384-well plate. This, together with the fact that we applied a calculated number of one cell per well (which theoretically results in ~37% of the wells containing a single cell) resulted in a higher throughput. Further, our procedure allowed for the microscopic determination of the cell size with the aim to directly compare it to the single-cell virus titer (section 4.2.2.). Note that in other single-cell virology studies, the dependency of cell size and virus titers was studied more indirectly (Delbruck, 1945b, Zhu et al., 2009, Xin et al., 2018, Dulbecco and Vogt, 1954). For instance, widths of yield and cell size distributions were compared (Dulbecco and Vogt, 1954, Delbruck, 1945b), or small and large cell populations were sorted using FACS to investigate their virus yields (Zhu et al., 2009, Xin et al., 2018).

Subsequent to incubation of the isolated and infected single cells, we quantified virus titers in the supernatants using plaque assays. The traditional plaque assay was also used in several other single-cell virology studies, e.g. (Delbruck, 1945b, Dulbecco and Vogt, 1954, Fischetti et al., 1968, De Paepe et al., 2010, Timm and Yin, 2012, Zhu et al., 2009, Schulte and Andino, 2014, Sekellick and Marcus, 1980, Combe et al., 2015), mainly due to its very high sensitivity, which allows to detect even one PFU per sample. Please note that we also tested and considered other virus quantification assays (e.g. HA assay, TCID₅₀ assay, real-time RT-qPCR,

ELISA, ns-TEM and virus counter “ViroCyt” (Rossi et al., 2015)). Yet, all these methods suffered from significantly higher quantification limits, or low throughputs (e.g. ns-TEM), which rendered them not suitable for single-cell analysis. After the removal of supernatants from the infected single cells (for the plaque assays), we lysed the remaining cells for subsequent real-time RT-qPCR, or conventional RT-PCR. In general, PCR-based methods are frequently used in single-cell-related research as they typically provide a very high sensitivity and a large quantification range (Xin et al., 2018, Schulte and Andino, 2014, Stahlberg et al., 2013). This is mainly caused by the fact that the analytes are amplified during the measurement. We used the real-time RT-qPCR for absolute quantification of IAV genomic vRNAs. This methodology was already established in the group (Frensing et al., 2014). However, the method was further optimized in the framework of this thesis for an improved sensitivity. One of the most critical parameters for such an optimization was the coefficient of dilution between the RT and qPCR (Stahlberg et al., 2013). Finally, the optimized procedure required only a small fraction of the single-cell lysate, which facilitated the quantification of up to four different vRNA segments at the same time. Similarly, we also optimized an established RT-PCR for the detection of DI RNAs (Frensing et al., 2014) to single-cell sensitivity in the context of this PhD work, and were then able to investigate DI RNAs on three genome segments simultaneously.

We compared single-cell- and cell population-based experiments and confirmed that the isolated infected single cells did not show an aberrant virus replication, as indicated by very similar cell-specific virus titers and vRNA levels (both measurements were in the same order of magnitude compared to cell population-derived measurements). This outcome confirmed that we did not investigate the biology of unnaturally behaving single cells with our workflow. However, this control was not performed in every single-cell virology study, except for poliovirus-infected cells (Schulte and Andino, 2014), FMDV-infected cells (Guo et al., 2017), and VSV-infected cells (Akpınar et al., 2016b). In the latter study, the single-cell- and population-derived measurements showed significant differences. Yet, the authors observed similar trends in the behavior within both conditions when comparing experimental perturbations (Akpınar et al., 2016b). Akpınar *et al.* concluded that either direct or indirect cell-cell interactions may be responsible for the deviation between single-cell- and population-based experiments. However, this appears to be only true for VSV infection, but not for poliovirus-, FMDV-, or IAV-infected cells (Schulte and Andino, 2014, Guo et al., 2017, Heldt et al., 2015). Furthermore, we determined the technical measurement error of the plaque assay and the real-time RT-qPCR. We observed a relatively small error for different analyte concentrations over a range that was typically observed for single-cell measurements. Please note that the

observed cell-to-cell heterogeneity (section 4.1.2.) exceeded these errors by far. These results indicate that the technical measurement error cannot artificially generate, or significantly contribute to the large between-cell variability. This was similarly confirmed for the analytics used for studying single-cell poliovirus replication (Schulte and Andino, 2014).

Alternative strategies for single-cell analysis of virus infection. In the following, we will briefly discuss some alternative strategies for single-cell analysis of IAV-infected cells. We did not utilize these approaches, as they did not meet many of the criteria for an optimal solution (described above). First of all, FACS was used in many other single-cell virology studies for the isolation of infected single cells into the cavities of a multi-well plate (Schulte and Andino, 2014, Zhu et al., 2009, Kirzner et al., 2016, Zanini et al., 2018, Xin et al., 2018). For example, Zhu *et al.* used this technology for VSV-infected BHK cells (Zhu et al., 2009). In this study, the authors used a recombinant strain of VSV expressing GFP. This was necessary for the detection of positively infected cells and for sorting these cells into the cavities of a multi-well plate. The major advantage of this procedure is the possibility to infect cells with a very low MOI (i.e. MOI=0.01), which ensured single-hit virus infections. For IAV infections, such a fluorescent protein tag can also be used (De Baets et al., 2015, Manicassamy et al., 2010). However, such recombinant viruses typically suffer from an attenuated virus replication (Ibricevic et al., 2006, Kittel et al., 2004), probably due to the large burden of the reporter gene on viral fitness (Breen et al., 2016). Because of this, we did not consider to use a fluorescent protein-tagged IAV in combination with FACS for our studies. Schulte *et al.* circumvented this drawback by using a non-fluorescent tagged virus (Schulte and Andino, 2014). Instead, the authors sorted single cells into cavities of a 96-well plate containing 200 μ L of media. After incubation and lysis (by freeze thawing), the authors divided that supernatant into fourths, each fourth used (i) to confirm the infection using an "infection find" assay, (ii) to quantify single-cell virus titers, (iii) to quantify intracellular viral (+) RNA, and (iv) viral (-) RNA. The major drawback of this procedure is the low sensitivity due to partitioning and diluting the single-cell samples in large volumes (Schulte and Andino, 2014). In contrast, we analyzed the whole supernatants of single cells for the quantification of virus titers. Moreover, the volume of our single-cell lysate (for measurements at the intracellular level) was only 5 μ L, which facilitates a higher concentration of analytes and thus, an increased sensitivity in the measurements of our single-cell samples.

The FluidFM appeared to be another promising technology at the beginning of this work (Stiefel et al., 2012, Amarouch et al., 2018). This technology is based on atomic force microscopy (AFM), in which a cantilever can be accurately positioned to single cells. The cantilever itself contains a nanofluidic channel, which allows for the deposition of fluids onto cells, or even the injection of substances into single cells, or cell nuclei (Meister et al., 2009, Guillaume-Gentil et al., 2014, Amarouch et al., 2018). For instance, this technology was used for the deposition of single vaccinia virus particles on single cells in order to study single-hit virus infections (Stiefel et al., 2012). However, again, fluorescent protein-tagged viruses were used, which can result in attenuated virus replication. Moreover, fluorescence was used to assess viral gene expression. Yet, as with all fluorescence-based readouts, the dynamic range is typically relatively narrow, which results in semi-quantitative results and not absolute quantification (Steuerman et al., 2018). In addition, the technology allows to pick and place the cells, for instance to a nano-well plate (Amarouch et al., 2018). However, the throughput would be limited and the access to the individual cavities containing single cells problematic. Altogether, we decided to exclude this approach for single-cell analysis of IAV infection due to several reasons: the high costs for the instrumentation, the long time required for the set-up and establishment, and most importantly, due to the fact it did not meet our most important requirements, i.e. a high throughput and an absolute quantification.

Microfluidics offers many opportunities for single-cell analysis applications (Armbrecht and Dittrich, 2017, Prakadan et al., 2017, Murphy et al., 2017). Single cells can be entrapped, cultivated and analyzed in many ways on-chip. However, the implementation of a complex lab-on-a-chip workflow typically requires a lot of interdisciplinary expertise, manpower and time for the establishment of each separate unit operation (Warrick et al., 2016, Murphy et al., 2017). Moreover, at the beginning of this work, a commercially available approach, suitable for our intentions, was not available. Later, in 2016, a microfluidic technology for single-cell analysis of virus infections was published that facilitated the analysis of hundreds (or up to roughly one thousand) of single cells per experiment (Warrick et al., 2016). The same workflow was later used to investigate VSV infection at the single-cell level (Akpinar et al., 2016b, Timm et al., 2017). The technology comprises a micro-well-based device, fluorescence-based imaging, a streamlined bioinformatics data analysis workflow and time-lapse analysis of single-cell virus infections (Warrick et al., 2016). A similar technology was later developed by another group for studying poliovirus infection at the single cell level (Guo et al., 2017). However, these approaches only offer semi-quantitative fluorescence-based read-outs, rather than absolute

quantification. Moreover, fluorescent protein-tagged viruses were utilized, which may be problematic (as discussed above).

scRNA-seq is a technology, which is presently used in many research areas, including single-cell virology (Russell et al., 2018, Zanini et al., 2018, Steuerman et al., 2018). Isolation of single cells before scRNA-seq can be performed using either FACS (Zanini et al., 2018, Steuerman et al., 2018), or droplet based microfluidics (Russell et al., 2018). In these studies, viral mRNAs were evaluated and used as a marker for the strength of virus replication of individual cells. Based on this, the host cell transcriptome was analyzed and related to virus replication. One drawback of this workflow is that the host cell mRNAs were not directly correlated to the extracellular virus titer of infected single cells. Such a procedure is, in principle, feasible with our experimental workflow. Please note that such a corresponding experiment is the subject of ongoing studies.

Summary. We have developed an experimental procedure for single-cell analysis of IAV-infected cells, which appeared to be highly suitable to study the cell-to-cell heterogeneity in IAV replication. The workflow offers an easy and rapid handling and a good throughput (of more than 100 single cells per experiment) for solid statistical analysis. Moreover, it allows for the absolute quantification of extracellular virus titers and intracellular vRNAs and the multi-parametric correlation of virus yields to additional parameters, such as the cell size, rRNAs, multiple different intracellular vRNAs, or to DI RNAs on different genome segments. Finally, the procedure does not seem to interfere with virus replication, which enables an unbiased analysis of single IAV-infected cells. This workflow may be further utilized to study the whole-cell transcriptome of infected single cells (Russell et al., 2018, Zanini et al., 2018, Steuerman et al., 2018) and specifically, to correlate it to the extracellular virus production.

4.1.4. Discussion of cell-to-cell heterogeneity in IAV replication

In virology, experiments are typically performed using cell populations. In contrast, we performed single-cell analysis to study the cell-to-cell heterogeneity in IAV replication. We observed an extreme variability in virus titers and intracellular vRNA levels between infected single cells. Moreover, the majority of the cells released only a few progeny virions while others were of a high productive phenotype. In addition, we observed large differences in the copy

number of different genomic vRNA segments within a cell. Together, we show that IAV replication is highly heterogeneous at the single-cell level (Heldt et al., 2015).

In particular, we observed that virus yields of single IAV-infected MDCK cells ranged from 1 to 970 PFU, which corresponds to quantitative differences that span almost three orders of magnitude. Such a high variability in virus titers was also observed for other animal cell-virus systems, such as for WEE virus-infected CEF cells (Dulbecco and Vogt, 1954). For VSV infections, a between-cell variability in virus yields of about 300-fold was observed (Zhu et al., 2009, Timm and Yin, 2012, Combe et al., 2015, Sekellick and Marcus, 1980). Moreover, poliovirus-infected single cells showed a production capacity of 269 PFU/cell to 4225 PFU/cell (Schulte and Andino, 2014). Similarly, for virus-infected bacteria, the differences in virus yields encompassed two to three orders of magnitude (Delbruck, 1945b, Fischetti et al., 1968, De Paepe et al., 2010, Kirzner et al., 2016). Interestingly, all these before-mentioned studies reported a left-skewed distribution of virus titers, with a bias towards low-productive cells, like in our study. Moreover, our experiments demonstrated a large variability in intracellular vRNA levels that covered approx. three orders of magnitude. For poliovirus-infected cells, a heterogeneity in viral RNA quantities of one to two orders of magnitude was observed (Schulte and Andino, 2014). Overall, other studies in single-cell virology agree well with our observation that virus replication is extremely diverse at the single-cell level and that population-based measurements can only describe average-cell behavior, which may be an inaccurate description of virus infections.

Stochastic mathematical modeling of the intracellular IAV life cycle, performed by Heldt *et al.*, revealed that a large proportion of the fluctuations in intracellular vRNA levels originate in the early infection stages as a result of the inherent randomness in biochemical reactions (Heldt et al., 2015). More specifically, it was shown that the autocatalytic nature of vRNA synthesis can amplify the noise generated early in virus replication. In support of this, a similar mechanism was also suggested to explain the large heterogeneity in viral burst sizes of phage-infected bacteria, which was also proposed to be a result of the autocatalytic intracellular virus growth (Delbruck, 1945a). Moreover, in this context, it was speculated that autocatalytic reaction cascades are prone to the amplification of noise (which was shown for chemical reactions (Delbruck, 1940)). The same notion was also used to establish a mathematical model that was able to explain the highly diverse distribution in viral burst sizes of the non-lytic filamentous virus m13 from *E. coli* (De Paepe et al., 2010). In addition, it was even suggested that the repetitive multiplicative propagation of noise in cascades of autocatalytic reactions can yield lognormal distributions of the components involved in the reaction cascade (Koch, 1966).

Intriguingly, we can observe such lognormal distributions for most vRNA segments in our study, in agreement with stochastic mathematical modeling (Heldt et al., 2015). Thus, this observation may be well explained by the autocatalytic amplification of vRNAs, given the inherent randomness of biochemical reactions.

The IAV genome comprises a segmented RNA genome with eight individual vRNA segments. In contrast to viruses that contain a single genomic RNA strand (like, for instance, poliovirus and VSV), the IAV vRNAs represent independent functional units that can (to a certain degree) replicate independently from one another. This genome segmentation provided us the opportunity to distinguish between extrinsic and intrinsic sources noise in virus replication, by assessing the vRNA levels of different genome segments in infected single cells. A similar experimental approach was performed by Elowitz *et al.*, who investigated source of noise in protein expression of *E. coli* (Elowitz et al., 2002). In our experiments, we observed a positive within-cell correlation in the levels of most genome segments (except for S7 vRNA, which did not correlate to other vRNAs, as discussed below). A positive intersegment correlation can be explained by sources of extrinsic noise in IAV replication. Such a noise is generated by deterministic factors, which are different between individual cell, and which can affect the replication of all the different vRNAs in a cell equally. However, we observed that this correlation was not perfect, as indicated by a deviation in the quantities between different genome segments from the ideal correlation. Such an intrinsic noise is the result of the inherent randomness of biochemical reactions (Elowitz et al., 2002). Taken together, IAV replication is affect by both, extrinsic and intrinsic noise. Moreover, note that we investigated both sources of noise for the first time in virus-infected cells (Heldt et al., 2015).

In addition, our single-cell infection studies with PR8-NIBSC virus resulted in very interesting observations: approx. 40% of the cells did not show a plaque titer and S7 vRNA did not show a correlation to other genome segments. Such characteristics were not observed for infections performed with the same virus strain, but from a different source (PR8-RKI virus). More specifically, the fraction of apparently non-productive cells was negligible (~1%) and S7 vRNA showed a positive correlation to other genome segments for PR8-RKI virus replication. The reader is here kindly referred to another section (4.3.), where we elucidate this phenomenon in detail. Nevertheless, note that the between-cell heterogeneity of PR8-RKI virus replication was similar as compared to PR8-NIBSC virus infection.

Summary. Our experiments reveal a large cell-to-cell heterogeneity in IAV replication with virus titers and vRNA levels that span roughly three orders of magnitude. Moreover, we observed a positive correlation in the abundance of the different vRNA segments, and show that IAV replication is affected by extrinsic and intrinsic sources of noise. Between-cell variability in IAV replication is, thus, affected by stochastic processes; however, the contribution of the influence of deterministic factors remains to be elucidated (chapter 4.2.). Finally, we observed that S7 vRNA does not show a correlation to other genome segments; yet, this was dependent on the virus strain used for infection. This very interesting observation will be thoroughly followed up in section 4.3. Collectively, our experiments contribute to challenging current beliefs that population-based infections are an accurate representation of virus infections (Delbruck, 1945a, Zhu et al., 2009, Schulte and Andino, 2014, Russell et al., 2018).

4.2. Sources of cell-to-cell heterogeneity in IAV replication

In the previous section (4.1.), we presented the experimental procedure for single-cell analysis and investigated the large cell-to-cell variability in IAV replication. The present section is now devoted to investigating potential sources of that large between-cell heterogeneity. In the first part of this section, we investigate virus-derived sources that can affect the cell-to-cell heterogeneity in virus infection (4.2.1.). Subsequently, we study the effects that may arise by cellular factors (4.2.2.). Finally, we study the impact of DIPs on the between-cell variability in IAV replication (4.2.3.). Please note that we used minor parts of the original publication in Nature Communications on single-cell analysis of IAV infection from Heldt and Kupke *et al.* in this section (Heldt et al., 2015).

4.2.1. Effect of virus-derived characteristics

4.2.1.1. Extrinsic noise

In the previous section (4.1.), we have shown that IAV-infected cells show a large between-cell variability in virus titers and intracellular vRNA levels. To investigate the dependency between virus yields and vRNAs, we quantified both parameters at the same time of infected single-cells. For this, we isolated PR8-NIBSC virus-infected (MOI=10) single cells (as described above (Figure 4.1.)) and cultivated the cells until 12 hpi. Subsequently, we quantified virus titers using the plaque assay and intracellular vRNAs of S5 and S8 using real-time RT-qPCR. We observed that the high-productive single cells showed overall elevated levels of intracellular vRNAs (Figure 4.8.). More specifically, the upper 10% of cells with regard to cell-specific productivity appeared to contain higher levels of both vRNAs (S5 and S8). As elaborated in section 4.1.4., the overall level of the different vRNAs are affected by sources of extrinsic noise. Hence, we conclude that the single-cell virus titer, which itself appears to depend on overall vRNA levels, must also be affected by sources of extrinsic noise (i.e., deterministic factors).

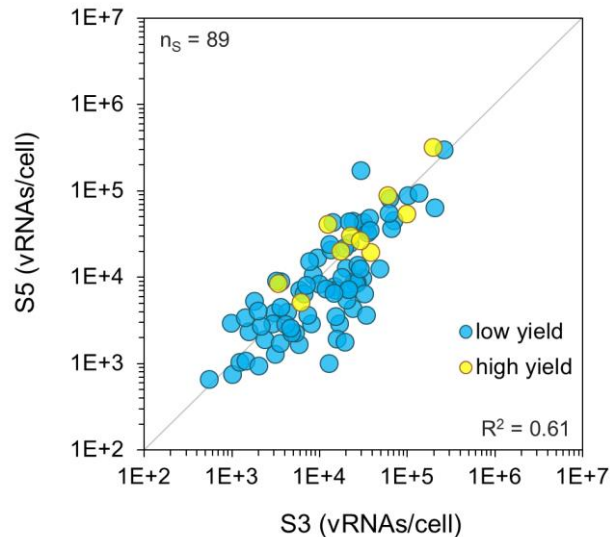


Figure 4.8. Dependency of virus titer on vRNA level. Single cells infected with PR8-NIBSC at an MOI of 10 were simultaneously assayed for their virus titer (by plaque assay) and intracellular vRNA levels (using real-time RT-qPCR) at 12 hpi. High yield cells comprise the upper 10% of cells regarding their virus release. The coefficient of determination (R^2) is provided and the parity line ($R^2=1$) is shown for reference. n_s indicates the number of single-cell measurements. Pooled data of multiple independent experiments ($n=4$) are shown. Figure adapted from (Heldt et al., 2015), licensed under CC BY 4.0.

4.2.1.2. Progress of infection

So far, every single-cell infection experiment, shown and discussed in the previous sections, was conducted until 12 hpi. In addition, we could only provide a snapshot analysis at this time point with our methodology. However, it is well known that single-cell virus replication is also highly diverse in the dynamic behavior (Timm and Yin, 2012, Warrick et al., 2016, Guo et al., 2017). To investigate whether the large between-cell heterogeneity (that we observed at 12 hpi) was generated by cells that are in different infection states, we compared different time points post infection. More specifically, we attempted to elucidate whether lowly-replicating cells (i.e. cells that show a low virus titers and/or low vRNA levels) become a highly-replicating cell at later times post infection. In such a case, more highly-replicating cells would be observable and the cell-to-cell variability would be reduced. Please note that some results shown in this subsection (i.e., of intracellular vRNA measurements in Figure 4.9A and B) are derived from of the BSc thesis of Kathrin Zumpf (Zumpf, 2015), which was conducted and supervised in the context of this PhD work.

4.2. Sources of cell-to-cell heterogeneity in IAV replication

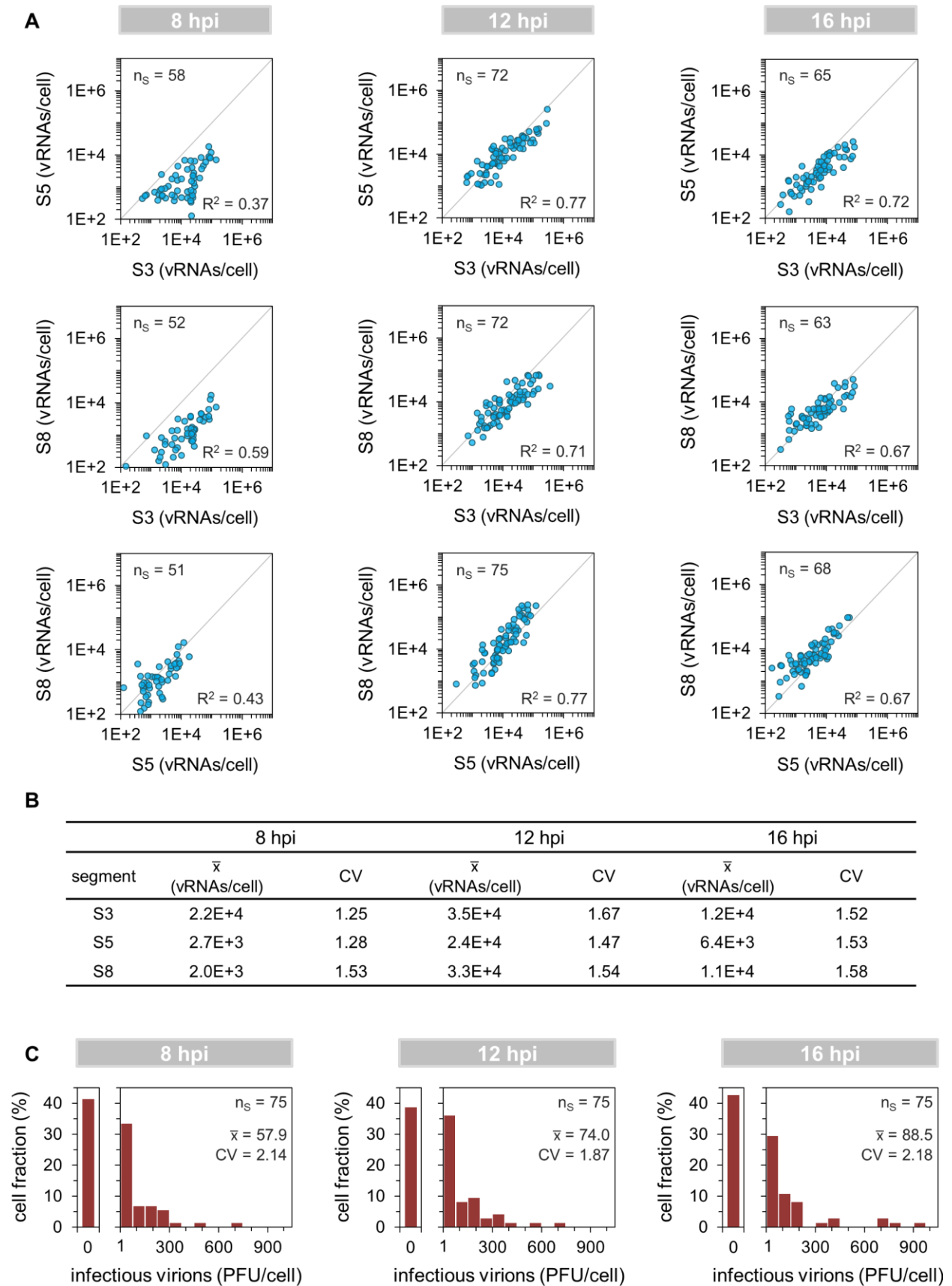


Figure 4.9. Single-cell virus replication at different times post infection. Single cells infected with PR8-NIBSC at an MOI of 10 were analyzed for their intracellular vRNA content using real-time RT-

4.2. Sources of cell-to-cell heterogeneity in IAV replication

qPCR and virus yields using the plaque assay at indicated time points post infection. (A) Correlation of vRNA segments. The coefficient of determination (R^2) is provided and the parity line ($R^2=1$) is shown for reference. (B) Means and CVs of the data shown in (A). (C) Histograms of virus titer of individual IAV-infected cells. The bar on the left hand side shows the fraction of cells that show no virus release (0 PFU). \bar{x} depicts mean and relative standard deviation CV is indicated. n_s indicates the number of single cells analyzed. Two independent experiments were performed for each time point and the pooled data is depicted.

Indeed, at 8 hpi, we observed that most of the infected single cells contained a low vRNA level, and later (at 12 hpi) more highly-replicating cells could be observed (Figure 4.9A). It, thus, appeared that some of the lowly-replicating cells (at 8 hpi) become highly-replicating at 12 hpi. However, the fraction of highly-replicating cells did not seem to further increase from 12 to 16 hpi. Concurrently, the cell-to-cell heterogeneity appeared to be similar between these two time points, as indicated by very similar average CVs in the per-cell vRNA levels (1.56 and 1.54 for 12 and 16 hpi, respectively (Figure 4.9B)). Please note that, in this context, the CVs of single-cell derived measurements may be used as a measure for the degree of cell-to-cell heterogeneity (Schulte and Andino, 2014). In addition, the results of the single-cell virus yield distributions at the different time points did not indicate a significant alteration in the fraction of non-, low-, or high-productive cells (Figure 4.9C). Furthermore, the CVs in these distributions appeared similar between infections performed until 8, 12, and 16 hpi. Although, note that the means of single-cell virus yields increased over time (as expected). Taken together, these results indicate that the large between-cell variability (observed so far at 12 hpi) did not seem to be generated by cells that are in different infection stages.

4.2.1.3. Multiplicity of infection

The single-cell infection experiments performed in this PhD work were primarily performed using an MOI of 10. However, at lower MOIs, it can be expected that the numbers of infecting virions per cell (and thus, the numbers of intracellular genome segments) are decreased. In such a scenario, stochastic effects should be more pronounced as compared to higher MOIs, in which the differences on individual RNA replication reactions are believed to average out, leading to a more stable and robust genomic RNA replication, as shown for VSV infections (Schulte and Andino, 2014). To test whether this is also true for IAV replication, we infected single cells at an MOI of 1 until 12 hpi (Figure 4.10.).

4.2. Sources of cell-to-cell heterogeneity in IAV replication

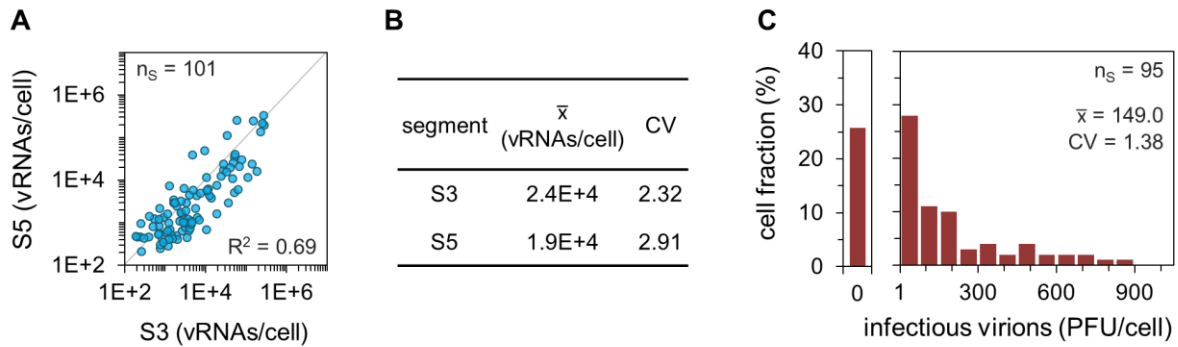


Figure 4.10. Single-cell virus replication at an MOI of 1. Single cells were infected with PR8-NIBSC at an MOI of 1 and then analyzed for their intracellular vRNA content using real-time RT-qPCR and virus yields using the plaque assay at 12 hpi. Cells that were tested negative in both intracellular vRNAs and released PFUs (non-infected cells) were excluded from analysis. n_s indicates the number of single-cell measurements. (A) Correlation of vRNA segments. The coefficient of determination (R^2) is provided, the parity line ($R^2=1$) is shown for reference. Pooled data of four independent experiments are depicted. (B) Means and CVs of vRNA levels depicted in (A). (C) Distribution of virus titers of single infected cells. The bar on the left hand side shows the fraction of cells that show no virus release (0 PFU). \bar{x} depicts mean and relative standard deviation CV is indicated. Pooled data of three independent experiments are shown.

Indeed, it appeared that the cell-to-cell variability in intracellular vRNA content was higher (Figure 4.10A) compared to infections performed at an MOI of 10 (Figure 4.5. and 4.9.). More specifically, we observed an elevated average CV of 2.62 in the vRNA levels of S3 and S5 (Figure 4.10B), which was significantly larger than the average CVs derived from infections at an MOI of 10 (1.33 and 1.56, from Figure 4.5. and 4.9., respectively). Moreover, it appeared that the deviation of vRNA levels from the ideal correlation, i.e. intrinsic noise (Elowitz et al., 2002), was slightly larger as compared to virus replication at an MOI of 10 (Figure 4.5. and 4.9.). To proof this, we quantified intrinsic noise η_{intr} of the single-cell data (i.e., the mean relative standard deviation in the quantities of two different vRNAs, as described in (Elowitz et al., 2002)). Indeed, intrinsic noise, calculated from S3 and S5 vRNA quantities, was higher ($\eta_{\text{intr}} \sim 60\%$) at an MOI of 1 as compared to infections performed at an MOI of 10 ($\eta_{\text{intr}} \sim 43\%$ and $\eta_{\text{intr}} \sim 40\%$ from Figure 4.6 and 4.9, respectively). Furthermore, note that the average per-cell vRNA level did not seem to be affected by the MOI. More specifically, cell-specific vRNA levels were in the same order of magnitude (for MOI=1) as compared to infection performed at an MOI of 10 (Figure 4.5. and 4.9.).

Interestingly, the between-cell heterogeneity in virus titers did not seem to be essentially affected by the MOI, as single-cell virus yields ranged from 1 to 833 PFU/cell (Figure 4.10C), similar to the range in virus titers of infections performed at an MOI of 10 (1-970 and 1-720

PFU/cell, from Figure 4.4. and 4.9., respectively). Yet, the CV of virus yield distributions was reduced for an MOI of 1 (CV=1.38) compared to infections performed at an MOI of 10 (1.87 and 2.04). This decrease may be explained by the reduction in the fraction of non-productive cells (~26%) compared to infections performed at high MOI (~39 and ~40%, from Figure 4.4. and 4.9., respectively). This may also explain the higher average cell-specific virus titers at an MOI of 1 (149.0 PFU/cell compared to 71.9 and 74.0 PFU/cell for infections at an MOI of 10). The higher fraction of non-productive cells at an MOI of 10 is likely caused by DIP co-infections, which suppress virus replication, and which are more frequent at a higher MOI. In summary, we show that single-cell infections performed at an MOI of 1 show a higher between-cell variability in intracellular vRNA content (but not in cell-to-cell heterogeneity in virus titers) compared to infections performed at an MOI of 10. Therefore, it appears that stochastic effects in vRNA synthesis are more pronounced at low MOIs. However, cell-to-cell heterogeneity in virus titers did not seem to be affected.

4.2.1.4. Virus-to-virus heterogeneity

Influenza virus particles are highly heterogeneous in their properties (Brooke, 2017, Marcus et al., 2009). In particular, a genetic variability between individual virions can be typically observed, which is a result of the error-prone nature of the viral RNA polymerase (Lauring and Andino, 2010). Therefore, we next investigated whether the diversity in the genetic background of the infecting virus particles can have an effect on cell-to-cell variability in IAV replication. For this, we performed plaque purification of the parental seed virus (PR8-NIBSC virus). In general, plaque purification is well known to reduce the between-virus genetic heterogeneity of a virus population. These plaque purified virus seeds were subsequently used for single-cell infection experiments to investigate whether the between-cell heterogeneity would be reduced compared to the original seed virus. The results of these single-cell infections (at an MOI of 10 until 12 hpi), using three different plaque purified virus seeds, are shown in Figure 4.11.

Surprisingly, we did not observe a reduction in the cell-to-cell variability in IAV replication as compared to cells infected with the parental seed virus (Figure 4.5., 4.6. and 4.9.). Specifically, average CVs of intracellular vRNA levels ranged from 1.12 to 1.46 for infections performed with the plaque purified isolates (Figure 4.11D), which did not seem to significantly differ compared to infections performed with the original virus seed (1.33 and 1.56 from Figure 4.5. and 4.9., respectively).

4.2. Sources of cell-to-cell heterogeneity in IAV replication

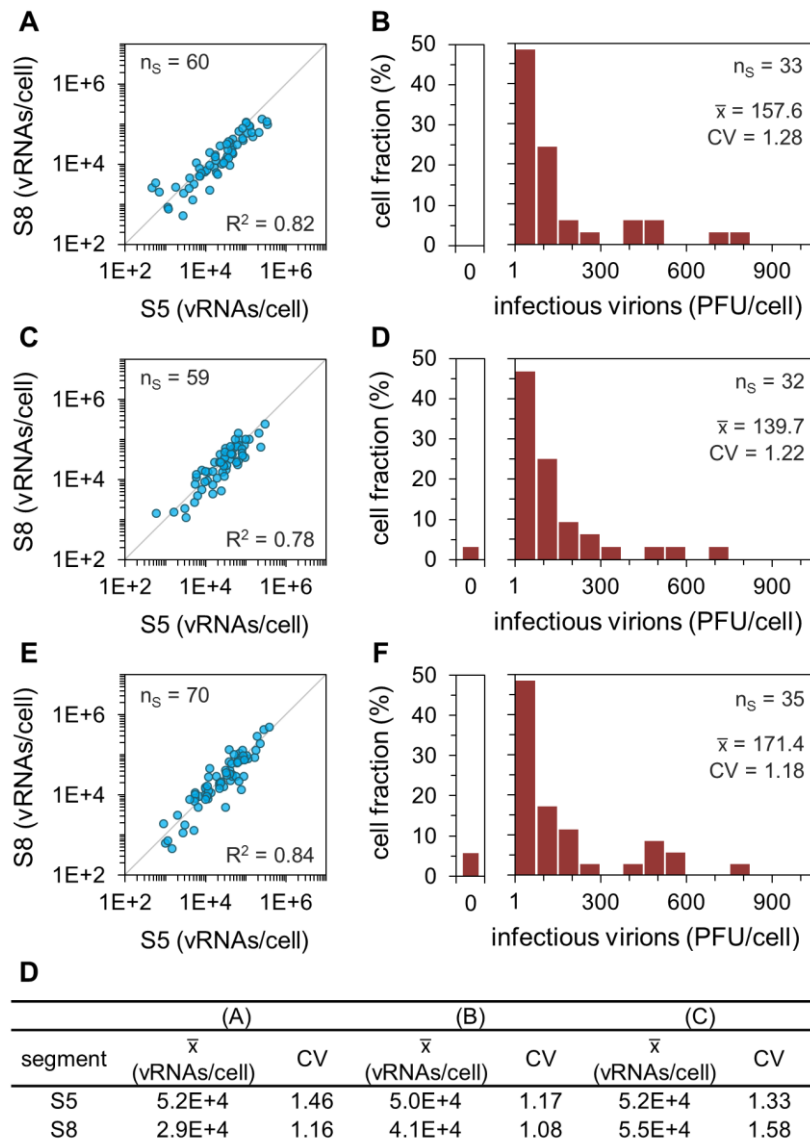


Figure 4.11. Single-cell virus infection with different plaque-purified seed viruses. PR8-NIBSC virus was thrice plaque-purified and afterwards expanded in MDCK cells. The obtained seed viruses were then used for single-cell infection experiments (MOI=10). Three different plaque-derived virus seeds were used (each shown in (A and B), (C and D), (E and F), respectively). At 12 hpi, cells were analyzed for their intracellular vRNA content using real-time RT-qPCR and virus yields using the plaque assay. n_s indicates the number of single cells analyzed. (A, C and E) Correlation of vRNA segments. The coefficient of determination (R^2) is provided and the parity line ($R^2=1$) is shown for reference. Pooled data of multiple independent experiments ($n=2$) are shown for each panel. (B, D and F) Histogram of virus yield. The bar on the left hand side shows the fraction of cells that show no virus release (0 PFU). Data of one experiment is shown for each infection. \bar{x} depicts mean and relative standard deviation CV is indicated. (D) Means and CVs of the data shown in (A, B and C).

In addition, the between-cell heterogeneity in virus yields did also not appear to be reduced upon infection with plaque purified viruses (Figure 4.11B, D and F). More specifically, virus titers ranged from 5-750, 1-710 and 1-790 PFU/cell compared to 1-970 and 1-720 PFU/cell for infections performed with the parental seed virus (Figure 4.4. and 4.9.). However, again, a reduction in the CVs of cell-specific virus titers and an increase in the mean PFU/cell quantities could be observed (Figure 4.11B, D and F) as compared to infections performed with the original seed virus (Figure 4.4. and 4.9.). Again, this can be explained by the reduction in the fraction of non-productive cells upon infection with plaque-purified seed viruses (Figure 4.11B, D and F). The low fraction of non-productive cells is likely caused by the depletion of DIPs, which typically occurs during plaque purification (Nayak et al., 1985, Nayak et al., 1978). Thus, it may appear that DIPs can affect the single-cell virus titer, but this is further thoroughly investigated in section 4.2.3. Taken together, we conclude that the genetic heterogeneity of the infecting virus population (with the exception of DIPs) does not seem to contribute to the large cell-to-cell heterogeneity in IAV replication.

4.2.2. Influence of cell-based characteristics

4.2.2.1. Cell size

Virus replication relies on the biosynthetic machinery of the host cell. We speculated that large cells may harbor an increased amount of cellular resources that are required for virus replication and production. To test whether the synthesis of progeny virions depends on the cell size, we simultaneously quantified virus titers and cell diameters of single infected cells. For this, we isolated infected single cells (as described above (Figure 4.1.) in 384-well plates of a “non-binding” type. This type of plate suppresses adherence of cells and causes them to remain spherical. Images of each single cell were captured and the diameters were then determined using the corresponding imaging software. Virus titers in the supernatant of these cells were quantified using plaque assays. Figure 4.12. shows the dependency of the single-cell virus titer on the cell diameter. We observed large differences in the cell size of single MDCK cells, with diameters that ranged from ~ 11.0 to ~ 25.5 μm (Figure 4.12B). Surprisingly, however, small and large cells showed a similar variability in virus titer, indicating that there is no apparent correlation of cell diameter and single-cell virus titer.

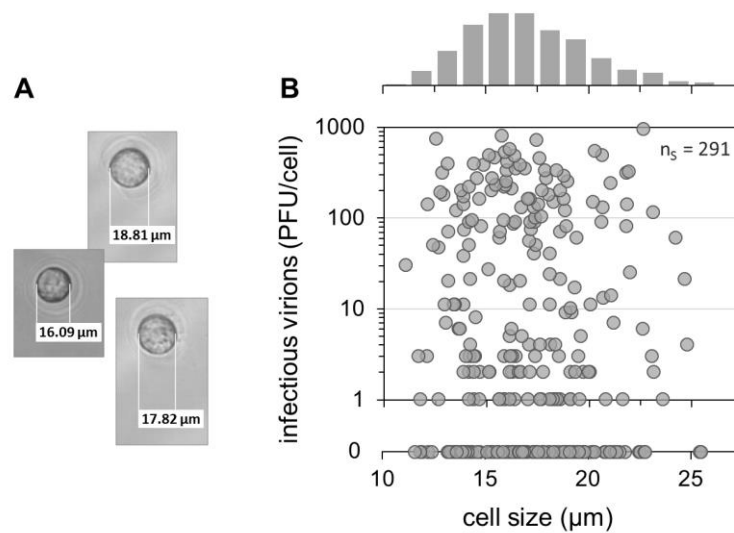


Figure 4.12. Effect of cell size on virus yield. Single cells infected with PR8-NIBSC (MOI=10) were incubated until 12 hpi. Afterwards, wells containing single cells were identified by phase-contrast microscopy, and images were acquired. Virus titers in the supernatant of the cells were analyzed using the plaque assay. The cell diameter of each single cell was determined using the imaging software Axiovision V 1.1 (Zeiss). (A) Three exemplary single cells with corresponding cell diameter. (B) Correlation between virus titer and cell size. n_s indicates the number of single-cell measurements. The pooled results of multiple independent experiments ($n=4$) are depicted. Figure adapted from (Heldt et al., 2015), licensed under CC BY 4.0.

4.2.2.2. Ribosome content

IAVs enter the host cell and hijack the cells' biosynthetic machinery, including the ribosomes. More specifically, the ribosomes need to be recruited so that they translate viral mRNAs into viral proteins, which are required for virus replication and virus particle production. Therefore, we next investigated whether the ribosome content of a single cell can affect its capacity to produce virus particles. For this, we used real-time RT-qPCR for assessing the intracellular ribosome content. Specifically, we quantified the 18S rRNA, which is associated with the small ribosomal subunit at exactly one 18S rRNA molecule per ribosome (Alberts, 2012). The evaluation of the expression of 18S rRNA was based on a modified $\Delta\Delta C_T$ -method, in which we calculated the fold change over the average single-cell 18S rRNA expression. Please note that this method and evaluation was developed in the context of the master thesis work of Alexander Ruff (Ruff, 2018), which was conducted and supervised in conjunction with this PhD work. The correlation of the ribosome content and the virus yield of single cells is shown in Figure 4.13. We observed an extreme cell-to-cell heterogeneity in the 18S rRNA content, with differences in the quantities that spanned more than four orders of magnitude. Yet, no correlation of the ribosome content and the single-cell virus titer was observed.

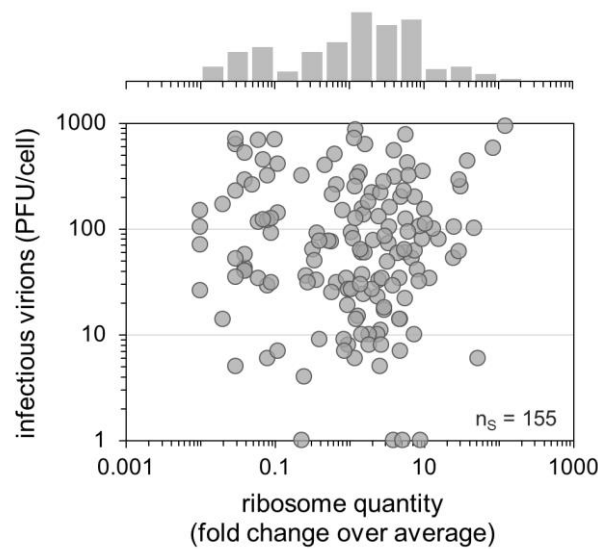


Figure 4.13. Dependency of single-cell virus titer on ribosome content. Single cells infected with PR8-RKI (MOI=10) were incubated until 12 hpi. Afterwards, virus titers in the supernatant of individual cells were analyzed using the plaque assay and intracellular 18S rRNA content by real-time RT-qPCR. n_s indicates the number of single cells analyzed. The pooled results of multiple independent experiments ($n=4$) are depicted.

4.2.2.3. Between-cell variability

We have shown that the genetic differences between individual virions (of the infecting virus population) did not seem to affect cell-to-cell heterogeneity in IAV replication (Figure 4.11.), despite large differences in the properties of individual IAV particles (Lauring and Andino, 2010, Brooke, 2017, Marcus et al., 2009). However, the MDCK cell line also shows a high between-cell variability its characteristics (Dukes et al., 2011, Nakazato et al., 1989, Cassio, 2013). To test whether the cell-to-cell differences in the MDCK cell line can affect the between-cell heterogeneity in IAV replication, we generated clonal MDCK cell populations. Such populations should be more homogenous in their properties. Next, we investigated whether we can observe a reduction in the between-cell variability in virus replication upon the infection of these clonal MDCK cell populations. Please note that a condensed summary of the master thesis of Annekathrin Leupelt (Leupelt, 2017), conducted and supervised in the context of this PhD work, will be presented in the following subsection, including the results shown in Figure 4.14.-4.16.

To generate clonal MDCK cell populations, we isolated non-infected single MDCK cells (of the parental cell line) in individual wells of a 384-well plate (as described above (Figure 4.1.)).

Afterwards, single cells in individual wells cells were cultivated, where the cells grew to small colonies until eventually, the cell monolayer reached confluency. The cells were then passaged and expanded, consecutively in cell culture vessels of increasing growth surface (from 384- to 96- and 6-well plates, and finally, in T75 cell culture flasks). Once a sufficiently large number of cells was generated per clonally-derived MDCK population, the cells were cryopreserved. In total, 31 clonal MDCK cell populations were generated. Afterwards, all 31 MDCK cell clones were thawed and cultivated simultaneously, to allow for the comparison of their properties in the subsequent experiments.

Growth of MDCK cell clones. Interestingly, we observed large differences in the growth characteristics between the clonal MDCK cell populations (Figure 4.14.). Specifically, the clonal cells showed large differences in their average cell diameters and total cell numbers at confluency (Figure 4.14A). More precisely, clones with a small cell diameter grew to higher cell numbers, and vice versa. These differences were large and very obvious; hence, we defined “small” and “large” clonal cells based on this observation (Figure 4.14A). The parental cell population displayed corresponding properties that appeared to be situated between “small” and “large” clonal MDCK cells. Next, we investigated the dynamics in cell growth of the clonal populations (Figure 4.14B). Please note that these experiments (results shown in Figure 4.14B) were conducted by Bissinger *et al.* (unpublished). We observed that the large differences in cell size and cell number were even obvious over all stages of cell growth.

Finally, we calculated the total cell volume (at confluent growth phase) for each clone (Figure 4.14C). Surprisingly, the large differences between “small” and “large” MDCK cell clones were no longer apparent anymore with respect to the total cell volume. Please note that the phenotypic differences between the MDCK cell clones were observed to be stable over several passages (approx. 10 passages were monitored). Taken together, we observed large differences in the cell size and cell density (at confluency) of clonal MDCK cell populations; yet, differences in the total cell volume appeared to be negligible.

4.2. Sources of cell-to-cell heterogeneity in IAV replication

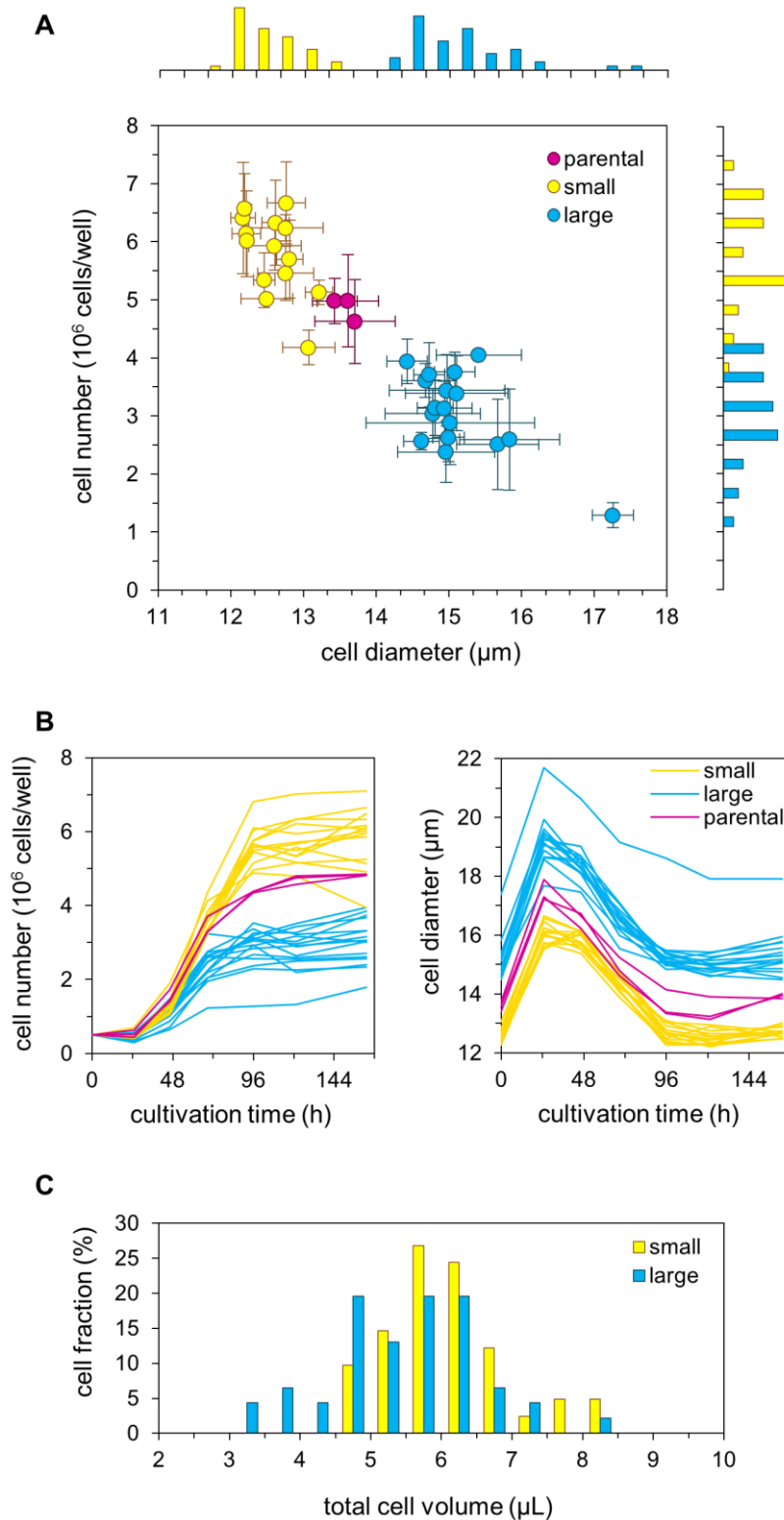


Figure 4.14. Growth of clonally-derived MDCK cell populations. Clonal MDCK cell populations were derived from single cells that were isolated in 384-well plates. Single cells in individual wells were subsequently cultivated, expanded and passaged (in cell culture vessels of increasing growth areas), and finally cryopreserved. In total, 31 single-cell derived MDCK cell clones were generated. Afterwards, all clones were thawed simultaneously for subsequent experiments. (A) Cell diameters and total cell numbers of clonal MDCK cell populations in stationary growth phase. Cells were cultured in 6-well plates with a

4.2. Sources of cell-to-cell heterogeneity in IAV replication

growth area of $\sim 9.6 \text{ cm}^2$ for 7d (168 hours). "Small" and "large" cells were defined based on the differences of the two depicted properties. Error bars indicates standard deviation of three independent experiments. (B) Growth of clonal MDCK cell populations. Initially, each cell clone was seeded with a number of 0.5×10^6 cells per well (of a 6-well plate). Result of one experiment is shown. Data shown in (B) was generated by Bissinger *et al.* (unpublished). (C) Histogram of the total cell volume of MDCK clones in stationary growth phase. Volume was calculated based on the data shown in (A).

Virus titers of MDCK cell clones from cell population-based experiments. Next, the clonal MDCK cell populations were tested in their virus production capacity at the cell population level (Figure 4.15.). For this, we infected the cells at an MOI of 10 and virus titers were determined at 12 hpi. Please note that although the clonal MDCK cell populations showed large differences in the growth behavior (Figure 4.14B), we ensured that they were all infected in exponential growth phase at fairly similar cell numbers (about $\sim 1.5 \times 10^6$ cells per well of a 6-well plate). Surprisingly, we observed that the virus titers (i.e., the HA and the infectious virus titer) of all clonally-derived MDCK cell populations were not significantly different and in the same order of magnitude (Figure 4.15A). More precisely, the differences in total and infectious virus particle concentrations between the clones ranged from factor three to four, but this appeared to be statistically insignificant, as with their cell-specific virus titers (Leupelt, 2017).

Considering that the total cell number at confluency showed large differences between "small" and "large" MDCK cell clones (Figure 4.14A and B), and that the cell-specific virus titer did not appear to be different (Leupelt, 2017), we speculated that we may find larger differences in virus titers, when the differences in the cell numbers are maximized. To this end, we infected (MOI=10) the clonal MDCK cells four days after seeding (please also see Figure 4.14B) and virus titers were quantified at 48 hpi, when the viral replication cycle was terminated, i.e., the full production capacity of the cells was reached. Surprisingly, in this experiment, we observed a significant difference in cell-specific virus titers between "small" and "large" clonal MDCK cell populations (Figure 4.15B). However, again, the volumetric virus titers did not appear to be different between "small" and "large" cell clones, which may be explained by their similar total cell volumes (Figure 4.15C). In summary, we did not observe significant differences in the virus titers between IAV-infected clonal MDCK cells. However, it appeared that the cell-specific virus titers showed minor differences between "small" and "large" clonal MDCK cell populations.

4.2. Sources of cell-to-cell heterogeneity in IAV replication

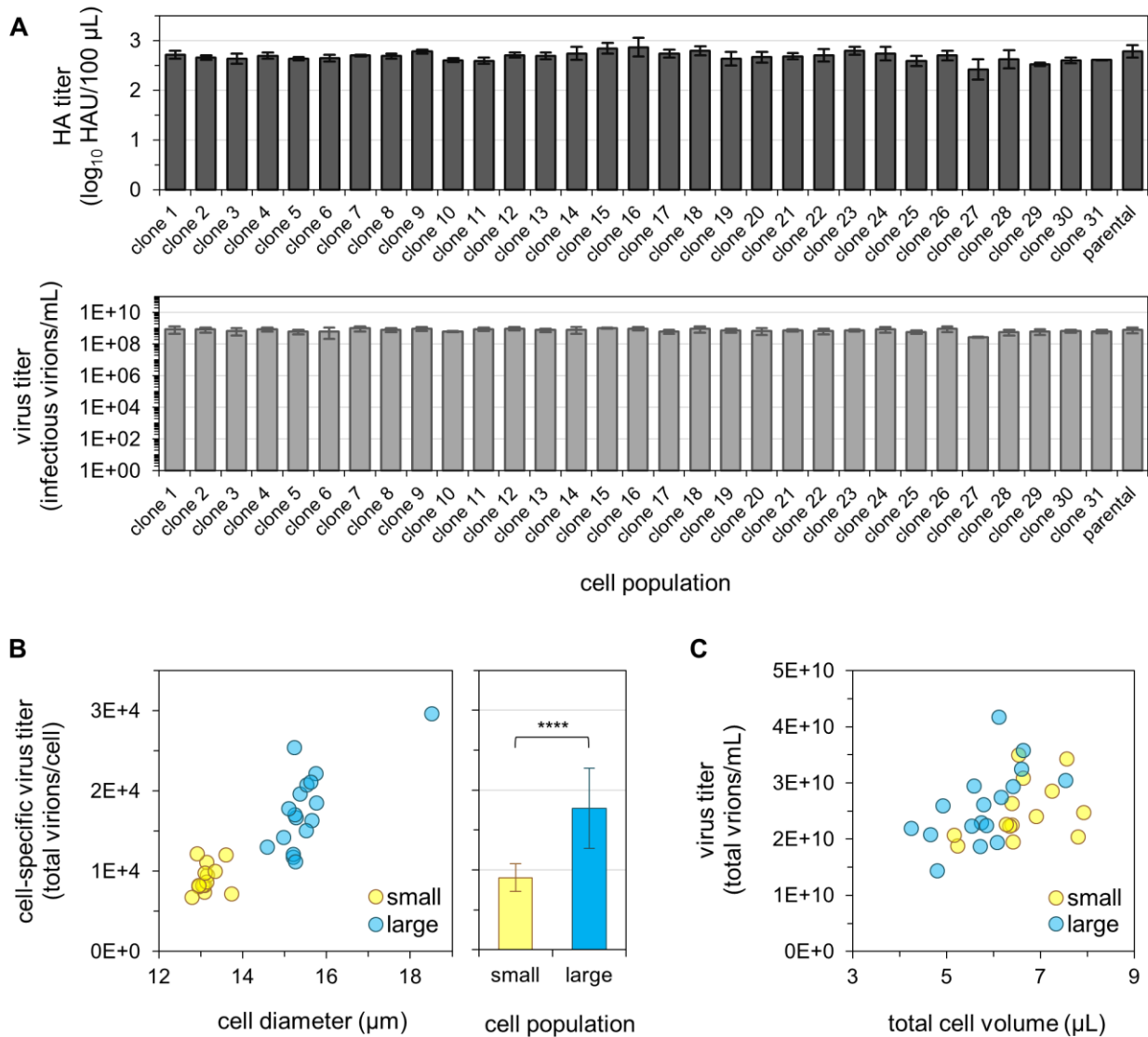


Figure 4.15. Virus production of infected clonal MDCK cell populations. (A) Virus titers of infected MDCK cell clones. Clonal MDCK cell populations were infected with PR8-RKI at an MOI of 10 and analyzed for their virus yields using the HA and plaque assay at 12 hpi. We assured that all clonal MDCK cell populations were infected simultaneously, in exponential growth, and at fairly consistent cell numbers per well ($\sim 1.5 \times 10^6$ cells). Three independent experiments were performed. (B) Cell-specific virus titers (of total virus particles) of infected “small” and “large” clonal MDCK cells. Numbers of total virus particles were calculated based on the HA titers. Cells were infected (MOI=10) four days after seeding into 6-well plates, when the differences in the cell number between “small” and “large” clonal populations was maximized (shown in Figure 4.14A). Virus titers were then determined after 48 hpi. ****, $p < 0.0001$ by Student’s *t*-test. Data of one experiment is shown. Error bar indicates standard deviation. (C) Dependency of the virus titer (of total virus particles) on the total cell volume of “small” and “large” clonal MDCK cell populations. Numbers of total virus particles were calculated based on the HA titers. Data from the experiment described in (B) is shown.

Single-cell virus replication in clonal MDCK cell populations. We next investigated whether we can observe a reduction in the cell-to-cell heterogeneity in IAV replication of clonal MDCK cell populations compared to the parental cell line. For this, we infected selected “small” and “large” clonal MDCK cells (i.e., clone 8 and 26, respectively), and then isolated and analyzed the infected single cells as described above (Figure 4.1.). Surprisingly, we did not observe a decreased single-cell variability in virus replication of the MDCK cell clones compared to the parental cell population (Figure 4.16). More precisely, the distributions of vRNA levels and virus titers of infected single cells showed CVs (indicative for the dispersion of a distribution (Schulte and Andino, 2014)) that did not appear to be significantly different as compared to the CVs of the parental cell population (Figure 4.16A-E). This was confirmed by the Siegel-Tukey test, which indicated no significant differences ($p \geq 0.05$) in the variances of the distributions of vRNA and virus titer between the MDCK cell clones and the parental cell population.

Moreover, the median of vRNA levels of the clonal MDCK cells was not significantly different compared to that of the parental cell population (Figure 4.16G); however, we observed a significant difference in the medians of virus titers (Figure 4.16H). More specifically, “small” clonal MDCK cells showed a lower cell-specific virus titer as compared to the “large” clones, and vice versa. This observation is in line with our previous cell population-based experiments (Figure 4.15B). Taken together, we observed “small” and “large” clonal MDCK cell populations that showed large phenotypic differences in the cell diameter and cell number at confluency, but not in the total cell volume. However, the “small” and “large” MDCK cell clones did not show differences in their volumetric virus titers (likely caused by their similar total cell volumes), but differences in the cell-specific virus titers. Finally, we observed no reduction in the cell-to-cell heterogeneity in IAV replication of clonal MDCK cell populations compared to that of the parental MDCK cell line.

4.2. Sources of cell-to-cell heterogeneity in IAV replication

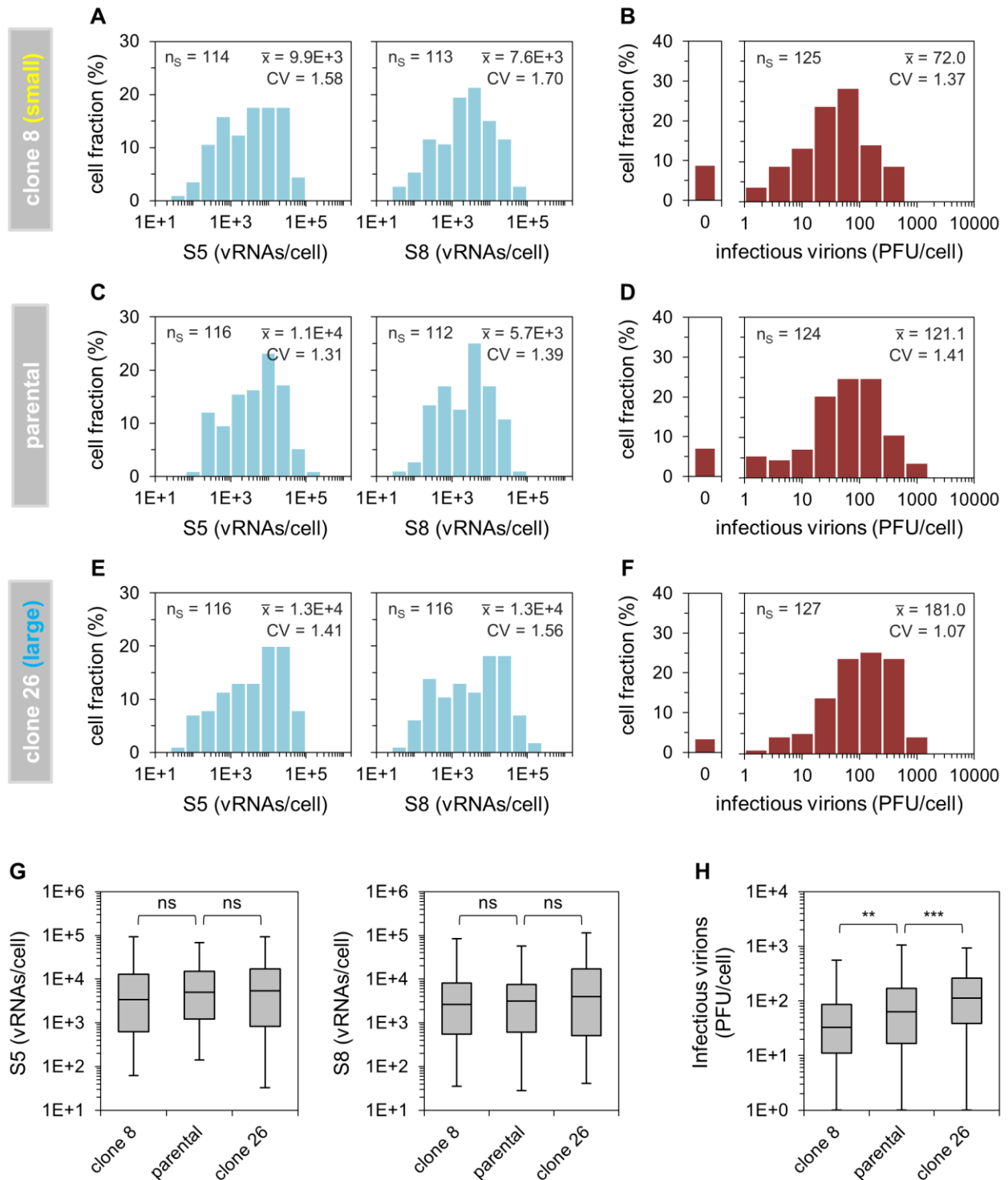


Figure 4.16. Single-cell analysis of IAV-infected clonal MDCK cells. Clonally-derived MDCK cell populations were infected with PR8-RKI at an MOI of 10. Subsequently, the infected single cells were isolated (as shown in Figure 4.1.) and cells were analyzed for their intracellular vRNA content using real-time RT-qPCR and virus yields using the plaque assay at 12hpi. (A, C and E) Distribution of single-cell vRNA levels of infected MDCK cell populations. (B, D and F) Histogram of virus titers. The bar on the left hand side shows the fraction of cells that show no virus release (0 PFU). \bar{x} depicts mean and relative standard deviation CV is indicated. n_s indicates the number of single-cell measurements. Pooled data of three independent experiments are depicted for each MDCK cell population. (G and H) Box-Whisker plots

of (G) single-cell vRNA levels and (H) single-cell virus titers of infected MDCK cell populations. Upper and lower quartile (top and bottom box), median (central line), minimum and maximum (whiskers) are indicated. **, $p < 0.01$ and ***, $p < 0.001$ by Mann-Whitney U test.

4.2.3. Effect of DIP co-infection

DIP co-infections are known to exert strong inhibitory effects on virus replication. Moreover, at a given fraction of DIPs in the infecting virus population, it has to be assumed that different numbers of DIPs can infect different individual cells and that some single cells may not even receive a DIP. We, thus, hypothesized that this supposed variability in DIP co-infections at the single-cell level may impact the cell-to-cell heterogeneity in IAV replication. To test this hypothesis, we modified an existing RT-PCR method for the detection of FL and DI RNAs (Frensing et al., 2014). Note that this method was further optimized in the context of this PhD work regarding the sensitivity to facilitate measurements at the single-cell level. This improved method was then utilized in the master thesis work of Alexander Ruff. A condensed summary of this MSc thesis (Ruff, 2018), conducted and supervised in conjunction with this PhD work, will be presented in this subsection, which includes the results shown in Figure 4.17B, C, and D.

Indeed, we observed a vast between-cell heterogeneity in the content of DI RNAs in infected single cells (Figure 4.17A). More specifically, the cell-to-cell variability comprised differences with respect to (i) the presence/absence, (ii) the amount and (iii) the size of the DI RNAs, and (iv) the genome segment on which DI RNAs occur. Note that we only investigated DI RNAs on S1, S2 and S3, as they predominantly occur on those genome segments. Interestingly, we observed that DI RNAs occurred less frequently in cells with higher cell-specific productivities. This was most apparently observed for S3 (Figure 4.17A). Moreover, signals corresponding to FL vRNAs were more often observed for high-productive single cells (in this context, the absence of a FL signal most likely indicates a very low concentration, below the LOD). Please also note the presence of high-productive cells that nevertheless contained DI RNAs. In this context, it was observed that not all deleted RNAs have the potency to interfere with STV replication in a coinfection scenario for unknown reasons (Nayak et al., 1985, Frensing, 2015). Alternatively, such cells may indicate to other factors that can affect the single-cell virus titer, despite the presence of DI RNAs.

4.2. Sources of cell-to-cell heterogeneity in IAV replication

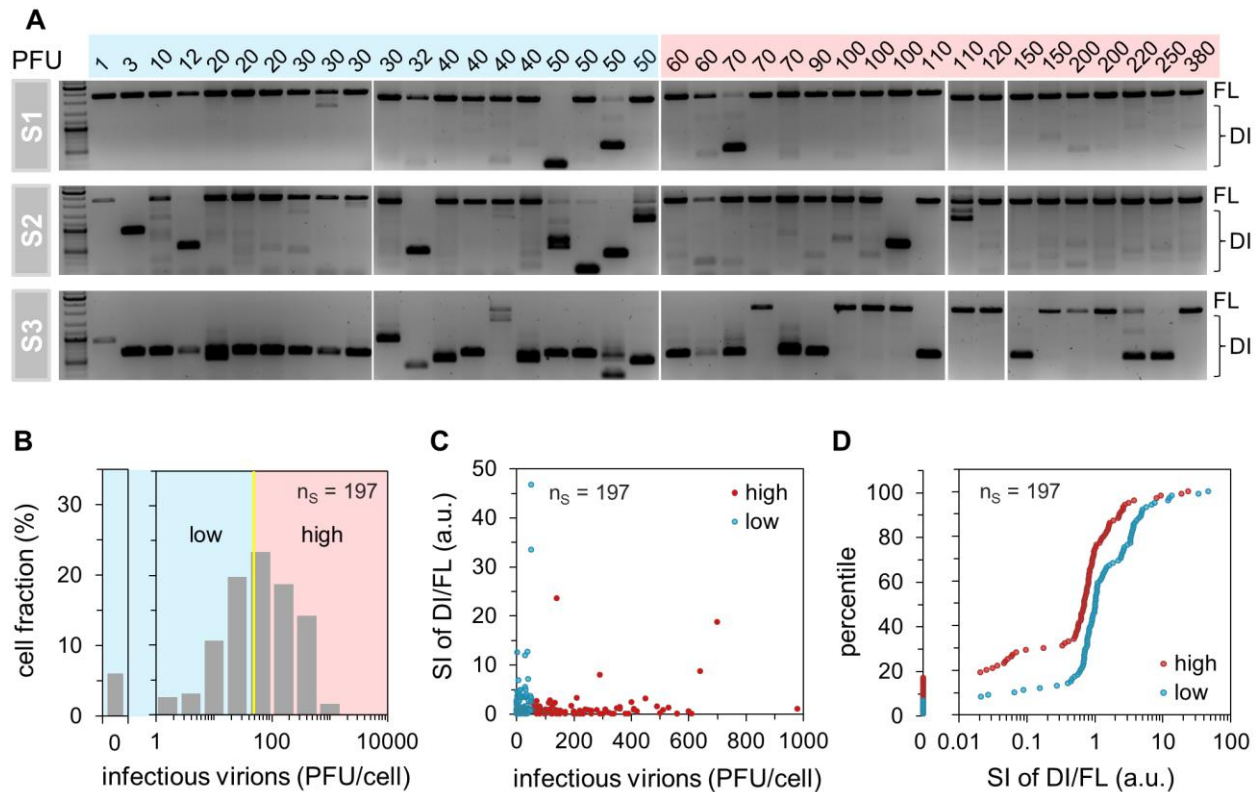


Figure 4.17. Effect of intracellular DI RNAs on single-cell virus titer. Single MDCK cells, infected with PR8-RKI at an MOI of 10, were isolated (as shown Figure 4.1.) and investigated regarding the presence of DI RNAs by single-cell DIP-PCR and released virus titers by plaque assay at 12 hpi. (A) Intracellular DI and FL RNAs of infected single cells. The presence of DI RNAs was investigated for S1, S2 and S3 for each single cell, along with the corresponding virus titer (shown at the top of the agarose gels). DNA ladder is shown at the left, with strong bands indicating the 500, 1000, and 3000 bp standard (from bottom to top). Data of one representative experiment is shown. 39 single cells were analyzed. (B) Distribution of single cell-derived virus titer. The bar on the left hand side shows the fraction of cells that show no virus release (0 PFU). Vertical line (yellow) indicates the median of virus titer, which separates the “high”- and “low”-productive single cells. Pooled data of six independent experiments are depicted. (C) Dependency of the quantity ratio of DI to FL RNAs on virus titers. Signal intensities of DI and FL were quantified from agarose gels using ImageJ and then used to calculate the ratios. (D) Percentile graph of the data shown in (C). n_s indicates the number of single-cell measurements.

To confirm our observations in a more objective way, we next performed quantification and statistical analysis of the results obtained from RT-PCR and subsequent agarose gel electrophoresis (one representative experiment is shown in Figure 4.17A). For this, we analyzed six independent experiments that yielded, in total, 197 single cell measurements. The distribution of single-cell virus titers of these experiments is shown in Figure 4.17B, in which we divided high- and low-productive cells based on the median of virus titer. We then used the image processing program “ImageJ” (National Institutes of Health, Bethesda, Maryland, USA) to quantify the signal intensities (considering both, the area and pixel value intensities) of DI

and FL RNAs on the agarose gel images. Afterwards, we calculated the following ratio for each individual cell: the sum of signal intensities of DI RNAs on S1-S3, divided by the sum of signal intensities of the FL RNAs. In line with our previous observation (Figure 4.17A), we observed that low-productive cells appeared to contain an overall higher quantity ratio of DI to FL RNAs (Figure 4.17C). A more obvious difference can be observed in the corresponding percentile graph (Figure 4.17D). Moreover, a statistically extremely significant difference between high- and low-productive cells was observed, as indicated by Mann-Whitney U test ($p=2.1 \times 10^{-5}$). Taken together, a vast diversity in DI RNA content between single IAV infected cells was observed. Moreover, we observed that the load of DI RNAs affected the productivity of an individual cell. Conclusively, it appears that DIPs can well contribute to cell-to-cell heterogeneity in IAV replication.

4.2.4. Discussion of the effect of virus-derived characteristics

In a previous section (4.1.2.), we show that the stochasticity in biochemical reactions and (yet unknown) deterministic factors can both contribute to the large cell-to-cell variability in IAV replication. As the stochasticity is intrinsic to all biochemical reactions, cellular, and viral processes, it can inevitably not be influenced. Thus, in the present section, we focused on identifying factors that are extrinsic (i.e. deterministic) to virus replication. In particular, we investigated potential sources that influence the cell-to-cell heterogeneity in cell-specific virus titers.

First of all, our data indicates that fluctuations in intracellular vRNA levels are one source for the large cell-to-cell variability in virus yields. More specifically, we observed that cells containing a high vRNA level are typically of a high productive phenotype. In line with these results, a dependency of intracellular viral RNAs and virus titers was also observed in single poliovirus-infected cells (Schulte and Andino, 2014). Yet, in contrast to poliovirus replication, our investigation of IAV infection at the single cell level allowed to differentiate between sources of extrinsic and intrinsic noise in virus replication (discussed in the previous section 4.1.4.). More specifically, we showed that extrinsic sources of noise can result in large fluctuations in overall vRNA levels, and these fluctuations, in turn, appear to affect the virus yield of an infected single cell. However, we also observed individual cells that showed a low virus titer despite containing high vRNA levels of S5 and S8 (Figure 4.8.). We hypothesized that such cells might contain a low vRNA level of an unmeasured segment, which would then ultimately limit virus formation and release of these particular cells. This hypothesis was

confirmed by stochastic mathematical simulation of IAV replication, conducted by Heldt *et al.* (Heldt et al., 2015). In the simulations, a similar population of low-yield single cells was observed at high vRNA levels of S5 and S8, and indeed, it was shown that these cells contained a low level of other vRNAs (i.e. of S4 or S6) (Heldt et al., 2015). Such a deviation of vRNA levels from equimolar quantities is typically caused by the stochasticity inherent to biochemical reactions (i.e., sources of intrinsic noise (Elowitz et al., 2002)). We, thus, conclude that both extrinsic and intrinsic sources of noise appear to influence the virus yield of a single IAV-infected cell (Heldt et al., 2015).

Our experimental procedure allows for static single-cell analysis, i.e., only separate time points can be analyzed and the dynamics in single-cell-derived virus growth cannot be investigated. However, it is well known that virus infections show large differences in the dynamics of virus growth between individual cells (Timm and Yin, 2012, Timm et al., 2017, Guo et al., 2017). We, thus, speculated the large cell-to-cell variability in IAV replication (observed so far at 12 hpi) may be generated by cells that are in varying states of the viral life cycle. Indeed, for 8 hpi, we observed a higher fraction of lowly replicating cells, of which some apparently become highly replicating at 12 hpi. However, we did not observe an increase in highly replicating cells, nor a decrease in lowly replicating cells from 12 to 16 hpi. These results indicate that some lowly-replicating cells can “catch up” and can become a highly replicating cell from 8 to 12 hpi, but not in the timeframe between 12 and 16 hpi. Most likely, this status quo will also not alter towards even later times post infection, as IAV-infected cells already start to become apoptotic (i.e., when the viral life cycle is terminated) between 16 and 20 hpi (Frensing et al., 2016). It, thus, appears that the cell-to-cell variability at 12 hpi does not seem to be generated by cells that are in different infection states, and that the observed between-cell heterogeneity at 12 hpi can well represent the single-cell variability in IAV replication. Therefore, we continued to investigate single-cell virus replication at 12 hpi for the identification of additional sources of cell-to-cell heterogeneity in virus yields.

Next, we showed that the between-cell variability in virus titers does not seem to be affected by the MOI. More specifically, at an MOI of 1, we observed a similar cell-to-cell heterogeneity in virus yields (with titers that spanned almost three orders of magnitude) as compared to an infection performed at an MOI of 10. In agreement with our results, no significant differences in the between-cell heterogeneity in virus yields of virus-infected bacterial cells and of VSV- and poliovirus-infected mammalian cells were observed between infections performed at high and low MOIs (Zhu et al., 2009, Timm and Yin, 2012, Schulte and Andino, 2014, Delbruck, 1945b). Interestingly, we observed that the cell-to-cell heterogeneity in viral genomic RNA

levels appeared to be larger at an MOI of 1 as compared to infections performed at an MOI of 10. This was similarly observed for poliovirus infection (Schulte and Andino, 2014). In this context, it was speculated that the inherent randomness in biochemical reactions may have a larger effect on viral RNA synthesis at lower MOIs, when fewer genomic RNA copies enter the cell. In such a scenario, the propagation of low initial copy numbers of viral RNA molecules may result in an increased noise in their levels at a given time post infection (Schulte and Andino, 2014). In contrast, at higher MOIs, these fluctuations were suggested to “average out”, due to an increased initial copy number of the replicating genomic RNAs, which would then lead to a decrease in the noise of their levels later on (Schulte and Andino, 2014). In agreement with the study conducted by Schulte *et al.*, we observed that intrinsic noise (i.e., vRNA fluctuations caused by the stochasticity in biochemical reactions, see also section 4.1.4.) was larger for infections performed at an MOI of 1 as compared to infections performed at an MOI of 10. However, despite more stochastic noise in intracellular vRNA synthesis at low MOIs, we observed that the virus titer distributions did not seem to be affected, just like in poliovirus infection (Schulte and Andino, 2014). This indicates that other sources (than the stochasticity in viral RNA synthesis) may have a stronger effect on virus release of a single infected cell. Specifically, it might be possible that the stochasticity present at another step of virus replication (or cellular response to virus infection) can additionally contribute to the cell-to-cell heterogeneity in virus infection.

It has to be assumed that each individual cell must be infected by different compositions of various virus particles, given that the infecting IAV population is highly heterogeneous, in particular, with respect to their genetic background (Lauring and Andino, 2010, Brooke, 2014, Brooke, 2017). Moreover, it was observed that the viral quasispecies composition can vary substantially between infected single cells (McWilliam Leitch and McLauchlan, 2013, Combe et al., 2015). To investigate whether this supposed heterogeneity of virus particle infection at the single-cell level can affect the cell-to-cell heterogeneity in IAV replication, we reduced the virus-to-virus genetic heterogeneity of IAV particle populations. For this, we prepared plaque-purified seed viruses (which are well known to contain a reduced genetic heterogeneity (Murata et al., 2011, Sack et al., 1980, Bijlenga and Duclos, 1989)) and then performed single-cell infection experiments using these virus populations. Surprisingly, we did not observe a reduction in the cell-to-cell variability, suggesting that the genetic diversity of IAV particles does not seem to contribute to the large single-cell diversity in IAV replication. In contrast, for VSV infection, it was shown that the viral genetic diversity can have a small influence (Zhu et al., 2009). More specifically, the authors isolated and expanded viruses produced from single

cells and these viruses were then used to infect cell populations. Zhu *et al.* observed that the viral progeny from some low-productive single cells persisted in their low-productive phenotype in the cell population-based experiments (Zhu et al., 2009). However, note that the presence of DIPs in these virus isolates was not tested, which could have explained their low-fitness phenotypes. Alternatively, it may be that the effect of the genetic diversity of virus particles on single-cell variability may be different for VSV infection compared to IAV replication. Please note that we discuss the effect of DIPs on cell-to-cell heterogeneity in IAV replication separately in section 4.2.6.

4.2.5. Discussion of the influence of cell-based characteristics

We show that single-cell IAV titers are independent of the cell diameter. This observation may further suggest that IAV yields are independent of the cell cycle stage, as the cell size and the cell cycle stage are typically correlated (Boucrot and Kirchhausen, 2008). The lack of a correlation between the cell cycle stage and the virus titer was also observed for poliovirus-infected single cells (Guo et al., 2017). Moreover, in agreement with our observation, it was concluded that the single-cell virus titer does not depend on the cell size for phage-infected bacteria and WEE-infected CEF cells (Delbruck, 1945b, Dulbecco and Vogt, 1954). However, in contrast to these studies and our results, it was shown that the cell size can have a weak effect on the virus titer for VSV- and FMDV-infected cells (Xin et al., 2018, Zhu et al., 2009). Yet, for VSV replication, it was concluded that this rather small difference cannot explain the very large cell-to-cell heterogeneity in virus yields (Zhu et al., 2009). Please also note that in the above mentioned studies, a rather indirect investigation of the link between cell-specific virus yields and the cell size was performed; i.e., either only the width of the distribution of cell size and virus yield was compared (Delbruck, 1945b, Dulbecco and Vogt, 1954), or small and large cell populations were sorted and enriched (using FACS) and subsequently tested for virus replication in cell-population based experiments (Zhu et al., 2009, Xin et al., 2018). In contrast, our experimental procedure allows for the direct correlation of the cell size and the virus titer of an infected single cell. In conclusion, it appears that the cell size can have a minor effect on single-cell virus titers; however, this appears to depend on the virus-host cell system. Nevertheless, the effect seems to be rather small and not sufficient to explain the large cell-to-cell heterogeneity that is typically observed between infected single cells.

The ribosome content of a cell can typically have a large influence on the protein yield (Perry, 2007). Moreover, a link between virus production and the capacity of cellular resources for

protein synthesis was suggested for T7 phage infection (You et al., 2002). Interestingly, we observed vast differences in the ribosome content of individual IAV-infected MDCK cells that spanned approx. four orders of magnitude. Yet, we did not observe a correlation between the single-cell virus titer and the ribosome content. This was similarly observed for poliovirus replication in single cells, which did also not seem to be limited by ribosome numbers (Schulte and Andino, 2014). Hence, despite its large between-cell variability, it may be that ribosomes are sufficiently present for virus production in each individual cell. Conclusively, the large between-cell heterogeneity in the ribosome content cannot account for the large cell-to-cell variability in IAV replication.

MDCK cells are not of clonal origin and typically show a high cell-to-cell heterogeneity in their properties (Lugovtsev et al., 2013, Liu et al., 2010). These differences in the MDCK cell line include morphological, electro-physiological, and biochemical characteristics (Lugovtsev et al., 2013, Dukes et al., 2011, Nakazato et al., 1989). Moreover, it was shown that individual MDCK cells can show alterations in the chromosome content upon long-term culture (Cassio, 2013). Thus, we hypothesized that the between-cell variability in the MDCK cell line may represent a potential source of single-cell heterogeneity in IAV replication. In agreement with these previous studies, we observed large phenotypic differences between clonally-derived MDCK cell populations. In particular, the cell size and the cell density at confluency showed significant differences between the clonal cell populations. More specifically, we observed two subsets of clonal MDCK cell populations: “small” clonal cells that grew to high cell densities and “large” clonal cells that grew to low cell densities at confluency. A similar observation was also reported in an earlier study, where various MDCK cell clones showed significantly different cell volumes (Barker and Simmons, 1981). Please note that we tested and confirmed the stability of the phenotype of the MDCK cells clones for 10 passages.

Surprisingly, we did not observe differences in the volumetric virus titer between infected clonal MDCK cell populations; however, “large” clonal cell populations showed a slightly higher cell-specific virus titer compared to the “small” MDCK cell clones. This, in turn, may be explained by the lower cell number of the “large” MDCK clones during cultivation and infection. Moreover, we show that “small” and “large” clonal MDCK cell populations do not significantly differ in their total cell volume, which, altogether, may indicate that the volumetric virus titer is connected to the total cell volume of MDCK cell clones (rather than the cell size or the cell number).

Please note that our observation of a higher cell-specific virus titer of “large” MDCK cell clones compared to “small” ones (Figure 4.15B) may appear contradictory to our previous observation of no correlation between the cell size and the single-cell virus yield (Figure 4.12.). It is reasonable that the vast cell-to-cell heterogeneity in virus titers (which span a factor of approx. 1000), was masking the rather small differences in virus yields between “small” and “large” MDCK cells (which showed quantitative differences of only a factor of approx. two). It appears that such small differences were not apparent in our previous single-cell infection experiments (Figure 4.12.). Nevertheless, these results do not alter our conclusion that the cell size cannot explain the large cell-to-cell variability in virus titers (discussed above).

In contrast to our results, it was recently shown that clonal MDCK cell populations can strongly differ in their virus production capacity (Liu et al., 2010, Lugovtsev et al., 2013). However, in these studies, different MDCK cell lines were used (NBL-2 from ATCC “CCL-34”) compared to our experiments (MDCK cells from ECACC). Moreover, the authors used different infection conditions. More specifically, low MOIs and late harvest time points (i.e., three to eight days post infection) were studied. In contrast, we studied single-cycle infections at high MOIs until 12 hpi. Furthermore, the large differences in the dynamics of cell growth between clonal MDCK cell populations were neither studied, nor considered for the design of the infection experiments. Lastly, Liu *et al.* generated and tested significantly higher numbers (>1000) of MDCK cell clones (Liu et al., 2010), which may have increased the chance to identify larger differences between clonal MDCK cells.

Nevertheless, we performed single-cell infection experiments with “small” and “large” MDCK cell clones and showed that the cell-to-cell heterogeneity in virus yield and vRNA was not reduced as compared to infections performed with the parental cell population. These results indicate that the large single-cell variability in IAV replication cannot be explained by the cell-to-cell heterogeneity in the properties of the parental MDCK cell line.

4.2.6. Discussion of the effect of DIP co-infection

We observed a multifaceted heterogeneity in the content of intracellular DI RNAs on S1-S3 in PR8-RKI virus-infected single cells. These differences comprise: (i) the presence/absence, (ii) the amount and (iii) the size of the DI RNAs, and (iv) the genome segment on which DI RNAs occur. This large cell-to-cell heterogeneity may well reflect the between-virus variability in the DI RNA content of the infecting virus population. Alternatively, some DI RNAs detected in

single cells might have originated *de novo* during the infection, although it is unlikely that they have accumulated to high levels until the time point investigated (12 hpi). Nevertheless, it appears that DI RNAs can affect the single-cell virus titer, as indicated by low-productive cells that show an overall higher DI/FL ratio, and vice versa. This observation is, in general, in line with previous studies, in which DIPs have shown to suppress the MDCK cell virus production yield in cell population-based experiments (Frensing et al., 2014). Please also note the presence of a few exceptions of this observation (i.e., high productive single cells that nevertheless contain DI RNAs). In this context, not all DI RNAs were shown to have the potency to interfere with STV replication in a coinfection scenario for unknown reasons (Nayak et al., 1985, Frensing, 2015). Alternatively, such cells may indicate the presence of other (yet unknown) factors that can affect the single-cell virus titer.

The influence of DIP coinfections on single-cell virus replication was also studied for VSV infections (Sekellick and Marcus, 1980, Akpınar et al., 2016b). However, in these studies, the authors did not directly correlate the load of intracellular DI RNAs to the virus titer of a single cell. Our methodology allows for the direct correlation of the two properties. Instead, in the above mentioned studies, varying MODIP (i.e., multiplicities of DIP) were applied to VSV-infected cells, and single-cell virus replication was monitored (Sekellick and Marcus, 1980, Akpınar et al., 2016b). In line with our results, the authors observed a suppression and delay in VSV replication in single cells upon DIP coinfection (Akpınar et al., 2016b, Sekellick and Marcus, 1980).

Summary. Our investigations show that sources of extrinsic noise (i.e., deterministic factors) and intrinsic noise in vRNA synthesis (created by the randomness in biochemical reactions) can both affect the single-cell virus titer to a certain degree (Heldt et al., 2015). However, we observed more intrinsic noise at lower MOIs, but the between-cell heterogeneity in virus yields was not affected. These results indicate that sources of noise intrinsic to vRNA synthesis may not have such a pronounced effect on the production of virions from single cells. Yet, the stochasticity present at another step of virus replication, or cellular response to virus infection, may still contribute to the large cell-to-cell heterogeneity in IAV infection, which remains to be elucidated. We showed that the cell size and the ribosome content did not seem to affect the virus yield of a single cell. Moreover, neither the variability present in the MDCK cell line, nor the genetic between-virus heterogeneity of the infecting virus population (except for DIPs) appeared to account for the large cell-to-cell heterogeneity in IAV replication. Finally, we

demonstrate that the content of DI RNAs in an infected single cell can influence the cell-specific virus titer, although the results also indicate that additional unknown factors may further affect the cell-to-cell variability in IAV replication. Altogether, our results advance single-cell virology research towards an understanding of the large cell-to-cell heterogeneity in virus infections.

4.3. Discovery of a novel type of DIP (OP7 virus)

In section 4.1., we show that IAV replication is highly diverse at the single-cell level. Moreover, we observed that most intracellular genomic vRNAs showed a positive quantitative correlation with each other, except for S7 vRNA. Interestingly, this behaviour appeared to depend on the seed virus that was used for the single-cell virus infections. In this section, we show that such an unusual behavior is caused by the co-infection by a yet unknown type of DIP, which is here referred to as "OP7" (over-proportional level of S7 vRNA) virus. In the first part of this section (4.3.1.), we describe the discovery and enrichment of OP7 virus. Subsequently, we present an in-depth analysis of the alterations of IAV replication upon co-infection with OP7 virus (4.3.2.). Finally, we investigate the interfering ability of OP7 virus against IAV replication (4.3.3.). Please note that we here used major parts of the original publication in Journal of Virology on the discovery of the novel form of DIP in this section (Kupke et al., 2018).

4.3.1. Discovery and enrichment

Viral subpopulation with unusual phenotype. To study the dependency of virus release on intracellular S7 vRNA quantity, which showed a large cell-to-cell variability (section 4.1.2.), we studied single cells infected with PR8-NIBSC and PR8-RKI virus (Figure 4.18.). Surprisingly, upon infection with PR8-NIBSC at a MOI of 10, individual cells that show a low infectious virus titer (0-10 PFU) contained a relatively high and disproportionate level of S7 vRNA in relation to S5 or S8 (Figure 4.18A). In particular, cells showing no plaque titer (0 PFU) almost exclusively contained this over-proportional quantity of the S7 segment. Most of the cells that released 1-10 PFU contained such levels as well. Furthermore, the distribution of virus titers between single cells appeared to be bimodal, as two subpopulations of cells can be observed, including a subset that released about 1-10 PFU (Figure 4.18B). In addition, it seemed that cells with over-proportional S7 level contained a different S7 vRNA sequence (compared to cells with equimolar ratios) as indicated by different denaturation temperatures of S7 amplicons in melting curve analysis (Figure 4.19.). We, thus, hypothesized that PR8 NIBSC may contain a subpopulation of virions with a different S7 segment.

To test whether such a subpopulation was also present in a different PR8 seed virus, we infected cells with PR8-RKI at an MOI of 10. However, no such an unusual behaviour was observed for S7. We neither observed over-proportional levels of S7 vRNA in comparison to S5 or S8 (Figure 4.18C), nor recognized any bimodality in the histogram of virus titer (Figure

4.3. Discovery of a novel type of DIP (OP7 virus)

4.18D). Concurrently, the fraction of cells showing no virus release was very low for PR8-RKI virus replication (only 3% in compared to 43% for the infection with PR8-NIBSC virus).

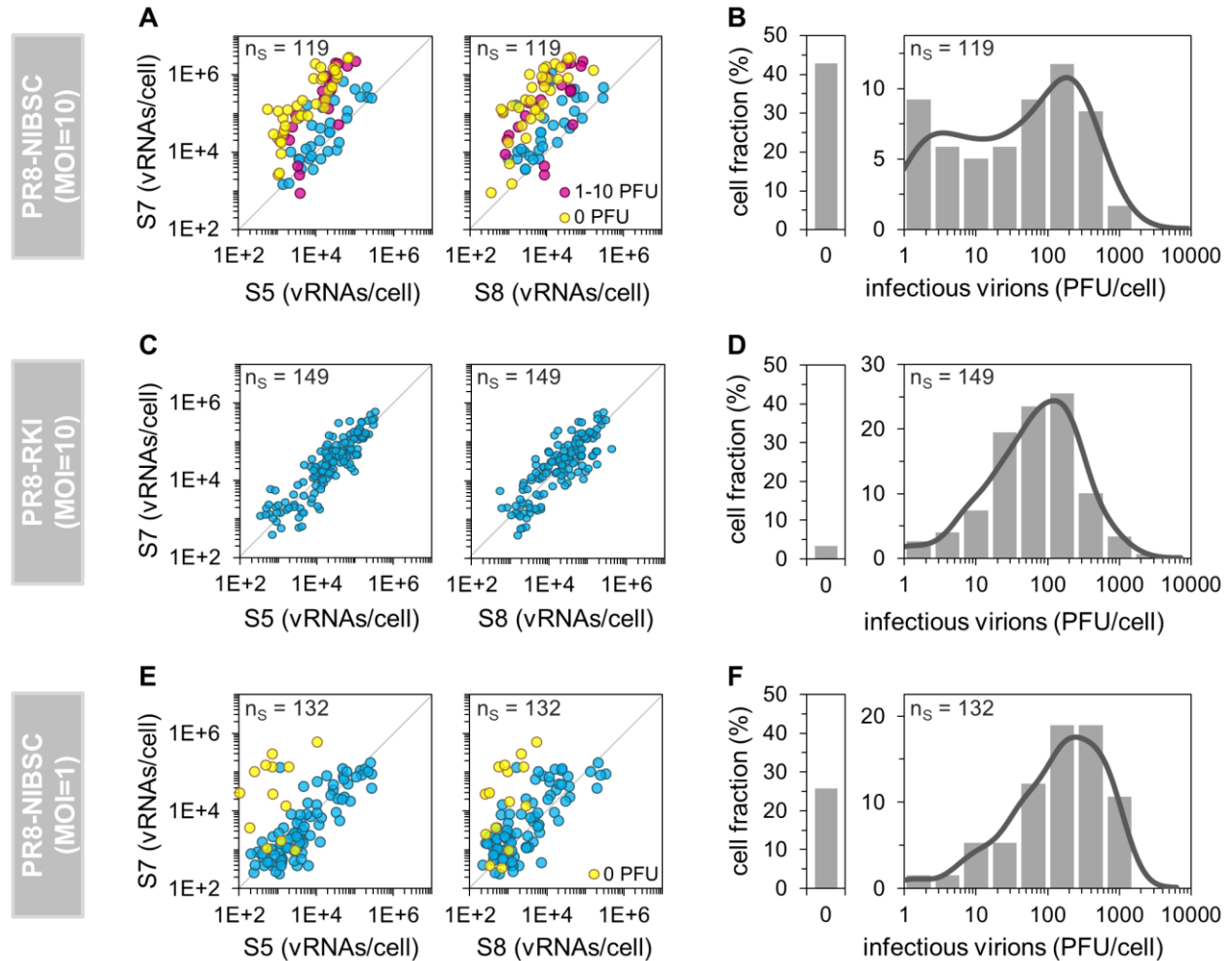


Figure 4.18. Dependency of virus titers on S7 vRNA level. Single MDCK cells, infected with indicated PR8 seed viruses at the indicated MOIs, were isolated (as shown Figure 4.1.) and analyzed for their intracellular vRNA content using real-time RT-qPCR and virus yields using the plaque assay at 12 hpi. (A, C and E) Effect of vRNA level on virus yield. Colors indicate amount of virus release, whenever significant; otherwise, cells are blue. The parity line ($r=1$) is shown for reference. (B, D and F) Distributions of virus titer. Solid lines indicate probability density function (calculated by Kernel density estimation). Cells that were tested negative in both intracellular vRNAs and released PFUs (non-infected cells) were excluded from analysis of infections performed at an MOI of 1 (E and F). Illustrations include pooled data of multiple independent experiments ($n=4$ for (B and C) and (D and E); $n=3$ for (F and G)). n_s indicates the number of single-cell measurements. Figure adapted from (Kupke et al., 2018), licensed under CC BY 4.0.

4.3. Discovery of a novel type of DIP (OP7 virus)

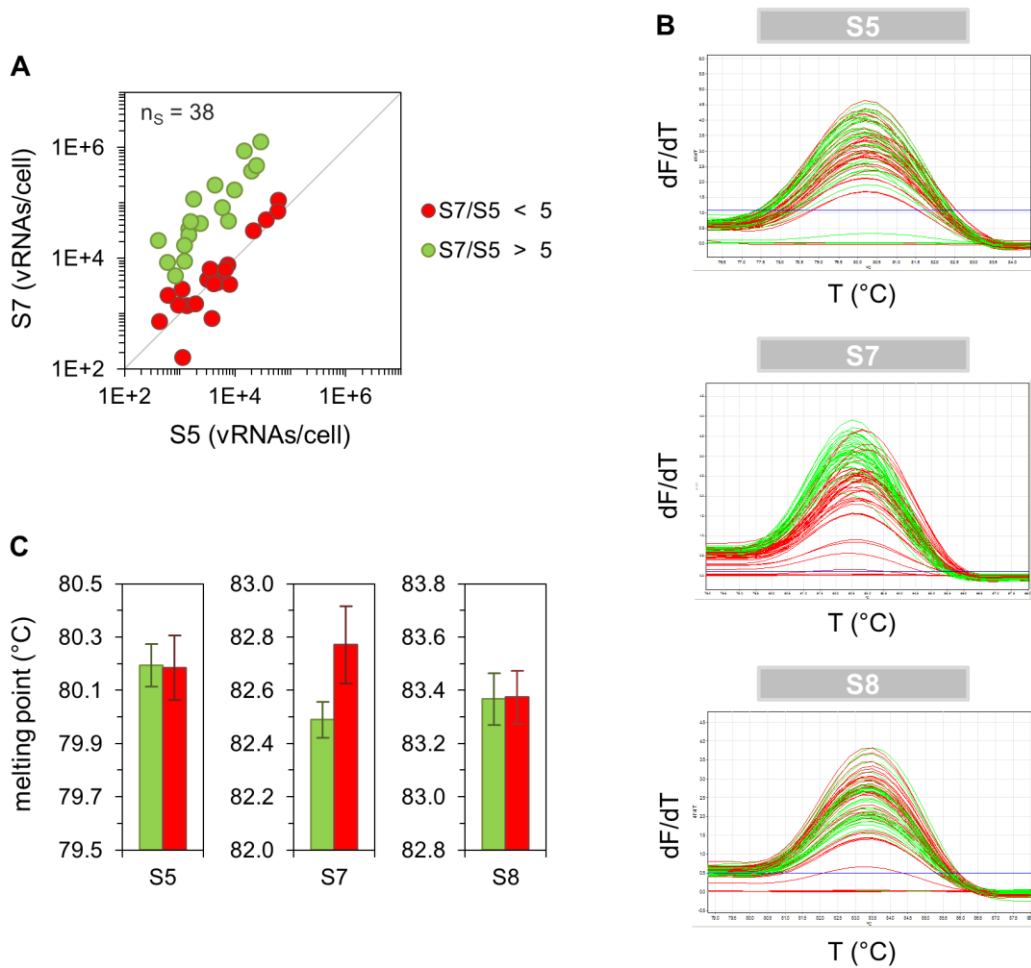


Figure 4.19. Melting curve analysis of qPCR amplicons. Infected single MDCK cells (derived from a cell population infected with PR8-NIBSC at an MOI of 10 as described in Figure 4.1.) were cultivated until 12 hpi and subsequently assayed for their intracellular vRNAs by real-time RT-qPCR. Subsequent to qPCR, melting curve analysis was performed. (A) Correlation between vRNA segments. Cells with equimolar and over-proportional levels of S7 (compared to S5) are shown in red and green, respectively. (B) Melting curves of qPCR amplicons. (C) Comparison of melting points. Error bars indicate standard deviation of the mean values depicted. Result of one representative experiment is shown. n_s indicates the number of single-cell measurements. Figure adapted from (Kupke et al., 2018), licensed under CC BY 4.0.

Interestingly, the occurrence of the unusual phenotype was reduced upon infection with PR8-NIBSC at an MOI of 1. More specifically, fewer cells contained an over-proportional level of S7 vRNA (Figure 4.18E) compared to infections performed at the higher MOI (Figure 4.18A). Moreover, the fraction of cells showing no virus release was decreased (26% in comparison to 43%), and a bimodal distribution of virus titer was not apparent anymore (Figure 4.18F). Hence, we presumed that replication of the putative subpopulation of virus in PR8-NIBSC may depend on co-infection with STV, which are less frequent at an MOI of 1. Furthermore, we

4.3. Discovery of a novel type of DIP (OP7 virus)

concluded that co-infection with such viruses results in an unusual phenotype, characterized by a low infectious virus titer and an over-proportional intracellular level of S7 vRNA in relation to other genome segments.

Enrichment and depletion. To investigate whether we can enrich the putative viral subpopulation in the PR8-NIBSC seed virus, we performed single-cell infection experiments at an MOI of 10 (as described in Figure 4.1.), and progeny virions in the complete supernatants of individual cells were expanded using confluent MDCK cells (Figure 4.20A) to yield seed viruses. Second, to test whether the putative subpopulation of virus can be depleted by the exclusion of co-infection events, we utilized plaque purification. For this, we picked and reseeded individual plaques from PR8-NIBSC virus in three consecutive assays (Figure 4.20C). The obtained virus was then multiplied in MDCK cells to yield virus seeds. All seed viruses obtained were then titrated for subsequent single-cell experiments at an MOI of 10, as described in Figure 4.1.

Indeed, infection experiments with three selected single-cell derived virus seeds (of 55 isolates) showed a strongly pronounced unusual phenotype (Figure 4.20B). In particular, the infected cells exclusively contained an over-proportional level of S7 vRNA in relation to S5 or S8. These viruses are here referred to as "OP7 seed virus". Moreover, 93% of cells infected with OP7 seed virus number 1 (OP7-1) showed no virus release, while for OP7-2 and OP7-5, the fraction was 95% and 90%, respectively. The remaining cells produced very low virus titers (1-10 PFU). Note that only five of the 55 single-cell derived virus seeds (obtained in four independent experiments) showed a strong markedness of the unusual phenotype (all five OP7 seed viruses are shown in Figure 4.21.), and additional ~20% of the isolates showed a weak phenotype, which were excluded from further experiments.

In addition, none of the cells infected with plaque-purified (PP) virus showed the aforementioned unusual phenotype (Figure 4.20D). More precisely, an over-proportional quantity of intracellular S7 vRNA (compared to S5 and S8) was not observed. Furthermore, only 4% of cells showed no virus release upon infection with PP virus number 1 (PP-1). Upon PP-4 and PP-5 virus infection, this fraction was 0% and 5%, respectively. In total, 43 plaque purified viruses were generated (in two independent experiments) and all isolates were tested negative regarding the unusual phenotype (selected isolates are shown in Figure 4.21.). Please note that due to the limited volume (~2 mL) of OP7 and PP seed viruses generated, only a low number of aliquots could be prepared, which allowed only a limited amount of subsequent infection experiments. We thus used three different OP7 seed viruses, each in one independent

4.3. Discovery of a novel type of DIP (OP7 virus)

infection, for each subsequent experiment. Also note that in Figure 4.21., all relevant isolates (investigated in this study) are shown. Taken together, our results demonstrate the presence of an OP7 virus subpopulation in the PR8-NIBSC seed virus and further, that it can be enriched utilizing single-cell infection experiments and depleted by plaque purification.

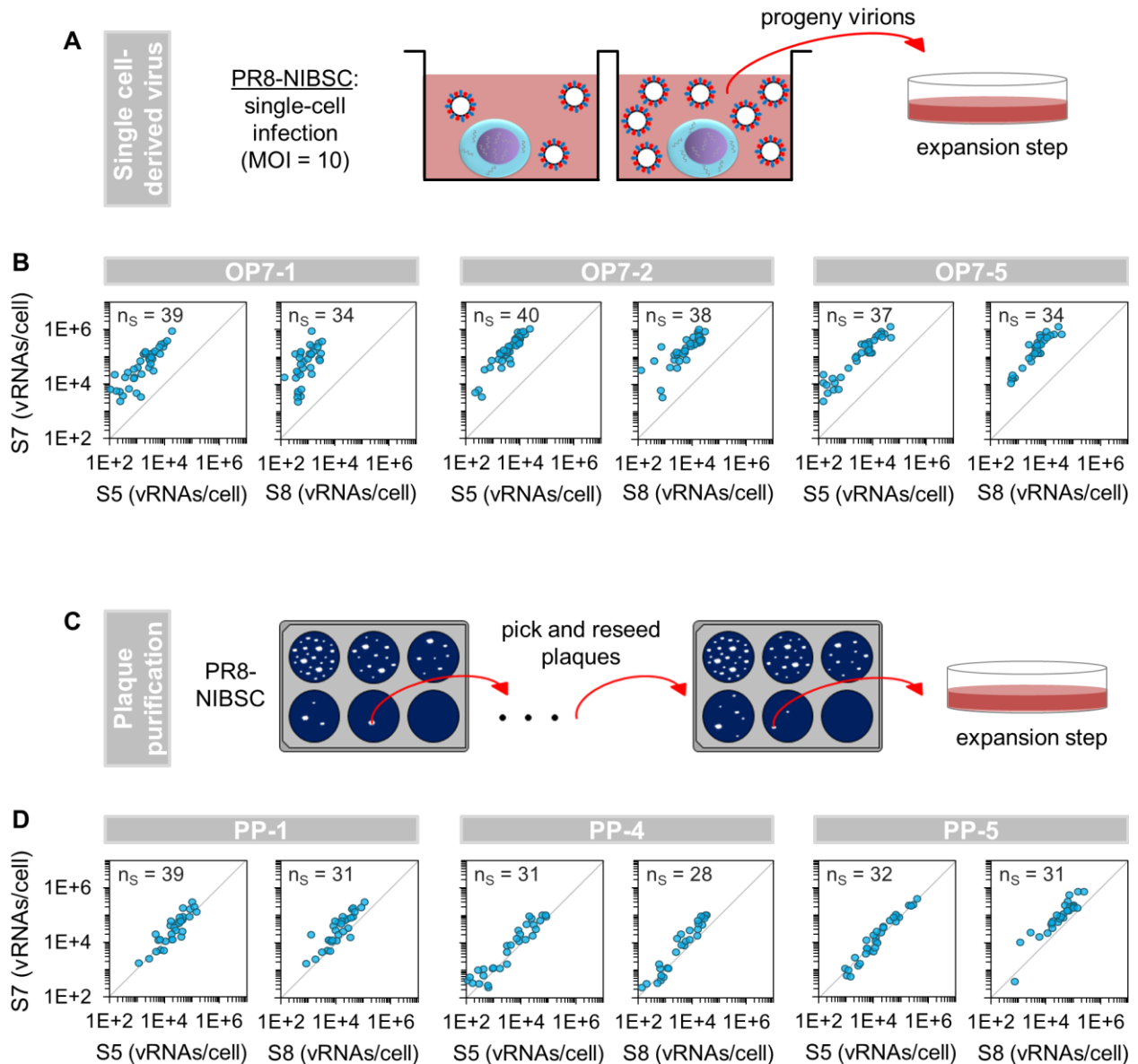


Figure 4.20. Enrichment of OP7 virus. (A) Generation of single-cell derived virus seeds. Infected single MDCK cells (derived from a cell population infected with PR8-NIBSC at an MOI of 10 as described in Figure 4.1.) were cultivated until 12 hpi. Subsequently, whole supernatants (containing all progeny virions) were expanded in confluent MDCK cells. Four independent experiments resulted in 55 virus seeds, of which five isolates showed a strongly pronounced OP7 virus phenotype (three are shown in (B) and all five in Figure 4.21.). Illustration adapted from (Heldt et al., 2015), licensed under CC BY 4.0. (B and D) Correlation between vRNA segments in infected single MDCK cells. Selected (B) OP7 and (D) PP seed viruses (preparation described in (A) and (C), respectively) were used to infect MDCK cells at an

4.3. Discovery of a novel type of DIP (OP7 virus)

MOI of 10. Single cells were then isolated as described in Figure 4.1. At 12 hpi, cells were assayed for vRNA via real-time RT-qPCR. Independent experiments were conducted, each using one virus seed. n_s indicates the number of single-cell measurements. The parity line ($r=1$) is shown for reference. (C) Scheme of plaque purification procedure. Plaques from PR8-NIBSC virus were picked and reseeded in three consecutive assays and finally propagated in confluent MDCK cells. Two independent experiments yielded 43 PP virus isolates. Figure adapted from (Kupke et al., 2018), licensed under CC BY 4.0.

4.3.2. In-depth characterization

4.3.2.1. Infectivity

As OP7 virus was successfully enriched, we next performed cell population-based experiments to explore additional features of OP7 seed virus infection. For this, we used the OP7 and PP seed viruses produced before (Figure 4.20A and C, respectively). MDCK cells were infected at an MOI of 10 and assessed for virus titers by HA assay and infectious virions by TCID₅₀ assay at 12 hpi. Intracellular vRNAs and vRNAs of released virions were quantified by real-time RT-qPCR. Please note that S5, S7 and S8 were quantified representatively for all genome segments.

Surprisingly, we did not find remarkable differences in the properties of OP7 seed viruses compared to PR8-RKI, PR8-NIBSC and the PP viruses (Figure 4.21A). All viruses showed high infectious titers, most likely due to the predominant presence of fully infectious STV. However, upon infection with OP7 seed virus at an MOI of 10, we observed again an over-proportional quantity of intracellular S7 vRNA in relation to S5 and S8 (Figure 4.21B, upper panel), similar to our previous single cell experiments. Interestingly, the levels of S5 and S8 were significantly reduced compared to PR8-RKI and PP virus replication (by at least one order of magnitude).

Moreover, the majority of virus progeny from OP7 seed virus-infected cells were non-infectious (Figure 4.21B, middle panel). Specifically, in comparison to PR8-RKI or PP virus replication, we observe a reduction in the infectivity of produced virions of almost three \log_{10} for OP7-5, and more than one \log_{10} for OP7-4 seed virus infection. The HA titer upon OP7 seed virus infection was (on average) reduced by 0.8 \log_{10} units compared to PR8-RKI and at least 0.3 \log_{10} units lower in comparison to PP virus replication. The low percentage of infectious virions cannot be explained by the presence of conventional DIPs, as the results of segment-specific PCR did not indicate a pronounced accumulation of subgenomic vRNAs in the produced virions upon OP7 seed virus infection (Figure 4.22.). In the following, we refer to virus particles released in infections with OP7 seed viruses as "OP7 virions".

4.3. Discovery of a novel type of DIP (OP7 virus)

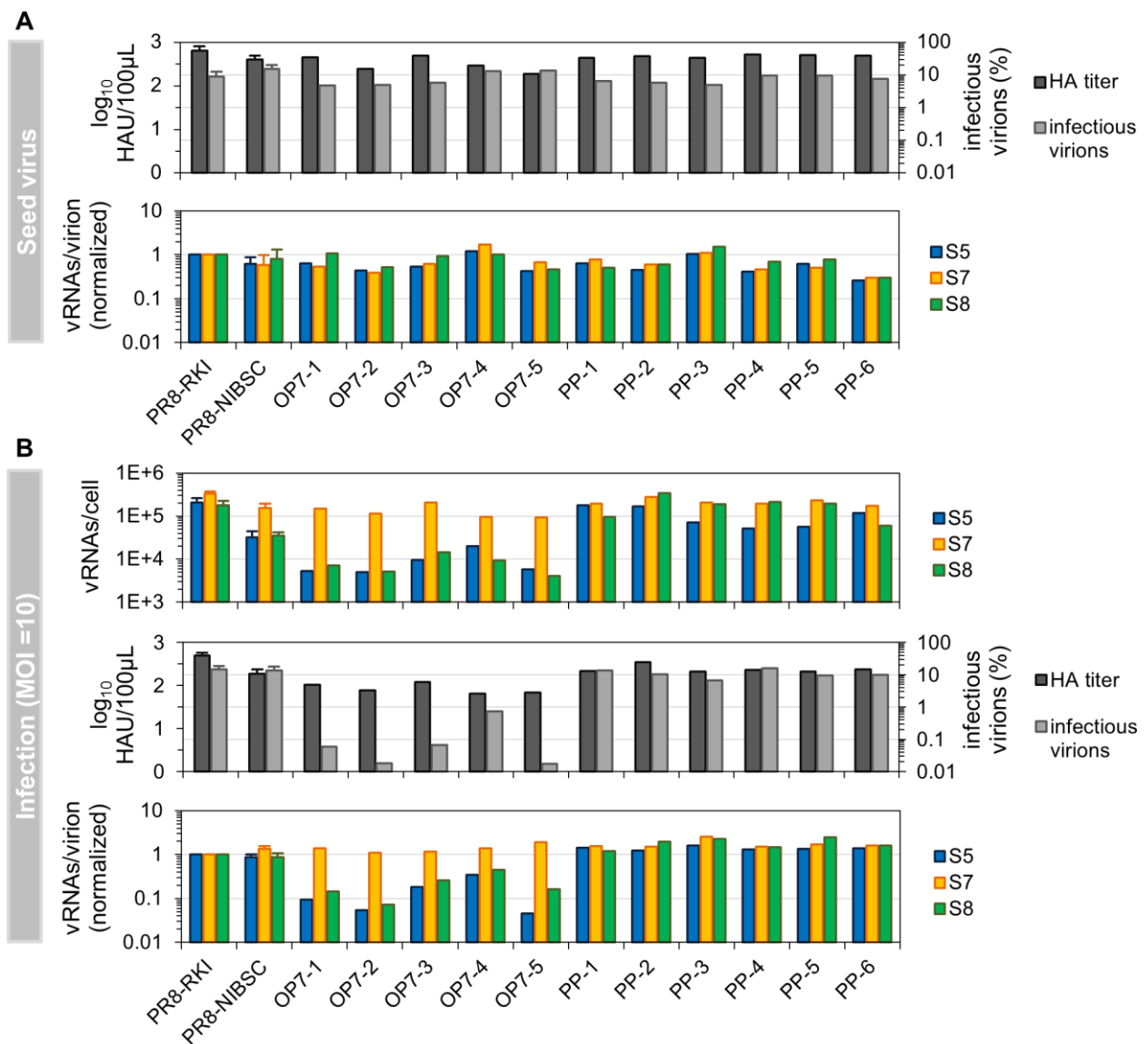


Figure 4.21. Cell population-based infections with OP7 seed viruses. (A) Infectivity and vRNA content of OP7 and PP seed viruses (from Figure 4.20A and C, respectively). Infectious virus titers were quantified by TCID₅₀ assay and purified vRNAs from virions by real-time RT-qPCR. Data was used to calculate fractions of infectious virus and numbers of vRNAs per virion based on virus particle concentration (derived from HA titer). Normalization of vRNAs per virion was based on PR8-RKI virus (as reference). (B) Outcome of high-MOI experiments using the seed viruses shown in (A). MDCK cells, infected at an MOI of 10, were assayed for the per-cell vRNA content at 12 hpi. Infectivity and vRNAs per virion are given for produced virions. Infection experiments with PR8-RKI and PR8-NIBSC virus were performed in independent experiments (n=3) and once with each OP7 and PP seed virus. Error bars indicate standard deviation of depicted mean values. Figure from (Kupke et al., 2018), licensed under CC BY 4.0.

4.3. Discovery of a novel type of DIP (OP7 virus)

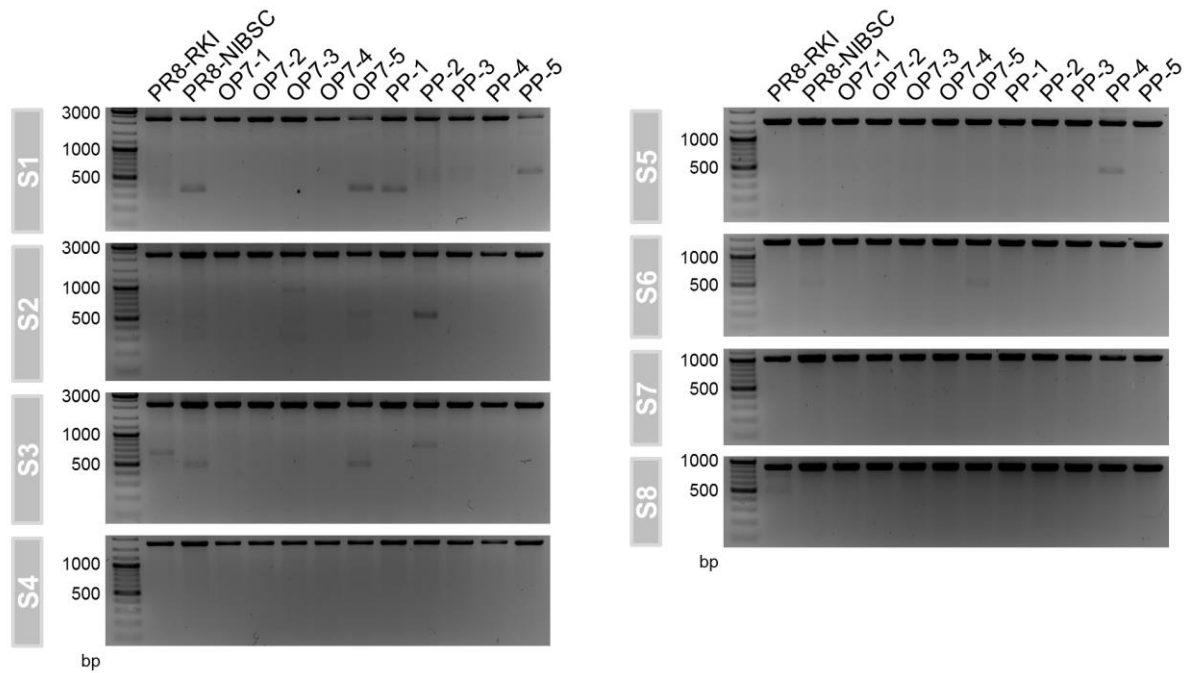


Figure 4.22. Subgenomic vRNAs in virus particles. Released viruses from MDCK cells, infected at an MOI of 10 (from the experiment shown in Figure 4.21B), were investigated for the presence of subgenomic vRNAs on S1-S8 by segment-specific RT-PCR at 12 hpi. FL and DI vRNAs appear in the upmost and lower part of the gel, respectively. Figure from (Kupke et al., 2018), licensed under CC BY 4.0.

The low infectivity of OP7 virions can be rather explained by their low vRNA content (Figure 4.21B, lower panel). More specifically, the calculated number of S5 and S8 per virion was reduced by approximately one order of magnitude compared PR8-RKI and PP virus particles. Intriguingly, the number of S7 vRNA was not affected. Hence, this result clearly indicates that OP7 virions are incomplete with respect to their vRNA content (except for S7), which would render them unable to reproduce upon a single-hit infection. The remaining infectivity is most likely conferred by the presence of STV. Furthermore, OP7 virions were smaller in comparison to PR8-RKI and PP virions, as indicated by ns-TEM (Figure 4.23., ns-TEM analysis was performed by Dietmar Riedel, Max Planck Institute for Biophysical Chemistry, Göttingen, Germany). Moreover, particle morphology did not seem to be affected, as we observed spherical OP7 virus particles with well-resolved surface spike proteins. In summary, our data strongly suggests that OP7 virions are non-infectious as a result of their lack in genomic vRNA content, with the exception of S7, which was predominantly incorporated.

4.3. Discovery of a novel type of DIP (OP7 virus)

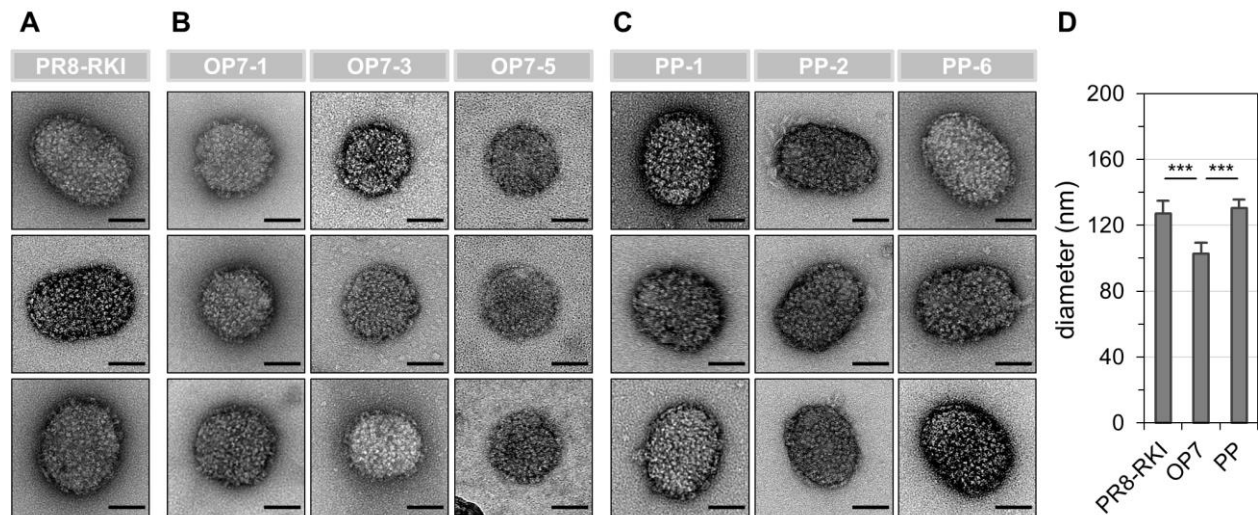


Figure 4.23. Virus particles imaged by ns-TEM. Released virions from infected MDCK cells (MOI=10, 12 hpi, experiment described in Figure 4.21B) are shown. Representative virus particles are depicted for each (A) PR8-RKI, (B) OP7 and (C) PP virus. Scale bar indicates 50 nm. (D) Diameters of virions, determined from ns-TEM images. For non-spherical particles, we determined means of the length and width. Diameters of 16, 17 and 23 virions were determined for PR8-RKI, OP7, and PP virus, respectively. Error bars indicate standard deviation. ***, $p < 0.001$ by Student's *t*-test. Figure from (Kupke et al., 2018), licensed under CC BY 4.0.

4.3.2.2. Genomic vRNA sequence

Next, we determined the sequence of vRNAs from OP7 virions to elucidate whether they contain genomic mutations. Our experiments revealed a significant number of point mutations on the vRNA of S7-OP7 (Figure 4.24A). The number of substitutions ranged from 36-41 in comparison to PR8-RKI, PP virus, and the reference sequence (RefSeq) of PR8 (NC_002016.1) from the National Center for Biotechnology Information (NCBI). In contrast, S5 and S8 showed fewer alterations, with substitutions in 8-16 nt compared to PR8-RKI virus and the NCBI RefSeq (NC_002019.1 for S5 and NC_002020.1 for S8) and 0-3 nt in comparison to PP virus. GenBank accession numbers of all vRNA sequences determined are given in the materials and methods section, subsection "data availability".

4.3. Discovery of a novel type of DIP (OP7 virus)

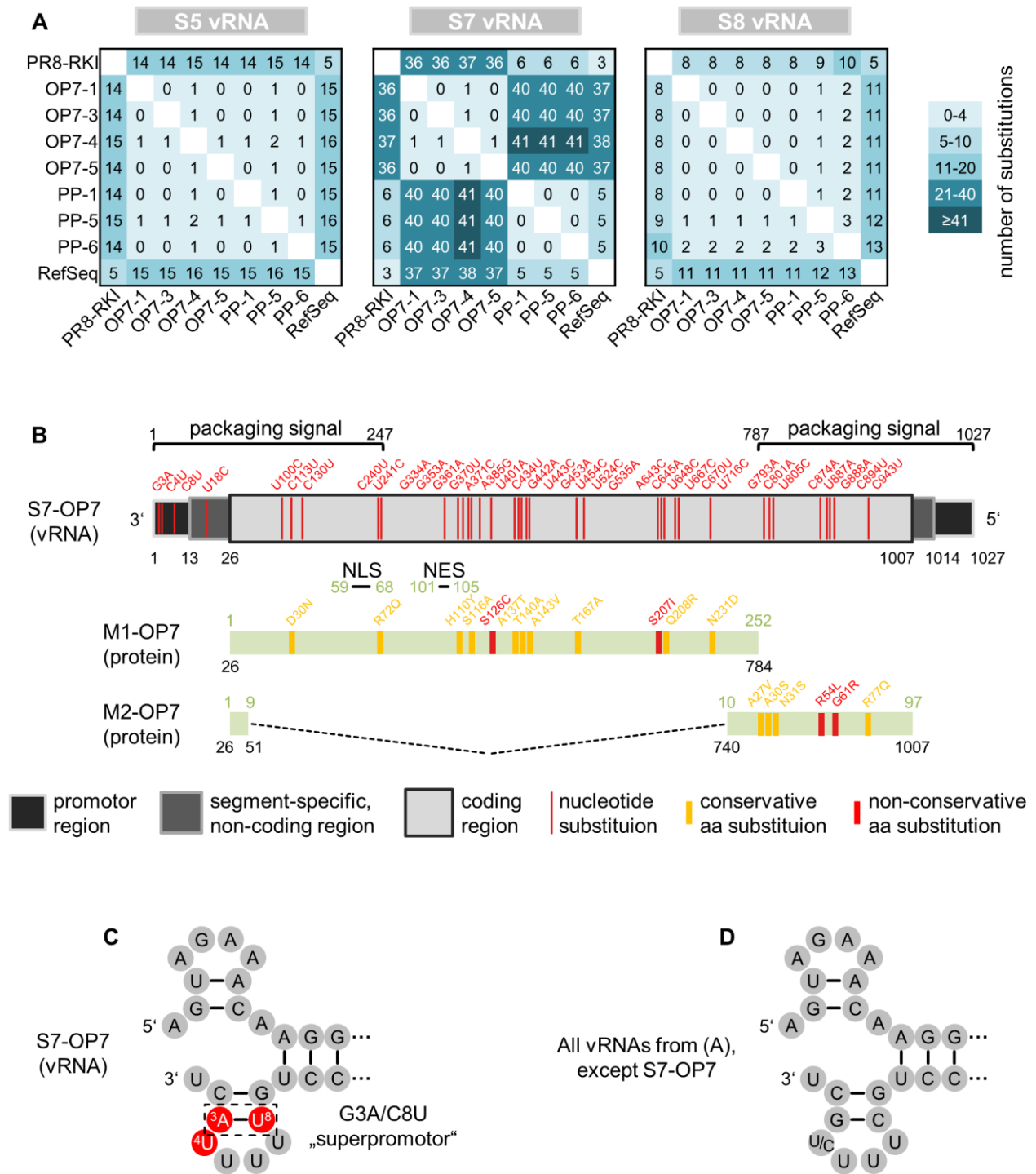


Figure 4.24. Nucleotide substitutions in genomic S7-OP7 vRNA. (A) Comparison of vRNA sequences. Sequences were determined from virions released at high MOI (from experiments depicted in Figure 4.21B). (B) Alterations in the functional regions of S7-OP7 vRNA. Nucleotide and amino acid positions are indicated in black and green numbers, respectively. (C and D) Corkscrew structure adopted by promoter regions. GenBank accession numbers of all vRNA sequences are provided in the materials and methods section, subsection “data availability”. Figure from (Kupke et al., 2018), licensed under CC BY 4.0.

Figure 4.24B illustrates the 37 point mutations of S7-OP7 vRNA in relation to the RefSeq, which concern several functional regions of the genome segment. Note that the investigated OP7 virus isolates showed an identical S7 sequence, except for OP7-4 that showed an additional substitution, which was excluded from analysis as the OP7 phenotype of this isolate was overall less pronounced (Figure 4.21., 4.25., 4.26. and 4.27.). The coding region contains 33 point mutations, resulting in 10 conservative and two non-conservative amino acid substitutions for the encoded M1, and four and two substitutions for M2, respectively. The M1 NLS (Ye et al., 1995) and nuclear export signal (NES) (Cao et al., 2012) did not show alterations, and no additional stop codons were observed in the M1 and M2 reading frames. Moreover, we did not find mutations at sites that affect splicing of M2 mRNA.

Four nucleotide substitutions were observed in the untranslated regions (UTRs), which involve promotor and segment-specific non-coding regions at both vRNA ends. The promotor regions are highly conserved and comprise the non-coding 13 and 12 nt at the 5' and 3' end of vRNA, respectively (Flick et al., 1996). Yet, on S7-OP7 vRNA, we identified the G3A/C8U substitutions (Figure 4.24B and C), which were previously described to result in the formation of the so-called "superpromotor" (Belicha-Villanueva et al., 2012). Further, we identified a substitution at the fourth position (C4U) at the 3' end, which is usually polymorphic (U/C), depending on the genome segment (Lee et al., 2003). Nucleotide substitutions at these three positions were neither found on other segments of OP7 virions, nor on all segments of PP and PR8-RKI virus (Figure 4.24D). Furthermore, the segment-specific genome packaging signal sequences of S7 (Ozawa et al., 2009), which include the UTRs and proximal parts of the coding region at both vRNA ends, were affected by 17 point mutations (Figure 4.24B). Taken together, the vRNA of S7-OP7 shows a significant amount of nucleotide substitutions, while the extent of substitutions in S5 and S8 sequences was lower. The 37 point mutations were distributed in the entire genome segment, affecting the M1 and M2 protein sequence, promotor regions and genome packaging signals.

4.3.2.3. Intracellular viral RNA dynamics

Each genomic vRNA segment is encapsidated into a vRNP complex, involving viral NP and the tripartite viral polymerase (Eisfeld et al., 2015). Once in the nucleus, they are engaged in both transcription of viral mRNA and replication of cRNA. cRNAs are themselves encapsidated in cRNPs and serve as a replication intermediate for the synthesis of progeny vRNA (Fodor, 2013). To study the potential effect of the promotor mutations (found on the vRNA of S7-OP7)

4.3. Discovery of a novel type of DIP (OP7 virus)

on viral RNA synthesis upon OP7 seed virus infection, we next investigated intracellular viral RNAs by real-time RT-qPCR and viral proteins by WB. In the following, we used PR8-RKI (and not PR8-NIBSC) virus for “reference”, or “PR8 wild-type” (WT) virus infection, as we showed that (i) OP7 virions are present in the PR8-NIBSC virus seed (Figure 4.18. and 4.20.), (ii) they seem to influence PR8-NIBSC virus replication (Figure 4.18. and 4.21.), and (iii) PR8-RKI seed virus appeared to be devoid of OP7 virions (Figure 4.18., 4.21. and 4.24.).

Until 12 hpi, the vRNA of S7 in OP7 seed virus infection reached quantities that were comparable to the levels of S5, S7 and S8 of PR8-RKI virus replication (Figure 4.25A). Yet, the level of S5 and S8 vRNA in OP7 seed virus infection was significantly reduced (by approximately one order of magnitude) in relation to S7, in agreement with our previous observation (Figure 4.21B). The mRNA of S7 reached higher peak quantities compared to S5 and S8 and in relation to all mRNAs of PR8-RKI virus replication, with a three- to six-fold increase observed between 6-8 hpi. Similarly, S7 cRNA reached elevated levels upon OP7 seed virus infection in comparison to other segments’ cRNA and compared to all measured cRNAs of PR8-RKI virus replication. This increase was roughly sevenfold between 6-8 hpi in relation to PR8-RKI virus replication. The quantity of S8 cRNA in OP7 seed virus infection was comparable to that of PR8-RKI virus replication; however, the level of S5 cRNA was slightly reduced.

In addition, intracellular M1 protein appeared to accumulate to higher quantities upon OP7 seed virus infection in comparison to PR8-RKI virus replication, while the amount of NP and PA proteins seemed to be reduced (Figure 4.25B, C and D). Furthermore, we observed an enhanced type I IFN induction in OP7 seed virus-infected cells compared to PR8 RKI virus replication, as indicated by an elevated IFN-beta and Mx1 transcript level (Figure 4.25E). In summary, compared to WT virus infection, a strongly altered intracellular viral RNA dynamics can be observed upon OP7 seed virus infection.

4.3. Discovery of a novel type of DIP (OP7 virus)

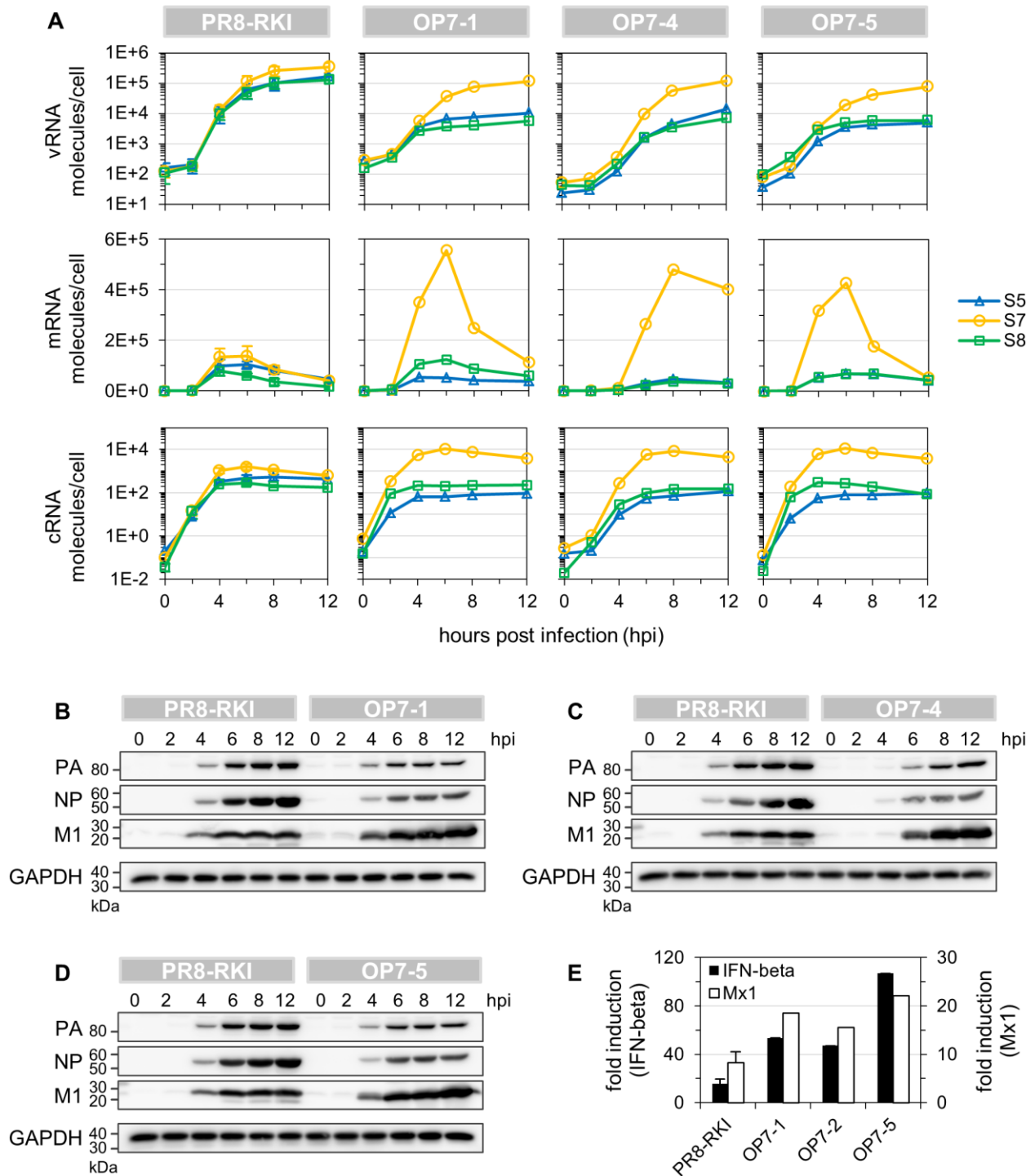


Figure 4.25. Viral RNA synthesis in OP7 seed virus-infected cells. MDCK cells infected at an MOI of 10 were assayed for intracellular viral RNAs by real-time RT-qPCR and viral protein content by WB. (A) Intracellular dynamics of vRNA, mRNA and cRNA quantities. (B, C and D) WB analysis of intracellular viral protein accumulation. (E) Induction of innate immune response at 12 hpi. IFN-beta and Mx1 expression was measured by real-time RT-qPCR and expressed as fold induction (over mock-infected cells) using the $\Delta\Delta C_T$ -method. Infections with PR8-RKI were performed in independent experiments ($n=3$) and once with each OP7 seed virus. Error bars indicate standard deviation of the mean values depicted. Figure from (Kupke et al., 2018), licensed under CC BY 4.0.

4.3.2.4. Intracellular viral protein localization dynamics

In the context of this PhD work, we have set-up, developed and established an imaging flow cytometric analysis of IAV infection. This methodology was then used for the generation of research data for publication by Frensing, Kupke and Bachmann *et al.* (Frensing et al., 2016). Moreover, we used the methodology for the study of OP7 seed virus replication, as described below.

Once in the nucleus, M1 mediates the nuclear export of vRNPs (Brunotte et al., 2014). As the M1 protein of OP7 virus (M1-OP7) showed modifications, we next explored whether intracellular protein trafficking was altered upon OP7 seed virus infection. To this end, we used imaging flow cytometry. Infected cells were stained using either anti-M1 or anti-vRNP monoclonal antibodies (mAbs) in combination with nuclear stains 7-AAD or DAPI, respectively. Fractions of respective proteins/complexes in the cell nuclei were calculated based on the amount of fluorescence signal that was co-localized with the nuclear signal.

Until 4.5 hpi, the fraction of M1 in the nucleus was steadily increasing in PR8-RKI virus replication, indicating the nuclear import of M1 subsequent to its production (Figure 4.26A). Concurrently, from 3-4.5 hpi, the percentage of vRNPs in the nucleus shows a steep decrease, which indicates nuclear export of the viral genomes (Figure 4.26B). Hence, the accumulation of M1 in the nucleus coincided with the nuclear export of vRNPs. In contrast, for OP7 seed virus-infected cells, we can observe a strong increase in the percentage of M1 in the nucleus even after 4.5 hpi (Figure 4.26A), also illustrated by images shown in Figure 4.26C. In addition, while a large proportion of vRNPs appeared to leave the nucleus from 3-4.5 hpi, some vRNPs seemed to remain in the nucleus from 9 hpi onwards, as indicated in comparison to PR8-RKI virus replication (Figure 4.26B). This difference in the vRNP localization dynamics may appear less obvious compared to the difference in the localization dynamics of M1 (Figure 4.26A). We therefore pooled the data of the three independent OP7 seed virus infection experiments (in each using a different OP7 seed virus) for statistical analysis (Figure 4.27.), which demonstrated a significant difference in the nuclear vRNP localization dynamics in relation to PR8-RKI replication as well. Moreover, the nuclear retainment of vRNPs in OP7 virus replication is further visualized by the imagery shown in Figure 4.26D. Please note that, due to the G3A/C8U "superpromotor" identified on the vRNA of S7-OP7, it has to be assumed that the majority of synthesized M1 protein is likely M1-OP7. In summary, image flow cytometric analysis indicates an enhanced nuclear accumulation of the mutated M1-OP7 upon OP7 seed virus infection, which may cause the apparent nuclear retainment of a fraction of vRNPs.

4.3. Discovery of a novel type of DIP (OP7 virus)

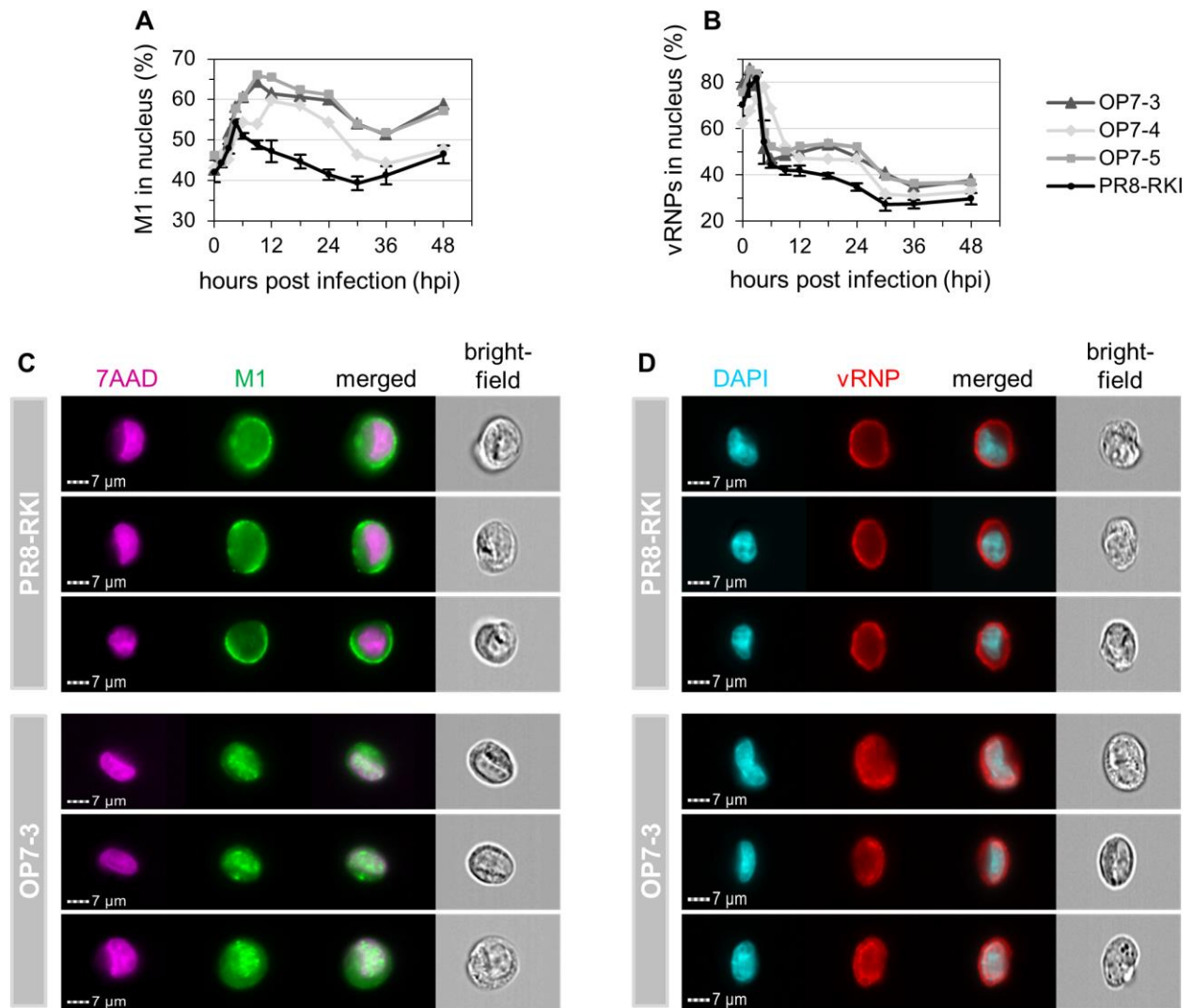


Figure 4.26. Intracellular M1 and vRNP localization dynamics upon OP7 seed virus infection.

Imaging flow cytometric analysis was performed for infected MDCK cells (MOI=10). (A and B) Dynamics of nuclear localization of M1 (A) and vRNPs (B). Cells were either stained for M1 or vRNPs and cell nuclei using 7-AAD or DAPI, respectively. Fractions of M1 or vRNPs in the nucleus were calculated based on the amount of fluorescence signal co-localized with the nuclear signal. 10,000 single cells were evaluated per sample. Infections with PR8-RKI virus were performed in independent experiments (n=3) and once with each OP7 seed virus. Error bars indicate standard deviation of illustrated mean values. Statistical analysis of data depicted in (B) is shown in Figure 4.27. (C and D) Images of representative cells stained for M1 at 9 hpi (C) and vRNPs at 18 hpi (D). Panels of one representative experiment are depicted. Figure from (Kupke et al., 2018), licensed under CC BY 4.0.

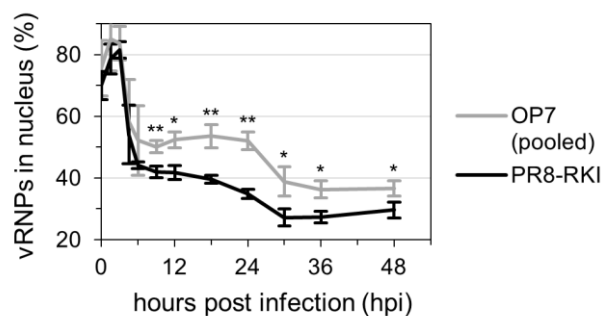


Figure 4.27. Statistical analysis of nuclear vRNP localization dynamics. Imaging flow cytometric analysis was performed for infected MDCK cells (MOI=10). Cells were stained for vRNPs and cell nuclei. Fractions of vRNPs in the nucleus were calculated based on the amount of fluorescence signal co-localized with the nuclear signal. 10,000 single cells were evaluated per sample. Infections with PR8-RKI virus were performed in independent experiments (n=3) and once with each OP7 seed virus (i.e. OP7-3, OP7-4 and OP7-5 virus, see also Figure 4.26.). Data set of OP7 seed virus infections was pooled for analysis. Error bars indicate standard deviation of the means depicted. *, $p < 0.05$ and **, $p < 0.01$ by Student's *t*-test. Figure from (Kupke et al., 2018), licensed under CC BY 4.0.

4.3.2.5. Interference with virus replication

Conventional DI RNAs are thought to have growth advantages over their FL counterparts, i.e. an enhanced genomic replication and a preferential incorporation into progeny virions. Intriguingly, the mutated vRNA of S7-OP7 seemed to have very similar advantages in propagation. We therefore hypothesized that OP7 virus may even share another feature with conventional DIPs: the interference with replication of STVs. To further explore this possibility, we simultaneously co-infected cells with IAV and OP7 virus.

Indeed, the co-infection experiments showed an attenuated replication of PR8-RKI virus (Figure 4.28.). In comparison to cells infected with only PR8-RKI (MOI=10), the co-infected cells (both OP7 and PR8-RKI virus at an MOI of 10) showed a reduced HA titer (by 0.8 units), a severe reduction in the infectivity of the released virions (≈ 3 orders of magnitude) and an over-proportional quantity of S7 vRNA in relation to S5 and S8 (intracellularly and in the released virus particles). The lower impact of OP7-4 virus may be explained by the additional point mutation found on the vRNA of S7 in comparison to other OP7 viruses (Figure 4.24A), or lower amounts of OP7 virions in the OP7-4 working seed.

4.3. Discovery of a novel type of DIP (OP7 virus)

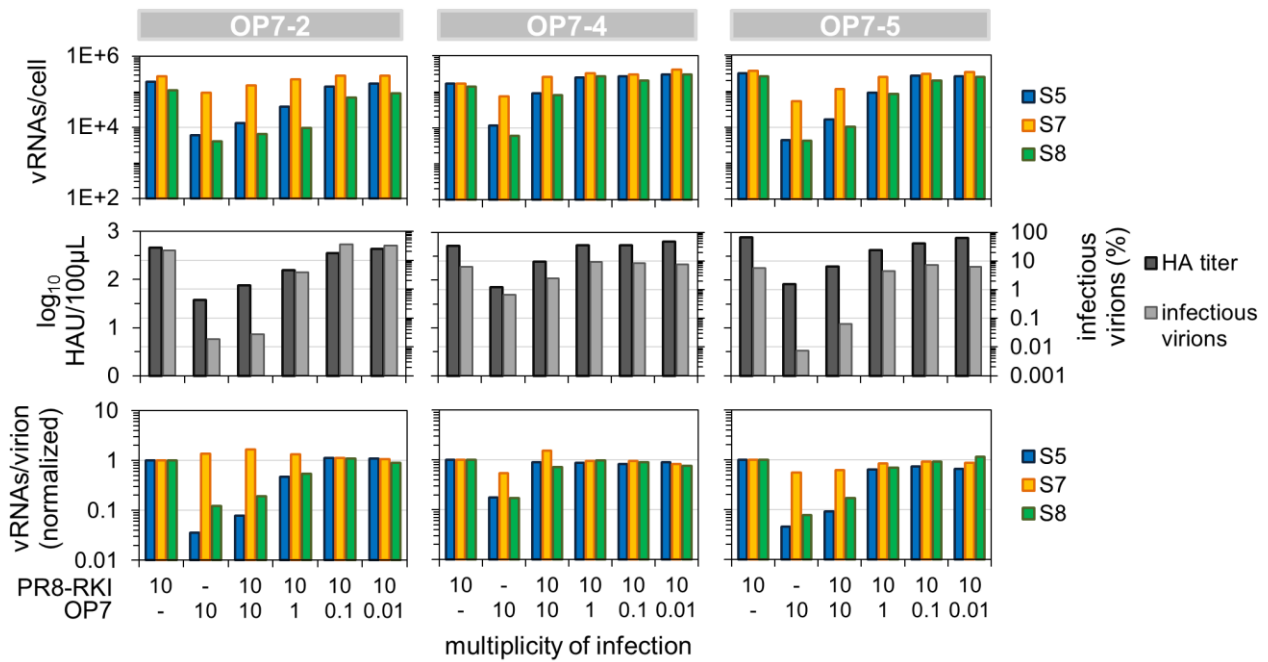


Figure 4.28. Co-infection of PR8-RKI virus-infected MDCK cells with OP7 seed virus. MDCK cells infected with PR8-RKI virus at an MOI of 10 were simultaneously co-infected with OP7 seed virus at the indicated MOIs until 12 hpi. Infectious virus titers were quantified by plaque assay and intracellular and purified vRNAs from virions by real-time RT-qPCR. Data were used to calculate fractions of infectious virus and numbers of vRNAs per virion using the virus particle concentration derived from HA titer. Normalization of vRNAs per virion was based on PR8-RKI virus (as reference). Three independent infection experiments were conducted, in each using PR8-RKI and one OP7 seed virus. Figure from (Kupke et al., 2018), licensed under CC BY 4.0.

To test whether OP7 virus also shows interference with PR8-RKI virus replication in human cell lines, we next used human embryonic kidney 293 (HEK 293) and A549 cells (derived from human lung carcinoma) in co-infection studies. Again, experiments revealed interference, as indicated by the reduction in HA titer, a strong decrease in the infectivity of released virions and an over-proportional level of S7 vRNA in the produced virus particles compared to cells infected with only PR8-RKI (Figure 4.29A and B). Similarly, co-infection studies in MDCK cells also demonstrated interference with the 2009 pandemic H1N1-pdm09 strain (i.e., influenza A/California/7/2009 of H1N1 subtype) and even with a H3N2 strain from 2014 (i.e., strain influenza A/Hong Kong/4801/2014 of H3N2 subtype) (Figure 4.29C and D). Taken together, our experiments demonstrated a strong interference of OP7 virus with replication of PR8-RKI virus in both, MDCK cells and two human cell lines, as well as interference with H1N1-pdm09 and H3N2 virus replication.

4.3. Discovery of a novel type of DIP (OP7 virus)

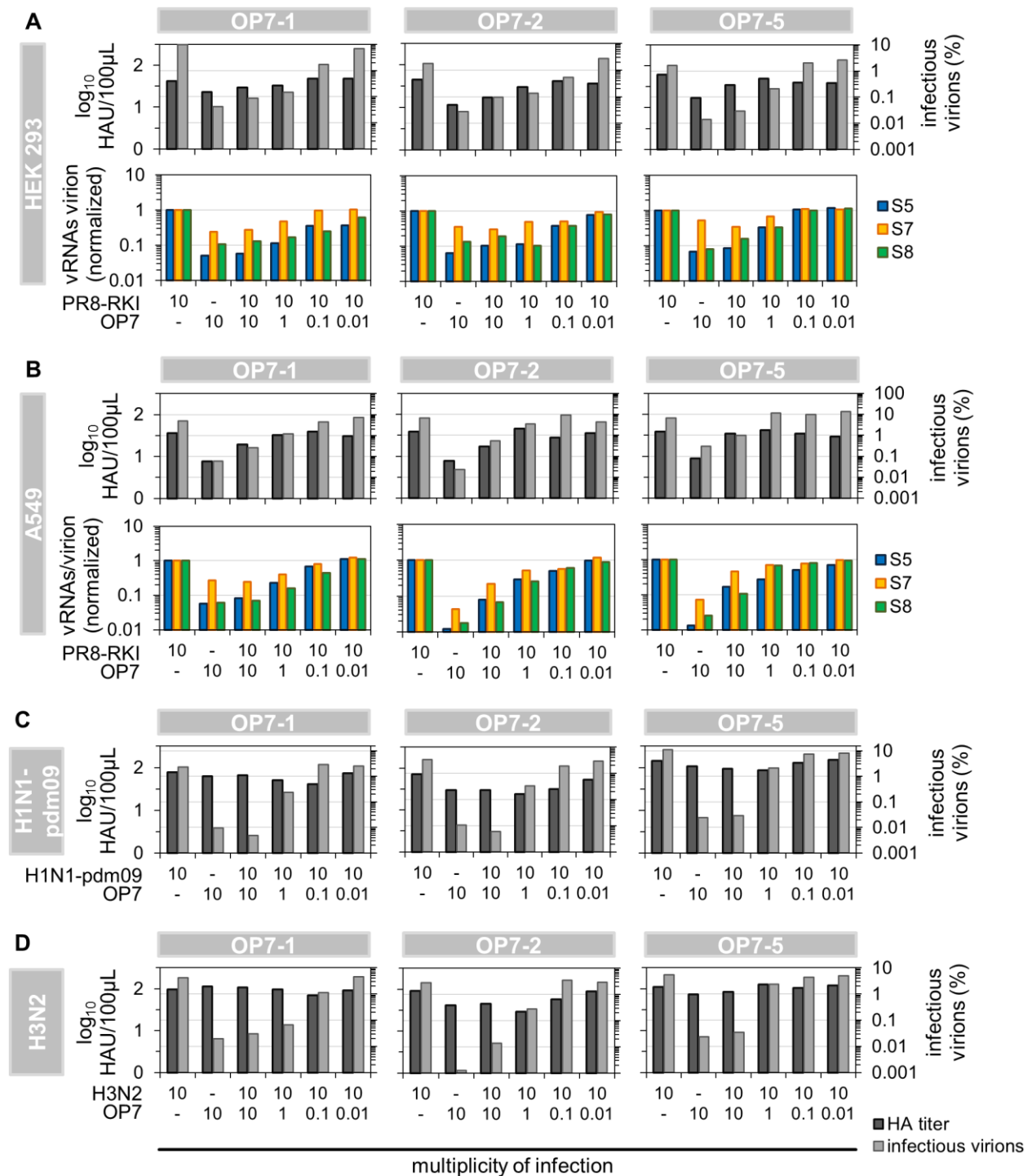


Figure 4.29. Interference of OP7 virus with replication of various IAV strains in different cell lines. Cells infected with WT virus at an MOI of 10 were simultaneously co-infected with OP7 seed virus at the indicated MOIs until 12 hpi. (A and B) Co-infection of PR8-RKI-infected human HEK 293 (A) and A549 (B) cell lines with OP7 seed virus. (C and D) Interference of OP7 virus with H1N1-pdm09 (C) and H3N2 (D) virus replication in MDCK cells. Infectious virus titers were quantified by plaque assay and intracellular and purified vRNAs from virions by real-time RT-qPCR. Data was used to calculate fractions of infectious virus and numbers of vRNAs per virion using the virus particle concentration (derived from HA titer). Normalization of vRNAs per virion was based on PR8-RKI virus (as reference). Each three independent infection experiments were conducted, in each using WT and one OP7 seed virus. Figure from (Kupke et al., 2018), licensed under CC BY 4.0.

4.3.3. Discussion of the novel type of DIP (OP7 virus)

Using the experimental approach for single-cell analysis of IAV infection (section 4.1.), we discovered a yet unknown form of IAV-derived DIP. So far, DIPs were primarily identified and characterized regarding their large genomic deletions. By contrast, OP7 virus contains nucleotide substitutions in one of its genome segments. OP7 virions shares very similar features with conventional DIPs, i.e. (i) an enhanced genomic replication of the DI genome over other segments, (ii) its predominant packaging into progeny virions, (iii) an enhanced induction of innate immune response upon infection, (iv) virus particles that appear to be non-infectious due to the lack of genomic information, and (v) interference with replication of STV. Yet, some of the underlying principles that lead to the afore mentioned observations appear to be different for OP7 virions in comparison to conventional DIPs.

Single-cell infection experiments allowed us to recognize the unusual OP7 phenotype in a subpopulation of cells. In order to multiply the OP7 virions released from these single cells, we infected $\sim 1 \times 10^6$ cells with the corresponding single-cell supernatants, which can only result in a low MOI scenario, as virus titers of single IAV-infected cells reach only up to roughly 1000 PFU (Heldt et al., 2015). Typically, low MOI experiments with virus seeds containing conventional DIPs lead to high infectious virus titers (Frensing, 2015), which was also true for the resulting OP7 seed viruses (Figure 4.21A). These infection conditions reduce co-infection events and cells are mostly infected by single virus particles. Hence, STV-infected cells release predominantly infectious viral progeny; however, DIP-only infected cells cannot contribute to virus production. Yet, for a certain time window, these cells may still become co-infected with newly released STV, which, in turn, converts these cells to a (primarily) DIP-producing form (Liao et al., 2016). Hence, for low MOIs, infectious virions usually dominate in the released virus population. In contrast, using the resulting OP7 seed viruses at high MOIs, we observed a very low infectivity of the released virions (Figure 4.21B); an outcome, which is also to be expected from seed viruses containing conventional DIPs (Frensing, 2015). This infection condition fosters co-infection events and thus, the complementation of DIP-infected cells with STVs early on. Hence, as a result of the propagation advantage of the DI genomes, mainly non-infectious DIPs accumulate in the resulting virus population.

Our data clearly suggest that OP7 virions are non-infectious due to their reduced vRNA content (Figure 4.21B). More specifically, the calculated number of vRNA per virion was decreased by roughly one order of magnitude compared to WT virions, while the quantity of S7 was not affected. These numbers can, theoretically, result in virus populations, where (i) only $\sim 10\%$ of

4.3. Discovery of a novel type of DIP (OP7 virus)

the particles are complete, i.e. they contain each of the eight different genome segments, while the remaining virions contain only S7 or (ii) all virus particles contain S7; yet, they lack a large proportion of the remaining seven segments. As the fraction of infectious virions was reduced by more than two orders of magnitude (compared to WT virions), only the second scenario seems to be conclusive. The remaining infectivity can be explained by the presence of residual STVs, the random packaging of eight functional segments (see below for more details), or the complementation of infected cells with all functional genome segments through co-infection. Furthermore, our conclusion that OP7 virions are defective in virus replication is further supported by the results of plaque purification from PR8-NIBSC virus (which contains OP7 virus). Each plaque is supposed to originate from the infection of a cell by a single virus particle. Yet, after threefold purification, none of the resultant 43 virus isolates showed the OP7 virus phenotype in infection experiments, which further emphasizes that OP7 virions are propagation-incompetent. The origin of the defect in virus replication of OP7 virions differs from conventional DIPs, which possess heavy deletions in their DI genome, whereas OP7 virions lack complete genomic vRNA segments, except their DI genome (i.e. vRNA of S7-OP7).

The segment-specific genome packaging signal sequences of S7 (Ozawa et al., 2009) were affected by 17 nucleotide substitutions, which may explain the unusual vRNA content of OP7 virions. Typically, virus assembly and budding is a well-organized process, in which the eight different vRNAs are selectively incorporated into each virus particle (Noda and Kawaoka, 2012, Chou et al., 2012), with the packaging signals being involved (Hutchinson et al., 2010, Fujii et al., 2003). Although, depending on the strain, up to 20% of virions can still fail to package at least one vRNA (Nakatsu et al., 2016), which mainly represent the so-called semi-infectious (SI) particles (Brooke et al., 2013). Nevertheless, it was suggested that S7 plays a key role in the IAV genome packaging process, as already four point mutations in the signal sequence can disrupt vRNA packaging (Hutchinson et al., 2008). Similar to our results of infection experiments using OP7 seed viruses, the authors observed a dramatic decrease in the infectivity of released virions (of more than two orders of magnitude) compared to WT virus replication. This decrease equaled the reduction predicted for a purely random packaging process (Nakajima and Sugiura, 1977, Laver and Downie, 1976), in which only a minority of virions would incorporate the complete genome. In contrast, Hutchinson and colleagues did not observe an over-representation of S7 vRNA in the released virus particles (Hutchinson et al., 2008). It is conceivable that a disrupted genome packaging mechanism, in combination with the over-proportional intracellular quantity of S7-OP7 vRNA can result in a predominant incorporation of S7-OP7. Alternatively, additional mechanisms may act via the mutated vRNA,

4.3. Discovery of a novel type of DIP (OP7 virus)

which might involve (i) the recently proposed incorporation signal (NCRs at both vRNA ends) and/or (ii) bundling signal (both terminal coding regions) (Goto et al., 2013), or even (iii) the selective decrease in packaging of individual genome segments originating from mutations on another vRNA (Brooke et al., 2014). Extensive research will be required to elucidate precise mechanisms, e.g. by utilizing reverse genetics (i.e. an eight-plasmid DNA transfection system (Hoffmann et al., 2000)), which is the subject of ongoing studies. However, the final outcome is a predominant incorporation of S7-OP7 vRNA over other genome segments; an observation that may show similarities to conventional DI RNAs, which are preferentially packaged over their FL counterparts (Duhaut and McCauley, 1996, Odagiri and Tashiro, 1997).

Previously, artificial IAVs carrying the G3A/C8U “superpromotor” on the vRNA of either S2 or S3 were reconstituted (Belicha-Villanueva et al., 2012). Upon infection, the observed phenotype showed very similar intracellular features, with respect to viral RNA and protein synthesis from the segments bearing G3A/C8U, as compared to S7-OP7 (which carries G3A/C8U) upon OP7 seed virus infection. More specifically, the authors observed (i) a strong decrease in vRNA levels of all genome segments, except for the vRNA carrying G3A/C8U, (ii) an enhanced synthesis of mRNA, cRNA and protein derived from the said segment and (iii) increased levels of type I IFN in comparison to WT virus replication. Regarding the latter observation, it was shown that this increased induction was likely caused by elevated amounts of immunostimulatory RNA molecules (Belicha-Villanueva et al., 2012). Such an enhanced induction of innate immunity is also observed for infections with conventional DIPs (Lopez, 2014, Strahle et al., 2006, Killip et al., 2013). Note that the additional G4U substitution (observed in S7-OP7) can also affect promotor function (Lee et al., 2003). Yet, due to the typically dramatic effect of G3A/C8U on viral RNA synthesis (also described elsewhere, e.g. (Neumann and Hobom, 1995, Vreede et al., 2008)), we conclude that a major part of the altered intracellular viral RNA dynamics upon OP7 seed virus infection must be accounted for by the promotor mutation G3A/C8U found on the vRNA of S7-OP7.

Importantly, please note that the G3A/C8U mutation alone does not appear to result in the whole OP7 virus phenotype, as vRNA segments bearing G3A/C8U were not predominantly packaged into progeny virions in the context of an infection (Belicha-Villanueva et al., 2012), unlike S7-OP7 in OP7 virus infection. This indicates that additional mutations (found on S7-OP7) are necessary, beyond G3A/C8U, for the defective and interfering phenotype of OP7 virus. Moreover, it was not described that the G3A/C8U mutation results in a DIP-like phenotype (Belicha-Villanueva et al., 2012, Neumann and Hobom, 1995, Vreede et al., 2008, Maamary et al., 2012). The G3A/C8U substitutions were, so far, only artificially introduced into

4.3. Discovery of a novel type of DIP (OP7 virus)

the vRNA of IAVs (Belicha-Villanueva et al., 2012, Neumann and Hobom, 1995, Vreede et al., 2008, Maamary et al., 2012). It is, thus, remarkable that S7-OP7 seemed to have obtained G3A/C8U “naturally” by selection. As a result, the genomic vRNA of S7-OP7 accumulates to roughly ten-fold higher intracellular levels compared to other genome segments. This feature shows again similarities to conventional DI genomes, which are preferentially synthesized over their FL counterparts (Akkina et al., 1984, Duhaut and McCauley, 1996); yet, for another reason, i.e. presumably as a result of a faster accumulation, due to their reduced length (Marriott and Dimmock, 2010, Nayak et al., 1985, Laske et al., 2016).

The coding region of S7-OP7 showed 33 point mutations, resulting in two non-conservative amino acid substitutions for both, the M1 and M2 (ion channel) protein. Among other functions, these proteins are also important for virus assembly (Iwatsuki-Horimoto et al., 2006), which may provide an additional explanation for the irregular vRNA content of OP7 virions. Moreover, alterations in the proteins can also affect virus morphology, which shows a variety morphotypes, including filamentous virions (Roberts et al., 1998, Burleigh et al., 2005). Yet, OP7 virions appeared similar to WT virus particles, but slightly smaller, which may be conclusive owing to their reduced vRNA content. Interestingly, DIPs from vesicular stomatitis virus are smaller as well due to the reduced size of their DI genomes (Holland, 1987).

The M1 protein is also involved in the nuclear export of vRNPs (Brunotte et al., 2014). Although we did not identify alterations in the NLS and NES of M1-OP7, the protein nevertheless showed an unusually high accumulation in the nucleus upon OP7 seed virus infection. Concurrently, it appeared that a fraction of vRNPs were retained in the nucleus (as compared to WT virus replication). In this context, M1 is thought to mediate the binding of the viral nuclear export protein (NEP) and the vRNPs, which in turn forms a complex that is exported from the nucleus by the NES located of NEP (Brunotte et al., 2014). Conceivably, the binding sites of M1-OP7 to NEP and/or the vRNPs are perturbed, which leads to the nuclear retainment of both, M1-OP7 and vRNPs. Yet, it must be assumed that some functional M1 protein is still synthesized from the co-infecting STV, which may explain the marked nuclear export vRNPs at early times post infection. The perturbed function of the mutated M1-OP7 may contribute to the interfering ability of OP7 virus, or even to its defect in virus replication. Reconstitution of pure OP7 virus seeds using reverse genetics (Hoffmann et al., 2000), in combination with overexpression experiments involving M1 or M1-OP7 (and other viral proteins) in OP7 or WT virus-infected cells, respectively, are the subject of ongoing studies and might shed more light into the role and functionality of M1-OP7.

4.3. Discovery of a novel type of DIP (OP7 virus)

OP7 virions may be a promising candidate for antiviral therapy as they show strong interference with virus replication of relevant IAV strains, and interference in human cell lines. Moreover, the enhanced induction of innate immunity, observed upon OP7 seed virus infection, may be further beneficial in the context of antiviral therapy. More precisely, the same stimulation, also induced by infection with conventional DIPs (Lopez, 2014, Strahle et al., 2006, Killip et al., 2013), is regarded to be useful for potential pan-specific treatment of respiratory virus diseases utilizing conventional DIPs (Dimmock and Easton, 2015). The appropriateness of OP7 virions for antiviral therapy may be further investigated *in vivo*, e.g. in mice or in ferrets, as it was previously accomplished using conventional DIPs (Dimmock et al., 2008, Dimmock et al., 2012b, Easton et al., 2011).

Interestingly, the presence of OP7 virus was presumably noticed before; yet, it was not recognized that they constitute separate virus particles, in particular a separate form of DIP. More specifically, the molar ratio of S7 vRNA relative to other genome segments was increased in virus preparations containing conventional IAV-derived DIPs (Davis et al., 1980, De and Nayak, 1980, Duhaut and McCauley, 1996, Janda and Nayak, 1979). Note that we made a similar observation for virus populations with increased numbers of OP7 virions (Figure 4.21B). It was presumed that some DIPs either contain only S7, or that they are polyploid with respect to S7 vRNA (De and Nayak, 1980). However, the presence of potential point mutations was not investigated; rather, the only indication of DIPs were large deletions in some vRNAs. Thus, OP7 virions may have been overlooked for IAVs, in particular as a distinct type of DIP with nucleotide substitutions in its genome. It is conceivable that similar DI genomes also exist in other IAV preparations, which are not recognized so far, as DIPs are traditionally primarily studied based on their large genomic deletions. Yet, the awareness of the potential presence of such DIPs may be important regarding the interpretation of experimental results, as they exert strong effects, both on virus replication and on host cell response, similar to conventional DIPs (Huang and Baltimore, 1970, Akpinar et al., 2016b, Marriott and Dimmock, 2010, Dimmock and Easton, 2014, Lopez, 2014, Strahle et al., 2006, Killip et al., 2013, Frensing et al., 2014).

Summary. Utilizing single-cell analysis, we here report the discovery of a yet unknown type of IAV-derived DIP. Instead of deletions, the genomic vRNA of S7 carried 37 point mutations compared to the reference sequence, affecting promotor regions, encoded proteins, and genome packaging signals. Co-infection experiments demonstrated strong interference of OP7 virus with IAV replication, manifested by a dramatic decrease in infectivity of released virions.

4.3. Discovery of a novel type of DIP (OP7 virus)

Moreover, an over-proportional quantity of S7 in relation to other genome segments was observed, both intracellularly and in the released virus population. Concurrently, OP7 virions lacked a large fraction of other vRNA segments, which appears to constitute its defect in virus replication. In conclusion, we believe that OP7 virus might be a promising candidate for antiviral therapy. Moreover, this novel form of DIP may have been overlooked in other IAV preparations.

5. Conclusion and outlook

In this PhD work, we conducted single-cell analysis of IAV-infected cells for applications in cell-culture based vaccine production. For this, we devised and established an experimental procedure. Next, single-cell analysis of IAV-infected cells revealed a large cell-to-cell heterogeneity in IAV replication. Furthermore, we showed that IAV infections are, to a certain degree, affected by stochastic effects. We, thus, challenge current beliefs that cell population-based measurements are an accurate representation of virus infections. Subsequently, we investigated potential sources of the vast between-cell variability in virus titers. The results obtained advance single-cell virology research towards an understanding of the large cell-to-cell heterogeneity in virus infections. Finally, we discovered a novel type of IAV-derived DIP, which was facilitated by single-cell analysis. Due to its strong interfering potency, we believe that it might represent a promising candidate for antiviral therapy.

Experimental workflow for single cell analysis. At the beginning of the PhD work, we formulated the requirements for a (theoretically) optimal experimental procedure for single-cell analysis of IAV-infected cells: absolute quantification of virus titers of infected single cells, a high throughput of single-cell measurements, multiparametric correlation of the single-cell virus yield to additional single-cell parameters, no perturbation of cell behavior (or virus replication) due to the single cell processing, innovation, commercially available instrumentation, and timely generation of research data. Surprisingly, we were able to fulfil most of the requirements. More specifically, the workflow offers: (i) absolute quantification of extracellular virus titers and intracellular vRNAs, (ii) a good throughput of single-cell measurements, (iii) correlation of the single-cell virus yield to either: the cell size, rRNAs, multiple different vRNAs, or to DI RNAs on various genome segments, (iv) no apparent perturbation of cellular behavior despite the processing and isolation of single cells, (v) a simple, rapid and efficient procedure that was straightaway commercially available and (vi) the timely generation and publication of research data. In future studies, the present methodology may be used to investigate the correlation of the extracellular single-cell IAV yields with the whole-cell transcriptome using scRNA-seq (Stegle et al., 2015). Moreover, in mid-2015, the “Polaris” single-cell analysis platform (developed by fluidigm) was released, which may allow for an even higher dimensionality of single cell analyses of virus infections. This microfluidic approach would allow,

on top of the opportunities offered by our method, for dynamic single-cell analysis by live-cell imaging (Wong et al., 2017, Wills et al., 2017, Ramalingam et al., 2016).

Cell-to-cell heterogeneity in IAV replication. The established single-cell analysis procedure was used to study IAV replication at the single-cell level. We observed a large cell-to-cell heterogeneity in virus titers and intracellular viral RNAs. These results helped in the collaboration with another researcher of the BPE group (who pursued a mathematical modelling approach) to develop a stochastic model of intracellular single-cell IAV replication (Heldt et al., 2015). Together, we contributed in promoting the notion that virus infections are highly variable at the single cell level and that cell population-based experiments are not an accurate representation of virus infections (Zhu et al., 2009, Delbruck, 1945b, Schulte and Andino, 2014). We further show that IAV replication is affected by the randomness in biochemical reactions to a certain degree. Moreover, our study was the first that described and investigated sources of extrinsic and intrinsic noise in virus infections. In particular, we showed that both sources of noise can affect the single-cell virus titer. Future research efforts of the BPE group (regarding mathematical modeling) comprise the extension of the stochastic description of IAV replication, to also account for DIP replication. Further, the stochastic model may be extended to describe the spread and propagation of viruses from cell to cell in a large cell population (multiscale model) for the simulation of IAV production in bioreactors.

Sources of cell-to-cell heterogeneity in IAV replication. Next, we investigated potential sources of the large cell-to-cell heterogeneity in IAV replication. First, we showed that intrinsic noise in vRNA synthesis (caused by the randomness in biochemical reactions) and extrinsic noise (caused by the between-cell variation in deterministic factors) can both contribute to the large cell-to-cell variability in IAV infection. However, although it appeared that sources of noise intrinsic to vRNA synthesis do not play such a pronounced role, it might still be possible that the stochasticity present at another step of virus replication, or cellular response to virus infection, can significantly contribute to the large cell-to-cell heterogeneity in virus infection. Therefore, more research in single-cell virology is required to resolve the contribution of stochasticity to the cell-to-cell heterogeneity in virus replication (in comparison to the contribution caused by sources of extrinsic noise).

Furthermore, we investigated deterministic factors and showed that the progress of infection, the between-virus heterogeneity in the genetics of the infecting virus population (except for DIPs), the cell size, the ribosome content and the cell-to-cell heterogeneity in the MDCK cell line did all not seem to influence the between-cell variability in IAV infection. However, the load of intracellular DI RNAs appeared to have a significant effect. The elucidation of factors that contribute to the large cell-to-cell heterogeneity in virus replication must be regarded as a complex multiparametric problem, in which many different factors each have an individual effect. Therefore, it is difficult to identify such influencing factors, as not all of these factors may have a sufficient effect on virus replication so that a tendency can be observed (as it was the case for the influence of intracellular DI RNAs on cell-to-cell variability in virus titers). Other sources that were shown to correlate to the strength of single-cell virus replication are: proteins involved in the ER translocation, signal peptide processing and membrane trafficking, the IFN and oxidative stress response, and mitochondrially encoded genes (Russell et al., 2018, Zanini et al., 2018, Steuerman et al., 2018). These targets were identified by whole-transcriptome analysis using scRNA-seq. However, the authors used intracellular viral mRNAs as a marker of the strength of virus replication, and the transcriptome was not directly correlated to the extracellular virus titer. Therefore, the use of our experimental procedure, in combination with scRNA-seq, may yield additional insights in future experiments.

Discovery of OP7 virus. Utilizing single-cell analysis, we discovered of a novel type of IAV-derived DIP, here referred to as "OP7 virus". More specifically, we observed a subpopulation of infected single cells that showed an exceptional behavior. We followed up on this observation, and discovered that this subpopulation of single cells was co-infected with OP7 virus. In this context, note that the discovery of cellular subpopulations is typically only possible with single-cell analysis. Instead of large internal deletions, OP7 virus contained numerous point mutations in the vRNA of S7-OP7. These mutations affected the promotor regions, encoded proteins and genome packaging signals. Upon STV co-infection, we observed an over-proportional level of S7-OP7 vRNA, both intracellularly and in the released virus population. Interestingly, the underlying principles that render OP7 virions interfering and apparently defective seem to differ from conventional DIPs. First, we believe that the predominant replication of S7-OP7 is most likely caused by the presence of the G3A/C8U "superpromotor", present on that segment. Moreover, OP7 virions lacked a large proportion of other vRNAs, which appear to constitute its defect in virus replication. The aberrant packaging of vRNA might be caused by the mutations found in the packaging signal sequence. Finally, we speculated that the mutated M1-OP7

protein may contribute to the interfering ability of OP7 virus, or even to its defect in virus replication. We did not provide proofs of our hypotheses yet; however, this might provide interesting targets for future research efforts.

OP7 virus showed strong interference with IAV replication of the PR8 strain, but also with replication of more recent strains that are relevant for human health. Specifically, we demonstrated interference against the 2009 pandemic H1N1-pdm09 strain and an H3N2 strain from 2014 (both strains were recommended as a vaccine strain by the WHO for the 2016/2017 influenza season). In addition, we showed that OP7 virus can interfere with IAV replication in two different human cells lines. Altogether, we believe that OP7 virions might be a promising candidate for antiviral therapy. Future research efforts comprise animal trials (for instance, in mice and in ferrets) and the development of cell culture-based manufacturing of OP7 virus. The STVs in the produced mixed virus population may be inactivated using UV light (Dimmock and Easton, 2014). Alternatively, the production of pure OP7 virions might be facilitated with a cell line that can complement the defect of OP7 virus replication (for instance, by the recombinant expression of the WT M1 protein). In either case, process intensification strategies (i.e., cultivation systems that allow for high-cell densities) may be utilized, like for instance approaches that include Alternating Tangential Flow (ATF) systems (Genzel et al., 2014b). For purification of OP7 virions, the use of latest downstream processing developments like steric exclusion chromatography (SEC) appear highly promising (Marichal-Gallardo et al., 2016).

Bibliography

- ABRAHAM, P. & MALIEKAL, T. T. 2017. Single cell biology beyond the era of antibodies: relevance, challenges, and promises in biomedical research. *Cell Mol Life Sci*, 74, 1177-1189.
- AKKINA, R. K., CHAMBERS, T. M. & NAYAK, D. P. 1984. Expression of defective-interfering influenza virus-specific transcripts and polypeptides in infected cells. *J Virol*, 51, 395-403.
- AKPINAR, F., INANKUR, B. & YIN, J. 2016a. Spatial-Temporal Patterns of Viral Amplification and Interference Initiated by a Single Infected Cell. *J Virol*, 90, 7552-7566.
- AKPINAR, F., TIMM, A. & YIN, J. 2016b. High-Throughput Single-Cell Kinetics of Virus Infections in the Presence of Defective Interfering Particles. *J Virol*, 90, 1599-612.
- ALBERTS, B. 2012. *Lehrbuch der Molekularen Zellbiologie*, Wiley.
- ALI, A., AVALOS, R. T., PONIMASKIN, E. & NAYAK, D. P. 2000. Influenza virus assembly: effect of influenza virus glycoproteins on the membrane association of M1 protein. *J Virol*, 74, 8709-19.
- AMAROUCHE, M. Y., EL HILALY, J. & MAZOUZI, D. 2018. AFM and FluidFM Technologies: Recent Applications in Molecular and Cellular Biology. *Scanning*, 2018, 7801274.
- AMBROSE, C. S., LEVIN, M. J. & BELSHE, R. B. 2011. The relative efficacy of trivalent live attenuated and inactivated influenza vaccines in children and adults. *Influenza Other Respir Viruses*, 5, 67-75.
- AMORIM, M. J., BRUCE, E. A., READ, E. K., FOEGLEIN, A., MAHEN, R., STUART, A. D. & DIGARD, P. 2011. A Rab11- and microtubule-dependent mechanism for cytoplasmic transport of influenza A virus viral RNA. *J Virol*, 85, 4143-56.
- ARMBRECHT, L. & DITTRICH, P. S. 2017. Recent Advances in the Analysis of Single Cells. *Anal Chem*, 89, 2-21.
- AUDSLEY, J. M. & TANNOCK, G. A. 2005. The growth of attenuated influenza vaccine donor strains in continuous cell lines. *J Virol Methods*, 123, 187-93.
- AUDSLEY, J. M. & TANNOCK, G. A. 2008. Cell-based influenza vaccines: progress to date. *Drugs*, 68, 1483-91.
- BARDIYA, N. & BAE, J. H. 2005. Influenza vaccines: recent advances in production technologies. *Appl Microbiol Biotechnol*, 67, 299-305.
- BARKER, G. & SIMMONS, N. L. 1981. Identification of two strains of cultured canine renal epithelial cells (MDCK cells) which display entirely different physiological properties. *Q J Exp Physiol*, 66, 61-72.
- BARRETT, A. D. & DIMMOCK, N. J. 1986. Defective interfering viruses and infections of animals. *Curr Top Microbiol Immunol*, 128, 55-84.
- BARRETT, P. N., MUNDT, W., KISTNER, O. & HOWARD, M. K. 2009. Vero cell platform in vaccine production: moving towards cell culture-based viral vaccines. *Expert Rev Vaccines*, 8, 607-18.
- BARRETT, P. N., PORTSMOUTH, D. & EHRlich, H. J. 2010. Developing cell culture-derived pandemic vaccines. *Curr Opin Mol Ther*, 12, 21-30.
- BAUDIN, F., PETIT, I., WEISSENHORN, W. & RUIGROK, R. W. 2001. In vitro dissection of the membrane and RNP binding activities of influenza virus M1 protein. *Virology*, 281, 102-8.
- BAUM, A. & GARCIA-SASTRE, A. 2011. Differential recognition of viral RNA by RIG-I. *Virulence*, 2, 166-9.
- BELICHA-VILLANUEVA, A., RODRIGUEZ-MADOZ, J. R., MAAMARY, J., BAUM, A., BERNAL-RUBIO, D., MINGUITO DE LA ESCALERA, M., FERNANDEZ-SESMA, A. & GARCIA-SASTRE, A. 2012. Recombinant influenza A viruses with enhanced levels of PB1 and PA viral protein expression. *J Virol*, 86, 5926-30.
- BENDALL, S. C., NOLAN, G. P., ROEDERER, M. & CHATTOPADHYAY, P. K. 2012. A deep profiler's guide to cytometry. *Trends Immunol*, 33, 323-32.
- BIJLENGA, G. & DUCLOS, P. 1989. Isolation and plaque purification of a syncytial forming component of myxoma virus. *Comp Immunol Microbiol Infect Dis*, 12, 83-9.
- BOUCROT, E. & KIRCHHAUSEN, T. 2008. Mammalian cells change volume during mitosis. *PLoS One*, 3, e1477.
- BOULO, S., AKARSU, H., RUIGROK, R. W. & BAUDIN, F. 2007. Nuclear traffic of influenza virus proteins and ribonucleoprotein complexes. *Virus Res*, 124, 12-21.

- BRANDS, R., VISSER, J., MEDEMA, J., PALACHE, A. M. & VAN SCHARRENBURG, G. J. 1999. Influvac: a safe Madin Darby Canine Kidney (MDCK) cell culture-based influenza vaccine. *Dev Biol Stand*, 98, 93-100; discussion 111.
- BREEN, M., NOGALES, A., BAKER, S. F. & MARTINEZ-SOBRIDO, L. 2016. Replication-Competent Influenza A Viruses Expressing Reporter Genes. *Viruses*, 8.
- BROOKE, C. B. 2014. Biological activities of 'noninfectious' influenza A virus particles. *Future Virol*, 9, 41-51.
- BROOKE, C. B. 2017. Population Diversity and Collective Interactions during Influenza Virus Infection. *J Virol*, 91.
- BROOKE, C. B., INCE, W. L., WEI, J., BENNINK, J. R. & YEWDELL, J. W. 2014. Influenza A virus nucleoprotein selectively decreases neuraminidase gene-segment packaging while enhancing viral fitness and transmissibility. *Proc Natl Acad Sci U S A*, 111, 16854-9.
- BROOKE, C. B., INCE, W. L., WRAMMERT, J., AHMED, R., WILSON, P. C., BENNINK, J. R. & YEWDELL, J. W. 2013. Most influenza A virions fail to express at least one essential viral protein. *J Virol*, 87, 3155-62.
- BRUNOTTE, L., FLIES, J., BOLTE, H., REUTHER, P., VREEDE, F. & SCHWEMMLE, M. 2014. The nuclear export protein of H5N1 influenza A viruses recruits Matrix 1 (M1) protein to the viral ribonucleoprotein to mediate nuclear export. *J Biol Chem*, 289, 20067-77.
- BURLEIGH, L. M., CALDER, L. J., SKEHEL, J. J. & STEINHAEUER, D. A. 2005. Influenza A viruses with mutations in the m1 helix six domain display a wide variety of morphological phenotypes. *J Virol*, 79, 1262-70.
- BURLESON, F. G., CHAMBERS, T. M. & WIEDBRAUK, D. L. 1992. Hemagglutination Assay. *Virology - A Laboratory Manual*. Academic Press.
- BURNET, F. M. 1929. A Method for the Study of Bacteriophage Multiplication in Broth. *British Journal of Experimental Pathology*, 10, 109-115.
- CALDER, L. J., WASILEWSKI, S., BERRIMAN, J. A. & ROSENTHAL, P. B. 2010. Structural organization of a filamentous influenza A virus. *Proc Natl Acad Sci U S A*, 107, 10685-90.
- CAO, S., LIU, X., YU, M., LI, J., JIA, X., BI, Y., SUN, L., GAO, G. F. & LIU, W. 2012. A nuclear export signal in the matrix protein of Influenza A virus is required for efficient virus replication. *J Virol*, 86, 4883-91.
- CARTER, M. J. & MAHY, B. W. 1982. Incomplete avian influenza virus contains a defective non-interfering component. *Arch Virol*, 71, 13-25.
- CASSIO, D. 2013. Long term culture of MDCK strains alters chromosome content. *BMC Res Notes*, 6, 162.
- CHATTOPADHYAY, P. K., GIERAHN, T. M., ROEDERER, M. & LOVE, J. C. 2014. Single-cell technologies for monitoring immune systems. *Nat Immunol*, 15, 128-35.
- CHATZIPRODROMIDOU, I. P., ARVANITIDOU, M., GUITIAN, J., APOSTOLOU, T., VANTARAKIS, G. & VANTARAKIS, A. 2018. Global avian influenza outbreaks 2010-2016: a systematic review of their distribution, avian species and virus subtype. *Syst Rev*, 7, 17.
- CHEN, B. J., LESER, G. P., MORITA, E. & LAMB, R. A. 2007. Influenza virus hemagglutinin and neuraminidase, but not the matrix protein, are required for assembly and budding of plasmid-derived virus-like particles. *J Virol*, 81, 7111-23.
- CHOU, Y. Y., VAFABAKHSH, R., DOGANAY, S., GAO, Q., HA, T. & PALESE, P. 2012. One influenza virus particle packages eight unique viral RNAs as shown by FISH analysis. *Proc Natl Acad Sci U S A*, 109, 9101-6.
- COHEN, E. M. & KOBILER, O. 2016. Gene Expression Correlates with the Number of Herpes Viral Genomes Initiating Infection in Single Cells. *PLoS Pathog*, 12, e1006082.
- COMBE, M., GARIJO, R., GELLER, R., CUEVAS, J. M. & SANJUAN, R. 2015. Single-Cell Analysis of RNA Virus Infection Identifies Multiple Genetically Diverse Viral Genomes within Single Infectious Units. *Cell Host Microbe*, 18, 424-32.

- COMPANS, R. W., CONTENT, J. & DUESBERG, P. H. 1972. Structure of the ribonucleoprotein of influenza virus. *J Virol*, 10, 795-800.
- COUCH, R. B. 2008. Seasonal inactivated influenza virus vaccines. *Vaccine*, 26 Suppl 4, D5-9.
- CROS, J. F., GARCIA-SASTRE, A. & PALESE, P. 2005. An unconventional NLS is critical for the nuclear import of the influenza A virus nucleoprotein and ribonucleoprotein. *Traffic*, 6, 205-13.
- CROS, J. F. & PALESE, P. 2003. Trafficking of viral genomic RNA into and out of the nucleus: influenza, Thogoto and Borna disease viruses. *Virus Res*, 95, 3-12.
- DAVIS, A. R., HITI, A. L. & NAYAK, D. P. 1980. Influenza defective interfering viral RNA is formed by internal deletion of genomic RNA. *Proc Natl Acad Sci U S A*, 77, 215-9.
- DAVIS, A. R. & NAYAK, D. P. 1979. Sequence relationships among defective interfering influenza viral RNAs. *Proc Natl Acad Sci U S A*, 76, 3092-6.
- DE BAETS, S., VERHELST, J., VAN DEN HOECKE, S., SMET, A., SCHOTSAERT, M., JOB, E. R., ROOSE, K., SCHEPENS, B., FIERS, W. & SAELENS, X. 2015. A GFP expressing influenza A virus to report in vivo tropism and protection by a matrix protein 2 ectodomain-specific monoclonal antibody. *PLoS One*, 10, e0121491.
- DE, B. K. & NAYAK, D. P. 1980. Defective interfering influenza viruses and host cells: establishment and maintenance of persistent influenza virus infection in MDBK and HeLa cells. *J Virol*, 36, 847-59.
- DE PAEPE, M., DE MONTE, S., ROBERT, L., LINDNER, A. B. & TADDEI, F. 2010. Emergence of variability in isogenic Escherichia coli populations infected by a filamentous virus. *PLoS One*, 5, e11823.
- DE WIT, E., BESTEBROER, T. M., SPRONKEN, M. I., RIMMELZWAAN, G. F., OSTERHAUS, A. D. & FOUCHIER, R. A. 2007. Rapid sequencing of the non-coding regions of influenza A virus. *J Virol Methods*, 139, 85-9.
- DELBRUCK, M. 1940. Statistical Fluctuations in Autocatalytic Reactions. *Journal of Chemical Physics*, 8, 120-124.
- DELBRUCK, M. 1942. Bacterial viruses (bacteriophages). *Advances in Enzymology and Related Subjects of Biochemistry*, 2, 1-32.
- DELBRUCK, M. 1945a. The Burst Size Distribution in the Growth of Bacterial Viruses (Bacteriophages). *J Bacteriol*, 50, 131-5.
- DELBRUCK, M. 1945b. The Burst Size Distribution in the Growth of Bacterial Viruses (Bacteriophages). *Journal of Bacteriology*, 50, 131-135.
- DIMMOCK, N. J., BECK, S. & MCLAIN, L. 1986. Protection of mice from lethal influenza: evidence that defective interfering virus modulates the immune response and not virus multiplication. *J Gen Virol*, 67 (Pt 5), 839-50.
- DIMMOCK, N. J., DOVE, B. K., MENG, B., SCOTT, P. D., TAYLOR, I., CHEUNG, L., HALLIS, B., MARRIOTT, A. C., CARROLL, M. W. & EASTON, A. J. 2012a. Comparison of the protection of ferrets against pandemic 2009 influenza A virus (H1N1) by 244 DI influenza virus and oseltamivir. *Antiviral Res*, 96, 376-85.
- DIMMOCK, N. J., DOVE, B. K., SCOTT, P. D., MENG, B., TAYLOR, I., CHEUNG, L., HALLIS, B., MARRIOTT, A. C., CARROLL, M. W. & EASTON, A. J. 2012b. Cloned defective interfering influenza virus protects ferrets from pandemic 2009 influenza A virus and allows protective immunity to be established. *PLoS One*, 7, e49394.
- DIMMOCK, N. J. & EASTON, A. J. 2014. Defective interfering influenza virus RNAs: time to reevaluate their clinical potential as broad-spectrum antivirals? *J Virol*, 88, 5217-27.
- DIMMOCK, N. J. & EASTON, A. J. 2015. Cloned Defective Interfering Influenza RNA and a Possible Pan-Specific Treatment of Respiratory Virus Diseases. *Viruses*, 7, 3768-88.
- DIMMOCK, N. J., RAINSFORD, E. W., SCOTT, P. D. & MARRIOTT, A. C. 2008. Influenza virus protecting RNA: an effective prophylactic and therapeutic antiviral. *J Virol*, 82, 8570-8.
- DOROSHENKO, A. & HALPERIN, S. A. 2009. Trivalent MDCK cell culture-derived influenza vaccine Optaflu (Novartis Vaccines). *Expert Rev Vaccines*, 8, 679-88.
- DUHAUT, S. D. & MCCAULEY, J. W. 1996. Defective RNAs inhibit the assembly of influenza virus genome segments in a segment-specific manner. *Virology*, 216, 326-37.

- DUKES, J. D., WHITLEY, P. & CHALMERS, A. D. 2011. The MDCK variety pack: choosing the right strain. *BMC Cell Biol*, 12, 43.
- DULBECCO, R. & VOGT, M. 1954. One-step growth curve of Western equine encephalomyelitis virus on chicken embryo cells grown in vitro and analysis of virus yields from single cells. *J Exp Med*, 99, 183-99.
- EASTON, A. J., SCOTT, P. D., EDWORTHY, N. L., MENG, B., MARRIOTT, A. C. & DIMMOCK, N. J. 2011. A novel broad-spectrum treatment for respiratory virus infections: influenza-based defective interfering virus provides protection against pneumovirus infection in vivo. *Vaccine*, 29, 2777-84.
- EISFELD, A. J., KAWAKAMI, E., WATANABE, T., NEUMANN, G. & KAWAOKA, Y. 2011. RAB11A is essential for transport of the influenza virus genome to the plasma membrane. *J Virol*, 85, 6117-26.
- EISFELD, A. J., NEUMANN, G. & KAWAOKA, Y. 2015. At the centre: influenza A virus ribonucleoproteins. *Nat Rev Microbiol*, 13, 28-41.
- ELLIS, E. L. & DELBRUCK, M. 1939. The Growth of Bacteriophage. *J Gen Physiol*, 22, 365-84.
- ELOWITZ, M. B., LEVINE, A. J., SIGGIA, E. D. & SWAIN, P. S. 2002. Stochastic gene expression in a single cell. *Science*, 297, 1183-6.
- ELTON, D., DIGARD, P., TILEY, L. & ORTIN, J. 2006. Structure and function of the influenza virus RNP. In: KAWAOKA, Y. (ed.) *Influenza Virology: Current Topics*. Hethersett, United Kingdom: Caister Academic Press.
- FENG, S. Z., JIAO, P. R., QI, W. B., FAN, H. Y. & LIAO, M. 2011. Development and strategies of cell-culture technology for influenza vaccine. *Appl Microbiol Biotechnol*, 89, 893-902.
- FISCHETTI, V. A., BARRON, B. & ZABRISKIE, J. B. 1968. Studies on streptococcal bacteriophages. I. Burst size and intracellular growth of group A and group C streptococcal bacteriophages. *J Exp Med*, 127, 475-88.
- FLICK, R., NEUMANN, G., HOFFMANN, E., NEUMEIER, E. & HOBOM, G. 1996. Promoter elements in the influenza vRNA terminal structure. *RNA*, 2, 1046-57.
- FODOR, E. 2013. The RNA polymerase of influenza a virus: mechanisms of viral transcription and replication. *Acta Virol*, 57, 113-22.
- FRENSING, T. 2015. Defective interfering viruses and their impact on vaccines and viral vectors. *Biotechnol J*, 10, 681-9.
- FRENSING, T., HELDT, F. S., PFLUGMACHER, A., BEHRENDT, I., JORDAN, I., FLOCKERZI, D., GENZEL, Y. & REICHL, U. 2013. Continuous influenza virus production in cell culture shows a periodic accumulation of defective interfering particles. *PLoS One*, 8, e72288.
- FRENSING, T., KUPKE, S. Y., BACHMANN, M., FRITZSCHE, S., GALLO-RAMIREZ, L. E. & REICHL, U. 2016. Influenza virus intracellular replication dynamics, release kinetics, and particle morphology during propagation in MDCK cells. *Appl Microbiol Biotechnol*, 100, 7181-92.
- FRENSING, T., PFLUGMACHER, A., BACHMANN, M., PESCHEL, B. & REICHL, U. 2014. Impact of defective interfering particles on virus replication and antiviral host response in cell culture-based influenza vaccine production. *Appl Microbiol Biotechnol*, 98, 8999-9008.
- FRITZSCH, F. S., DUSNY, C., FRICK, O. & SCHMID, A. 2012. Single-cell analysis in biotechnology, systems biology, and biocatalysis. *Annu Rev Chem Biomol Eng*, 3, 129-55.
- FUJII, Y., GOTO, H., WATANABE, T., YOSHIDA, T. & KAWAOKA, Y. 2003. Selective incorporation of influenza virus RNA segments into virions. *Proc Natl Acad Sci U S A*, 100, 2002-7.
- FULVINI, A. A., RAMANUNNINAIR, M., LE, J., POKORNY, B. A., ARROYO, J. M., SILVERMAN, J., DEVIS, R. & BUCHER, D. 2011. Gene constellation of influenza A virus reassortants with high growth phenotype prepared as seed candidates for vaccine production. *PLoS One*, 6, e20823.
- GALLO-RAMIREZ, L. E., NIKOLAY, A., GENZEL, Y. & REICHL, U. 2015. Bioreactor concepts for cell culture-based viral vaccine production. *Expert Rev Vaccines*, 14, 1181-95.
- GAUSH, C. R., HARD, W. L. & SMITH, T. F. 1966. Characterization of an established line of canine kidney cells (MDCK). *Proc Soc Exp Biol Med*, 122, 931-5.

- GAUSH, C. R. & SMITH, T. F. 1968. Replication and plaque assay of influenza virus in an established line of canine kidney cells. *Appl Microbiol*, 16, 588-94.
- GENZEL, Y., BEHRENDT, I., KONIG, S., SANN, H. & REICHL, U. 2004. Metabolism of MDCK cells during cell growth and influenza virus production in large-scale microcarrier culture. *Vaccine*, 22, 2202-8.
- GENZEL, Y., DIETZSCH, C., RAPP, E., SCHWARZER, J. & REICHL, U. 2010. MDCK and Vero cells for influenza virus vaccine production: a one-to-one comparison up to lab-scale bioreactor cultivation. *Appl Microbiol Biotechnol*, 88, 461-75.
- GENZEL, Y., FISCHER, M. & REICHL, U. 2006. Serum-free influenza virus production avoiding washing steps and medium exchange in large-scale microcarrier culture. *Vaccine*, 24, 3261-72.
- GENZEL, Y. & REICHL, U. 2007. Vaccine production - state of the art and future needs in upstream processing. In: PÖRTNER, R. (ed.) *Methods in biotechnology: animal cell biotechnology*. Totowa, NJ: Humana Press Inc.
- GENZEL, Y. & REICHL, U. 2009. Continuous cell lines as a production system for influenza vaccines. *Expert Rev Vaccines*, 8, 1681-92.
- GENZEL, Y., RODIG, J., RAPP, E. & REICHL, U. 2014a. Vaccine production: upstream processing with adherent or suspension cell lines. *Methods Mol Biol*, 1104, 371-93.
- GENZEL, Y., VOGEL, T., BUCK, J., BEHRENDT, I., RAMIREZ, D. V., SCHIEDNER, G., JORDAN, I. & REICHL, U. 2014b. High cell density cultivations by alternating tangential flow (ATF) perfusion for influenza A virus production using suspension cells. *Vaccine*, 32, 2770-81.
- GIACHETTI, C. & HOLLAND, J. J. 1989. Vesicular stomatitis virus and its defective interfering particles exhibit in vitro transcriptional and replicative competition for purified L-NS polymerase molecules. *Virology*, 170, 264-7.
- GOTO, H., MURAMOTO, Y., NODA, T. & KAWAOKA, Y. 2013. The genome-packaging signal of the influenza A virus genome comprises a genome incorporation signal and a genome-bundling signal. *J Virol*, 87, 11316-22.
- GROHSKOPF, L. A., SOKOLOW, L. Z., BRODER, K. R., WALTER, E. B., FRY, A. M. & JERNIGAN, D. B. 2018. Prevention and Control of Seasonal Influenza with Vaccines: Recommendations of the Advisory Committee on Immunization Practices-United States, 2018-19 Influenza Season. *MMWR Recomm Rep*, 67, 1-20.
- GROSS, A., SCHOENDUBE, J., ZIMMERMANN, S., STEEB, M., ZENGERLE, R. & KOLTAY, P. 2015. Technologies for Single-Cell Isolation. *Int J Mol Sci*, 16, 16897-919.
- GUILLAUME-GENTIL, O., POTTHOFF, E., OSSOLA, D., FRANZ, C. M., ZAMBELLI, T. & VORHOLT, J. A. 2014. Force-controlled manipulation of single cells: from AFM to FluidFM. *Trends Biotechnol*, 32, 381-8.
- GUO, F., LI, S., CAGLAR, M. U., MAO, Z., LIU, W., WOODMAN, A., ARNOLD, J. J., WILKE, C. O., HUANG, T. J. & CAMERON, C. E. 2017. Single-Cell Virology: On-Chip Investigation of Viral Infection Dynamics. *Cell Rep*, 21, 1692-1704.
- GUO, M. T., ROTEM, A., HEYMAN, J. A. & WEITZ, D. A. 2012. Droplet microfluidics for high-throughput biological assays. *Lab Chip*, 12, 2146-55.
- HALPERIN, S. A., NESTRUCK, A. C. & EASTWOOD, B. J. 1998. Safety and immunogenicity of a new influenza vaccine grown in mammalian cell culture. *Vaccine*, 16, 1331-5.
- HAMPSON, A. W. & MACKENZIE, J. S. 2006. The influenza viruses. *Med J Aust*, 185, S39-43.
- HANNOUN, C. 2013. The evolving history of influenza viruses and influenza vaccines. *Expert Rev Vaccines*, 12, 1085-94.
- HARRIS, A., CARDONE, G., WINKLER, D. C., HEYMANN, J. B., BRECHER, M., WHITE, J. M. & STEVEN, A. C. 2006. Influenza virus pleiomorphy characterized by cryoelectron tomography. *Proc Natl Acad Sci U S A*, 103, 19123-7.
- HEATH, J. R., RIBAS, A. & MISCHEL, P. S. 2016. Single-cell analysis tools for drug discovery and development. *Nat Rev Drug Discov*, 15, 204-16.
- HELDT, F. S., KUPKE, S. Y., DORL, S., REICHL, U. & FRENSING, T. 2015. Single-cell analysis and stochastic modelling unveil large cell-to-cell variability in influenza A virus infection. *Nat Commun*, 6, 8938.

- HENLE, W. & HENLE, G. 1943. Interference of Inactive Virus with the Propagation of Virus of Influenza. *Science*, 98, 87-9.
- HOFFMANN, E., NEUMANN, G., KAWAOKA, Y., HOBOM, G. & WEBSTER, R. G. 2000. A DNA transfection system for generation of influenza A virus from eight plasmids. *Proc Natl Acad Sci U S A*, 97, 6108-13.
- HOLLAND, J. J. 1987. Defective interfering rhabdoviruses. In: WAGNER, R. R. (ed.) *The Rhabdoviruses*. New York: Springer Science+Business Media.
- HOLLAND, J. J. & VILLARREAL, L. P. 1975. Purification of defective interfering T particles of vesicular stomatitis and rabies viruses generated in vivo in brains of newborn mice. *Virology*, 67, 438-49.
- HU, J., SEALFON, S. C., HAYOT, F., JAYAPRAKASH, C., KUMAR, M., PENDLETON, A. C., GANEE, A., FERNANDEZ-SESMA, A., MORAN, T. M. & WETMUR, J. G. 2007. Chromosome-specific and noisy IFN β 1 transcription in individual virus-infected human primary dendritic cells. *Nucleic Acids Res*, 35, 5232-41.
- HU, P., ZHANG, W., XIN, H. & DENG, G. 2016. Single Cell Isolation and Analysis. *Front Cell Dev Biol*, 4, 116.
- HUANG, A. S. 1973. Defective interfering viruses. *Annu Rev Microbiol*, 27, 101-17.
- HUANG, A. S. & BALTIMORE, D. 1970. Defective viral particles and viral disease processes. *Nature*, 226, 325-7.
- HUTCHINSON, E. C., CURRAN, M. D., READ, E. K., GOG, J. R. & DIGARD, P. 2008. Mutational analysis of cis-acting RNA signals in segment 7 of influenza A virus. *J Virol*, 82, 11869-79.
- HUTCHINSON, E. C. & FODOR, E. 2012. Nuclear import of the influenza A virus transcriptional machinery. *Vaccine*, 30, 7353-8.
- HUTCHINSON, E. C. & FODOR, E. 2013. Transport of the influenza virus genome from nucleus to nucleus. *Viruses*, 5, 2424-46.
- HUTCHINSON, E. C., VON KIRCHBACH, J. C., GOG, J. R. & DIGARD, P. 2010. Genome packaging in influenza A virus. *J Gen Virol*, 91, 313-28.
- IBRICEVIC, A., PEKOSZ, A., WALTER, M. J., NEWBY, C., BATTAILLE, J. T., BROWN, E. G., HOLTZMAN, M. J. & BRODY, S. L. 2006. Influenza virus receptor specificity and cell tropism in mouse and human airway epithelial cells. *J Virol*, 80, 7469-80.
- IWATSUKI-HORIMOTO, K., HORIMOTO, T., NODA, T., KISO, M., MAEDA, J., WATANABE, S., MURAMOTO, Y., FUJII, K. & KAWAOKA, Y. 2006. The cytoplasmic tail of the influenza A virus M2 protein plays a role in viral assembly. *J Virol*, 80, 5233-40.
- JANDA, J. M. & NAYAK, D. P. 1979. Defective influenza viral ribonucleoproteins cause interference. *J Virol*, 32, 697-702.
- JENNINGS, P. A., FINCH, J. T., WINTER, G. & ROBERTSON, J. S. 1983. Does the higher order structure of the influenza virus ribonucleoprotein guide sequence rearrangements in influenza viral RNA? *Cell*, 34, 619-27.
- JORBA, N., COLOMA, R. & ORTIN, J. 2009. Genetic trans-complementation establishes a new model for influenza virus RNA transcription and replication. *PLoS Pathog*, 5, e1000462.
- KALBFUSS, B., KNOCHLEIN, A., KROBER, T. & REICHL, U. 2008. Monitoring influenza virus content in vaccine production: precise assays for the quantitation of hemagglutination and neuraminidase activity. *Biologicals*, 36, 145-61.
- KALISKY, T., BLAINEY, P. & QUAKE, S. R. 2011. Genomic analysis at the single-cell level. *Annu Rev Genet*, 45, 431-45.
- KAMINSKI, T. S., SCHELER, O. & GARSTECKI, P. 2016. Droplet microfluidics for microbiology: techniques, applications and challenges. *Lab Chip*, 16, 2168-87.
- KANTER, I. & KALISKY, T. 2015. Single cell transcriptomics: methods and applications. *Front Oncol*, 5, 53.
- KARLSSON HEDESTAM, G. B., FOUCHIER, R. A., PHOGAT, S., BURTON, D. R., SODROSKI, J. & WYATT, R. T. 2008. The challenges of eliciting neutralizing antibodies to HIV-1 and to influenza virus. *Nat Rev Microbiol*, 6, 143-55.

- KAWAKAMI, E., WATANABE, T., FUJII, K., GOTO, H., WATANABE, S., NODA, T. & KAWAOKA, Y. 2011. Strand-specific real-time RT-PCR for distinguishing influenza vRNA, cRNA, and mRNA. *J Virol Methods*, 173, 1-6.
- KELSEY, G., STEGLE, O. & REIK, W. 2017. Single-cell epigenomics: Recording the past and predicting the future. *Science*, 358, 69-75.
- KILBOURNE, E. D. 1969. Future influenza vaccines and the use of genetic recombinants. *Bull World Health Organ*, 41, 643-5.
- KILLIP, M. J., JACKSON, D., PEREZ-CIDONCHA, M., FODOR, E. & RANDALL, R. E. 2017. Single-cell studies of IFN-beta promoter activation by wild-type and NS1-defective influenza A viruses. *J Gen Virol*, 98, 357-363.
- KILLIP, M. J., YOUNG, D. F., GATHERER, D., ROSS, C. S., SHORT, J. A., DAVISON, A. J., GOODBOURN, S. & RANDALL, R. E. 2013. Deep sequencing analysis of defective genomes of parainfluenza virus 5 and their role in interferon induction. *J Virol*, 87, 4798-807.
- KIRZNER, S., BARAK, E. & LINDELL, D. 2016. Variability in progeny production and virulence of cyanophages determined at the single-cell level. *Environ Microbiol Rep*, 8, 605-613.
- KISTNER, O., BARRETT, P. N., MUNDT, W., REITER, M., SCHÖBER-BENDIXEN, S. & DÖRNER, F. 1998. Development of a mammalian cell (Vero) derived candidate influenza virus vaccine. *Vaccine*, 16, 960-8.
- KITTEL, C., SEREINIG, S., FERKO, B., STASAKOVA, J., ROMANOVA, J., WOLKERSTORFER, A., KATINGER, H. & EGOROV, A. 2004. Rescue of influenza virus expressing GFP from the NS1 reading frame. *Virology*, 324, 67-73.
- KLEIN, A. M., MAZUTIS, L., AKARTUNA, I., TALLAPRAGADA, N., VERES, A., LI, V., PESHKIN, L., WEITZ, D. A. & KIRSCHNER, M. W. 2015. Droplet barcoding for single-cell transcriptomics applied to embryonic stem cells. *Cell*, 161, 1187-1201.
- KOCH, A. L. 1966. The logarithm in biology. 1. Mechanisms generating the log-normal distribution exactly. *J Theor Biol*, 12, 276-90.
- KUPKE, S. Y., RIEDEL, D., FRENSING, T., ZMORA, P. & REICHL, U. 2018. A novel type of influenza A virus-derived defective interfering particle with nucleotide substitutions in its genome. *Journal of Virology*, JVI.01786-18.
- LAMB, R. A. & KRUG, R. M. 2001. Orthomyxoviridae: the viruses and their replication. In: KNIPE, D. M. & HOWLEY, P. M. (eds.) *Fields virology*. Philadelphia: Lippincott Williams & Wilkins.
- LASKE, T., HELDT, F. S., HOFFMANN, H., FRENSING, T. & REICHL, U. 2016. Modeling the intracellular replication of influenza A virus in the presence of defective interfering RNAs. *Virus Res*, 213, 90-99.
- LAURING, A. S. & ANDINO, R. 2010. Quasispecies theory and the behavior of RNA viruses. *PLoS Pathog*, 6, e1001005.
- LAVER, W. G. & DOWNIE, J. C. 1976. Influenza virus recombination. I. Matrix protein markers and segregation during mixed infections. *Virology*, 70, 105-17.
- LAWSON, D. A., BHAKTA, N. R., KESSENBROCK, K., PRUMMEL, K. D., YU, Y., TAKAI, K., ZHOU, A., EYOB, H., BALAKRISHNAN, S., WANG, C. Y., YASWEN, P., GOGA, A. & WERB, Z. 2015. Single-cell analysis reveals a stem-cell program in human metastatic breast cancer cells. *Nature*, 526, 131-5.
- LAZZARINI, R. A., KEENE, J. D. & SCHUBERT, M. 1981. The origins of defective interfering particles of the negative-strand RNA viruses. *Cell*, 26, 145-54.
- LEE, D. H., BERTRAN, K., KWON, J. H. & SWAYNE, D. E. 2017. Evolution, global spread, and pathogenicity of highly pathogenic avian influenza H5Nx clade 2.3.4.4. *J Vet Sci*, 18, 269-280.
- LEE, M. K., BAE, S. H., PARK, C. J., CHEONG, H. K., CHEONG, C. & CHOI, B. S. 2003. A single-nucleotide natural variation (U4 to C4) in an influenza A virus promoter exhibits a large structural change: implications for differential viral RNA synthesis by RNA-dependent RNA polymerase. *Nucleic Acids Res*, 31, 1216-23.
- LEE, M. S. & HU, A. Y. 2012. A cell-based backup to speed up pandemic influenza vaccine production. *Trends Microbiol*, 20, 103-5.

- LEIN, E., BORM, L. E. & LINNARSSON, S. 2017. The promise of spatial transcriptomics for neuroscience in the era of molecular cell typing. *Science*, 358, 64-69.
- LESER, G. P. & LAMB, R. A. 2005. Influenza virus assembly and budding in raft-derived microdomains: a quantitative analysis of the surface distribution of HA, NA and M2 proteins. *Virology*, 342, 215-27.
- LEUPELT, A. 2017. *Clonal heterogeneity of the MDCK cell population: Effect on cell-to-cell variability in influenza A virus replication*. Master Thesis, Anhalt University of Applied Sciences.
- LEVY, E. & SLAVOV, N. 2018. Single cell protein analysis for systems biology. *Essays Biochem*, 62, 595-605.
- LI, I. W., CHAN, K. H., TO, K. W., WONG, S. S., HO, P. L., LAU, S. K., WOO, P. C., TSOI, H. W., CHAN, J. F., CHENG, V. C., ZHENG, B. J., CHEN, H. & YUEN, K. Y. 2009. Differential susceptibility of different cell lines to swine-origin influenza A H1N1, seasonal human influenza A H1N1, and avian influenza A H5N1 viruses. *J Clin Virol*, 46, 325-30.
- LIAO, L. E., IWAMI, S. & BEAUCHEMIN, C. A. 2016. (In)validating experimentally derived knowledge about influenza A defective interfering particles. *J R Soc Interface*, 13.
- LINNARSSON, S. & TEICHMANN, S. A. 2016. Single-cell genomics: coming of age. *Genome Biol*, 17, 97.
- LIU, J., MANI, S., SCHWARTZ, R., RICHMAN, L. & TABOR, D. E. 2010. Cloning and assessment of tumorigenicity and oncogenicity of a Madin-Darby canine kidney (MDCK) cell line for influenza vaccine production. *Vaccine*, 28, 1285-93.
- LIU, J., SHI, X., SCHWARTZ, R. & KEMBLE, G. 2009. Use of MDCK cells for production of live attenuated influenza vaccine. *Vaccine*, 27, 6460-3.
- LIU, Z., WANG, L., WELCH, J. D., MA, H., ZHOU, Y., VASEGHI, H. R., YU, S., WALL, J. B., ALIMOHAMADI, S., ZHENG, M., YIN, C., SHEN, W., PRINS, J. F., LIU, J. & QIAN, L. 2017. Single-cell transcriptomics reconstructs fate conversion from fibroblast to cardiomyocyte. *Nature*, 551, 100-104.
- LOHR, V., GENZEL, Y., JORDAN, I., KATINGER, D., MAHR, S., SANDIG, V. & REICHL, U. 2012. Live attenuated influenza viruses produced in a suspension process with avian AGE1.CR.pIX cells. *BMC Biotechnol*, 12, 79.
- LOHR, V., RATH, A., GENZEL, Y., JORDAN, I., SANDIG, V. & REICHL, U. 2009. New avian suspension cell lines provide production of influenza virus and MVA in serum-free media: studies on growth, metabolism and virus propagation. *Vaccine*, 27, 4975-82.
- LOPEZ, C. B. 2014. Defective viral genomes: critical danger signals of viral infections. *J Virol*, 88, 8720-3.
- LUGOVITSEV, V. Y., MELNYK, D. & WEIR, J. P. 2013. Heterogeneity of the MDCK cell line and its applicability for influenza virus research. *PLoS One*, 8, e75014.
- MA, M. J., YANG, Y. & FANG, L. Q. 2019. Highly Pathogenic Avian H7N9 Influenza Viruses: Recent Challenges. *Trends Microbiol*, 27, 93-95.
- MAAMARY, J., PICA, N., BELICHA-VILLANUEVA, A., CHOU, Y. Y., KRAMMER, F., GAO, Q., GARCIA-SASTRE, A. & PALESE, P. 2012. Attenuated influenza virus construct with enhanced hemagglutinin protein expression. *J Virol*, 86, 5782-90.
- MACOSKO, E. Z., BASU, A., SATIJA, R., NEMESH, J., SHEKHAR, K., GOLDMAN, M., TIROSH, I., BIALAS, A. R., KAMITAKI, N., MARTERSTECK, E. M., TROMBETTA, J. J., WEITZ, D. A., SANES, J. R., SHALEK, A. K., REGEV, A. & MCCARROLL, S. A. 2015. Highly Parallel Genome-wide Expression Profiling of Individual Cells Using Nanoliter Droplets. *Cell*, 161, 1202-1214.
- MANICASSAMY, B., MANICASSAMY, S., BELICHA-VILLANUEVA, A., PISANELLI, G., PULENDRAN, B. & GARCIA-SASTRE, A. 2010. Analysis of in vivo dynamics of influenza virus infection in mice using a GFP reporter virus. *Proc Natl Acad Sci U S A*, 107, 11531-6.
- MARCUS, P. I., NGUNJIRI, J. M. & SEKELICK, M. J. 2009. Dynamics of biologically active subpopulations of influenza virus: plaque-forming, noninfectious cell-killing, and defective interfering particles. *J Virol*, 83, 8122-30.
- MARICHAL-GALLARDO, P., PIELER, M. M., WOLFF, M. W. & REICHL, U. 2016. Steric exclusion chromatography for purification of cell culture-derived influenza A virus using regenerated cellulose membranes and polyethylene glycol. *J Chromatogr A*.

- MARRIOTT, A. C. & DIMMOCK, N. J. 2010. Defective interfering viruses and their potential as antiviral agents. *Rev Med Virol*, 20, 51-62.
- MATLIN, K. S., REGGIO, H., HELENIUS, A. & SIMONS, K. 1981. Infectious entry pathway of influenza virus in a canine kidney cell line. *J Cell Biol*, 91, 601-13.
- MCKIMM-BRESCHKIN, J. L. 2013. Influenza neuraminidase inhibitors: antiviral action and mechanisms of resistance. *Influenza Other Respir Viruses*, 7 Suppl 1, 25-36.
- MCWILLIAM LEITCH, E. C. & MCLAUCHLAN, J. 2013. Determining the cellular diversity of hepatitis C virus quasispecies by single-cell viral sequencing. *J Virol*, 87, 12648-55.
- MEISTER, A., GABI, M., BEHR, P., STUDER, P., VOROS, J., NIEDERMANN, P., BITTERLI, J., POLESEL-MARIS, J., LILEY, M., HEINZELMANN, H. & ZAMBELLI, T. 2009. FluidFM: combining atomic force microscopy and nanofluidics in a universal liquid delivery system for single cell applications and beyond. *Nano Lett*, 9, 2501-7.
- MILIAN, E. & KAMEN, A. A. 2015. Current and emerging cell culture manufacturing technologies for influenza vaccines. *Biomed Res Int*, 2015, 504831.
- MIYAMOTO, D. T., LEE, R. J., STOTT, S. L., TING, D. T., WITTNER, B. S., ULMAN, M., SMAS, M. E., LORD, J. B., BRANNIGAN, B. W., TRAUTWEIN, J., BANDER, N. H., WU, C. L., SEQUIST, L. V., SMITH, M. R., RAMASWAMY, S., TONER, M., MAHESWARAN, S. & HABER, D. A. 2012. Androgen receptor signaling in circulating tumor cells as a marker of hormonally responsive prostate cancer. *Cancer Discov*, 2, 995-1003.
- MOELLER, A., KIRCHDOERFER, R. N., POTTER, C. S., CARRAGHER, B. & WILSON, I. A. 2012. Organization of the influenza virus replication machinery. *Science*, 338, 1631-4.
- MOMOSE, F., KIKUCHI, Y., KOMASE, K. & MORIKAWA, Y. 2007. Visualization of microtubule-mediated transport of influenza viral progeny ribonucleoprotein. *Microbes Infect*, 9, 1422-33.
- MORESCO, K. A., STALLKNECHT, D. E. & SWAYNE, D. E. 2010. Evaluation and attempted optimization of avian embryos and cell culture methods for efficient isolation and propagation of low pathogenicity avian influenza viruses. *Avian Dis*, 54, 622-6.
- MOSS, R. B., DAVEY, R. T., STEIGBIGEL, R. T. & FANG, F. 2010. Targeting pandemic influenza: a primer on influenza antivirals and drug resistance. *J Antimicrob Chemother*, 65, 1086-93.
- MURATA, H., MACAULEY, J., LEWIS, A. M., JR. & PEDEN, K. 2011. Plaque purification as a method to mitigate the risk of adventitious-agent contamination in influenza vaccine virus seeds. *Vaccine*, 29, 3155-61.
- MURPHY, T. W., ZHANG, Q., NALER, L. B., MA, S. & LU, C. 2017. Recent advances in the use of microfluidic technologies for single cell analysis. *Analyst*, 143, 60-80.
- NAKAJIMA, K. & SUGIURA, A. 1977. Three-factor cross of influenza virus. *Virology*, 81, 486-9.
- NAKATSU, S., SAGARA, H., SAKAI-TAGAWA, Y., SUGAYA, N., NODA, T. & KAWAOKA, Y. 2016. Complete and Incomplete Genome Packaging of Influenza A and B Viruses. *MBio*, 7.
- NAKAZATO, Y., SUZUKI, H. & SARUTA, T. 1989. Characterization of subclones of Madin-Darby canine kidney renal epithelial cell line. *Biochim Biophys Acta*, 1014, 57-65.
- NAVIN, N. & HICKS, J. 2011. Future medical applications of single-cell sequencing in cancer. *Genome Med*, 3, 31.
- NAYAK, D. P., CHAMBERS, T. M. & AKKINA, R. K. 1985. Defective-interfering (DI) RNAs of influenza viruses: origin, structure, expression, and interference. *Curr Top Microbiol Immunol*, 114, 103-51.
- NAYAK, D. P., HUI, E. K. & BARMAN, S. 2004. Assembly and budding of influenza virus. *Virus Res*, 106, 147-65.
- NAYAK, D. P., TOBITA, K., JANDA, J. M., DAVIS, A. R. & DE, B. K. 1978. Homologous interference mediated by defective interfering influenza virus derived from a temperature-sensitive mutant of influenza virus. *J Virol*, 28, 375-86.
- NEUMANN, G. & HOBOM, G. 1995. Mutational analysis of influenza virus promoter elements in vivo. *J Gen Virol*, 76 (Pt 7), 1709-17.

- NICOLSON, C., MAJOR, D., WOOD, J. M. & ROBERTSON, J. S. 2005. Generation of influenza vaccine viruses on Vero cells by reverse genetics: an H5N1 candidate vaccine strain produced under a quality system. *Vaccine*, 23, 2943-52.
- NOBLE, S., MCLAIN, L. & DIMMOCK, N. J. 2004. Interfering vaccine: a novel antiviral that converts a potentially virulent infection into one that is subclinical and immunizing. *Vaccine*, 22, 3018-25.
- NODA, T. & KAWAOKA, Y. 2010. Structure of influenza virus ribonucleoprotein complexes and their packaging into virions. *Rev Med Virol*, 20, 380-91.
- NODA, T. & KAWAOKA, Y. 2012. Packaging of influenza virus genome: robustness of selection. *Proc Natl Acad Sci U S A*, 109, 8797-8.
- NODA, T., MURAKAMI, S., NAKATSU, S., IMAI, H., MURAMOTO, Y., SHINDO, K., SAGARA, H. & KAWAOKA, Y. 2018. Importance of the 1+7 configuration of ribonucleoprotein complexes for influenza A virus genome packaging. *Nat Commun*, 9, 54.
- NODA, T., SAGARA, H., YEN, A., TAKADA, A., KIDA, H., CHENG, R. H. & KAWAOKA, Y. 2006. Architecture of ribonucleoprotein complexes in influenza A virus particles. *Nature*, 439, 490-2.
- NOH, J. Y. & KIM, W. J. 2013. Influenza vaccines: unmet needs and recent developments. *Infect Chemother*, 45, 375-86.
- NOTTON, T., SARDANYES, J., WEINBERGER, A. D. & WEINBERGER, L. S. 2014. The case for transmissible antivirals to control population-wide infectious disease. *Trends Biotechnol*, 32, 400-5.
- O'NEILL, R. E., JASKUNAS, R., BLOBEL, G., PALESE, P. & MOROIANU, J. 1995. Nuclear import of influenza virus RNA can be mediated by viral nucleoprotein and transport factors required for protein import. *J Biol Chem*, 270, 22701-4.
- ODAGIRI, T. & TASHIRO, M. 1997. Segment-specific noncoding sequences of the influenza virus genome RNA are involved in the specific competition between defective interfering RNA and its progenitor RNA segment at the virion assembly step. *J Virol*, 71, 2138-45.
- OLSEN, L. R., LEIPOLD, M. D., PEDERSEN, C. B. & MAECKER, H. T. 2018. The anatomy of single cell mass cytometry data. *Cytometry A*.
- ONIONS, D., EGAN, W., JARRETT, R., NOVICKI, D. & GREGERSEN, J. P. 2010. Validation of the safety of MDCK cells as a substrate for the production of a cell-derived influenza vaccine. *Biologicals*, 38, 544-51.
- OSTERHAUS, A., FOUCHIER, R. & RIMMELZWAAN, G. 2011. Towards universal influenza vaccines? *Philos Trans R Soc Lond B Biol Sci*, 366, 2766-73.
- OZAWA, M., MAEDA, J., IWATSUKI-HORIMOTO, K., WATANABE, S., GOTO, H., HORIMOTO, T. & KAWAOKA, Y. 2009. Nucleotide sequence requirements at the 5' end of the influenza A virus M RNA segment for efficient virus replication. *J Virol*, 83, 3384-8.
- PALACHE, A. M., BRANDS, R. & VAN SCHARRENBURG, G. J. 1997. Immunogenicity and reactogenicity of influenza subunit vaccines produced in MDCK cells or fertilized chicken eggs. *J Infect Dis*, 176 Suppl 1, S20-3.
- PALESE, P., ZAVALA, F., MUSTER, T., NUSSENZWEIG, R. S. & GARCIA-SASTRE, A. 1997. Development of novel influenza virus vaccines and vectors. *J Infect Dis*, 176 Suppl 1, S45-9.
- PARTRIDGE, J., KIENY, M. P. & WORLD HEALTH ORGANIZATION, H. N. I. V. T. F. 2010. Global production of seasonal and pandemic (H1N1) influenza vaccines in 2009-2010 and comparison with previous estimates and global action plan targets. *Vaccine*, 28, 4709-12.
- PATERSON, D. & FODOR, E. 2012. Emerging roles for the influenza A virus nuclear export protein (NEP). *PLoS Pathog*, 8, e1003019.
- PATIL, S., FRIBOURG, M., GE, Y., BATISH, M., TYAGI, S., HAYOT, F. & SEALFON, S. C. 2015. Single-cell analysis shows that paracrine signaling by first responder cells shapes the interferon-beta response to viral infection. *Sci Signal*, 8, ra16.
- PAU, M. G., OPHORST, C., KOLDIJK, M. H., SCHOUTEN, G., MEHTALI, M. & UYTDEHAAG, F. 2001. The human cell line PER.C6 provides a new manufacturing system for the production of influenza vaccines. *Vaccine*, 19, 2716-21.

- PAUL GLEZEN, W., SCHMIER, J. K., KUEHN, C. M., RYAN, K. J. & OXFORD, J. 2013. The burden of influenza B: a structured literature review. *Am J Public Health*, 103, e43-51.
- PERDUE, M. L., ARNOLD, F., LI, S., DONABEDIAN, A., CIOCE, V., WARF, T. & HUEBNER, R. 2011. The future of cell culture-based influenza vaccine production. *Expert Rev Vaccines*, 10, 1183-94.
- PEREZ, D. R. & DONIS, R. O. 1998. The matrix 1 protein of influenza A virus inhibits the transcriptase activity of a model influenza reporter genome in vivo. *Virology*, 249, 52-61.
- PERRAULT, J. 1981. Origin and replication of defective interfering particles. *Curr Top Microbiol Immunol*, 93, 151-207.
- PERRY, R. P. 2007. Balanced production of ribosomal proteins. *Gene*, 401, 1-3.
- POON, L. L., PRITLOVE, D. C., FODOR, E. & BROWNLEE, G. G. 1999. Direct evidence that the poly(A) tail of influenza A virus mRNA is synthesized by reiterative copying of a U track in the virion RNA template. *J Virol*, 73, 3473-6.
- PRAKADAN, S. M., SHALEK, A. K. & WEITZ, D. A. 2017. Scaling by shrinking: empowering single-cell 'omics' with microfluidic devices. *Nat Rev Genet*, 18, 345-361.
- PRICE, P. M., REICHELDERFER, C. F., JOHANSSON, B. E., KILBOURNE, E. D. & ACS, G. 1989. Complementation of recombinant baculoviruses by coinfection with wild-type virus facilitates production in insect larvae of antigenic proteins of hepatitis B virus and influenza virus. *Proc Natl Acad Sci U S A*, 86, 1453-6.
- PROSERPIO, V. & LONNBERG, T. 2016. Single-cell technologies are revolutionizing the approach to rare cells. *Immunol Cell Biol*, 94, 225-9.
- RAJ, A., PESKIN, C. S., TRANCHINA, D., VARGAS, D. Y. & TYAGI, S. 2006. Stochastic mRNA synthesis in mammalian cells. *PLoS Biol*, 4, e309.
- RAJ, A. & VAN OUDENAARDEN, A. 2008. Nature, nurture, or chance: stochastic gene expression and its consequences. *Cell*, 135, 216-26.
- RAMALINGAM, N., FOWLER, B., SZPANKOWSKI, L., LEYRAT, A. A., HUKARI, K., MAUNG, M. T., YORZA, W., NORRIS, M., CESAR, C., SHUGA, J., GONZALES, M. L., SANADA, C. D., WANG, X., YEUNG, R., HWANG, W., AXSOM, J., DEVARAJU, N. S., ANGELES, N. D., GREENE, C., ZHOU, M. F., ONG, E. S., POH, C. C., LAM, M., CHOI, H., HTOO, Z., LEE, L., CHIN, C. S., SHEN, Z. W., LU, C. T., HOLCOMB, I., OOI, A., STOLARCZYK, C., SHUGA, T., LIVAK, K. J., LARSEN, C., UNGER, M. & WEST, J. A. 2016. Fluidic Logic Used in a Systems Approach to Enable Integrated Single-Cell Functional Analysis. *Front Bioeng Biotechnol*, 4, 70.
- RAND, U., RINAS, M., SCHWERK, J., NOHREN, G., LINNES, M., KROGER, A., FLOSSDORF, M., KALY-KULLAI, K., HAUSER, H., HOFER, T. & KOSTER, M. 2012. Multi-layered stochasticity and paracrine signal propagation shape the type-I interferon response. *Mol Syst Biol*, 8, 584.
- RASER, J. M. & O'SHEA, E. K. 2004. Control of stochasticity in eukaryotic gene expression. *Science*, 304, 1811-4.
- REED, C., MELTZER, M. I., FINELLI, L. & FIORE, A. 2012. Public health impact of including two lineages of influenza B in a quadrivalent seasonal influenza vaccine. *Vaccine*, 30, 1993-8.
- REHWINKEL, J., TAN, C. P., GOUBAU, D., SCHULZ, O., PICHLMAIR, A., BIER, K., ROBB, N., VREEDE, F., BARCLAY, W., FODOR, E. & REIS E SOUSA, C. 2010. RIG-I detects viral genomic RNA during negative-strand RNA virus infection. *Cell*, 140, 397-408.
- RHIM, A. D., MIREK, E. T., AIELLO, N. M., MAITRA, A., BAILEY, J. M., MCALLISTER, F., REICHERT, M., BEATTY, G. L., RUSTGI, A. K., VONDERHEIDE, R. H., LEACH, S. D. & STANGER, B. Z. 2012. EMT and dissemination precede pancreatic tumor formation. *Cell*, 148, 349-61.
- ROBERTS, P. C., LAMB, R. A. & COMPANS, R. W. 1998. The M1 and M2 proteins of influenza A virus are important determinants in filamentous particle formation. *Virology*, 240, 127-37.
- ROSSI, C. A., KEARNEY, B. J., OLSCHNER, S. P., WILLIAMS, P. L., ROBINSON, C. G., HEINRICH, M. L., ZOVANYI, A. M., INGRAM, M. F., NORWOOD, D. A. & SCHOEPP, R. J. 2015. Evaluation of ViroCyt(R) Virus Counter for rapid filovirus quantitation. *Viruses*, 7, 857-72.
- ROSSMAN, J. S., JING, X., LESER, G. P. & LAMB, R. A. 2010. Influenza virus M2 protein mediates ESCRT-independent membrane scission. *Cell*, 142, 902-13.

- ROSSMAN, J. S. & LAMB, R. A. 2011. Influenza virus assembly and budding. *Virology*, 411, 229-36.
- ROUZINE, I. M. & WEINBERGER, L. S. 2013. Design requirements for interfering particles to maintain coadaptive stability with HIV-1. *J Virol*, 87, 2081-93.
- RUFF, A. 2018. *Cell-to-Cell Heterogeneity in Influenza A Replication: Influence of Defective Interfering Particle Co-Infection and Ribosome Quantity*. Master thesis, Albstadt-Sigmaringen University.
- RUMSCHLAG-BOOMS, E. & RONG, L. 2013. Influenza a virus entry: implications in virulence and future therapeutics. *Adv Virol*, 2013, 121924.
- RUSSELL, A. B., TRAPNELL, C. & BLOOM, J. D. 2018. Extreme heterogeneity of influenza virus infection in single cells. *Elife*, 7.
- SACK, G. H., FELIX, J. S. & LANAHAN, A. A. 1980. Plaque formation and purification of BK virus in cultured human urinary cells. *J Gen Virol*, 50, 185-9.
- SAIRA, K., LIN, X., DEPASSE, J. V., HALPIN, R., TWADDLE, A., STOCKWELL, T., ANGUS, B., COZZI-LEPRI, A., DELFINO, M., DUGAN, V., DWYER, D. E., FREIBERG, M., HORBAN, A., LOSSO, M., LYNFIELD, R., WENTWORTH, D. N., HOLMES, E. C., DAVEY, R., WENTWORTH, D. E., GHEDIN, E., GROUP, I. F. S. & GROUP, I. F. S. 2013. Sequence analysis of in vivo defective interfering-like RNA of influenza A H1N1 pandemic virus. *J Virol*, 87, 8064-74.
- SALIBA, A. E., WESTERMANN, A. J., GORSKI, S. A. & VOGEL, J. 2014. Single-cell RNA-seq: advances and future challenges. *Nucleic Acids Res*, 42, 8845-60.
- SAMSON, M., PIZZORNO, A., ABED, Y. & BOIVIN, G. 2013. Influenza virus resistance to neuraminidase inhibitors. *Antiviral Res*, 98, 174-85.
- SCHUIND, A., SEGALL, N., DRAME, M. & INNIS, B. L. 2015. Immunogenicity and Safety of an EB66 Cell-Culture-Derived Influenza A/Indonesia/5/2005(H5N1) AS03-Adjuvanted Vaccine: A Phase 1 Randomized Trial. *J Infect Dis*, 212, 531-41.
- SCHULTE, M. B. & ANDINO, R. 2014. Single-cell analysis uncovers extensive biological noise in poliovirus replication. *J Virol*, 88, 6205-12.
- SCOTT, P. D., MENG, B., MARRIOTT, A. C., EASTON, A. J. & DIMMOCK, N. J. 2011. Defective interfering influenza A virus protects in vivo against disease caused by a heterologous influenza B virus. *J Gen Virol*, 92, 2122-32.
- SEKELLICK, M. J. & MARCUS, P. I. 1980. Viral interference by defective particles of vesicular stomatitis virus measured in individual cells. *Virology*, 104, 247-52.
- SHAFFER, S. M., DUNAGIN, M. C., TORBORG, S. R., TORRE, E. A., EMERT, B., KREPLER, C., BEQIRI, M., SPROESSER, K., BRAFFORD, P. A., XIAO, M., EGGAN, E., ANASTOPOULOS, I. N., VARGAS-GARCIA, C. A., SINGH, A., NATHANSON, K. L., HERLYN, M. & RAJ, A. 2017. Rare cell variability and drug-induced reprogramming as a mode of cancer drug resistance. *Nature*, 546, 431-435.
- SHANG, L., CHENG, Y. & ZHAO, Y. 2017. Emerging Droplet Microfluidics. *Chem Rev*, 117, 7964-8040.
- SHAW, A. 2012. New technologies for new influenza vaccines. *Vaccine*, 30, 4927-33.
- SHAW, M. L. & PALESE, P. 2013. Orthomyxoviridae. In: FIELDS, B. N. & KNIPE, D. M. (eds.) *Fields virology*. Philadelphia: Wolters Kluwer.
- SHAW, M. L., STONE, K. L., COLANGELO, C. M., GULCICEK, E. E. & PALESE, P. 2008. Cellular proteins in influenza virus particles. *PLoS Pathog*, 4, e1000085.
- SIMONSEN, L., SPREEUWENBERG, P., LUSTIG, R., TAYLOR, R. J., FLEMING, D. M., KRONEMAN, M., VAN KERKHOVE, M. D., MOUNTS, A. W., PAGET, W. J. & TEAMS, G. L. C. 2013. Global mortality estimates for the 2009 Influenza Pandemic from the GLaMOR project: a modeling study. *PLoS Med*, 10, e1001558.
- SKEHEL, J. J. & WILEY, D. C. 2000. Receptor binding and membrane fusion in virus entry: the influenza hemagglutinin. *Annu Rev Biochem*, 69, 531-69.
- SPENCER, S. L., CAPPELL, S. D., TSAI, F. C., OVERTON, K. W., WANG, C. L. & MEYER, T. 2013. The proliferation-quiescence decision is controlled by a bifurcation in CDK2 activity at mitotic exit. *Cell*, 155, 369-83.
- SPITZER, M. H. & NOLAN, G. P. 2016. Mass Cytometry: Single Cells, Many Features. *Cell*, 165, 780-91.

- STAHLBERG, A., RUSNAKOVA, V., FOROOTAN, A., ANDEROVA, M. & KUBISTA, M. 2013. RT-qPCR workflow for single-cell data analysis. *Methods*, 59, 80-8.
- STANLEY, W. M. 1945. The Preparation and Properties of Influenza Virus Vaccines Concentrated and Purified by Differential Centrifugation. *J Exp Med*, 81, 193-218.
- STEGLE, O., TEICHMANN, S. A. & MARIONI, J. C. 2015. Computational and analytical challenges in single-cell transcriptomics. *Nat Rev Genet*, 16, 133-45.
- STEUERMAN, Y., COHEN, M., PESHES-YALLOZ, N., VALADARSKY, L., COHN, O., DAVID, E., FRISHBERG, A., MAYO, L., BACHARACH, E., AMIT, I. & GAT-VIKS, I. 2018. Dissection of Influenza Infection In Vivo by Single-Cell RNA Sequencing. *Cell Syst*, 6, 679-691 e4.
- STEWART-ORNSTEIN, J., WEISSMAN, J. S. & EL-SAMAD, H. 2012. Cellular noise regulons underlie fluctuations in *Saccharomyces cerevisiae*. *Mol Cell*, 45, 483-93.
- STIEFEL, P., SCHMIDT, F. I., DORIG, P., BEHR, P., ZAMBELLI, T., VORHOLT, J. A. & MERCER, J. 2012. Cooperative vaccinia infection demonstrated at the single-cell level using FluidFM. *Nano Lett*, 12, 4219-27.
- STOHR, K., KIENY, M. P. & WOOD, D. 2006. Influenza pandemic vaccines: how to ensure a low-cost, low-dose option. *Nat Rev Microbiol*, 4, 565-6.
- STOTT, S. L., LEE, R. J., NAGRATH, S., YU, M., MIYAMOTO, D. T., ULKUS, L., INSERRA, E. J., ULMAN, M., SPRINGER, S., NAKAMURA, Z., MOORE, A. L., TSUKROV, D. I., KEMPNER, M. E., DAHL, D. M., WU, C. L., IAFRATE, A. J., SMITH, M. R., TOMPKINS, R. G., SEQUIST, L. V., TONER, M., HABER, D. A. & MAHESWARAN, S. 2010. Isolation and characterization of circulating tumor cells from patients with localized and metastatic prostate cancer. *Sci Transl Med*, 2, 25ra23.
- STRAHLE, L., GARCIN, D. & KOLAKOFSKY, D. 2006. Sendai virus defective-interfering genomes and the activation of interferon-beta. *Virology*, 351, 101-11.
- STUBBINGTON, M. J. T., ROZENBLATT-ROSEN, O., REGEV, A. & TEICHMANN, S. A. 2017. Single-cell transcriptomics to explore the immune system in health and disease. *Science*, 358, 58-63.
- SU, S., FU, X., LI, G., KERLIN, F. & VEIT, M. 2017a. Novel Influenza D virus: Epidemiology, pathology, evolution and biological characteristics. *Virulence*, 8, 1580-1591.
- SU, Y., SHI, Q. & WEI, W. 2017b. Single cell proteomics in biomedicine: High-dimensional data acquisition, visualization, and analysis. *Proteomics*, 17.
- SUBBARAO, K. & KATZ, J. M. 2004. Influenza vaccines generated by reverse genetics. *Curr Top Microbiol Immunol*, 283, 313-42.
- SVEC, D., ANDERSSON, D., PEKNY, M., SJOBACK, R., KUBISTA, M. & STAHLBERG, A. 2013. Direct cell lysis for single-cell gene expression profiling. *Front Oncol*, 3, 274.
- TALEMI, S. R. & HOFER, T. 2018. Antiviral interferon response at single-cell resolution. *Immunol Rev*, 285, 72-80.
- TAN, J., ASTHAGIRI ARUNKUMAR, G. & KRAMMER, F. 2018. Universal influenza virus vaccines and therapeutics: where do we stand with influenza B virus? *Curr Opin Immunol*, 53, 45-50.
- TAPIA, K., KIM, W. K., SUN, Y., MERCADO-LOPEZ, X., DUNAY, E., WISE, M., ADU, M. & LOPEZ, C. B. 2013. Defective viral genomes arising in vivo provide critical danger signals for the triggering of lung antiviral immunity. *PLoS Pathog*, 9, e1003703.
- TEH, S. Y., LIN, R., HUNG, L. H. & LEE, A. P. 2008. Droplet microfluidics. *Lab Chip*, 8, 198-220.
- TELLEZ-GABRIEL, M., ORY, B., LAMOUREUX, F., HEYMANN, M. F. & HEYMANN, D. 2016. Tumour Heterogeneity: The Key Advantages of Single-Cell Analysis. *Int J Mol Sci*, 17.
- TIMM, A. & YIN, J. 2012. Kinetics of virus production from single cells. *Virology*, 424, 11-7.
- TIMM, A. C., WARRICK, J. W. & YIN, J. 2017. Quantitative profiling of innate immune activation by viral infection in single cells. *Integr Biol (Camb)*, 9, 782-791.
- TRINCHIERI, G. 2010. Type I interferon: friend or foe? *J Exp Med*, 207, 2053-63.
- VALIHRACH, L., ANDROVIC, P. & KUBISTA, M. 2018. Platforms for Single-Cell Collection and Analysis. *Int J Mol Sci*, 19.
- VANDERLINDEN, E. & NAESENS, L. 2014. Emerging antiviral strategies to interfere with influenza virus entry. *Med Res Rev*, 34, 301-39.

- VASIN, A. V., TEMKINA, O. A., EGOROV, V. V., KLOTCHENKO, S. A., PLOTNIKOVA, M. A. & KISELEV, O. I. 2014. Molecular mechanisms enhancing the proteome of influenza A viruses: an overview of recently discovered proteins. *Virus Res*, 185, 53-63.
- VERMEULEN, L., TODARO, M., DE SOUSA MELLO, F., SPRICK, M. R., KEMPER, K., PEREZ ALEA, M., RICHEL, D. J., STASSI, G. & MEDEMA, J. P. 2008. Single-cell cloning of colon cancer stem cells reveals a multi-lineage differentiation capacity. *Proc Natl Acad Sci U S A*, 105, 13427-32.
- VON MAGNUS, P. 1951. Propagation of the PR8 strain of influenza A virus in chick embryos. II. The formation of incomplete virus following inoculation of large doses of seed virus. *Acta Pathol Microbiol Scand*, 28, 278-93.
- VON MAGNUS, P. 1954. Incomplete forms of influenza virus. *Adv Virus Res*, 2, 59-79.
- VON RECUM-KNEPPER, J., SADEWASSER, A., WEINHEIMER, V. K. & WOLFF, T. 2015. Fluorescence-Activated Cell Sorting-Based Analysis Reveals an Asymmetric Induction of Interferon-Stimulated Genes in Response to Seasonal Influenza A Virus. *J Virol*, 89, 6982-93.
- VREEDE, F. T., GIFFORD, H. & BROWNLEE, G. G. 2008. Role of initiating nucleoside triphosphate concentrations in the regulation of influenza virus replication and transcription. *J Virol*, 82, 6902-10.
- WANG, D. & BODOVITZ, S. 2010. Single cell analysis: the new frontier in 'omics'. *Trends Biotechnol*, 28, 281-90.
- WAREING, M. D. & TANNOCK, G. A. 2001. Live attenuated vaccines against influenza; an historical review. *Vaccine*, 19, 3320-30.
- WARRICK, J. W., TIMM, A., SWICK, A. & YIN, J. 2016. Tools for Single-Cell Kinetic Analysis of Virus-Host Interactions. *PLoS One*, 11, e0145081.
- WATANABE, K., HANDA, H., MIZUMOTO, K. & NAGATA, K. 1996. Mechanism for inhibition of influenza virus RNA polymerase activity by matrix protein. *J Virol*, 70, 241-7.
- WEAVER, W. M., TSENG, P., KUNZE, A., MASAELI, M., CHUNG, A. J., DUDANI, J. S., KITTUR, H., KULKARNI, R. P. & DI CARLO, D. 2014. Advances in high-throughput single-cell microtechnologies. *Curr Opin Biotechnol*, 25, 114-23.
- WHITE, K. M., AYLON, J., MENA, I., POTENSKI, A., KRAMMER, F. & GARCIA-SASTRE, A. 2018. Influenza B virus reverse genetic backbones with improved growth properties in the EB66(R) cell line as basis for vaccine seed virus generation. *Vaccine*, 36, 1146-1153.
- WHO. 2019. [https://www.who.int/en/news-room/fact-sheets/detail/influenza-\(seasonal\)](https://www.who.int/en/news-room/fact-sheets/detail/influenza-(seasonal)) [Online]. [Accessed January 7th 2019].
- WIDJAJA, I., DE VRIES, E., ROTTIER, P. J. & DE HAAN, C. A. 2012. Competition between influenza A virus genome segments. *PLoS One*, 7, e47529.
- WILLS, Q. F., MELLADO-GOMEZ, E., NOLAN, R., WARNER, D., SHARMA, E., BROXHOLME, J., WRIGHT, B., LOCKSTONE, H., JAMES, W., LYNCH, M., GONZALES, M., WEST, J., LEYRAT, A., PADILLA-PARRA, S., FILIPPI, S., HOLMES, C., MOORE, M. D. & BOWDEN, R. 2017. The nature and nurture of cell heterogeneity: accounting for macrophage gene-environment interactions with single-cell RNA-Seq. *BMC Genomics*, 18, 53.
- WONG, A. H., LI, H., JIA, Y., MAK, P. I., MARTINS, R., LIU, Y., VONG, C. M., WONG, H. C., WONG, P. K., WANG, H., SUN, H. & DENG, C. X. 2017. Drug screening of cancer cell lines and human primary tumors using droplet microfluidics. *Sci Rep*, 7, 9109.
- WRIGHT, P. F., NEUMANN, G. & KAWAOKA, Y. 2013. Orthomyxoviruses. In: FIELDS, B. N. & KNIPE, D. M. (eds.) *Fields virology*. Philadelphia: Wolters Kluwer Lippincott Williams & Wilkins.
- XIN, X., WANG, H., HAN, L., WANG, M., FANG, H., HAO, Y., LI, J., ZHANG, H., ZHENG, C. & SHEN, C. 2018. Single-Cell Analysis of the Impact of Host Cell Heterogeneity on Infection with Foot-and-Mouth Disease Virus. *J Virol*, 92.
- YANGUEZ, E. & NIETO, A. 2011. So similar, yet so different: selective translation of capped and polyadenylated viral mRNAs in the influenza virus infected cell. *Virus Res*, 156, 1-12.
- YE, Z., ROBINSON, D. & WAGNER, R. R. 1995. Nucleus-targeting domain of the matrix protein (M1) of influenza virus. *J Virol*, 69, 1964-70.

- YIN, L., ZHANG, Z., LIU, Y., GAO, Y. & GU, J. 2018. Recent advances in single-cell analysis by mass spectrometry. *Analyst*.
- YORK, A. & FODOR, E. 2013. Biogenesis, assembly, and export of viral messenger ribonucleoproteins in the influenza A virus infected cell. *RNA Biol*, 10, 1274-82.
- YOU, L., SUTHERS, P. F. & YIN, J. 2002. Effects of Escherichia coli physiology on growth of phage T7 in vivo and in silico. *J Bacteriol*, 184, 1888-94.
- YOUIL, R., SU, Q., TONER, T. J., SZYMKOWIAK, C., KWAN, W. S., RUBIN, B., PETRUKHIN, L., KISELEVA, I., SHAW, A. R. & DISTEFANO, D. 2004. Comparative study of influenza virus replication in Vero and MDCK cell lines. *J Virol Methods*, 120, 23-31.
- YUAN, G. C., CAI, L., ELOWITZ, M., ENVER, T., FAN, G., GUO, G., IRIZARRY, R., KHARCHENKO, P., KIM, J., ORKIN, S., QUACKENBUSH, J., SAADATPOUR, A., SCHROEDER, T., SHIVDASANI, R. & TIROSH, I. 2017. Challenges and emerging directions in single-cell analysis. *Genome Biol*, 18, 84.
- ZANINI, F., PU, S. Y., BEKERMAN, E., EINAV, S. & QUAKE, S. R. 2018. Single-cell transcriptional dynamics of flavivirus infection. *Elife*, 7.
- ZAWATZKY, R., DE MAEYER, E. & DE MAEYER-GUIGNARD, J. 1985. Identification of individual interferon-producing cells by in situ hybridization. *Proc Natl Acad Sci U S A*, 82, 1136-40.
- ZHANG, J., PEKOSZ, A. & LAMB, R. A. 2000. Influenza virus assembly and lipid raft microdomains: a role for the cytoplasmic tails of the spike glycoproteins. *J Virol*, 74, 4634-44.
- ZHAO, H., TO, K. K. W., CHU, H., DING, Q., ZHAO, X., LI, C., SHUAI, H., YUAN, S., ZHOU, J., KOK, K. H., JIANG, S. & YUEN, K. Y. 2018. Dual-functional peptide with defective interfering genes effectively protects mice against avian and seasonal influenza. *Nat Commun*, 9, 2358.
- ZHENG, G. X., TERRY, J. M., BELGRADER, P., RYVKIN, P., BENT, Z. W., WILSON, R., ZIRALDO, S. B., WHEELER, T. D., MCDERMOTT, G. P., ZHU, J., GREGORY, M. T., SHUGA, J., MONTESCLAROS, L., UNDERWOOD, J. G., MASQUELIER, D. A., NISHIMURA, S. Y., SCHNALL-LEVIN, M., WYATT, P. W., HINDSON, C. M., BHARADWAJ, R., WONG, A., NESS, K. D., BEPPU, L. W., DEEG, H. J., MCFARLAND, C., LOEB, K. R., VALENTE, W. J., ERICSON, N. G., STEVENS, E. A., RADICH, J. P., MIKKELSEN, T. S., HINDSON, B. J. & BIELAS, J. H. 2017. Massively parallel digital transcriptional profiling of single cells. *Nat Commun*, 8, 14049.
- ZHENG, H., LEE, H. A., PALESE, P. & GARCIA-SASTRE, A. 1999. Influenza A virus RNA polymerase has the ability to stutter at the polyadenylation site of a viral RNA template during RNA replication. *J Virol*, 73, 5240-3.
- ZHENG, W. & TAO, Y. J. 2013. Structure and assembly of the influenza A virus ribonucleoprotein complex. *FEBS Lett*, 587, 1206-14.
- ZHU, X. D., CHU, J. & WANG, Y. H. 2018. Advances in Microfluidics Applied to Single Cell Operation. *Biotechnol J*, 13.
- ZHU, Y., YONGKY, A. & YIN, J. 2009. Growth of an RNA virus in single cells reveals a broad fitness distribution. *Virology*, 385, 39-46.
- ZUMPF, K. 2015. *Untersuchung der intrazellulären Virusreplikation von IAV-infizierten MDCK Zellen auf der Einzelzellebene*. Bachelor thesis, Otto von Guericke University.
- ZVONARJEV, A. Y. & GHENDON, Y. Z. 1980. Influence of membrane (M) protein on influenza A virus virion transcriptase activity in vitro and its susceptibility to rimantadine. *J Virol*, 33, 583-6.

List of publications

Publications

Heldt FS*, **Kupke SY***, Dorl S, Reichl U, Frensing T (2015) Single-cell analysis and stochastic modelling unveil large cell-to-cell variability in influenza A virus infection. *Nature Comm* 6: 8938

Frensing T*, **Kupke SY***, Bachmann M*, Fritzsche S, Gallo-Ramirez L, Reichl U (2016) Influenza virus intracellular replication dynamics, release kinetics and particle morphology during propagation in MDCK cells. *Appl Microbiol Biotech* 100: 7181-92

Kupke SY*, Riedel D, Frensing T, Zmora P, Reichl U (2018) A novel type of influenza A virus-derived defective interfering particle with nucleotide substitutions in its genome. *J Virol* JVI.01786-18

Ruediger D*, **Kupke SY**, Laske T, Zmora P, Reichl U (2019) Multiscale modeling of influenza A virus replication in cell cultures predicts infection dynamics for highly different infection conditions. *PLoS Comp Biol* 15(2):e1006819

* first author

Supervised theses

Zumpf K (2015) Untersuchung der intrazellulären Virusreplikation von IAV-infizierten MDCK Zellen auf der Einzelzellebene. *Bachelor thesis*. Faculty for Process and Systems Engineering, Otto von Guericke University, Magdeburg, Germany

Leupelt A (2017) Clonal heterogeneity of the MDCK cell population: Effect on cell-to-cell variability in influenza A virus replication. *Master thesis*. Department of Applied Biosciences and Process Engineering, Anhalt University of Applied Sciences, Köthen, Germany

Ruff A (2018) Cell-to-Cell Heterogeneity in Influenza A Replication: Influence of Defective Interfering Particle Co-Infection and Ribosome Quantity. *Master thesis*. Faculty Life Sciences, Albstadt-Sigmaringen University, Sigmaringen, Germany

Talks

Kupke SY, Heldt FS, Reichl U, Frensing T (2015) Single-Cell Analysis of Influenza A Virus-Infected Cells for the Optimization of Cell Culture-based Vaccine Manufacturing. *24th ESACT Meeting*. Barcelona, Spain (short talk for poster price)

Kupke SY, Heldt FS, Frensing T, Reichl U (2016) Single-Cell Analysis of Influenza A Virus-Infected Cells. *26th Annual Meeting of the Society for Virology*. Münster, Germany

Kupke SY, Heldt FS, Frensing T, Reichl U (2016) Heterogeneity in Influenza A Virus Infection Unveiled by Single-Cell Analysis and Stochastic Mathematical Modeling. *Single Cell Technologies 2016*. Frankfurt/Main, Germany

Kupke SY, Heldt FS, Frensing T, Reichl U (2016) Single-Cell Analysis of Influenza A Virus-infected Cells for the Optimization of Cell Culture-based Vaccine Production. *Vaccine Technology VI*. Albufeira, Portugal

Kupke SY, Riedel D, Frensing T, Zmora P, Reichl U (2018) Single-Cell Analysis Uncovers a Novel Influenza A Virus Defective Interfering Particle for Antiviral Therapy. *Vaccine Technology VII*. Mont Tremblant, Quebec, Canada

Kupke SY, Riedel D, Frensing T, Zmora P, Reichl U (upcoming in 2019) A novel type of defective interfering particle for antiviral therapy. *26th ESACT Meeting*. Copenhagen, Denmark (short poster spotlight presentation)

Posters

Kupke SY, Heldt FS, Reichl U, Frensing T (2015) Single-Cell Analysis of Influenza A Virus-Infected Cells for the Optimization of Cell Culture-based Vaccine Manufacturing. *24th ESACT Meeting*. Barcelona, Spain

Kupke SY, Heldt FS, Reichl U, Frensing T (2015) Heterogeneity in Influenza A Virus Infection Unveiled by Single-Cell Analysis and Stochastic Mathematical Modeling. *3rd Annual Single Cell Analysis Congress*. London, United Kingdom

Kupke SY, Riedel D, Frensing T, Zmora P, Reichl U (upcoming in 2019) A novel type of defective interfering particle for antiviral therapy. *26th ESACT Meeting*. Copenhagen, Denmark

Patents

Kupke SY, Zmora P, Frensing T, Reichl U (2018) Protective interfering nucleic acid molecule and virus-like particle, viral vector, or virus particle containing the same as well as pharmaceutical composition containing the protective interfering nucleic acid and its use. *EP18159908*, pending

List of figures

Figure 2.1. IAV particle structure.	5
Figure 2.2. Intracellular IAV replication cycle.	7
Figure 2.3. Structure and generation of conventional IAV-derived DI genomes.	11
Figure 2.4. Single-cell analysis.	18
Figure 2.5. Extrinsic and intrinsic noise in gene expression.	19
Figure 4.1. Workflow for single-cell analysis of IAV replication.	50
Figure 4.2. Comparison of single cell- and population-derived measurements.	52
Figure 4.3. Technical measurement error.	53
Figure 4.4. Distribution of virus titer of single IAV-infected cells.	54
Figure 4.5. Histograms of vRNA level of IAV-infected single cells.	55
Figure 4.6. Quantitative correlation between different vRNA segments.	56
Figure 4.7. Single-cell analysis of PR8-RKI virus replication.	58
Figure 4.8. Dependency of virus titer on vRNA level.	69
Figure 4.9. Single-cell virus replication at different times post infection.	70
Figure 4.10. Single-cell virus replication at an MOI of 1.	72
Figure 4.11. Single-cell virus infection with different plaque-purified seed viruses.	74
Figure 4.12. Effect of cell size on virus yield.	76
Figure 4.13. Dependency of single-cell virus titer on ribosome content.	77
Figure 4.14. Growth of clonally-derived MDCK cell populations.	79
Figure 4.15. Virus production of infected clonal MDCK cell populations.	81
Figure 4.16. Single-cell analysis of IAV-infected clonal MDCK cells.	83
Figure 4.17. Effect of intracellular DI RNAs on single-cell virus titer.	85

Figure 4.18. Dependency of virus titers on S7 vRNA level.	95
Figure 4.19. Melting curve analysis of qPCR amplicons.	96
Figure 4.20. Enrichment of OP7 virus.	98
Figure 4.21. Cell population-based infections with OP7 seed viruses.	100
Figure 4.22. Subgenomic vRNAs in virus particles.	101
Figure 4.23. Virus particles imaged by ns-TEM.	102
Figure 4.24. Nucleotide substitutions in genomic S7-OP7 vRNA.	103
Figure 4.25. Viral RNA synthesis in OP7 seed virus-infected cells.	106
Figure 4.26. Intracellular M1 and vRNP localization dynamics upon OP7 seed virus infection.	108
Figure 4.27. Statistical analysis of nuclear vRNP localization dynamics.	109
Figure 4.28. Co-infection of PR8-RKI virus-infected MDCK cells with OP7 seed virus.	110
Figure 4.29. Interference of OP7 virus with replication of various IAV strains in different cell lines.	111

List of tables

Table 3.1. Primers for RNA reference standard generation.	38
Table 3.2. Tagged primers for RT (for quantification of viral RNAs).	39
Table 3.3. Primers for qPCR (for quantification of viral RNAs).	39
Table 3.4. qPCR primers (for analysis of innate immune response).	41
Table 3.5. Primers for segment-specific RT-PCR (of population-based samples).	42
Table 3.6. Primers for segment specific RT-PCR (of single-cell-derived samples).	44
Table 3.7. Primers for vRNA sequence determination.	45
Table A.1. List of chemicals and cell culture reagents.	143
Table A.2. List of kits, enzymes and antibodies.	144
Table B.1. List of equipment and consumables.	145

Appendix

Appendix A - List of chemicals and reagents

Table A.1. List of chemicals and cell culture reagents

Name	Manufacturer	Article No.
7-AAD	Merck	4000-0061
Acrylamide 30%	AppliChem	A3626, 1000
Agarose	AppliChem	A2114, 1000
Ammoniumperoxidisulfat (APS)	Merck	2300
BSA	AppliChem	A1391, 0100
Crystal violet	Roth	C.I. 42555
DAPI	Invitrogen	D1306
DMEM	Gibco	41966-029
EDTA	Sigma-Aldrich	EDS-100g
Ethanol	Roth	9065.4
FCS	Pan Biotech	10270-106
Gentamycin	Invitrogen	15710064
Glycine	Roth	3790.2
GMEM powder	Gibco	22100-093
Isopropanol	Merck	1096342511
Methanol	Roth	CP43.1
Milk powder	Roth	T1452
Peptone	Lab M	LAB204
PFA	Sigma-Aldrich	P6148
Ponceau S red	Sigma-Aldrich	09276
SDS	AppliChem	A2263, 0100
Standard count agar	Sigma-Aldrich	1016210500
TEMED	GE Healthcare	17-1312-01
Tris-Cl	AppliChem	A3452
Triton X-100	Sigma-Aldrich	9002-93-1
Trypane blue	Merck	1117320025
Trypsin	Gibco Sigma-Aldrich	1188797 T7409, T1426
Tween 20	Merck	655204-100ML
β -Mercaptoethanol	Merck	44420
β -propiolactone	Serva Electrophoresis	33672.01

Table A.2. List of kits, enzymes and antibodies

Name	Manufacturer/Origin	Article No.
Alexa Fluor 647-conjugated goat anti-mouse pAb	LifeTechnologies	A21235
BSA solution	Thermo Scientific	B14
dNTPs	Thermo Scientific	R0193
Donkey anti-mouse pAb conjugated with HRP	Jackson ImmunoResearch	715-036-151
FastDigest Green Buffer	Thermo Scientific	B72
FITC-conjugated mAb mouse anti-M1	AbD serotec	MCA401FX
GeneRuler DNA Ladder Mix	Thermo Scientific	SM0333
HRP-conjugated goat anti-rabbit pAb	Jackson ImmunoResearch	111-035-003
InnuPrep PCRpure Kit	Analytik Jena	845-KS-5010250
mAb mouse anti-NP	Fumitaka Momose, Kitasato University, Tokyo, Japan	mAb61A5
Magic Marker Protein Ladder	Invitrogen	LC5602
Maxima H Minus Reverse Transcriptase 5× RT buffer	Thermo Scientific	EP0753
Mouse anti-GAPDH	Merck	CB1001
Mouse anti-M1 mAb	AbD serotech	MCA401
Mouse anti-NP monoclonal antibody	Abcam	ab128193
NucleoSpin RNA	Macherey-Nagel	740955.250
NucleoSpin RNA Clean-up	Macherey-Nagel	740948.250
NucleoSpin RNA Virus	Macherey-Nagel	740956.250
oligo(dT) primer	Thermo Scientific	SO132
Phusion High-Fidelity DNA Polymerase 5x Phusion HF Buffer 5x Phusion GC Buffer MgCl ₂	Thermo Scientific	F530L
Phusion Hot Start II DNA Polymerase	Thermo Scientific	F549L
Primers	Thermo Scientific	-
PureLink RNase A	LifeTechnologies	12091021
QIAquick Gel Extraction Kit	Qiagen	28706
Rabbit anti-PA polyclonal antibody	GeneTex	GTX125932
Random Hexamer Primer	Thermo Scientific	SO142
RevertAid H Minus Reverse Transcriptase	Thermo Scientific	EP0451
RiboLock RNase Inhibitor	Thermo Scientific	EO0382
Roti-GelStain	Roth	3865.2
Rotor-Gene SYBR Green PCR Kit	Qiagen	204074
SuperSignal West Dura Extended Duration Substrate	Thermo Scientific	34075
T4 RNA Ligase 1 10x T4 RNA Ligase Reaction Buffer ATP solution	New England BioLabs	M0204S
TranscriptAid T7 High Yield Transcription Kit	Thermo Scientific	K0441

Appendix B - List of equipment

Table B.1. List of equipment and consumables

Equipment	Manufacturer	Model
384 well plate	Greiner Bio-One	NON-BINDING 781901
Autoclave	HP Medizintechnik	Varioklav 65T
Balance	Sartorius	TE 1502S Cubis precision
Biological safety cabinet	Thermo Scientific	Heraeus HERAsafe SAFE 2020
Cell counter	Beckman Coulter	Vi-Cell XR
Cell scraper	Greiner Bio-One	Scraper 540080
Centrifuge	Thermo Scientific Beckman Coulter	Heraeus Biofuge PrimoR, Fresco 17 Avanti J 20, Optima LE 80K
Chemoluminescence Imager	Intas	ChemoCam HR 16 3200
Agarose gel electrophoresis equipment	Biomed Analytik VWR Gibco Biometra	Agagel Maxi Biometra Power Source 300V BRL UV Transilluminator BioDocAnalyzer
Image flow cytometer	Amnis	ImageStream X Mark II
Incubator	Heraeus	HERAcell 240, 240i HERAcell T6060
Microplate reader	Tecan	Infinite 200 Pro NanoQuant
Microscope	Zeiss	Axioskop 2, Observer.A1 Axiovert 25, 40C, S100
Microtiter plates	Greiner Bio-One	96-well, 6-well CELLSTAR
Multichannel and multistep pipet	Eppendorf	Xplorer plus 50-1200µL
PCR cabinet	Peqlab	PCR Workstation Pro
Pipetting robot	Qiagen	QIAgility
Plate centrifuge	FastGene	Plate Centrifuge
PVDF membrane	Millipore	IPVH00010
real-time PCR cyclers	Qiagen	Rotor-Gene Q
T flasks	Greiner Bio-One	CELLSTAR 75, 175
Thermocycler	Biometra	T3000 T Professional Thermocycler
Ultrapure water purification system	Millipore	Milli-Q Advantage A10
Vortexer	VWR Scientific Industries	Analog Vortex Mixer Vortex-Genie 2
Water bath	VWR Fluke	Ultrasonic Cleaner Isotemp 202
Western Blot Equipment	Biorad Heidolph	Mini Trans-Blot System Power Pac 200 Polymax 1040, MRHei-Standard

Appendix C - Operating Instructions

All SOPs are available upon request from the Bioprocess Engineering group of the Max Planck Institute for Dynamics of Complex Technical Systems (Magdeburg, Germany), headed by Prof. Dr.-Ing. Udo Reichl.

Appendix C.1 - Text excerpt (Generation of clonal MDCK cells)

Short text excerpt of the Master thesis of Annekathrin Leupelt (Leupelt, 2017), conducted and supervised in the context of this PhD work.

4.2.1.5 Cloning and expansion of subclones

The cloning of MDCK cells was carried out by limiting dilution followed by microscopic identification of single cells. The clones were expanded by stepwise passaging in culture vessels of increasing growth area up to a T75 flask.

The cloning procedure described below is the outcome of cloning experiments whereby selected parameters were varied (see paragraph 5.1.1).

For the limiting dilution technique, an MDCK preculture was grown by inoculating a T75 flask with $3.5 \cdot 10^6$ cells and incubated for three days to obtain cells in exponential growth phase. A $0.5 \cdot 10^6$ cells/mL dilution of these cells was then used to seed $1 \cdot 10^6$ cells in 35-mm dishes. Keeping the cells exponentially growing, those were incubated for another 24 h in a humidified atmosphere preventing evaporation of the medium. Two dishes were used to measure the cell count. Therefor, the supernatant was first discarded and the cells were washed with 1 mL PBS. Then 0.5 mL trypsin/EDTA solution was added and the dishes were incubated at 37 °C for up to 15 min and carefully jolted in appropriate intervals to detach the cells. After complete detachment, 0.5 mL Z-medium was added to stop the enzymatic reaction and the cells were suspended by pipetting the liquid up and down several times. The complete cell suspension was applied to the cell count device (paragraph 4.2.1.2) and the obtained cell counts were averaged. The cells in a third dish served for the actual cloning procedure. For that purpose, they were first trypsinized as described above and then serially diluted in 2 mL microcentrifuge tubes (to $3 \cdot 10^5$ cells/mL, $3 \cdot 10^4$ cells/mL and $3 \cdot 10^3$ cells/mL), in a 15 mL centrifuge tube (to $3 \cdot 10^2$ cells/mL) and in a 50 mL centrifuge tube up to a final concentration of $3 \cdot 10^2$ cells/mL which corresponds to an average of 1.5 cells per 50 μ L. The Z-medium used for dilution (conditioned medium was optionally used to improve communication in low cell density scenarios) as well as a non-binding 384-well plate were prewarmed to 37 °C before. The cell suspension was then quickly dispensed to 50 μ L per well onto the 384-well plate with the help of a multichannel multistep pipet in order to isolate single cells. The plate was then optionally incubated in a humidified atmosphere preventing evaporation of the medium until the phase contrast microscopic examination.

Directly or up to 24 h post seeding, the wells of the plate were screened for the presence of single cells by phase contrast microscopy. To promote the cells to settle down, the plate was briefly centrifuged at 150 g for 30 s before. Positive wells were recorded and monitored during the following days to exclude faulty detected ones.

The proliferation and colony formation originating from single cells was documented by taking photos and noting observations like the cell morphology, the confluency and the color of the medium. The medium was exchanged at least once a week to prevent exhaustion. To improve communication in low cell density scenarios conditioned medium was optionally used. When the cells reached a medium to high confluency of 30-70 % and the medium started to shift the color to orange, they were passaged to a larger culture vessel and again grown under the same conditions. This procedure was repeated using a 96-well plate, a 24-well plate (optionally), a 6-well plate and finally a T75 flask as culture vessels. The passaging was performed according to the volumes given in Table 4-7.

Table 4-7: Volumes for passaging of clonal MDCK cells for expansion in different cell culture vessels; arrows indicate the transfer of the cells to the next cell culture vessel; 24-well plate optionally skipped.

Cell culture vessel	Trypsinization			Inoculation	
	PBS	Trypsin/EDTA	Z-medium	Cell suspension	Z-medium
384-well plate	50 μ L	10 μ L	40 μ L		
96-well plate	200 μ L	30 μ L	170 μ L	50 μ L	150 μ L
24-well plate	1 mL	150 μ L	850 μ L	200 μ L	800 μ L
6-well plate	1 mL	500 μ L	500 μ L	200 μ L or 1 mL	1.8 mL or 2 mL
75 cm ² flask	10-15 mL	6 mL	6 mL	1 mL	50 mL

Therefore, the supernatant was first discarded and the cells were washed with PBS. Then trypsin/EDTA solution was added and the plate was incubated at 37 °C for 15-30 min and carefully jolted every 6-7 min to detach the cells. After complete detachment, Z-medium was added to stop the enzymatic reaction and the cells were suspended by pipetting the liquid up and down several times. Without checking the cell count the complete suspension served as a seed for inoculation of plates or flasks prefilled with fresh Z-medium. The cells were then homogeneously distributed by wave movements and put into the incubator.

In case of a limited proliferation due to the formation of tight discrete colonies, the cells were trypsinized as described above and then reseeded into an equivalent cell culture vessel.

When cells reached confluency in the 75 cm² cell culture flask, they were grown at least one more day until cryopreservation (paragraph 4.2.1.6). In case the cell number was not sufficient, the cells were reseeded in a 75 cm² cell culture flask to further expand them and cryopreserved subsequently.

4.2.1.6 Cryopreservation and thawing

The clonal MDCK cell populations were cryopreserved in liquid nitrogen (-196 °C) for long-term storage. Dimethyl sulfoxide (DMSO) served as a cryoprotectant.

Appendix C.2 - Text excerpt (Quantification of ribosomes)

Short text excerpt of the Master thesis of Alexander Ruff (Ruff, 2018), conducted and supervised in the context of this PhD work.

Material and Methods

2.2.6 Analysis of ribosome quantity by 18s rRNA real-time RT-qPCR

Intracellular 18s rRNA in single cells was quantified by real-time reverse transcription quantitative PCR without an intermediate purification step. The reverse transcription transcribes 18s rRNA in complementary DNA using a random hexamer primer. The transcribed cDNA is then used as template for the specific amplification of double-stranded DNA fragments in qPCR. Quantification is achieved by using a fluorescent dye (SYBR green) which intercalates in DNA, thus enabling signal recording during elongation phase (Mühlhardt, 2009).

Reverse transcription and qPCR protocol are described in the following as well as analysis of qPCR results. All samples and reagents were handled on ice and pipetting steps occurred under a PCR hood.

18s rRNA reverse transcription

The reaction was carried out using a PCR cycler. First, mastermix 1 for reverse transcription was prepared according to table 21. First, 5,5 μ l of mastermix 1 were pipetted into each cavity of the PCR plate.

Table 21: Composition of mastermix 1 for reverse transcription of 18s rRNA

Reagent	Volume per reaction [μ l]
dNTPs (10 mM each)	0,5
Random hexamer (100 μ M)	0,5
RNase free water	4,5
Total	5,5

1 μ l of each cell lysate from single-cell isolation was added in cavities containing mastermix 1. After homogenizing, samples were centrifuged for 30 s before removing secondary RNA structures by heating up the samples to 65 $^{\circ}$ C for 5 min. After cooling down to 4 $^{\circ}$ C, 3,5 μ l of mastermix2 (table 22) were added and samples were homogenized and centrifuged (30 s).

Material and Methods

Table 22: Composition of mastermix 2 for reverse transcription of 18s rRNA

Reagent	Volume per reaction [μ l]
5x RT buffer	2,0
RiboLock RNase Inhibitor	0,25
RNase free water	1,0
Maxima H minus transcriptase	0,25
Total	3,5

After centrifugation, reverse transcription reaction was started in a PCR cycler according to temperature profile shown in table 23. Samples were stored at -20 °C after reverse transcription reaction.

In addition, a no template control (RNase free water instead of sample), no enzyme control (RNase free water instead of maxima H minus transcriptase) and a population control were added. For the population control the population-derived intracellular 12 h.p.i. sample, carried with each single-cell isolation (see 2.2.2), was used. After RNA purification, sample was diluted to single-cell level after equation 4. Since 1μ l out of 5μ l cell lysate was used in the described single-cell reaction (0,2 cells per reaction), the population control was diluted to 200 cells/ml. 1μ l of diluted population-derived sample was brought into reverse transcription reaction and therefore achieving 0,2 cells per reaction as well.

$$V_p = \frac{C_D * V_D}{C_p}$$

Equation 4: Calculation of dilution for population control used in 18s rRNA RT-qPCR

C_D = Concentration of dilution [cells/ml]

C_p = Concentration of purified population-derived sample [cells/ml]

V_p = Volume of purified population-derived sample [ml]

V_D = Volume of dilution [ml]

Material and Methods

Table 23: Temperature program of reverse transcription for 18s rRNA using a random hexamer primer

Reaction step	Temperature [°C]	Time [min]
Preheating / Denaturation	65	5
Pause	4	∞
cDNA synthesis	25	10
	50	30
Termination	85	5
Pause	4	∞

Real-time quantitative PCR

The real-time qPCR was carried out on a Rotor-Disc 100 in a dedicated real-time qPCR cyclers. Each sample and control received from reverse transcription was analyzed as two technical replicas. Additionally, two cavities of the Rotor-Disc 100 contained RNase free water as control. For the reaction a qPCR mastermix was prepared according to table 24.

Table 24: Composition of real-time qPCR master mix

Reagent	Volume per reaction [μl]
QuantiTect SYBR green PCR mastermix (2x)	5,0
Forward primer 18s rRNA (10 μM)	0,5
Reverse primer 18s rRNA (10 μM)	0,5
RNase free water	1,0
Total	7,0

A pipet robot filled each cavity of the Rotor-Disc 100 with 7 μl mastermix and 3 μl product received from reverse transcription or RNase free water. Afterwards the Rotor-Disc 100 was sealed and put into the real-time qPCR cyclers. The reaction was carried out using the following temperature profile (table 25).

Material and Methods

Table 25: Temperature profile for 18s rRNA real-time qPCR

Reaction step	Temperature [°C]	Time [min:s]
1 Initial Denaturation	95	5:00
2 Denaturation ³	95	00:10
3 Extension	62	00:20
4 Final denaturation	95	00:15
	65	01:30
5 Melting curve	ramp $\Delta=1$	00:05
	90	each step

After completion of real-time qPCR, C_t -values (cycle threshold) were generated by setting the threshold of the fluorescence signal to 0.05. The C_t -values of all single-cell samples, measured in one run, were used to calculate the ribosome quantity. Since no quantification standard was used, an absolute quantification was not achievable. Therefore, a relative quantification was carried out by using the $\Delta\Delta C_t$ -method. However, the method was adapted since no housekeeping gene could be used due to the large cell-to-cell heterogeneity of single cells (see chapter 1.4). Therefore, the C_t -value of the single-cell sample is directly used as the ΔC_t -value. Furthermore, we calculated the fold change in regard to the average of all C_t -values per run. The fold change over average expresses the amount of ribosomes in one cell compared to the average of all measured cells. Therefore a fold change over average of 2 means that the cell has two times more ribosomes than the average cell.

First, the arithmetic mean was calculated out of all C_t -values per run. In a second step the arithmetic mean was used to calculate the fold change over average by equation 5.

$$\begin{aligned} \Delta C_t &= X_{SC} \\ \Delta\Delta C_t &= X_{SC} - \bar{X}_{SC} \\ \text{Fold Change}_{Average} &= 2^{-\Delta\Delta C_t} \end{aligned}$$

Equation 5: Calculation of fold change over average from real-time RT-qPCR measurements

X_{SC} = C_t -value of single-cell sample

\bar{X}_{SC} = Arithmetic mean of all C_t -values per run

³ Reaction step 2 and 3 were repeated 40 times before continuing with reaction step 4.

Appendix C.3 - Operating instructions (Imaging flow cytometry)

Datum: 07.02.2018
Bearbeiter: Juliana Coronel / Sascha Y. Kupke
Arbeitsbereich: Labor NO.11
Aktualisiert: 26.10.2018

**Max-Planck-Institut
Bioprozesstechnik
Sandtorstr. 1
39106 Magdeburg**

Imaging flow cytometry: sample preparation, staining and data acquisition

The protocol describes the double staining - vRNP complex and cellular nucleus - after infection by Influenza virus (IAV). The monoclonal anti-NP antibody used preferentially binds to NP in the conformation of the vRNP complex, and 4',6-diamidino-2-phenylindole (DAPI) is widely used as nuclear staining.

This protocol can be adapted to other labeling techniques, following selection of appropriate fluorochromes that are excited by the lasers in the ImageStream (375, 488, 561, and 642 nm; besides the scatter laser 785 nm), and corresponding antibodies in the recommended dilutions.

For spectral compensation, it is important to have cells labeled with a single-color positive control for each fluorochromes used. These controls are used to set laser power and also for acquisition of compensation files, which are later used during data analysis to remove the fluorescence that leaks into other channels.

For the positive controls (for each fluorochromes used), samples from two time points of the infection experiment should be mixed (e.g. from early infection and late infection). Thus, cells in different physiological states and cells presenting different amounts of viral proteins are obtained. In case two positive controls are needed (like for NP staining and DAPI), the positive control can be divided into two tubes. One control will be stained with the viral protein antibody and the other with the nuclear marker DAPI.

For infection studies, it is also important to have a "mock infected" experimental control, to set gate for negative cells.

1. Maintenance and troubleshooting

- The instrument should be turned at least twice a month, following the procedures in Section 5;
- We have a contract for "Service Advanced Plan" which includes annual preventive maintenance and the costs regarding repair and service when necessary. Please check the "Instrument Support" brochure attached. For the preventive maintenance, a kit is shipped to our labs and the engineer visit is scheduled;
- Contacts:
General: BioM.maintenance.EU@merckgroup.com
Dr. Peter Rhein, Flow and Imaging Cytometry Application Specialist: peter.rhein@merckgroup.com,
Mobile: +49 (0) 151 1454 8435.

2. Materials

- Ethanol 70% (v/v)
- Paraformaldehyde (PFA) 4% (w/v) **Note:** PFA is a hazardous substance and must be handled following safety instruction.
- FACS Buffer [PBS, 2% (w/v) Glycin, 0.1% (w/v) BSA]
- Blocking Buffer [PBS, 1% (w/v) BSA]

- Nuclear staining: DAPI, 10X concentrated
- 2 mL microtubes with V-bottom

Antibodies for vRNPs (IAV):

- Primary: monoclonal mouse anti-NP mAb61A5 (Momose et al., doi:10.1016/j.micinf.2007.07.00)
- Secondary: Alexa Fluor 647-conjugate polyclonal goat anti-mouse (#A21235, Life Technologies)

3. Sampling, fixation and storage

1. Sample $2 \cdot 10^6$ cells (minimum recommended is $1 \cdot 10^6$ cells) in 15 mL falcon tubes and add PFA to a final concentration of 2%. Incubate on ice for 30 min. Adherent cells must be trypsinized before fixation with PFA.
2. Centrifuge (300 x g, 10 min., 4°C), discard the supernatant and resuspend in approx. 1 mL PBS.
Note: The supernatant containing PFA must be discarded in an identified hazardous chemical waste.
3. Add this suspension drop-wise to 4.5 mL ethanol (70%) in 15 mL falcon tubes, while vortexing the ethanol, and store the aliquots at -20°C until use.

4. Cell staining for NP protein and DAPI

Notes: Before beginning, turn on the centrifuge and set it to 4°C;
In the first step, it is important to use the lowest deceleration as possible to avoid pellet loss;
The sample handling must be done on ice.

1. Centrifuge (300 x g, 10 min., at 4°C). Carefully remove part of the supernatant, leaving 0.5 mL in the tubes. Wash the cells by adding 4.5 mL of FACS Buffer.
2. Centrifuge (300 x g, 10 min., at 4°C). Carefully discard supernatant, without touching the pellet. If necessary, leave some liquid. Wash the cells by adding 1.5 mL of FACS Buffer and transfer every sample suspension to a 2 mL microtube (preferentially with V-bottom).
3. Centrifuge (300 x g, 10 min., at 4°C). Carefully discard supernatant.
4. For blocking, add 25uL of blocking buffer per microtube. Mix it by flicking the microtubes or by knocking the rack. Incubate for 30 minutes at 37°C.
5. Wash the cells by adding 1.5 mL of FACS Buffer. Centrifuge (300 x g, 10 min., at 4°C). Carefully discard supernatant.
6. For vRNP staining, add 25uL per microtube of the anti-NP antibody diluted 1:500 in FACS Buffer. Mix it by flicking the microtubes or by knocking the rack. Incubate for 60 minutes at 37°C in the dark. **Note:** For DAPI positive control, do not add vRNP antibodies (steps 6 & 8).
7. Wash the cells by adding 1.5 mL of FACS Buffer. Centrifuge (300 x g, 10 min., at 4°C). Carefully discard supernatant.
8. Add 25uL per microtube of the secondary antibody diluted 1:500 in FACS Buffer. Mix it by flicking the microtubes or by knocking the rack. Incubate for 60 minutes at 37°C in the dark.
9. Wash the cells by adding 1.5 mL of FACS Buffer. Centrifuge (300 x g, 10 min., at 4°C). Carefully discard supernatant.
10. Repeat step 9.
11. Add 3-5 μ L per microtube of DAPI 10x, assuming that the remaining volume inside the microtube is approximately 30-50 μ L. It is not necessary to incubate for DAPI.
Note: For vRNP positive control, do not add DAPI.
12. Right before each measurement, resuspend the sample and transfer it to a 1.5 mL microtube for acquisition.

5. To begin operation of ISX-MkII

Please consult the INSPIRE ImageStreamX® System Software User's Manual, Version Mark 11, January 2013.

1. Turn on the Linux PC.
2. Check the fluidics, accordingly to the INSPIRE manual (Chapter 3, pg. 14). All buffer containers should be full and the waste tank should be empty. To empty the waste bottle, disconnect the tubing pushing on the quick-disconnect buttons and transfer the liquid to a schott flask for discard (please identify that the waste contains hypochlorite).

Note: Do not add pure hypochlorite to the empty waste tank if the ISX is not going to be used for several days, otherwise it may break up, and the hypochlorite can leak to inner compartments of the ISX. It is recommended to empty the waste bottle and add the hypochlorite short before use.

3. Turn on the instrument.

4. Turn on the Windows PC, login at ad\Amnis, and open the ISX software. Two windows will be open: INSPIRE for the ISX mkII™, where data acquisition is done; and ISX, the command prompt (cmd) that is the "black window".

Note: Do not close the cmd while the program is running.

5. Select "startup". Wait until all calibrations and tests are passed, and the ASSIST button turns green. When all tests are successfully finished, close the calibrations/tests windows.

Note: If any test fails (as indicated in red), repeat it. If it continues to fail, please contact the technical support.

6. Data acquisition

Before starting, please read the detailed instructions in INSPIRE manual (Chapter 3, pgs. 30-34). In the beginning, until you load the samples, run the equipment with PBS buffer to avoid air bubbles in the tubing.

Important notes:

- Samples should contain at least 1 million cells, and the recommended working volume is 50 µL;
- To load samples, only use 1.5 mL microtubes;
- After running the samples, press "Return" to collect the remaining cells (in case it is necessary to repeat the measurement). Control samples are used to set acquisition parameters and to acquire compensation files, as explained below;
- Data is only acquired (and saved) after pressing "Acquire";
- When selecting "Shutdown", everything will be automatically shutdown, including the PCs.

Procedures

The procedures are divided chronologically: before acquisition and acquisition. They should be done accordingly to the sample order (1-7). The power for the lasers must be set before acquisition of all samples of one experiment.

Sample order:

Before acquisition

1. Any sample can be used to set gate for single cells;
2. Single color fluorescence control (no DNA dye) (e.g. vRNP marker) to set laser power and to set gate for positive vRNP cells;
3. Single color DNA dye control (e.g. DAPI) to set laser power and to set gate for positive DAPI cells;
4. Recommended: bleach to wash out DNA dye followed by a tube of PBS for approx. 1 min;

Note: The bleach is 0.4-0.7% hypochlorite. Never use 10% sodium hypochlorite!

Acquisition

5. Control used in step 2, to acquire compensation file;
6. DNA dye control used in step 3, to acquire compensation file;
7. Recommended: bleach 0.4-0.7% (repeat step 4);
8. Experimental samples, double stained.

Before acquisition, it is necessary to adjust parameters and to gate cells.

- **Magnification:**

Usually 60x, for high resolution. EDF off.

- **Fluidics:**

Usually low, for sharpness.

- **Gating on single cells:**

The gate is done to eliminate debris or double cells, and to exclude the Speed Beads.

Set brightfield (BF) to Channel 6. Turn BF on.

Create a scatterplot, of all cells, using the feature "Area" versus "Aspect Ratio". Both features use the brightfield imagery (Channel 6).

Using any sample (recommended: sample 2), gate the single cells. Area values are usually higher than 50 (up to 1,000), and aspect ratio should be higher than 0.6 (up to 1.0).

- **Illumination and Gating on positive cells:**

The power for each laser is determined using the respective single color control (sample 2 and then sample 3), and this is done with all lasers used in the experiment ON and BF ON.

Create histograms, of gated population single cells, using the "Raw Max Pixel" for each channel used (in this case, Channels 1 and 5). The laser power (mW values) should be adjusted until each fluorochrome has Raw Max Pixel intensities between 200 and 1.500.

Notes: While adjusting laser power, do not forget to reset plots every time the value is changed;

Do not change laser settings once established.

Channel 1 (375 nm) is used for DAPI and channel 5 (642 nm), for vRNP.

Gate the positive cells for each single color control only after the laser power is adjusted. Create histograms, of all cells, using the "Intensity" for each channel used (do not use the gate 'single cells'). To set the gate, consider approx. 99% of cells as positive, and excluding the Speed Beads.

Acquisition

- In "File Acquisition", select the filename, destination folder (in the network: MPI LabData/BPE/Amnis), and the number of events.

- For compensation, usually 2.500 counts of positive cells of single color controls (e.g. vRNP positive and DAPI positive) are collected (samples 5 and 6).

Compensation data must be acquired with all lasers used in the experiment ON and **BF OFF**.

- Experimental samples: Usually 10.000 counts of single cells are collected. Alternatively, all events can be collected.

Experimental data must be acquired with all lasers used in the experiment ON and **BF ON**.

